

Quantitative Spectroscopy of BA-type Supergiants in the Small Magellanic Cloud

Den Naturwissenschaftlichen Fakultäten der Friedrich-Alexander-Universität
Erlangen-Nürnberg

zur

Erlangung des Doktorgrades Dr. rer. nat.

vorgelegt von

Florian Schiller

aus Sulzbach-Rosenberg

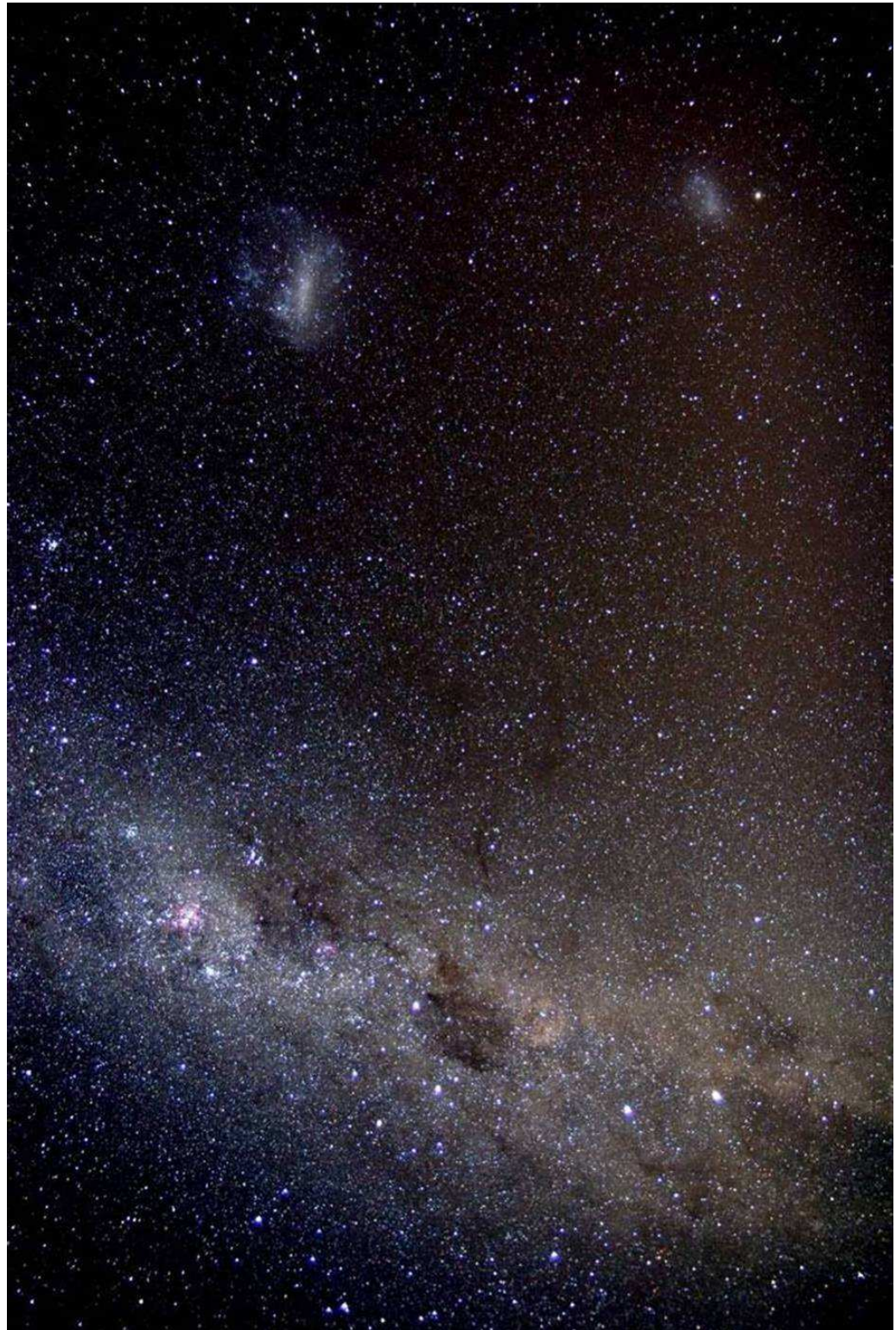
Als Dissertation genehmigt
von der Naturwissenschaftlichen Fakultät
der Friedrich-Alexander-Universität Erlangen-Nürnberg

Tag der mündlichen Prüfung: 29.07.2010

Vorsitzender der Promotionskommission: Prof. Dr. Eberhard Bänsch

Erstberichterstatter: Prof. Dr. Ulrich Heber

Zweitberichterstatter: Prof. Dr. Rolf-Peter Kudritzki



A panoramic view of the southern sky. The foggy band along the bottom is our own galaxy, the Milky Way. Up left and right are the Large and the Small Magellanic Cloud respectively – two neighbour galaxies of the Milky Way some 200 000 lightyears away.

Zusammenfassung

Überriesen der Spektraltypen B und A (BA Überriesen) gehören zu den visuell hellsten Sternen im Universum. Sie können einige zehn Sonnenmassen schwer werden und eine Ausdehnung erreichen, die mit der Umlaufbahn der Erde um die Sonne vergleichbar ist. Durch ihre intrinsische visuelle Helligkeit – in der Größenordnung ganzer Kugelsternhaufen oder sogar kleiner Zwerggalaxien – sind sie selbst in großen Entfernungen hervorragend beobachtbar.

Ihre recht extreme Natur spiegelt sich auch in ihren Atmosphären wider. Die niedrigen Dichten und intensiven Strahlungsfelder verlangen den Einsatz aufwändiger Analysetechniken. Die gängige, doch (zu) einfache Annahme eines Lokalen Thermodynamischen Gleichgewichts (LTE) muss aufgegeben werden. An dessen Stelle tritt die viel allgemeinere Forderung nach Stationarität der atomaren Besetzungsdichten. Die Komplexität der non-LTE Modellierung der untersuchten chemischen Elemente (hier H, He, C, N, O, Mg, S, Ti und Fe) ist ein Grund dafür, dass BA Überriesen bisher relativ spärlich studiert wurden.

Sind die mit einer Analyse verbundenen Schwierigkeiten jedoch überwunden eröffnen sich weitreichende Perspektiven. Insbesondere kann aufgrund der Möglichkeit, diese Sterne auch in anderen Galaxien im Detail zu untersuchen, folgenden Fragestellungen nachgegangen werden:

1. Überprüfung von Entwicklungsmodellen massereicher Sterne in einer Vielzahl unterschiedlicher galaktischer Umgebungen.
2. Untersuchung von Elementhäufigkeitsverteilungen und -gradienten in anderen Galaxien und damit deren chemischer Entwicklung.
3. Verwendung als Standardkerzen zur Entfernungsbestimmung mittels der flussgewichteten Schwerebeschleunigungs–Leuchtkraft Relation (flux-weighted gravity–luminosity relationship, FGLR).

Die vorliegende Arbeit befasst sich mit allen drei Forschungsaspekten durch eine detaillierte quantitative Spektralanalyse von BA Überriesen in der Kleinen Magellanschen Wolke (KMW) – einer relativ nahen (~ 60 kpc) Nachbargalaxie, deren Metallgehalt nur ein Fünftel der Milchstraße beträgt. Hochaufgelöste Spektren mit gutem Signal-zu-Rausch-Verhältnis von 38 Objekten, die mit dem FEROS Spektrograph am 2.2 m Teleskop der Europäischen Südsternwarte (La Silla, Chile) aufgenommen wurden, konnten durch die Anpassung synthetischer Spektren analysiert werden. Diese synthetischen Spektren basieren auf einem ausgefeiltem hybriden non-LTE Ansatz. Atmosphärische Parameter wie Effektivtemperatur (T_{eff}), Oberflächenschwerebeschleunigung ($\log g$) sowie verschiedene chemische Häufigkeiten wurden bestimmt. 1σ -Unsicherheiten für T_{eff} konnten auf wenige Prozent und für $\log g$ sowie Häufigkeiten auf ~ 10 – 20% reduziert werden. Die Qualität des Beobachtungsmaterials und die ausgeklügelte Modellierung erlaubten eine gleichzeitige Reproduktion verschiedener Indikatoren im beobachteten Spektrum und damit eine *Bestimmung* aller wichtigen atmosphärischen Parameter. Dies sorgt für ein bisher nicht erreichtes

Maß an Selbstkonsistenz bei extragalaktischen Spektralanalysen dieser Sterne. Mit Blick auf die zuvor genannten Forschungsschwerpunkte ergeben sich folgende Schlussfolgerungen:

1. Die mit den beschriebenen Methoden erreichte Genauigkeit bei der Bestimmung von Elementhäufigkeitsverhältnissen erlaubt erstmals signifikante Tests von Sternentwicklungsmodellen bei niedriger Metallizität. Zentraler Punkt hierbei ist die Durchmischung der Sternatmosphären mit nuklear prozessiertem Material aus dem Kern eines Sterns. Ausgeprägte Anzeichen für die Präsenz von im CNO-Zyklus prozessiertem Material (Stickstoff-Anreicherung und Kohlenstoff-Abreicherung) wurden in den Atmosphären von allen Sternen entdeckt. Dies legt nahe, dass die Überriesen des Samples entweder viel weiter in ihrer Entwicklung fortgeschritten sind als von der Theorie vorhergesagt oder aber deutlich effizientere Mischungsprozesse vorliegen als bisher angenommen. Solch effiziente Mischungsprozesse werden beispielsweise von den neuesten Sternentwicklungsmodellen vorhergesagt, welche das Wechselspiel von Rotation und Magnetfeldern berücksichtigen.
2. Die genauen Häufigkeiten für die einzelnen Sterne legen zudem einen sehr hohen Grad an chemischer Homogenität (typische 1σ -Streuung 0.1 dex) für die Elemente nahe, die noch nicht durch die Entwicklung in den untersuchten Sternen an- oder abgereichert wurden. Dementsprechend wurden auch keine aussagekräftigen Häufigkeitsmuster oder -gradienten innerhalb der KMW – weder in zwei noch in drei Dimensionen – gefunden.
3. Die Anwendung der FGLR zur Bestimmung der Entfernungen zu den einzelnen Überriesen offenbart eine deutliche Tiefenausdehnung der KMW von $\sim 10\text{--}15$ kpc – ein beachtlicher Wert wenn man ihre Breitenausdehnung auf der Himmelssphäre von ~ 4 kpc bedenkt. Außerdem erscheint die Tiefenverteilung bimodal.

Abstract

Supergiants of spectral type B and A (BA-type supergiants) are among the visually brightest stars in the universe. They may reach masses of several ten times the mass of our Sun and radii comparable to Earth's *orbit* around the Sun. Because of their enormous intrinsic visual brightness – of the order of the *integrated* light of globular clusters or even dwarf galaxies – they are also well accessible from the observational point of view up to large distances.

Their rather extreme nature, though, demands a more extensive treatment from the theoretical point of view. In particular, their extended atmospheres with low densities and intense radiation require a sophisticated physical description accounting for deviations from the (too) simple assumption of Local Thermodynamic Equilibrium (LTE) in order to avoid large systematic uncertainties. The more complicated treatment of the statistical equilibrium of atomic population densities in non-LTE for the elements under investigation (here H, He, C, N, O, Mg, S, Ti, and Fe) may be an important reason why BA-type supergiants have been investigated rather scarcely to date.

However, the difficulties involved are more than balanced by the opportunities. A major aspect is the possibility to investigate these stars with quantitative spectral analyses at large distances (\sim Mpc), including other galaxies. Thus, they may serve

1. to study the evolution of massive stars in a variety of environments,
2. to examine chemical abundance patterns and gradients in other galaxies and thus their chemical evolution, and
3. as independent distance indicators via the flux-weighted gravity–luminosity relationship (FGLR)

The present work addresses all three research aspects through a detailed quantitative spectral analysis of BA supergiants in the Small Magellanic Cloud – a close (\sim 60 kpc) neighbour to our Galaxy with only about one fifth solar metallicity. High-resolution, high signal-to-noise spectra of 38 targets observed with the FEROS spectrograph on the 2.2m telescope of the European Southern Observatory (La Silla, Chile) were analysed by spectral line fitting. The synthetic spectra were calculated using a sophisticated hybrid non-LTE approach and used to determine atmospheric parameters such as effective temperature T_{eff} and surface gravity $\log g$ as well as elemental abundances. 1σ -uncertainties for T_{eff} are reduced to few per cent while $\log g$ and abundances are constrained to ~ 10 – 20% – a precision unprecedented for extragalactic studies of BA-type supergiants. Unlike many previous analyses, a high degree of consistency was achieved by fitting several spectral indicators simultaneously while all important atmospheric parameters are *determined* in a self-consistent way. With respect to the above mentioned applications, the following conclusions can be made:

1. The accurate and consistent abundances allow for the first time to measure abundance ratios of important species, e.g. N/C, with sufficient accuracy to

provide observational constraints on stellar evolution models – in particular with respect to mixing processes. Pronounced signatures of CN-processed matter (nitrogen enrichment and carbon depletion) in the atmosphere are found for all stars and suggest either that the supergiants of the sample must be far more evolved than predicted by theory or that the mixing must be much more efficient than previously thought. In this respect, the efficiency of the mixing corresponds to the predictions from recent stellar evolution models including the interplay of rotation and magnetic fields.

2. The accurate abundances of individual stars also indicate a very high degree of chemical homogeneity (with typical 1σ -scatters of 0.1 dex) for the elements not affected by the evolution of the sample stars. Thus, no clear abundance patterns or gradients – neither in two nor in three dimensions – could be found within the SMC.
3. Applying the FGLR in order to derive distances to the individual targets revealed a significant extension of the SMC in the line-of-sight of ~ 10 - 15 kpc – a remarkable scale given the extension of the SMC in the field-of-view of only ~ 4 kpc. Moreover, the radial star distribution appears to be bimodal.

Contents

1	Introduction	1
2	Basic Properties of Stars	7
2.1	Basic Stellar Parameters	7
2.1.1	Intensity, Magnitudes, and Effective Temperature	7
2.1.2	Spectral Classification	9
2.2	The Inner Structure	10
2.3	Fusion Processes	12
3	Stellar Evolution Theory	17
3.1	Evolutionary Time Scales	17
3.2	Early and mid Phases of Stellar Evolution	17
3.3	Final Stages of Stellar Evolution	21
3.4	Chemical Evolution and Mixing of (Massive) Stars	22
4	Stellar Model Atmospheres	27
4.1	The Absorption of Radiation	28
4.2	Interaction of Radiation and Matter in Local Thermodynamic Equilibrium (LTE)	28
4.3	The Generalisation of non-LTE	32
4.4	Radiative Transfer	33
4.5	Spectral Line Formation	34
4.6	Line Broadening Mechanisms	34
4.7	Radial Velocity, Rotational Velocity, and Macroturbulence	37
5	Structure and Evolution of Galaxies	39
5.1	Basic Galaxy Classification	39
5.2	Principles of Galactic Evolution Theory	41
5.3	Examples for Model Predictions and Observational Constraints	44
5.3.1	Determination of Star Formation Rates and Age-metallicity relations (in the SMC)	44
5.3.2	Element Ratios in Various Environments	44
5.3.3	Abundance Gradients	47
6	Observational Data	51
6.1	Overview of the Sample	51
6.2	Data Reduction	58
7	Quantitative Spectral Analysis	63
7.1	Model Atmospheres and Synthetic Spectra Using a Hybrid non-LTE Approach	63
7.2	Spectroscopic Indicators for Various Atmospheric Parameters	68
7.2.1	Effective Temperature and Surface Gravity	68
7.2.2	Helium Abundance	72

7.2.3	Metallicity and Microturbulence	73
7.2.4	Projected Rotational Velocity and Macroturbulence	74
8	Basic Atmospheric Parameters	77
8.1	Results for the Sample Stars	77
8.2	Projected Rotational Velocity and Macroturbulence	81
8.3	Comparison with Previous Analyses	81
9	Chemical Abundance Analysis	85
9.1	Results for the Sample Stars	85
9.2	Systematics in Abundances	94
9.2.1	Trends with the Temperature	94
9.2.2	Systematic Uncertainties from Parameter Variations	96
9.3	Comparison with Abundance Results for the Sample Stars in the Literature	96
9.4	Constraints on Chemical Mixing in Massive Stars	100
9.5	Chemical Homogeneity of the Small Magellanic Cloud	104
9.6	Previous Abundance Studies in the SMC	107
9.6.1	Young Stellar Populations	107
9.6.2	Old Stellar Populations (Red Giants)	108
9.6.3	Interstellar Medium: H II Regions	111
9.6.4	Summary and Connection to the Present Supergiant Sample	112
10	Distance and Depth Extension of the SMC – the Flux-weighted Gravity–Luminosity Relationship (FGLR)	113
10.1	Theoretical and Observational Motivation	114
10.2	An Attempt to Calibrate the FGLR in the low-Metallicity Environment of the SMC	116
10.3	Probing the Depth Extension of the Small Magellanic Cloud	122
10.4	Distance and Depth Extension of the Small Magellanic Cloud in the Literature	126
10.5	Searching for Abundance Patterns in Three Dimensions	131
10.6	Microturbulence and Luminosity	133
11	Conclusions	135
A	List of Investigated Spectral Lines	139
A.1	Overview About all Employed Spectral Lines with Atomic Information	139
A.2	Lines Employed in Specific Stars with Abundance Information	143
B	Acknowledgements	155

List of Figures

1.1	The galaxy NGC3621	2
1.2	Schematic representation of the Local Group of galaxies	3
2.1	Spectral features for various spectral types	10
2.2	Physical Hertzsprung-Russell-Diagram	11
2.3	Nuclear binding energy	13
2.4	Reaction steps in the pp-chains	14
2.5	Reaction steps in the CNO-cycle	15
3.1	Convection zones for various stellar masses	18
3.2	Theoretical evolution tracks	19
3.3	Onion skin model for massive stars	21
3.4	Elemental distribution in an evolved massive star	22
3.5	Convection zones in massive stars	23
3.6	Meridional currents	24
3.7	Theoretical evolution tracks w/o rotation	25
4.1	Temperature dependence of the ionisation of H and He	30
4.2	Principles of LTE and non-LTE in stellar atmospheres	31
5.1	Hubble classification of galaxies	40
5.2	Colour-magnitude diagram of SMC stars	45
5.3	Star formation rate of the SMC	46
5.4	Age-metallicity relation of the SMC	46
5.5	Element Ratios due to galactic evolution	47
5.6	Element-to-iron ratios in the Milky Way	48
5.7	Oxygen and iron abundances in different environments	48
5.8	Galactic abundance gradients	49
6.1	Location of the sample stars in the SMC (with photo)	52
6.2	Location of the sample stars (plot with new coordinate range)	53
6.3	Raw spectrum from FEROS	58
6.4	Example spectra after data reduction	60
7.1	Illustration of the non-LTE calculations with DETAIL and SURFACE	64
7.2	Basic analysis scheme	67
7.3	Basic determination of temperature and gravity	69
7.4	Examples for fits of spectral lines	70
7.5	Example of a fit of the spectral energy distribution	72
7.6	Helium line fits	73
7.7	Line profile fits to determine rotation and macroturbulence	75
8.1	Overview of projected rotational velocities	81
8.2	Overview of macroturbulent velocities	82
9.1	Atmospheric abundances compared to the solar composition (a)	85
9.2	Atmospheric abundances compared to the solar composition (b)	90
9.3	Abundance trends with the temperature	95
9.4	Chemical mixing: N/C as a function of N/O	101
9.5	Chemical mixing: N/C in the $T_{\text{eff}}-\log g$ diagram	102
9.6	Chemical mixing: He abundance as a function of N/O	103

9.7	Mean stellar abundances at different positions in the SMC (a)	105
9.8	Mean stellar abundances at different positions in the SMC (b)	106
10.1	Flux-weighted gravity–luminosity relationship – a previous calibration	115
10.2	Absolute bolometric magnitudes and flux-weighted gravities	118
10.3	Histogram of distance moduli derived from a given FGLR	123
10.4	Histogram of distance moduli with additional objects	123
10.5	Distances to the sample stars at different positions in the SMC	125
10.6	Distances to eclipsing binaries from the literature	130
10.7	Mean stellar abundances as a function of the line-of-sight distance	132
10.8	Mean stellar abundances as a function of the 3D distance to the center	133
10.9	Microturbulence and Luminosity	134

List of Tables

6.1	Observational summary of the sample stars	54
7.1	Non-LTE model atoms	65
7.2	Observational material for fits of the spectral energy distribution	71
8.1	Basic atmospheric parameters and ionisation equilibria	78
8.2	Comparison of atmospheric parameters with literature sources	83
9.1	Overview of elemental abundances	86
9.2	Systematic abundance uncertainties due to parameter uncertainties	97
9.3	Comparisons of abundances with literature sources	99
9.4	Mean abundances in the SMC and possible 2D gradients therein	104
9.5	Mean abundances in the SMC from the literature for various objects	109
10.1	Flux-weighted gravities, absolute bolometric magnitudes, and distances	119
10.2	Parameters from additional objects	124
10.3	Distance moduli and depth extensions of the SMC from the literature	127
10.4	Possible 3D gradients	134
A.1	Investigated Spectral Lines with Atomic Information	139
A.2	Investigated Spectral Lines in Specific Stars with Derived Abundances	143

1 Introduction

Massive stars are of fundamental importance for the energy and momentum balance of galaxies. They represent major sources for ionising UV radiation, creating bright H II regions within the interstellar medium. The considerable momentum contribution mainly comes from the natural end of massive stars: a supernova explosion as a consequence of the core collapse of the star. These explosions transfer momentum to the interstellar medium and compress it through shockwaves thus triggering new star formation in their surroundings. They also enrich the interstellar medium with helium and heavier chemical elements (= metals) via stellar winds as well as supernova explosions. These elements have been effectively produced in nuclear reactions during the normal life of such stars. Moreover, the supernova explosions themselves are generally believed to be the source of the r-process elements produced by neutron captures.

Massive stars are thus important ingredients for the cosmic cycle of matter by ejecting chemically enriched material into the interstellar medium and triggering at the same time the formation of new generations of stars out of the enriched material. Of course, there are other important contributions to the chemical enrichment of a galaxy from the wind of asymptotic giant branch stars and explosions of low-mass stars as supernovae of type Ia. However, they act on much longer timescales than massive stars. Investigations of massive stars thus allow for constraints on the – not fully understood – evolution of massive stars themselves as well as on the closely related chemodynamic evolution of their host galaxies.

Supergiants of spectral types B and A (BA supergiants) are massive stars which have already evolved away from their birth configuration on the so-called main sequence. They possess up to several ten solar masses, which imply very short lifetimes of a few ten million to several million years, several ten thousand to several hundred thousand times the luminosity of the Sun, and extend from several ten to a few hundred solar radii – a scale of the order of the distance Sun-Earth. It is, hence, not surprising that they are among the visually brightest stars in the universe which makes them suitable targets for extragalactic stellar astronomy probing various galactic environments. Bresolin et al. (2001) have shown that it is possible to get at least a very good idea of the overall metallicities of single stars out to distances of about seven megaparsecs (e.g. in the galaxy NGC3621, Fig. 1.1) with the Very Large Telescope of the European Southern Observatory using intermediate resolution spectroscopy. Other examples of extragalactic stellar studies with determinations of parameters and average metallicities from intermediate resolution spectra are provided by Kudritzki et al. (2008), Urbaneja et al. (2005), Bresolin et al. (2002), Urbaneja et al. (2008), and U et al. (2009) for the galaxies NGC300, WLM, and M33 (all at distances of the order of a Mpc). More detailed investigations of individual elemental and ionic species are feasible at high spectral resolution for distances of the order of several hundred kpc with the state-of-the-art 8-10 m class telescopes. Other prominent examples are M31 as studied by Venn et al. (2000), NGC6822 (Venn et al. 2001), WLM (Venn et al. 2003), and Sextans A (Kaufer et al. 2004).

BA supergiants are thus excellent targets to map the chemical abundance distri-

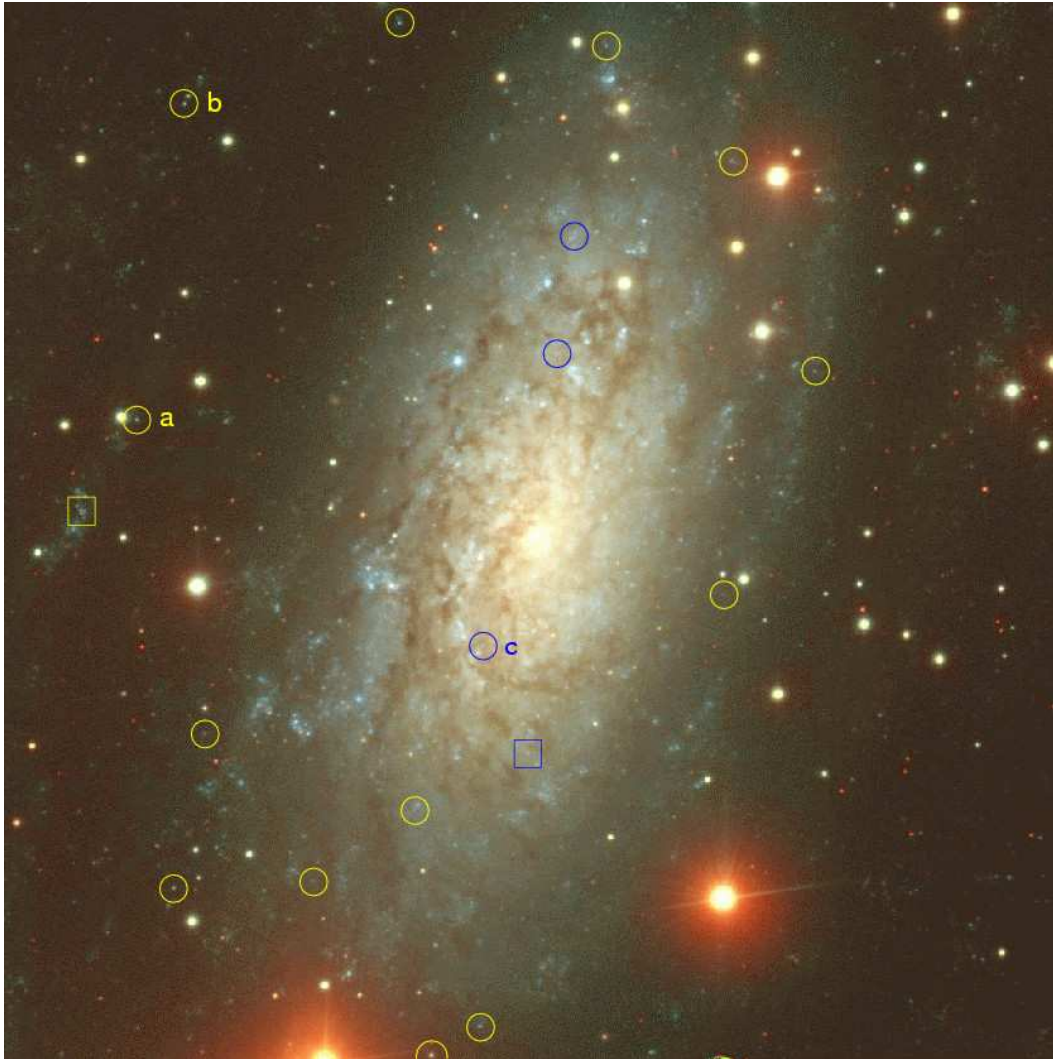


Figure 1.1: NGC3621 at a distance of 6.7 Mpc or 22 Mly. The circles and rectangles denote BA supergiants and H II regions, respectively, from which Bresolin et al. (2001) were able to obtain spectra with FORS1 at the Very Large Telescope.

butions of various species throughout a galaxy and to search for abundance gradients of these elements. This allows to obtain constraints on the chemical evolution of galaxies in a variety of environments. Furthermore, one can study the abundances of elements which are processed in nuclear reactions *deep inside* a star during its life (especially those of He, C, and N). Derived *atmospheric* abundances thus represent important input in order to theoretically describe the efficiency of mixing into the stellar atmosphere. At present, this is an active area of research and several mechanisms including the effects of rotation (e.g. Heger & Langer 2000; Meynet & Maeder 2003) and magnetic fields (Heger et al. 2005; Maeder & Meynet 2005) are being discussed.

In addition to the abundance aspect, BA supergiants also offer a high potential

stars in an environment of low metallicity in great detail.

The present work combines these two interesting fields of research – massive stars and evolution of galaxies – by investigating BA-type supergiants in the Small Magellanic Cloud. One major aspect of this work is the distribution of abundances of various elements throughout this irregular galaxy. For those elements not yet affected by the nuclear processes in the star, possible patterns over the galaxy or the relative abundances of multiple elements with respect to each other allow conclusions on the present-day chemical composition this galaxy (because of the short-lived nature of these stars).

Moreover, abundance ratios of nuclear processed elements (such as He, C, and N) allow to investigate the efficiency of mixing processes in such a metal-poor environment. These may vary with the metallicity of the medium in which a star is formed. According to Maeder & Meynet (2001) or Meynet & Maeder (2005), the lower metallicity leads to more compact stars with faster rotation because of the smaller opacity of the stellar material. This is also the reason for a reduced mass loss through stellar winds which again reduces the slowing down of the rotation due to loss of angular momentum connected to winds. All in all, this is expected to strengthen the efficiency of rotationally induced mixing of processed material from the stellar core into the atmosphere – an effect which we want to test by accurate quantitative spectroscopic analyses.

In addition, the distance determination employing the FGLR is investigated in the low-metallicity environment of the SMC. It will be attempted to check for a metallicity dependence of the FGLR calibration. Moreover, assuming an existing calibration, the distances to individual stars are examined in order to study the line-of-sight extension of the SMC.

In order to draw such conclusions, a sophisticated analysis technique based on hybrid non-LTE spectrum synthesis (Przybilla 2002; Przybilla et al. 2006) is used for investigating high resolution ($R=48\,000$), high signal-to-noise (~ 100) spectra of 38 BA supergiants via line profile fits. Basic atmospheric parameters such as the effective temperature, the surface gravity, microturbulence, helium abundance, and metallicity are determined with great care and form the basis for abundance determinations employing modern atomic data.

The atmospheres of BA supergiants possess in general relatively high temperatures and low densities, representing a considerable challenge for a theoretical description. It is e.g. necessary to account for deviations from the convenient but (too) simple approximation of Local Thermodynamic Equilibrium (LTE) in order to avoid significant systematic effects on the atmospheric parameters as well as on abundances. Such non-LTE calculations also strongly depend on the availability of large amounts of reliable atomic data. Before applying them to the spectral analysis, they have to be calibrated for the parameter ranges present in such atmospheres. This is a considerable effort which might be one reason why (extragalactic) supergiants have been rather scarcely studied in the past. A-type supergiants in the SMC have only been studied so far by Venn (1999, 10 objects). Several hotter (early) B supergiants

were analysed by Trundle et al. (2004, 7 objects), Trundle & Lennon (2005, 10), Lee et al. (2005, 4) and Trundle et al. (2007, 7).

The present work can thus provide an important contribution to the investigation of these remarkable objects especially in an interesting extragalactic environment. The thesis is organised as follows: Section 2 gives an introduction to basic stellar parameters and nuclear processes. This is used to present some information on stellar evolution theory necessary to interpret the main results of this work in Sect. 3. Section 4 provides an overview of the basic concepts behind the description of the matter and the photon flux in a stellar atmosphere. In Sect. 5, the structure and evolution of galaxies is explained in order to be able to draw some conclusions in this respect from the results of this work.

The underlying observational material of the sample stars of this thesis and its processing into a useful form (data reduction) is presented in Sect. 6. The computation of the synthetic spectra used to analyse the observed spectra is explained in Sect. 7 along with the strategy for deriving various atmospheric parameters employing multiple spectral features. The results for those parameters are presented, discussed, and compared with previous analyses in Sect. 8. With these parameters at hand, it is then straight-forward to obtain abundance information for several ionic and elemental species in Sect. 9. Based on the available model atoms, features of He I, C I/II, N I/II, O I/II, Mg I/II, S II/III, Ti II, and Fe II (I denote neutral species, II singly ionised ones and so on) can be analysed in non-LTE in the sample stars. The present work thus represents the most comprehensive non-LTE abundance study of BA-type supergiants at high spectral resolution in an extragalactic environment with the largest set of observed targets – all analysed in a homogeneous way. The derived abundances allow to discuss implications for stellar evolution and the present-day chemical composition of the SMC such as (two-dimensional) abundance patterns. Moreover, in Sect. 10, it is tried to calibrate the FGLR in the low metallicity environment of the SMC. Then, a given FGLR is used to probe the depth extension of the SMC and to investigate possible three-dimensional abundance patterns of this galaxy. Finally, the results are summarised in Sect. 11.

2 Basic Properties of Stars

This section provides a short overview of fundamental properties of stars. It shall mostly address non-astronomers and make them familiar with the sometimes – let us say – unusual quantities and ideas of astronomers.

2.1 Basic Stellar Parameters

2.1.1 Intensity, Magnitudes, and Effective Temperature

Let us define the *specific intensity* I_ν as the radiation power emitted per frequency interval $\Delta\nu$ in the direction of the solid angle $\Delta\omega$ when considering the surface element ΔA under the angle Θ

$$I_\nu := \frac{\Delta E}{\Delta\nu\Delta t\Delta\omega\Delta A\cos(\Theta)} \quad (2.1)$$

The intensity including all possible frequencies is then called the *total intensity*

$$I = \int I_\nu d\nu \quad (2.2)$$

The distant observer on earth is in virtually all cases only able to observe the *integrated* starlight over the whole stellar disc. We therefore define the *flux density* as

$$F_\nu = \oint I_\nu \cos(\vartheta) d\omega \quad (2.3)$$

Again, the *total flux density* is defined as the integral over all frequencies:

$$F = \int F_\nu d\nu \quad (2.4)$$

In order to characterise a star or a stellar atmosphere – the part of a star from which radiation can escape – it is a good idea to assign a characteristic temperature. As there is of course a temperature stratification in a stellar atmospheres because of the fusion processes inside a star, some meaningful average value is necessary. One possibility here is to compare the flux of a star to that of a black body radiator. According to the Stefan Boltzmann law it is

$$F_{\text{bb}} = \sigma T^4. \quad (2.5)$$

where σ is the Stefan Boltzmann constant. Of course, a star is not entirely in thermodynamic equilibrium, however, we can define the *effective temperature* of a star as the temperature of the black body emitting the same total flux F :

$$F = \sigma T_{\text{eff}}^4. \quad (2.6)$$

The effective temperature is a fundamental astrophysical quantity describing a star and a major parameter for stellar atmosphere modelling. BA-type supergiants

as treated in the present work show effective temperatures at the order of $\sim 8000 - 20\,000$ K.

As mentioned above, an observer on earth may only study the light integrated over the whole stellar surface except for the Sun and few giant stars close to the Sun. However, F is the flux on the stellar surface. The observable quantity is therefore

$$f_\nu = F_\nu \frac{R^2}{d^2} \quad (2.7)$$

where R is the radius of the star and d its distance from the observer. The luminosity is the total radiation power of a star:

$$L = 4\pi R^2 \cdot F = 4\pi R^2 \cdot \sigma T_{\text{eff}}^4. \quad (2.8)$$

The quantities defined so far are very logical and easy to understand. However, due the long history of astronomy, several not-so-logical quantities are still in use. One of those is the so-called *magnitude*. It goes back over 2000 years to Hipparch who divided stars based on their brightness in the sky into six classes – 1 being the brightest objects and 6 the faintest ones still visible to the naked eye. This and the fact that the human eye responds logarithmically to incidence of light led to the definition of the *apparent magnitude*

$$m = -2.5 \log \frac{F}{F_0} + m_0 \quad (2.9)$$

where F_0 and m_0 are the flux and magnitude of some standard object – usually the star Vega for historical reasons. Various filters and corresponding magnitudes can be used to characterise a star such as m_U ($/U$, ultraviolet), m_B ($/B$, blue), or m_V ($/V$, visual). Besides this *UBV* system developed by Johnson & Morgan in the early 1950's, other magnitude systems (e.g. of Strömberg) are in use.

Besides the magnitudes themselves, measured *colour indices* or just *colours* are also useful to characterise a star:

$$\begin{aligned} (U - B) &= m_U - m_B \\ (B - V) &= m_B - m_V \end{aligned} \quad (2.10)$$

Absorption/scattering of the starlight by the interstellar matter changes the *intrinsic* colours ($(B - V)_0$, etc.) of a star leading to a *colour excess*:

$$E(B - V) = (B - V) - (B - V)_0 \quad (2.11)$$

In order to subtract distance effects when comparing magnitudes, one can define the *absolute magnitudes* M as the magnitudes when a star is at a distance of 10 pc. Therefore, m and M are related via the distance d (in pc):

$$m - M = -2.5 \log \left(\frac{l}{L} \right) = 5 \cdot \log d - 5 + A_V \quad (2.12)$$

where A_V is the *extinction* in the visual band due to the same effect leading to a colour excess. A_V and $E(B - V)$ are related via

$$A_V = R_V \cdot E(B - V). \quad (2.13)$$

Usually, R_V is ≈ 3.1 , however, it may vary according to different chemical compositions of the medium which the light is passing through.

The *absolute bolometric magnitude* m_{bol} covers the energy emitted in all frequencies. In practice, it is of course not possible to determine the flux over an infinite wavelength range. In order to describe the bolometric flux one therefore uses the *bolometric correction*

$$B.C. = M_{\text{bol}} - M_V \quad (2.14)$$

The absolute bolometric magnitude is directly related to the luminosity by

$$M_{\text{bol}} = -2.5 \log \left(\frac{L}{L_{\odot}} \right) + 4.74. \quad (2.15)$$

with +4.74 being the absolute bolometric magnitude of the Sun.

2.1.2 Spectral Classification

One major scheme for the classification of stars based on stellar spectra is the *Harvard Spectral Classification*. According to several spectral features, stars are classified as

O B A F G K M.

E.g., A-stars show strong hydrogen lines in the spectrum while B-stars have strong lines of neutral helium. Later, it was found that these spectral classes are a temperature sequence in the mentioned order with O stars having the highest effective temperatures ($\sim 30\,000 - 50\,000$ K) and M stars the lowest ones ($\gtrsim 3000$ K). Usually, a finer classification is provided by adding a number from 0 to 9 after the letter, with lower numbers meaning higher temperatures. Figure 2.1 summarises the strengths of lines (equivalent width) of various species present in different spectral types.

The temperature alone can only provide a very rough classification as two stars of the same temperature may have different luminosities by several orders of magnitude. The *Yerkes Spectral Classification* (later the MK classification, after Morgan and Keenan) therefore introduced a second dimension for classification based on the widths of hydrogen lines and relative strengths of ionised elements, the luminosity class:

- Ia most luminous supergiants
- Ib less luminous supergiants
- II luminous giants
- III normal giants
- IV subgiants
- V main sequence stars (dwarfs)

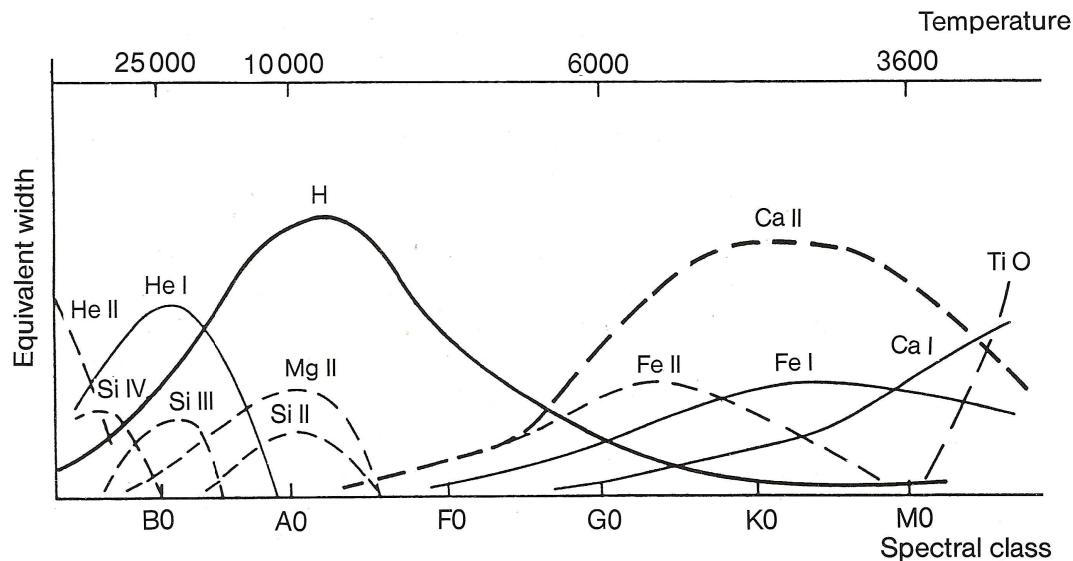


Figure 2.1: Overview of various molecules, elements, and ionic species visible in a stellar spectrum according to the spectral type or effective temperature (from Karttunen et al. 1994).

These designations are very appropriate as differences in the emitted power at constant temperatures comes from varying radii (Eqn. 2.8). A *Hertzsprung-Russell-Diagram (HRD)* shows the absolute magnitudes of stars versus the spectral type. Figure 2.2 presents a more physical version of such a diagram by including luminosity and effective temperature. The *main sequence*, where stars spend the largest fraction of their lives burning hydrogen to helium in the core, is clearly visible and contains stars with luminosity class V. The main sequence is parameterised by the stellar mass, with higher masses providing higher luminosities. The giants and supergiants above belong to later stages of stellar evolution (see Sect. 3). Lines of constant radii are overplotted. For supergiants showing significant emission due to strong stellar wind in the weakly bound atmosphere one has introduced the class Iae.

As was already explained, the spectral type is closely related to the effective temperature of the stellar surface/atmosphere. The luminosity class again is related to the size or – in terms of the physics on the microscopic scale – the density of the stellar atmosphere.

2.2 The Inner Structure

Stars such as our Sun are stable and shine steadily for billions of years. This equilibrium can be described mathematically by four basic equations. The inward gravitational pull on the stellar material shall be matched by its pressure demanding a *hydrostatic equilibrium*

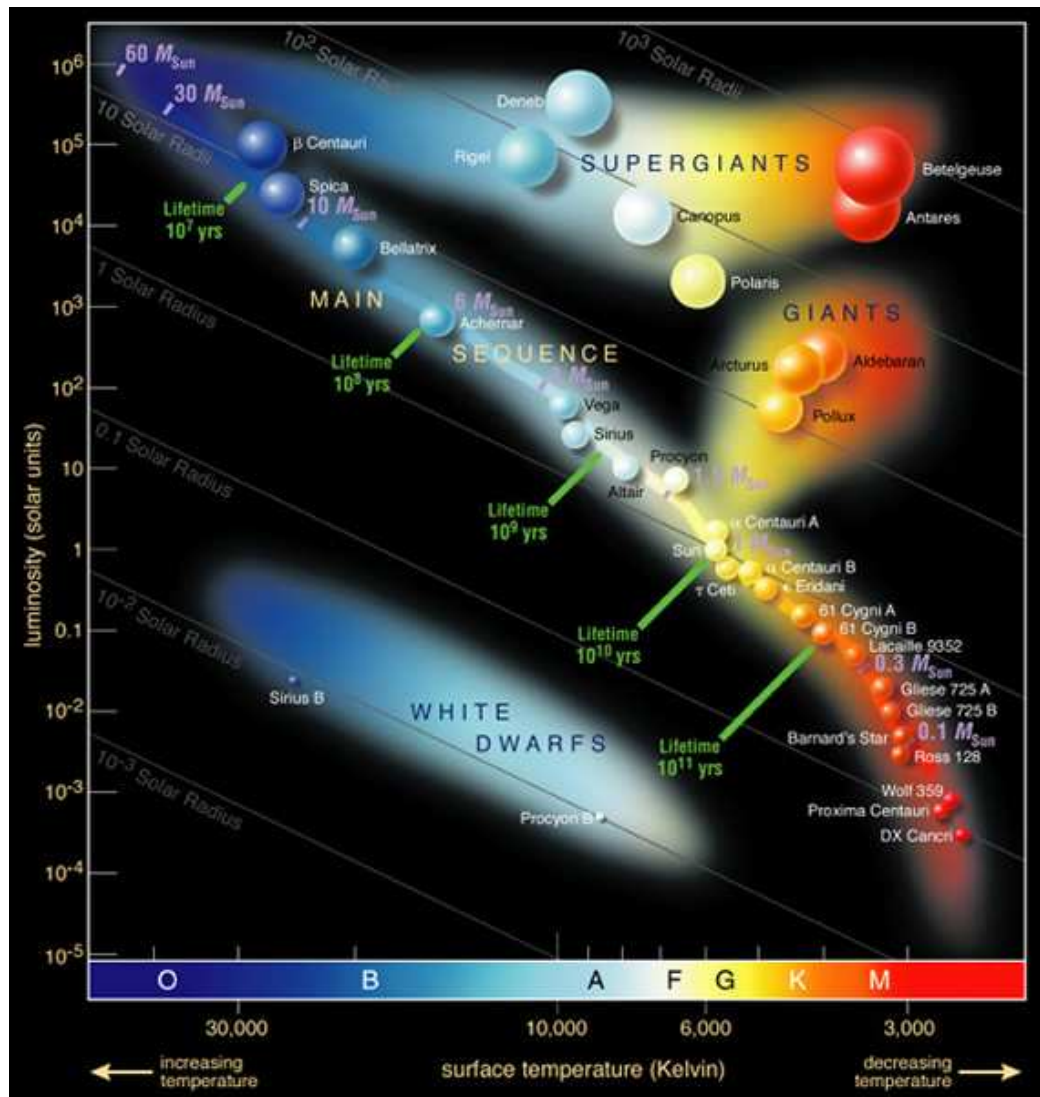


Figure 2.2: Physical Hertzsprung-Russell-Diagram showing luminosities and effective temperatures for a large population of stars.

$$\frac{dP}{dr} = -\frac{GM_r\rho}{r^2}. \quad (2.16)$$

Here, G is the gravitational constant, ρ the density, M_r the mass inside a sphere of radius r and P the pressure. The second equation ensures *mass continuity*:

$$\frac{dM_r}{dr} = 4\pi r^2 \rho. \quad (2.17)$$

Essentially all the energy radiated by a star is produced in the nuclear reaction in the stellar core and needs to be transported outwards to the atmosphere. *Energy conservation* then demands

$$\frac{dL_r}{dr} = 4\pi r^2 \rho \epsilon \quad (2.18)$$

where L_r is the power passing through the surface with radius r and ϵ the amount of energy released in the star per unit time and mass. The energy transport towards the stellar surface can in principle happen through conduction, convection and radiation. As conduction is very inefficient for most stars (except e.g. white dwarfs or neutron stars), energy transport and thus the temperature gradient inside a star is given by

$$\frac{dT}{dr} = -\frac{3}{4ac} \frac{\rho \kappa}{T^3} \frac{L_r}{4\pi r^2} \quad (\text{radiative}) \quad (2.19)$$

$$\frac{dT}{dr} = \left(1 - \frac{1}{\gamma}\right) \frac{T}{P} \frac{dP}{dr} \quad (\text{convective}). \quad (2.20)$$

where a is the radiation constant, c the speed of light, κ the absorption coefficient (amount of absorption per unit mass) and γ the adiabatic exponent. The temperature gradient thus depends on the temperature, density, and chemical composition.

The high temperatures *inside* stars ionise the material almost completely and the interactions between individual particles are small. Therefore the equation of state for an ideal gas is a good approximation:

$$P = \frac{k}{\mu m_{\text{H}}} \rho T \quad (2.21)$$

where k is the Boltzmann constant, μ the mean molecular weight in units of m_{H} , and m_{H} the mass of the hydrogen atom. μ can be deduced from the mass fractions of hydrogen, helium, and heavier elements: X , Y , and Z respectively (for stellar interiors):

$$\mu = \frac{1}{2X + \frac{3}{4}Y + \frac{1}{2}Z} \quad (2.22)$$

In case of high temperatures equation 2.21 must be completed with the radiation pressure $P_{\text{rad}} = \frac{1}{3}aT^4$. In case of a degenerate material as in the iron cores of far evolved stars or in white dwarfs, the following formulae describe the electron gas:

$$P = \frac{h^2}{m_e} \left(\frac{\mu_e}{m_{\text{H}}}\right)^{-5/3} \rho^{5/3} \quad (\text{classical}) \quad (2.23)$$

$$P = hc(\mu_e m_{\text{H}})^{-4/3} \rho^{4/3} \quad (\text{relativistic}) \quad (2.24)$$

2.3 Fusion Processes

Per definition stars are bodies which are bound by self-gravity and which radiate energy supplied by an internal source. For a small fraction of stars, this internal source can be gravitational energy released by contraction or collapse during the contraction of a proto-star towards the main sequence or by cooling e.g. in white

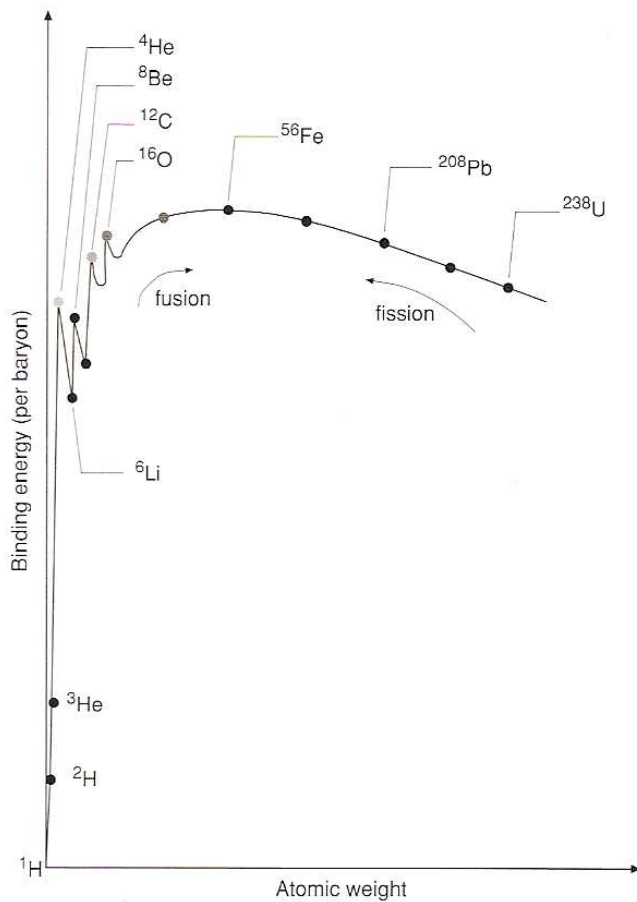


Figure 2.3: Binding energy of various isotopes per nucleon as a function of atomic weight. Fusion of light elements can provide energy up to ${}^{56}\text{Fe}$, the most stable nucleus (from Prialnik 2010).

dwarfs. For the large majority, however, the energy is provided by a set of nuclear reactions fusing light elements to heavier ones inside the stars. Which elements can in principle be used to release energy with fusion reactions? Figure 2.3 shows the binding energy per nucleon versus the atomic weight for several species. Obviously, fusion processes of the light elements, being also the most abundant in the universe, is only possible up to iron – the most stable atomic core. Moreover, the fusion step from ${}^1\text{H}$ to ${}^4\text{He}$ provides the largest amount of energy per reactant atom. Together with the fact that hydrogen is – by far – the most abundant element in the universe, it is easy to accept that fusing hydrogen to helium (hydrogen *burning*) can support and stabilise stars for the major part of their lives.

Therefore, we start our little excursion on fusion processes with the mechanisms available for turning hydrogen into helium. Two basic schemes, the *pp-chain* and the *CNO-cycle* take place in stars. Figure 2.4 is summarising the various reaction steps for the *pp-chain* where different sub-chains (pp I–III) are plotted. Several steps are necessary as assembling four hydrogen cores at the same place in order to fuse them to one helium core is highly unlikely. Instead, several intermediate stages including Li, Be, and B isotopes are employed, with the pp I chain being the dominant process.

The first reaction step in the *pp-chain*, the fusion of two protons to deuterium, has the smallest probability and is responsible for the billions of years of lifetime in

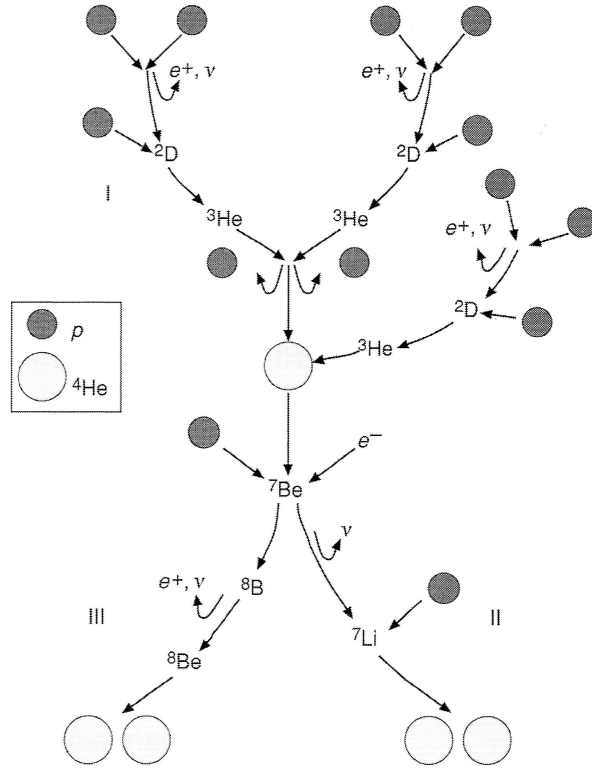


Figure 2.4: The nuclear reactions of the pp-chains: ppI, II, and III (from Prialnik 2010). The ppI branch is the most probable one producing over 90% of the energy in stars like our Sun. For higher temperature, ppII and III contribute more to the energy output.

(low-mass) stars. This is due to the Coulomb barrier between the equally charged atomic nuclei/protons. This barrier is easier to overcome with increased kinetic energy implying that the temperature inside the star where fusion reactions take place is also strongly influencing the reaction speed or the rate of energy released per unit mass:

$$q_{pp} \propto \rho T^4 \tag{2.25}$$

where ρ and T are the local density and temperature respectively.

The second major process for hydrogen burning is the CNO-(bi)-cycle illustrated in Fig. 2.5. The right part of the figure is showing the dominant process. In the CNO-cycle, carbon nitrogen and oxygen act as catalysts with various isotopes of these elements being destroyed and reformed while positrons, neutrinos, and photons are emitted.

As atomic nuclei with much higher charges than in the pp-chain are involved in the CNO-cycle, it is clear that the CNO-cycle is much more sensitive to the local temperature than the pp-chain. The rate of energy released per unit mass for the CNO-cycle may be approximated by a steep power law:

$$q_{CNO} \propto \rho T^{16} \tag{2.26}$$

In addition to the local temperature, the reaction rate in the CNO-cycle also depends on the abundance of the necessary catalysts. Assuming an elemental composition as in our Sun, the pp-chain and the CNO-cycle are equally efficient at a

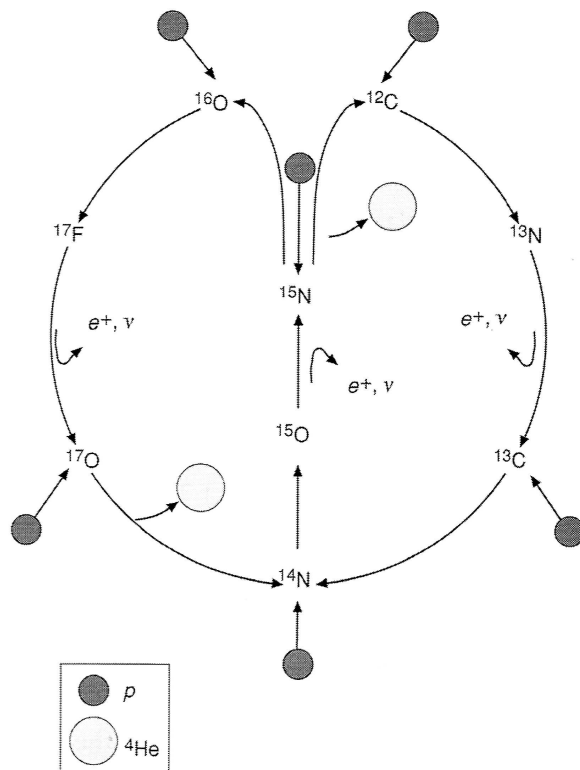


Figure 2.5: The nuclear reactions involved in the CNO-(bi)-cycle (from Prialnik 2010). The right half of the figure shows the main cycle providing the largest energy output.

temperature of about $17.5 \cdot 10^6$ K. Below that temperature, the pp-chain is the dominant process, above it the CNO-cycle.

Higher stellar masses lead to a stronger gravitational pull compressing the core matter to higher densities and also higher temperatures. Therefore, the hot stars on the main sequence are the more massive ones. This also means that the relative contribution of pp-chain and CNO-cycle to the stellar energy output is primarily a function of the stellar mass. The “critical” mass where pp-chain and CNO-cycle produce the same yield is $1.5 M_{\odot}$. At higher masses, CNO burning is dominating.

It is worth mentioning here that the single reaction steps in the main CNO-cycle (right part of Fig. 2.5) exhibit significantly different reaction times. The slowest reaction step is that from ${}^{14}\text{N}$ to ${}^{15}\text{O}$. Because of this bottleneck, the chemical composition will change towards higher nitrogen and lower carbon abundances where the CNO-cycle takes place – deep inside the star (see also Sect. 3.4 for a further discussion of this composition change).

Fusion of hydrogen cores (i.e. protons) may also happen with other atomic nuclei such as Ne or Mg. The corresponding NaNe and MgAl cycles are only important at very high temperatures ($\gtrsim 4 \cdot 10^8$ K) and involve several isotopes of these elements. They are of special interest in the extreme conditions of nova outbursts.

In the later stages of stellar evolution (see Sect. 3) further fusion processes for heavier elements than hydrogen may take place. One of them is the triple- α reaction where three α particles or ${}^4\text{He}$ nuclei are fused to one ${}^{12}\text{C}$ nucleus, with ${}^8\text{Be}$ as interstage.

Several further processes including burning of carbon, oxygen, and silicon up to iron as final product may appear in stars. Heavier elements may be produced through neutron capture in s- and r-processes in the course of the main fusion processes or in supernovae explosions.

3 Stellar Evolution Theory

Relying on the nuclear processes described above, a basic overview on stellar evolution is given. The main focus will be on the evolution of massive stars as they are the objects under investigation here.

3.1 Evolutionary Time Scales

First of all, let us introduce some important timescales for stellar evolution. The *nuclear time scale* is defined as the time in which a star radiates away all the energy that can be released by nuclear reaction. Based on nuclear physics and the assumption that only $\sim 10\%$ of the stellar hydrogen content is turned into helium, one can deduce

$$t_n = \frac{M/M_\odot}{L/L_\odot} \cdot 10^{10} \text{ yr} \quad (3.1)$$

When interpreting this equation one must consider that the luminosity L strongly depends on the stellar mass M . From an empirical calibration one finds the mass–luminosity relation

$$L \propto M^\alpha \quad (3.2)$$

where $\alpha \approx 3$ for a wide range of masses. With that, we obtain

$$t_n \propto M^{1-\alpha} \approx M^{-2}. \quad (3.3)$$

Thus, we come again to the result that the nuclear reactions and hence the lifetime of a star is a function of the total mass. As an example, the nuclear time scale for an $1 M_\odot$ star is $\sim 10^9 \text{ yr}$ and for a $15 M_\odot$ star only $\sim 10^7 \text{ yr}$.

The *thermal time scale* is the time in which a star would radiate away all its thermal energy if the nuclear energy production would suddenly stop:

$$t_{\text{th}} = \frac{(M/M_\odot)^2}{(L/L_\odot)(R/R_\odot)} \cdot 2 \cdot 10^7 \text{ yr}. \quad (3.4)$$

Finally, the last and shortest timescale is the time it would take for the gravitational collapse of a star if the supporting pressure is turned off:

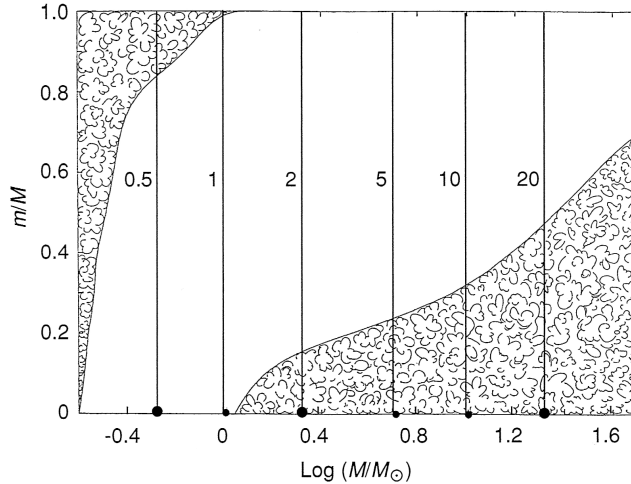
$$t_{\text{ff}} = \sqrt{\frac{R^3}{GM}}. \quad (3.5)$$

3.2 Early and mid Phases of Stellar Evolution

At the very beginning stars are formed out of interstellar dust clouds contracting under their own gravity. The lower mass limit for overcoming the pressure of a gas cloud is given by the Jeans mass

$$M_J \approx 3 \cdot \sqrt{\frac{T^3}{n}} \cdot M_\odot \quad (3.6)$$

Figure 3.1: Overview of convection zones during the main sequence in a wide spectrum of stellar masses (from Prialnik 2010). The y-axis indicates the depth via the mass m contained inside a sphere at the respective depth relative to the total mass. For high-mass stars only the inner layers are convective while for low-mass stars only the outer layers are convective. Stars with $M \leq 0.26 M_{\odot}$ are fully convective.



where n is the density in atoms/m³. Typical properties of the interstellar clouds lead to Jeans masses of about $30\,000 M_{\odot}$. Although much lower Jeans masses are theoretically possible, it is very unlikely to form just one star in such a process. Usually, such clouds fragment forming many stars at a time. The initial impulse for contraction may come from compression of gas in spiral arms or supernova explosions of massive stars (see below).

While contracting the matter is heated up from the release of gravitational energy as soon as the cloud gets optically thick enough. If such a fragment of the cloud ends up with at least $0.08 M_{\odot}$ nuclear fusions in the form of hydrogen burning in the stellar *core* sets in. Hydrogen burning happens on nuclear timescales and stabilises a star for the longest part of its life on the main sequence of the HRD.

Hydrogen burning is producing a core of helium ash being inert in the first instance. While the amount of hydrogen fuel is decreasing in the core, hydrogen burning is gradually transferred into a shell around the core. The star is leaving the main sequence and evolving towards cooler temperatures becoming a red (super)giant. The total mass of the star is then decisively influencing the further evolution. Stars with $M \lesssim 0.6 M_{\odot}$ only experience hydrogen burning. The further discussion is limited to stars $M \gtrsim 0.6 M_{\odot}$

As described in Sect. 2.3, **low-mass** stars burn hydrogen via the pp-chain. As this process is not as sensitive to the temperature as the CNO-cycle in massive stars, the fusion processes are widely spread in the stellar core. Therefore, radiation is effective enough in order to transport the released energy to the stellar surface. However, due to the generally low temperatures in the outer layers, the opacity is high there rendering radiation insufficient to transport the energy. Convection will set in. Fig. 3.1 shows the depth zones where convection takes place for a wide range of masses.

The typical life of a $M > 0.6 m_{\odot}$ star is explained based on the evolutionary tracks of the $1 M_{\odot}$ star in Fig. 3.2. After the main sequence stage, the dislocation of the hydrogen burning zones to outer zones leaves the helium core unsupported by the energy release of nuclear reactions. It will therefore contract increasing its temperature until an equilibrium is found. As hydrogen burns in outer and larger zones and

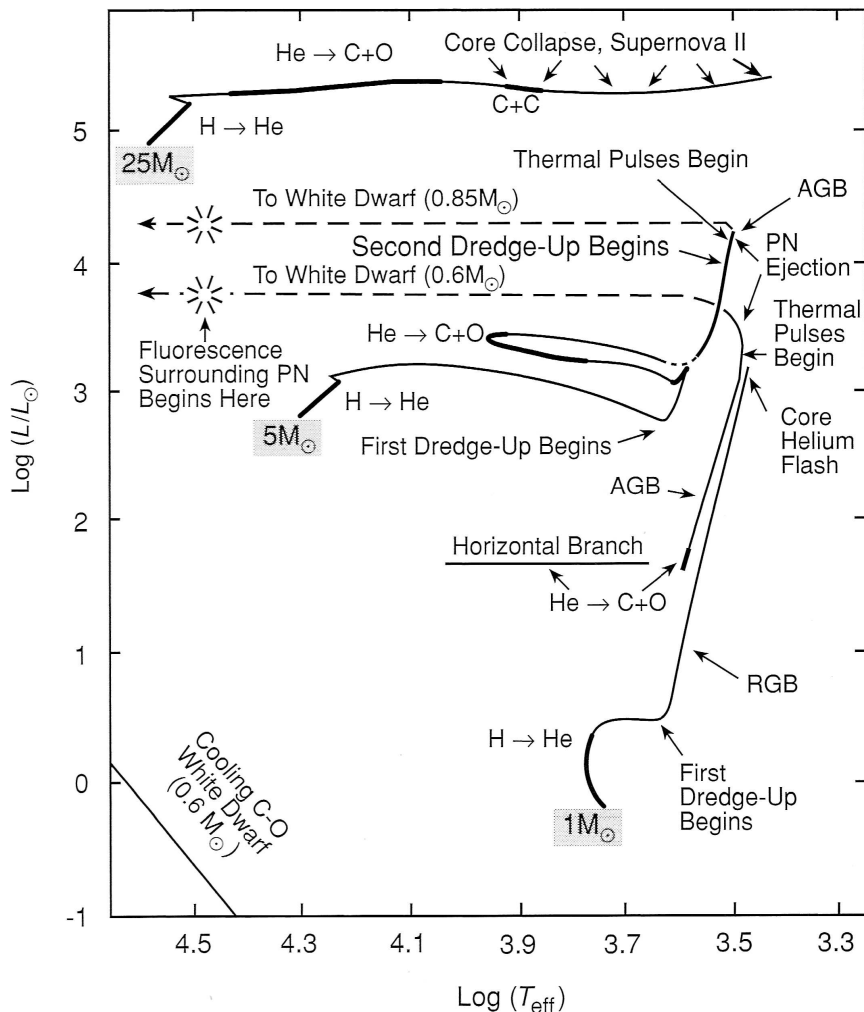


Figure 3.2: Examples for evolutionary tracks in the physical Hertzsprung-Russell diagram for various initial masses (1 , 5 , and $25 M_{\odot}$), from Prialnik (2010). Several important stages in the stellar life are indicated. See text for further explanations. The main sequence can be inferred from the starting point of the three tracks (close to the small shaded areas).

as the core is heated up more and more, the luminosity increases accompanied by a cooling-down of the surface due to an expansion of the envelope. The star then moves along the *red giant branch* or RGB, see Fig. 3.2. An end of this process is reached as soon as helium core burning starts when central temperatures rise to $\sim 10^8$ K.

In low-mass stars, this temperature is not reached before the formerly ideal electron gas in the stellar core becomes degenerate, stabilised by the degenerate pressure. In general, the gas is degenerate only to some extent. Assuming full degeneracy, the gas is described by Eqn. 2.23 or 2.24 in case of an extreme gas with high particle velocities. When helium burning sets in under these conditions, the energy released in this process is not used to expand the core because of no volume dependence in the equations. The energy is therefore only turned into thermal energy raising the core temperature which in turn raises the – extremely temperature sensitive – helium burning rate. This thermal runaway process is also called *helium flash*.

Although this onset of helium burning can be extremely violent, most of its energy is absorbed by the outer layers of the star. After the flash, the star is back to lower lu-

minosities and slightly hotter temperatures on the *horizontal branch* burning steadily helium to carbon in the core with the triple- α process. At some point, also helium will start to burn in a shell forcing the star on the *asymptotic giant branch* or AGB. At those giant branches, the outer layers are weakly gravitationally bound leading to pronounced loss of matter which eventually forms a *planetary nebula* around the star. During this process, the hot inner layers of the star are exposed and the star moves to the left in the diagram. Finally, after the nuclear reactions have stopped, the star mainly consists of a C/O core and is stabilised by the electron pressure. It is cooling down to a white dwarf (see Sect. 3.3) emitting thermal radiation.

Massive stars evolve – apart from the increased evolution speed – in a different way. First of all, they possess a different inner structure on the main sequence. As hydrogen burning is dominated by the CNO-cycle releasing much more energy due to the strong temperature dependence, the core of massive stars is convective as radiation is not sufficient for the outward transport of this energy. Then, in contrast to low-mass stars, the envelopes of massive stars are relatively hot keeping opacities quite low thus allowing radiation to do the job of bringing the energy the last step to the surface.

Moreover, because of the significantly higher core temperature, helium core burning sets in under ideal gas condition, avoiding explosive helium flashes. The star moves upwards in the Hertzsprung-Russell diagram towards higher luminosities at almost constant temperatures (see the tracks for $5 M_{\odot}$ in Fig. 3.2). In this phase after igniting helium burning in the core, the star may experience *blue loops*. The cause for this phase is still a matter of debate and depends on subtle details. An overview of the discussion and effects of helium abundance or metal content on the extent of blue loops is given by Xu & Li (2004a, 2004b). The higher the stellar mass, the smaller the extent of these blue loops. Moreover, there seems to be a dependence on the metallicity so that blue loops are favoured at quite low (0.004 mass fraction) and quite high (0.02) metallicities. Two effects leading to this behaviour are suggested. Firstly, the reduced opacity at lower metallicity leads to a hotter stellar envelope which favours energy transport by conduction (and thus blue loops) in contrast to convection. Secondly, rather high metallicities and thus rather high abundances of ^{14}N makes the hydrogen shell burning more efficient through a larger contribution from the second cycle of the CNO bi-cycle (left part of Fig. 2.5). This pushes the star more effectively into a blue loop.

With sufficiently high masses further fusion processes may take place (under non-degenerate conditions) leading to multiple layers with distinct burning processes working their way outwards and leaving the ashes behind as fuel for the next process. This onion skin model is schematically presented in Fig. 3.3. As the difference in binding energy per nucleon decreases towards the fusion of higher elements, each process must happen faster to stabilise the star. Figure 3.4 shows the distribution of various elements throughout an evolved massive star. The last possible reaction is reached by fusing silicon to iron which shows the highest binding energy per nucleon (see Sect. 2.3) taking place in about one *day*. Further energy then can not be gained through fusion reaction and a core collapse supernova is produced as soon as the inert iron core has grown to a certain threshold, the *Chandrasekhar mass* (see Sect. 3.3).

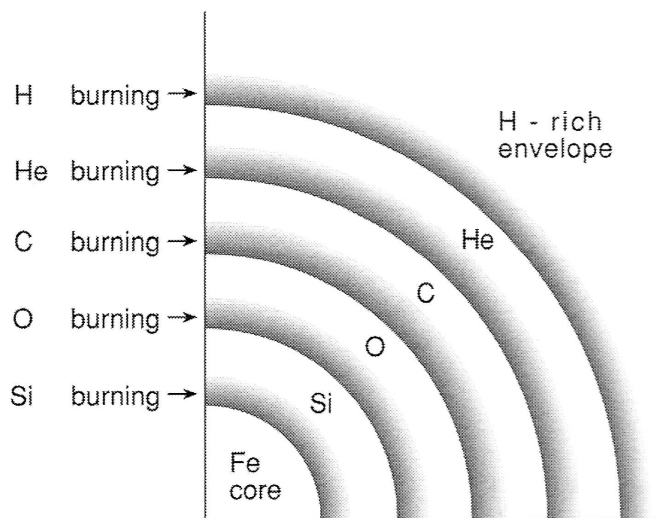


Figure 3.3: Onion skin model for massive stars ($M \geq 8 M_{\odot}$) from Prialnik (2010). This is situation immediately before the collapse of the inert iron core leading to a type II supernova.

These explosions are possible sites for the formation of elements heavier than iron through neutron-capture of nuclei in the r-process on the iron seeds. In addition to the chemical enrichment of the interstellar medium, these explosion may also trigger new star formation through the resulting shock waves.

3.3 Final Stages of Stellar Evolution

For completeness, the final stages of stellar evolution are briefly summarised here. It will not surprise that the final fate of star again depends on the mass. However, note that mass is usually meant as “mass at the end of the evolution”. During the red (super)giant phase there is pronounced mass loss due to the small gravitational pull on the outer layers. Moreover, for massive stars, there can also be significant mass loss before that stage because of the strong radiation field leading to strong stellar winds. The subject is too complex and extensive for a detailed discussion at this point. As a guide, mass loss from the solar wind is of the order of few $10^{-14} M_{\odot}/\text{yr}$ while for a $30 M_{\odot}$ main sequence star it is roughly $10^{-5.5} M_{\odot}/\text{yr}$ depending on the temperature. For stars in the red giant phase it can range – again depending on the temperature – from $\sim 10^{-8} - 10^{-2} M_{\odot}/\text{yr}$ due to the strong increase of the stellar radius and the consequently weakly bound outer layers.

In case of final masses below the *Chandrasekhar mass* ($M_{\text{Ch}} = 1.44 M_{\odot}$ for a C/O- or He core) the final state will be a *white dwarf* which is stabilised by the degenerate pressure of the electron gas. The equations 2.23 or 2.24 as well as 2.16 and 2.17 fully describe the star and imply

$$R \propto \frac{1}{\sqrt[3]{M}} \quad (3.7)$$

meaning that the radius of a white dwarf is decreasing when additional material is added. For arbitrarily large masses, the white dwarf would contract to arbitrarily small radii. This problem is “solved” by using the relativistic equations which predict

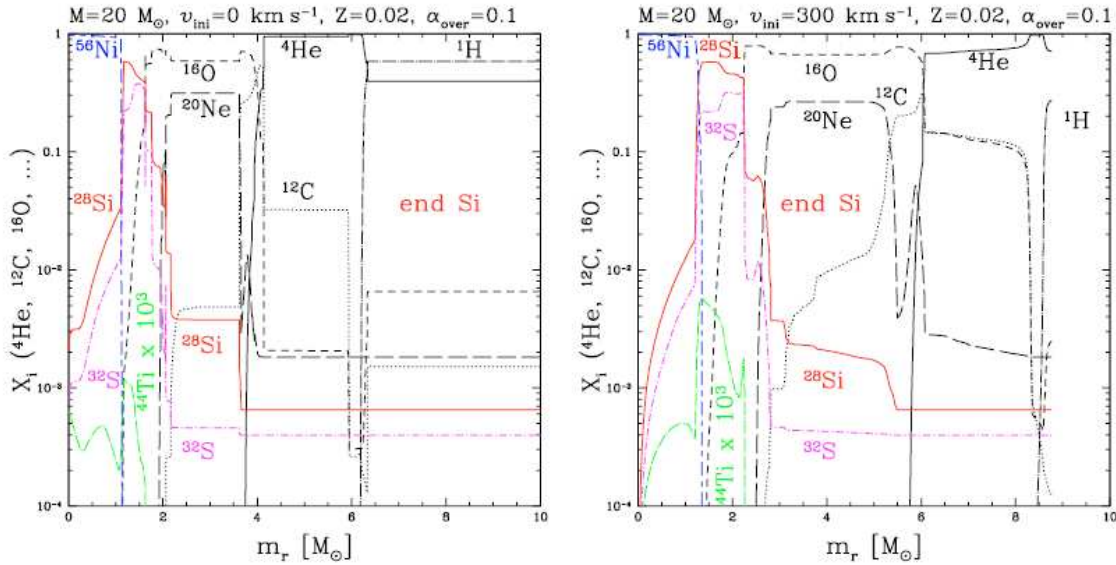


Figure 3.4: Elemental distribution in an evolved massive star as a function of mass inside a certain radius m_r at the end of silicon burning, from Hirschi et al. (2004). The models were calculated for a $20 M_{\odot}$ star at solar metallicity ($Z = 0.02$) for initial rotational velocities of 0 (left) and 300 (right) km s^{-1} . The general effect of rotation is that burning zones and cores reach further towards the surface.

zero radii as soon as the Chandrasekhar mass is reached. Of course, this does not really solve the problem as zero radii or infinitely large densities are impossible. If a white dwarf is *accreting* mass and gets close to the Chandrasekhar mass it will thus explode as supernova type Ia – a thermonuclear reaction disintegrating the whole star.

In the case of massive stars with iron core masses higher than M_{Ch} at the end where all fusion sources are exhausted, the result will be a collapse towards densities as in atomic nuclei. A *neutron star* is formed which is supported by the degenerate pressure of the neutron gas created when protons and electrons are forced to react to neutrons.

Above end masses higher than the *Oppenheimer-Volkoff mass* ($\sim 3 M_{\odot}$) even pure neutrons are no longer able to provide support against gravitation. The star will collapse to a *black hole*. Neutron stars or black holes are the products of core collapse supernova explosions of a massive star.

3.4 Chemical Evolution and Mixing of (Massive) Stars

As described so far, stars and in particular massive stars undergo various phases of evolution including multiple fusion processes happening *inside* the star where conditions are sufficient. These newly produced elements, the ashes of the burning processes, may be distributed into the interstellar medium when a massive star finally explodes and is disrupted. However, observing these elements deep inside a star is impossible as the light which could be used for an analysis originates from the stellar

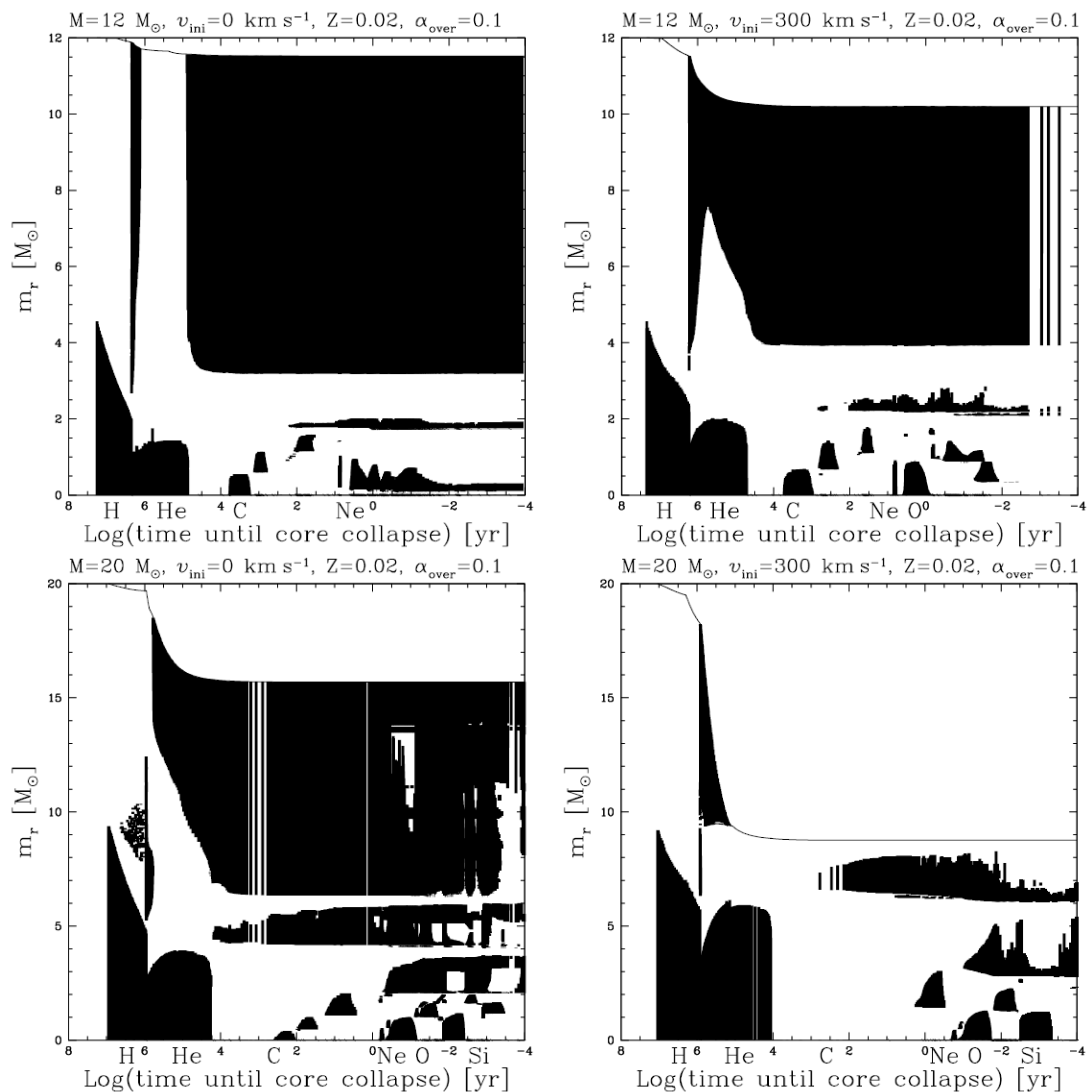


Figure 3.5: Kippenhahn diagrams indicating convective zones at certain depths in the star (black areas) from Hirschi et al. (2004). *Up/down*: Model for $12/20 M_{\odot}$, *left/right*: initial rotational velocities of $0/300 \text{ km s}^{-1}$. Indicated along the x-axis are the various burning phases in addition to the logarithmic timescale. The $12 M_{\odot}$ model for no rotation shows no convection for a certain period of time (after the sharp black area from the top) indicating a blue loop phase. The models with rotation or higher masses avoid this state and show also significant mass loss.

atmosphere. Thus, in order to “see” the results of these processes, there has to be mixing of some kind between the deep burning layers inside the star and the outer atmosphere. Which processes for transporting matter are effective in a star?

One important process is *convection*, the most effective form for matter transport. In Sect. 3.2, we saw that convection already happens in main sequence stars of all masses either in the stellar core (massive stars) or in the outer layers and the atmosphere (low-mass stars) in order to transport the energy output of the nuclear

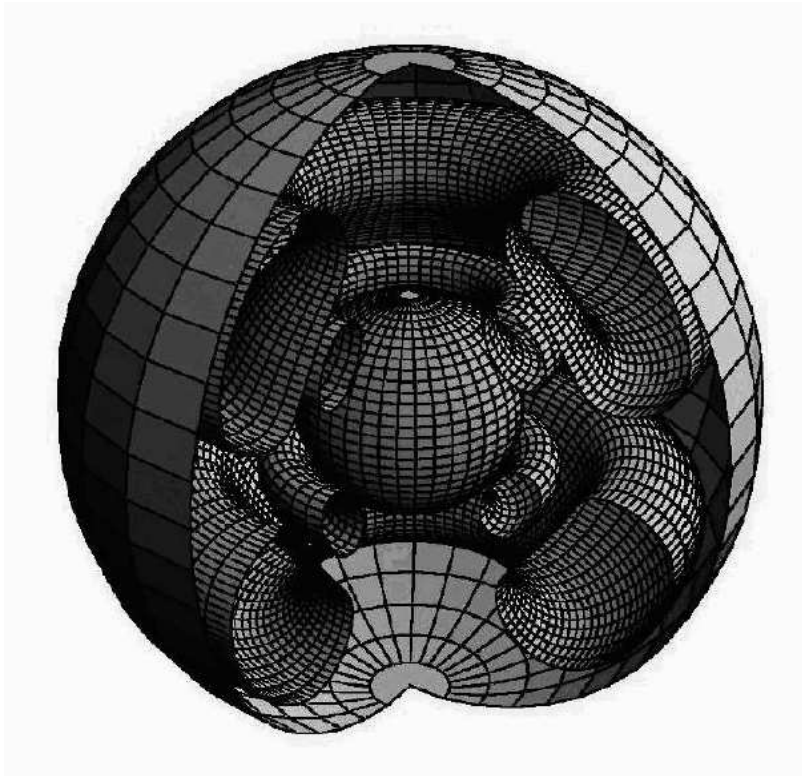


Figure 3.6: A 3D contour plot by G. Meynet representing the inner structure of a massive rotating star. The toroidal shape of the meridional currents is clearly visible.

reactions to the stellar surface (see also Fig. 3.1). This convection would in principle also transport matter and thus burning products throughout the star. *However*, these convection zones never cover all the necessary depths from the atmosphere down to the burning core (except for very low-mass stars). Therefore, during the main sequence, convection is inappropriate to reveal abundance patterns due to nuclear reactions to an external observer.

However, during more evolved phases in the evolution of massive (and also low-mass) stars, convection plays an important role for mixing as can be seen in Fig. 3.5. For the $12 M_{\odot}$ models (upper two plots), the convection zone in the core on the main sequence due to the extensive energy release in the CNO-cycle is nicely visible (black area down left). In that phase, processed material is transported up to radii corresponding to $m_r \lesssim 4 - 5$ but not to the surface. This may happen at later stages when further nuclear reactions set in. The sharp black area from the surface down to $m_r \sim 3$ is the convection zone created at a later phase of hydrogen shell burning and the onset of central helium burning. This is called the *first dredge-up*. As the convection zone in this dredge-up goes deeper than the previous convection zone from the hydrogen burning, nuclear processed matter can reach the surface and may thus be detected by studying atmospheric abundances. During the further life as red supergiant there are further opportunities for extensive mixing between nuclear processed matter from the stellar core and the atmosphere by convection.

Convection (in the late phases of stellar evolution) is not the only mechanism that can lead to mixing. During the main sequence and before the red supergiant stage, *meridional currents* (Fig. 3.6) induced by rotation may already lead to mixing. (Stars

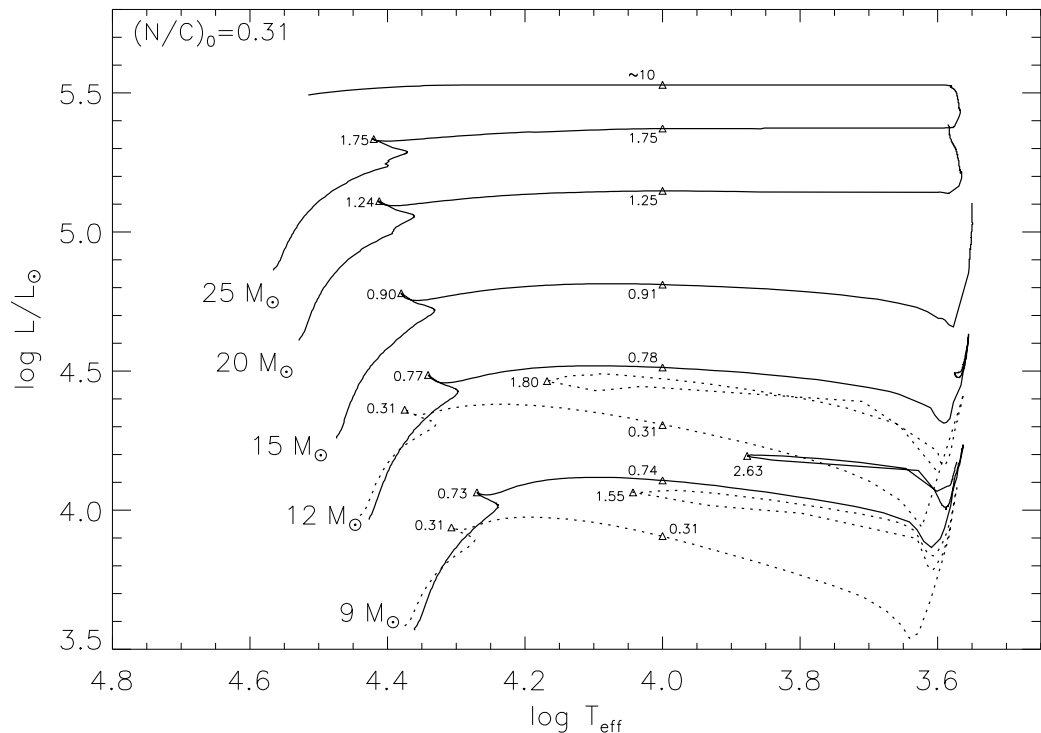


Figure 3.7: Theoretical evolution tracks for massive stars with zero-age main sequence masses from 9 to $25 M_{\odot}$. The tracks are based on the models provided by Meynet & Maeder (2003) including mass-loss (depending on the initial mass and the evolutionary state, e.g. $10^{-5.5} M_{\odot}/\text{yr}$ for the rotating $15 M_{\odot}$ model at $10\,000\text{ K}$). Dotted curves are calculated for non-rotating models while solid lines account for an initial rotational velocity of 300 km s^{-1} . The numbers along the tracks indicate the N/C mass ratio starting with $(\text{N/C})_0 = 0.31$ on the main sequence.

are born with high angular momentum and, hence, rotate quickly.) The meridional currents can have several reasons. One reason comes from the flattening of a rotating star on the poles due to centrifugal forces. This leads to higher temperatures on the poles than present along the equator inducing currents surfacing at the poles and diving back at the equator. A second reason for rotationally induced mixing is based on differential rotation. Rotational velocities on the poles are smaller than along the equator leading to friction in the star and thus to turbulences (shear instabilities) and matter transport.

In this picture, fast-rotating stars are expected to experience more efficient mixing. Moreover, models predict higher mixing rates for larger stellar masses despite a reduced lifetime (see Fig. 3.7). In massive stars, more efficient mixing will e.g. appear as enhanced N/C and N/O ratios due to the physics of the CNO-cycle (see Sect. 2.3). Precise determinations of stellar atmospheric abundances through observations thus provide important input and constraints for stellar evolution models of massive stars.

4 Stellar Model Atmospheres

Virtually all information about stars is derived from the emitted light – in the *stellar atmosphere*. The atmosphere is defined as the region of a star from which photons can escape into space. (Of course, this must be a matter of probabilities and wavelength-dependent.) Information on the stellar atmosphere and other characteristic stellar parameters can be derived by analysing the observed *spectrum* created therein. One important approach is the comparison of *synthetic spectra* based on *model atmospheres* – a set of parameters (such as temperature or density) as a function of depth.

This section shall provide an overview of the physical principles embedded in codes which were employed in the present study. A detailed picture is given e.g. by Mihalas (1970) or Hubeny (1997). The model atmospheres used in this work for supergiants of spectral types B and A are based on several assumptions:

- *Plane-parallel geometry.* Even in the extended atmospheres of supergiants, the thickness of the atmosphere is rather small compared to the total radius of the star. The (small) curvature of the layers can therefore be neglected for the processes which need to be described. The typical relative thickness of the atmosphere with respect to the stellar radius is of the order of several percent for most objects in this study and up to $\sim 20\%$ in the most extreme cases.
- *Homogeneity.* The various depths points or layers in the (model) atmosphere are expected to be homogenous e.g. in terms of chemical composition or density (granulations). One depth coordinate is thus sufficient. Popular quantities therefore are z ($= 0$ in the center and increasing outward) or τ (optical depth, $= 0$ at the surface and increasing inward).
- *Stationarity.* Atmosphere are expected to be time-independent excluding such effects as pulsations.
- *Hydrostatic equilibrium.* In analogy to Eqn. 2.16, hydrostatic equilibrium including the effects of radiative acceleration is given as

$$\frac{dP}{dz} = -\rho(g - g_{\text{rad}}) \quad (4.1)$$

with the radiative acceleration g_{rad} defined in Sect. 4.4. Stellar winds are driven by radiation and result from $g_{\text{rad}} > g$. Therefore, stellar winds cannot be addressed in hydrostatic approaches.

- *Radiative Equilibrium.* In a static atmosphere, energy is transported to the surface in the form of radiation. The consequential radiative equilibrium demands that the amount of energy absorbed by atmospheric matter equals the loss due to emission. In particular, this ignores convection in atmospheric layers in the present analyses. The Schwarzschild criterion implies that convection will take place if the temperature gradient in the atmosphere is larger than the adiabatic gradient. It can be shown that convection is not relevant for B and A supergiants.

4.1 The Absorption of Radiation

A basic model for describing the absorption of radiation through matter is provided by considering an absorbing ion as a damped harmonic oscillator with the damping constant γ and the eigenfrequency ω_0 corresponding to the energy difference for the various electronic states. The radiation field in a star can then be treated as periodic excitation with frequency ω leading to the following solution for the equation of motion:

$$x(t) = \frac{eE_0}{m} \cdot \frac{\omega_0^2 - \omega^2 - i\omega\gamma}{(\omega_0^2 - \omega^2)^2 - \gamma^2\omega^2} \cdot e^{i\omega t}. \quad (4.2)$$

Electrodynamics then provides the emitted average power:

$$\overline{P} = \frac{2e^2}{3c^3} \cdot \overline{[\ddot{x}]^2} \propto \varphi(\nu) \quad (4.3)$$

with $\varphi(\nu)$ being the *profile function* describing the power emitted (or absorbed) at various frequencies ν . $\varphi(\nu)$ is the Fourier transformation of the solution $x(t)$ in frequency space and may be approximated with

$$\varphi(\nu) = \frac{\frac{\gamma}{4\pi^2}}{(\nu_0 - \nu)^2 + \left(\frac{\gamma}{4\pi}\right)^2} \quad (4.4)$$

for $\nu \approx \nu_0$. Quantum mechanical calculations yield very similar results as this classical approach with the only difference being an additional factor to the *absorption coefficient* $\kappa(\nu)$:

$$\kappa(\nu) = n_l \cdot \frac{\pi e^2}{mc} \cdot f_{lu} \cdot \varphi(\nu) \quad (4.5)$$

with n_l being the occupation density in the lower (l) state. The *oscillator strength* f_{lu} varies between 0 and 1 and depends on the detailed properties of each transition. For example, Balmer lines show oscillator strengths of 0.64, 0.12, and 0.04 for $H\alpha$, $H\beta$, and $H\gamma$. Although the oscillator strengths for the (higher) Balmer lines are quite small, Balmer lines are quite strong in most stars due to the large abundance of hydrogen. Moreover, all Balmer lines have similar strength as the strength is a function of $g \cdot f$ with g being the statistical weight (see below) which is again proportional to n^2 .

4.2 Interaction of Radiation and Matter in Local Thermodynamic Equilibrium (LTE)

A good understanding of the basic physics in stellar atmospheres can be achieved by considering *thermodynamic equilibrium* (TE). Any system in equilibrium is described by three fundamental equations: the Maxwell velocity distribution, the Boltzmann formula and the Saha equation.

The Maxwell distribution indicates the probability of finding a particle of mass m in a system with temperature T in a velocity interval $[v_i, v_i + dv_i]$ (with $i = x, y, z$):

$$P(\vec{v})dv_x dv_y dv_z = \left(\frac{m}{2\pi k_B T}\right)^{\frac{3}{2}} \cdot \exp\left(-\frac{m}{2k_B T}(v_x^2 + v_y^2 + v_z^2)\right) dv_x dv_y dv_z \quad (4.6)$$

where k_B is the Boltzmann constant. This relation can be applied to free electrons as well as to heavier ions.

For one ionic species, the *occupation ratios* n_u/n_l between two discrete energy levels separated by the energy ΔE are described in thermodynamic equilibrium by Boltzmann's formula:

$$\frac{n_u}{n_l} = \frac{g_u}{g_l} \cdot e^{\left(\frac{-\Delta E}{k_B T}\right)} \quad (4.7)$$

with the g s being the statistical weights of the respective energy levels. These are given by the number of possibilities to distribute electrons over the levels. This number for the upper (u) and lower (l) levels depends on different quantum mechanical rules such as the Pauli principle. The occupation with respect to all N particles is given by

$$\frac{n_u}{N} = \frac{g_u e^{-\frac{\Delta E}{k_B T}}}{U_u(T)} \quad (4.8)$$

with

$$U_u(T) = \sum_i g_i e^{-\frac{\Delta E}{k_B T}} \quad (4.9)$$

being the *partition function* over all possible states. In principle, there is a infinite number of levels for an atom as levels can get arbitrarily close to the ionisation threshold. However, reality inhibits this since interaction with particles close-by lead to a smearing of the levels, "cancelling" levels with high energies. Thus, the sum becomes finite.

Describing *ionisation* is a bit more complex as the momenta of free electron can in principle adopt arbitrary values leading to an infinite number of possibilities and statistical weights. Relief comes from the Pauli principle limiting the number of electrons in a phase space volume h^3 (h : Planck's constant) to two. With that, one can derive the *Saha equation* for the occupation ratios of different ionisation stages:

$$\frac{N_{j+1}}{N_j} = \frac{1}{n_e} 2 \left(\frac{2\pi m_e k T}{h^2}\right)^{3/2} \frac{U_{j+1}}{U_j} \cdot e^{\left(-\frac{E_{j,\text{Ion}}}{k_B T}\right)} \quad (4.10)$$

where N_j is the total number of atoms in the ionisation stage j and $E_{j,\text{Ion}}$ the ionisation energy between the two stages. Worth mentioning are the proportionality to the electron density n_e and to $T^{3/2}$. Defining the ionisation degree x

$$x := \frac{n_e}{N} \quad (4.11)$$

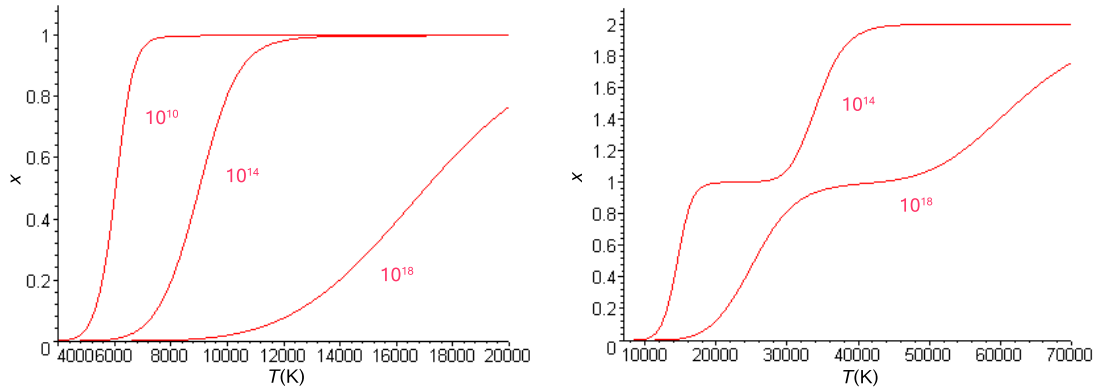


Figure 4.1: Ionisation degree for hydrogen (*left*) and helium (*right*) as a function of temperature for various densities. Solving the equations and plotting was done with MAPLE. The numbers next to the curves indicate the density in cm^{-3} . A density of 10^{14} cm^{-3} is of the order of the density in the atmospheres of main sequence stars.

with N being the number of atoms in all ionisation stages one may solve the Saha equation using particle number conservation and charge conservation as additional constraints. Fig. 4.1 shows such a simple solution for hydrogen and helium for various densities if only the ground states are considered. This is a good approximation because of the high energies of the first levels above the ground state.

The ranges of small inclination in the figure correspond to the various ionisation stages. In the right part of Fig. 4.1 at the small slope at $x = 1$, all helium atoms are singly ionised *on the average*. From now on, neutral elements shall be denoted with the usual astronomical labelling such as He I while singly ionised species are indicated as He II and so on.

With the ideas and the formalism of excitation (Boltzmann) and ionisation (Saha) in mind, it is straight-forward to understand the curves in Fig. 2.1. Below a certain temperature, there are not enough hydrogen atoms with their electron in the first excited state ($n=2$) as these is the level from which absorption leads to the observed Balmer lines in the *optical* part of the spectrum. In case of much higher temperature, significant ionisation will take place leaving few absorbers which could cause a line to form.

Comparing Fig. 2.1 with the curve for helium (Fig. 4.1, right) at a density of 10^{14} cm^{-3} (typical for a stellar atmosphere) reveals that the maximum for absorption for He I and its ionisation to He II are located at roughly the same temperature ($\sim 25\,000 \text{ K}$). Although some simplifications have been made for Fig. 4.1, this is reasonable as the lines considered for spectral classification originate again from excited levels of He I lying close the ionisation border.

These principles are also applicable for heavier elements than hydrogen and helium which are all called *metals* in astronomy. However, metals usually do not have high excitation energies for their visible spectral lines.

The formulae and discussions so far were based on the assumption of thermodynamic equilibrium (TE) implying a Planck-curve as specific intensity and a Maxwell

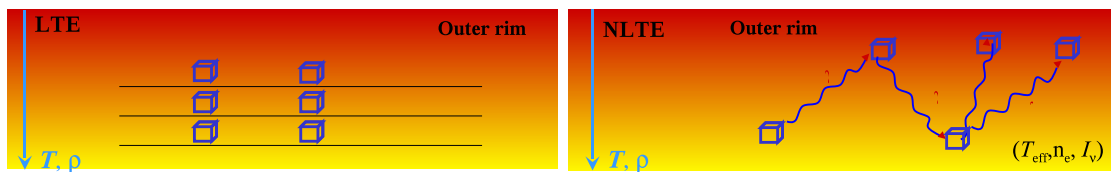


Figure 4.2: Schematic representation of a LTE (*left*) and a non-LTE (*right*) atmosphere. LTE is based on the assumption of small isolated volume elements (blue boxes) each of them being in thermodynamic equilibrium. At high temperatures or/and low densities, photons may connect the various volume elements (with different temperatures) cancelling the isolation.

velocity distribution for all particles for a given temperature. However, TE demands a black body with a constant temperature throughout a closed system (i.e. no photons leaking out). As we obviously can *see* stars as they emit radiation, that assumption cannot be true for the system star. This is also easy to accept because of the hot stellar interior (powered by nuclear burning) and the cold outer space.

Help comes from the idea of assuming *local* thermodynamic equilibrium (LTE). In this picture, the star is divided into many small volume elements dV which are each – independently of the others – in thermodynamic equilibrium. The specific intensity in this picture is then produced from overlapping many Planck curves from various volume elements with different temperatures. Figure 4.2 illustrates the idea of isolated volume elements and temperature stratification.

Of course, also LTE is only an approximation which may be less accurate under certain circumstances when the isolation of the volume elements is no longer (quite) valid. Isolation can be “broken” by photons travelling relatively large distances in the stellar atmosphere “connecting” volume elements of different temperatures thus disturbing the equilibrium (see Fig. 4.2, right). This may happen at two basic conditions:

- *Low densities.* The lower the density in the stellar atmosphere, the larger the mean free paths for photons and the easier it is for photons to connect volume elements of significantly different thermodynamic states. Moreover, the lower densities reduces the collision rates of electrons which thermalise the plasma.
- *High temperature.* Because of the high sensitivity of the photon flux to the temperature ($\propto T^4$), the flux will rapidly increase with higher temperatures. This will make it much more probable that photons are able to bridge certain distances and thus also to disturb the LTE.

As a consequence, effects of deviations from LTE may become relatively important and need to be accounted for in the hot, low-density atmospheres of BA-type supergiants of the present work.

4.3 The Generalisation of non-LTE

Dropping the assumption of LTE leads to the more general picture of non-LTE (also NLTE). While level population and ionisation are no longer fully described by the Boltzmann and Saha equations, the Maxwell velocity distribution is still valid with kinetic temperature T . Boltzmann and Saha equations are thus replaced by demanding *statistical equilibrium*

$$\frac{dn_i}{dt} = 0 \quad (4.12)$$

implying that the occupation densities n_i of each level i are time independent. Expressed in *rate coefficients* for *collisionally* (C_{ij}) and *radiatively* (R_{ij}) induced transitions from levels i to j , one arrives at

$$\begin{aligned} \sum \text{processes depopulating } i &= \sum \text{processes populating } i & (4.13) \\ n_i \sum_{j \neq i} (R_{ij} + C_{ij}) &= \sum_{j \neq i} n_j (R_{ji} + C_{ji}) \end{aligned}$$

Both radiative and collisional transitions may be further distinguished in bound-bound (bb) and bound-free (bf) transitions. Collisional excitations for bb and bf are given by

$$C_{ij} = n_e \cdot \int_{v_0}^{\infty} \sigma_{ij} f(v) v dv \quad (4.14)$$

where $\sigma_{ij}(v)$ is the collisional cross-section at velocity v , n_e the electron density and $f(v)$ the distribution function for the velocities. The integration starts at v_0 being the minimum energy threshold for this transition. The downward rates are then described by

$$C_{ji} = \frac{n_i^*}{n_j^*} \cdot C_{ij} \quad (4.15)$$

with the asterisk denoting LTE populations. For the radiative bb and bf excitation, one finds

$$R_{ij} = 4\pi \cdot \int_{\nu_0}^{\infty} \alpha_{ij}(\nu) \cdot \frac{J_\nu}{h\nu} \cdot d\nu \quad (4.16)$$

where α_{ij} is again the atomic cross-section of this transition and J_ν is the integral of the specific intensity over all angles:

$$J_\nu = \frac{1}{2} \int_{-1}^1 I_\nu(\mu) d\mu. \quad (4.17)$$

ν_0 is the smallest frequency at which the transition may occur. Downward processes are given as

$$R_{ji} = 4\pi \cdot \frac{n_i^*}{n_j^*} \cdot \int_{\nu_0}^{\infty} \alpha_{ij}(\nu) \left[\frac{2\nu^2}{c^2} + \frac{J_\nu}{h\nu} \right] \cdot \exp\left(-\frac{h\nu}{kT}\right) d\nu \quad (4.18)$$

with the two terms in square brackets describing spontaneous and induced emission, respectively. Additional relevant processes such as free-free processes or auto-ionisation are discussed in detail in Mihalas (1970).

The statistical equilibrium equations for all levels of an atom may then be solved by introducing the total number conservation as additional constraint.

4.4 Radiative Transfer

In the non-convective atmospheres of BA-type supergiants radiation is transporting the energy outwards. This section over *radiative transfer* is thus giving a basic overview about the respective principles.

The physical processes involved can be characterised as true emission (a photon is draining kinetic energy from the gas), true absorption (a photon is destroyed adding its energy to the thermal energy of the gas) and scattering (frequency and direction change of a photon, hardly any energy transfer). Scattering includes absorption and re-emission of photons as well as Thomson scattering. True absorption comprises for example ionisation and excitation by photons followed by a collision. Reversing these processes provide examples for true emission.

Mathematically, any alteration to the specific intensity I_ν (see Sect. 2.1.1) along a distance s can be the result of absorption with *absorption coefficient* or *opacity* κ_ν and emission with *emission coefficient* η_ν :

$$\frac{dI_\nu}{ds} = \eta_\nu - \kappa_\nu \cdot I_\nu. \quad (4.19)$$

The absorption leads to a radiative acceleration

$$g_{\text{rad}} = \frac{1}{c\rho(z)} \int_0^\infty \kappa_\nu F_\nu d\nu. \quad (4.20)$$

With the *source function*

$$S_\nu := \frac{\eta_\nu}{\kappa_\nu} \quad (4.21)$$

the *radiative transfer equation* is written as

$$\frac{dI_\nu}{ds} = \kappa_\nu (S_\nu - I_\nu). \quad (4.22)$$

Instead of linear distance s one often deals with the *optical depth* τ :

$$\begin{aligned} d\tau &= \kappa dt \\ \tau(\nu, t) &= \int_{t=0}^t \kappa_\nu(t') dt'. \end{aligned} \quad (4.23)$$

Here, t is a parameter measuring the depth from the surface on inwards. τ is indicating the distance in units of the mean free path and gives an idea on how strongly radiation at the respective frequency is damped. The larger τ the smaller the detectable intensity and the more outward the depth point from which the radiation finally escapes into space (see also Sect. 4.5).

A *formal solution* of the transfer equation is given by

$$I_\nu(\tau_1, \mu) = I_\nu(\tau_2, \mu) \exp\left(-\frac{\tau_2 - \tau_1}{\mu}\right) + \int_{\tau_1}^{\tau_2} S_\nu \exp\left(-\frac{t_\nu - \tau_1}{\mu}\right) \frac{dt_\nu}{\mu} \quad (4.24)$$

where $\mu = \cos\theta$. The solution is formal since S_ν is again a function of I_ν in the general case.

The first term describes the specific intensity emitted at a depth τ_2 which is partly (exponentially) absorbed until it reaches the depth τ_1 . The second term accounts for the gain in intensity by reemission at t_ν (integration variable ranging from τ_2 to τ_1) which is again partly absorbed when passing from the depths t_ν to the depth τ_1 where $I_\nu(\tau_1, \mu)$ is observed. A possible strategy to solve the transfer equation is briefly explained in Sect. 7.1.

4.5 Spectral Line Formation

Line formation in stellar atmospheres can in principle be understood with the wavelength or frequency dependent opacity κ_ν . At spectral lines, the opacity is higher due to the possibility of transitions and the resulting higher probability for an absorption of a photon with an appropriate energy. These photons are thus absorbed and emitted repeatedly leading to a random walk in the stellar atmosphere whereas a continuum photon easily passes the atmosphere. Therefore, the material in the atmosphere is more opaque at wavelengths of spectral lines reducing the mean free paths of photons with corresponding frequencies or wavelengths.

This implies that line photons originate from outer parts in the atmosphere and thus – as *outer* usually means *cooler* – from parts with lower temperatures. With Planck’s law stating that hotter matter is more luminous one can easily see that – at spectral lines – we observe outer, cooler, and less luminous parts in a stellar atmosphere finally leading to an *absorption* profile.

For spectral analyses, the spectral continuum is often normalised (rectified) to 1 and spectral lines are dips directed downward to 0. With that, the *equivalent width* of a spectral line is defined as the area in the normalised spectrum between a spectral line and the continuum at 1. The equivalent width can also be interpreted as the width of a rectangle with that area and depth and is a measure for the strength of a line.

4.6 Line Broadening Mechanisms

Spectral lines are transitions between *discrete* energy levels of an atom or ion. Several mechanisms in stellar atmospheres may affect the formation and width of (initially sharp) spectral lines yielding the relatively broad lines then observed in a spectrum.

- *Natural damping.* Every energy level of an atom – except the ground state – possesses a finite lifetime

$$\tau = \frac{1}{\sum_{i<j} A_{ji}} \quad (4.25)$$

where the A_{ij} are the Einstein coefficients for spontaneous emission from level j to i . With Heisenberg's uncertainty principle

$$\Delta E \cdot \tau \geq \frac{h}{2\pi} \quad (4.26)$$

indicating that the energy levels cannot be infinitely sharp the natural line width can be described with a Lorentz profile with damping constant

$$\gamma = \frac{1}{\tau_u} + \frac{1}{\tau_l} = \sum_{k<u} A_{uk} + \sum_{k<l} A_{ul} \quad (4.27)$$

where j and i are the levels involved in the transition. Lorentz profiles and damping constant γ are also described in Eqn. 4.4.

- *Pressure broadening.* Collisions between the radiant atom or ion with other particle may result in pressure broadening. These collisions can be interpreted as disturbances to the phases of the original oscillation leading to a Lorentz profile as profile function with damping

$$\gamma_{\text{col.}} = \frac{2}{\tau} \propto N \quad (4.28)$$

where τ is the mean time between two collisions and N the density of colliding particles. The pressure broadening may also be interpreted as (linear or quadratic) Stark effect. The denser the charged particles, the stronger the Stark effect and the splitting of the levels. Superpositions over many layers in the atmospheres with different pressure and thus different density finally lead to continuous line broadening.

Further pressure broadening mechanisms are van der Waals interaction between neutral particles or broadening due to inherent pressure with the latter being caused by neutral particles of the same species. Due to the large abundance of hydrogen, interactions between hydrogen atoms are the most important process of this kind.

- *Thermal Doppler broadening* results from the thermal movement of the absorbing particles and the Doppler effect thus caused. With that, absorption is no longer restricted to frequencies close to the rest transition frequency but may extend to Doppler-shifted frequencies. As only the line-of-sight movement to an observer is important, a one-dimensional Maxwell distribution $P(v)dv$ is sufficient:

$$P(v)dv = \frac{1}{v_0\sqrt{\pi}} \cdot \exp\left(-\frac{v^2}{v_0^2}\right)dv \quad (4.29)$$

with v as the velocity component in direction to an observer and

$$v_0 = \sqrt{\frac{2k_{\text{B}}T}{m}}. \quad (4.30)$$

where m is the mass of the atomic species under investigation. The more atoms at a certain velocity (interval), the stronger the absorption at the respective Doppler-shifted frequency. The resulting absorption line profile will thus reflect the velocity profile to yield the typical Gaussian Doppler broadening

$$\varphi_{\nu} = \frac{1}{\sqrt{\pi}\Delta\nu_{\text{D}}} \cdot \exp\left(-\frac{\Delta\nu}{\Delta\nu_{\text{D}}}\right)^2 \quad (4.31)$$

where $\Delta\nu = \nu - \nu_0$ (ν_0 is the unshifted natural frequency of the transition) and $\Delta\nu_{\text{D}}$ the Doppler width of the line,

$$\Delta\nu_{\text{D}} = \frac{\nu_0}{c} \cdot v_0 \quad (4.32)$$

- *Microturbulence.* In hydrostatic model atmospheres as employed in the present study, an additional parameter characterising non-thermal turbulences on small scales (small relative to the mean-free-path photons) is usually necessary for a consistent agreement between observations and theory.

It is assumed that these turbulences also show a Gaussian distribution leading to a modification of the Doppler width to

$$\Delta\nu_{\text{D}} = \frac{\nu_0}{c} \sqrt{v_0^2 + \xi^2} \quad (4.33)$$

where ξ is the value referred to as *microturbulence*.

All broadening mechanisms described so far directly affect the absorption of the radiation causing both a larger equivalent width and a broader line profile.

In a star, all these broadening mechanisms act together. The mathematical treatment of this is a convolution over all profile functions where the convolution of the two Gaussian profiles (thermal and microturbulent broadening) leads to another Gaussian profile with quadratic addition of the typical widths and the convolution of the two Lorentzian profiles leads to another Lorentz profile with linear addition of the typical widths. The convolution of the Gaussian and the Lorentzian profile finally yields a Voigt profile which has no analytical expression but has to be evaluated by numerical integration.

4.7 Radial Velocity, Rotational Velocity, and Macroturbulence

The *radial velocity* of the whole star in the line of sight towards an observer leads to a Doppler shift of the whole spectrum according to

$$\frac{\Delta\lambda}{\lambda} = \frac{v_r}{c}. \quad (4.34)$$

Moreover, the Doppler effect is important when accounting for the *rotation* of a star. Various points on the stellar surface are thus moving towards the observer or away from him with a distribution of velocities. Points close to the rotation axis move slowly in the line of sight and experience a small Doppler shift. A spectral line is therefore smeared, however, its equivalent width does *not* change.

Of course, the overall effect of a certain rotational velocity depends on the orientation of the rotation axis with respect to the observer. No effects of rotation can for example be measured if the axis points directly to the observer. Therefore, in most cases, it is only possible to measure the *projected* rotational velocity as $v_{\text{rot}} \sin i$ where i is the inclination angle between the line of sight and the rotation axis.

Another effect changing the line profile but not the equivalent width is given by the *macroturbulence*. In the macroturbulent velocity ζ , one summarises large-scale (compared to the mean free path of photons), radial-tangential movements in the stellar atmosphere.

There is still an ongoing discussion in the literature on the nature of the macroturbulence. Convection can be ruled out (in supergiants) due to the radiative nature of the atmosphere in massive stars. Lucy (1976) suggested non-radial pulsations in A-type supergiants to be identified with macroturbulence. This idea was recently supported by Aerts et al. (2009) who could mimic macroturbulent-like effects in line profiles based on time series of synthetic spectra which were calculated for various phases during pulsations.

5 Structure and Evolution of Galaxies

In order to understand the role of the Small Magellanic Cloud in the general picture of the evolution of dwarf galaxies and to put the results of this work into the context an overview of the structure and evolution of galaxies is given.

5.1 Basic Galaxy Classification

A basic classification of galaxies was first proposed by Hubble in 1926 (with further improvement later on). Solely based on their morphology (in blue colours), galaxies are classified according to the so-called Hubble sequence as depicted in Fig. 5.1. Although this sequence is not a priori an evolutionary sequence, the galaxy types on the left are referred to as “early types” and the ones on the right as “late types”.

The basic distinction is made between *elliptical galaxies* (E) without any prominent features such as dust bands or bright stars and *spiral galaxies* (S). Both groups are “connected” by the *lenticular galaxies* (S0).

The ellipticals are further classified by their (apparent) flatness from E0 to E7 with smaller numbers indicating a more circular shape. The spirals are distinguished based on the presence (SB) or absence (S) of a bar. They exhibit a central bulge which is structurally similar to an elliptical as well as a disc (like in an S0 galaxy) consisting of stars and gas. A further sub-classification is made as S(B)a, S(B)b, and S(B)c with later types showing a smaller central area and a more delicate structure of the spiral arms. Discs of lenticulars are not structured, i.e. they do not show spiral arms.

In addition to these, systems showing no rotational symmetry or spiral arms are defined as *irregular galaxies* (Irr). Both Magellanic Clouds are examples for irregulars.

Elliptical galaxies show a brightness distribution which may be approximated (pretty well in most cases) by formula of the kind

$$\frac{I(R)}{I_0} = \frac{1}{\left(1 + \frac{R}{R_c}\right)^2} \quad \text{or} \quad (5.1)$$

$$\frac{I(R)}{I_e} = \exp\left(-7.67 \left[\left(\frac{R}{R_e}\right)^{\frac{1}{4}} - 1\right]\right) \quad (5.2)$$

where R is measured along the major axis, I_0 is the central intensity, R_c is the distance from the center where the brightness is down to $0.25 I_0$, R_e is the radius within which half of the luminosity of the system is emitted and I_e is the surface brightness at this position. Population synthesis indicates that stars in elliptical galaxies formed in a narrow time interval. They consist mainly of old stars with most of their light emitted by red giants. The interstellar medium in ellipticals contains very little amounts of gas or dust which would be visible as emissions of H II regions or as absorption bands. Although small amounts of gas have been detected in those galaxies, no noteworthy star formation is going on in these systems.

Ellipticals show a colour–luminosity relation indicating that brighter galaxies are also redder and a decreasing metallicity with lower brightness. The statistical move-

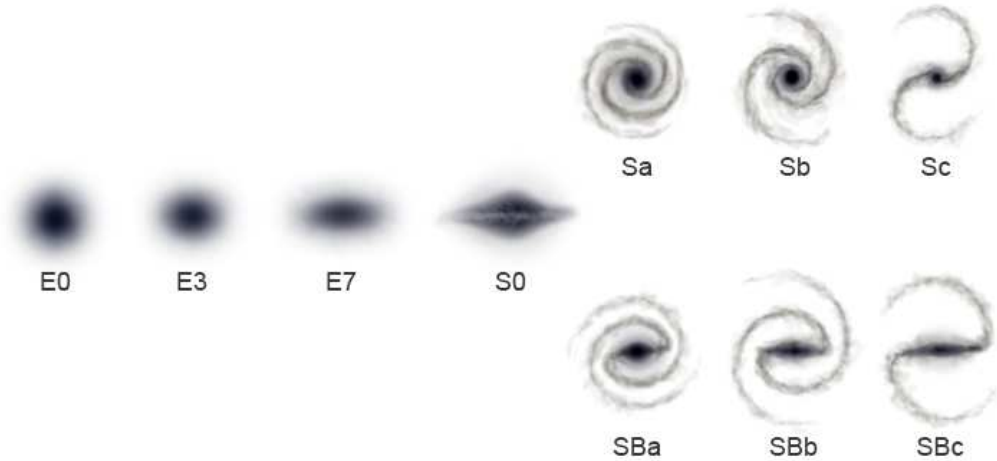


Figure 5.1: Hubble sequence for classification of galaxies. (This image is based on the image “The Hubble sequence: classification of galaxies” from “de.wikipedia.org” and was published under the GNU license for free documentation, author: Ville Koistinen; image was colour inverted for printing.)

ment of the stars is more important than a large-scale rotation around some axis which means that elliptical galaxies are supported by the pressure of the “star gas”.

Spiral galaxies, in contrast, are mainly shaped by an ordered rotation of disk and bulge. Moreover, there is still a considerable amount of interstellar gas present (concentrated in the plane) which is compressed and expanded by density waves (an interpretation of the spiral arms) triggering the formation of new stars. The spiral arms thus contain many young/blue stars and are the main sites for the ongoing star formation in these galaxies. The brightness distribution of the galaxy disc described by an exponential decline in radial direction

$$I(R) = I_0 \cdot e^{-\frac{R}{R_d}} \quad (5.3)$$

where R_d is called the scale length.

The intensity of the disc is also declining exponentially perpendicular to the plane

$$I(z) = I_0 \cdot e^{-\frac{z}{z_d}}. \quad (5.4)$$

The scale height z_d depends of the type of objects ranging from <100 pc for gas and dust to more than 1000 pc for the oldest stellar populations, the so-called thick disc.

The Magellanic Clouds (MCs) are the prototypes of *irregular galaxies*. There is still a significant amount of gas in the MCs, especially in the SMC where the gas is distributed in a very complex way – probably due to the gravitational interaction

of both the Large Magellanic Cloud and the Milky Way. Previous studies found a metallicity of $\sim 1/5$ solar implying a different history of star formation and chemical enrichment than in the Milky Way (see Sect. 9 for a deeper discussion). Both Clouds still contain young stars and young globular clusters in addition to an older population.

It is worth mentioning here that the Hubble classification only provides a somewhat limited view on the galaxy classification. The Hubble sequence is limited to observations in the visual while galaxies may show pronounced differences in the UV (e.g. from star formation) or in the X-ray (e.g. high energy phenomena in the central region such as active galactic nuclei) and the radio (e.g. cold gas in H I regions that extends much further out as it does not form stars). Nevertheless, the Hubble types are still commonly used and give a good first impression on the overall structure.

5.2 Principles of Galactic Evolution Theory

In order to develop a basic understanding of the predictions of galactic evolution theory, the basic principles behind the models shall be briefly explained. The (chemical) evolution of a galaxy is closely related to the evolution of many generations of its stars. The *star formation history* (SFH) is the evolution with time of the amount of stars (i.e. their total mass) formed – defined as the *star formation rate* SFR – and their initial chemical composition – described via the *age metallicity relation* AMR. The star formation history may thus be expressed as

$$\Upsilon = \Upsilon(\Psi(t), \Phi(t)) \quad (5.5)$$

where $\Psi(t)$ is the SFR and $\Phi(t)$ the AMR. Of course, the star formation rate and the age metallicity relation will affect each other with every new generation of stars ejecting their nuclear-processed matter into the interstellar medium during supernova explosions or strong stellar winds in evolved stages.

In order to trace the chemical evolution of a galaxy through the chemical evolution of its matter in gas and stars by means of stellar evolution theory, we further need to know the distribution function of stellar masses at birth, the *initial mass function* (IMF) describing the number of stars (dn) born with a mass between M and $M+dM$:

$$\frac{dn}{dM} = CM^{-x} \quad (5.6)$$

where C is a normalisation constant. This relation is known as *Salpeter's law* with $x = 2.35$. Recent investigations (Kroupa 2001) confirm $x \approx 2.35$ for $M \geq 0.5 M_{\odot}$ whereas for $0.1 \leq M/M_{\odot} < 0.5$, x seems to be smaller (around 1.3). Anyway, the results imply that star formation favours low-mass stars. Moreover, the IMF appears to be quite universal (Kroupa 2001).

Following Salaris & Cassisi (2008), the evolution of the total mass $M(t)$ of the galaxy neglecting possible dark matter is then described as

$$M(t) = g(t) + s(t) \quad (5.7)$$

$$\frac{dM(t)}{dt} = F(t) - E(t) \quad (5.8)$$

where $g(t)$ and $s(t)$ are the amount of matter in the interstellar gas or in stars respectively and $F(t)$ and $E(t)$ are the rates of accretion of matter from outside the system and the ejection of matter out of the system, respectively.

With ejection of gas from the stars due to any possible process (winds, explosions as provided by stellar evolution models) $e(t)$ the evolution of the mass in gas and stars is then

$$\frac{dg(t)}{dt} = F(t) - E(t) + e(t) - \Psi(t) \quad (5.9)$$

$$\frac{ds(t)}{dt} = \Psi(t) - e(t). \quad (5.10)$$

The time evolution of the mass fraction $X_i(t)$ of a (non-radioactive) element i is then given as

$$\frac{dg(t)X_i(t)}{dt} = e_{X_i}(t) - X_i(t)\Psi(t) + X_i^F(t)F(t) - X_i(t)E(t) \quad (5.11)$$

where $e_{X_i}(t)$ is the total mass of the element i ejected from stars, $X_i(t)\Psi(t)$ the mass locked into stars in star formation, $X_i^F(t)F(t)$ is the addition of mass from inflowing material into the system and $X_i(t)E(t)$ the mass loss due to ejection out of the system.

Some insight in the chemical evolution of galaxies can already be gained by considering the ‘Simple’ model with instantaneous recycling described by four assumptions:

- (1) The system is isolated allowing no inflow or outflow of matter:

$$F(t) = E(t) = 0 \rightarrow M(t) = M = \text{const.} \quad (5.12)$$

- (2) The system starts with all the matter in the gas phase:

$$g(0) = M \quad (5.13)$$

- (3) The system is well mixed at all times implying that the abundances are the same in the gas as well as in newly formed stars

- (4) The delay between the formation of a generation of stars and the injection of the nuclear processed matter inside the stars into the interstellar medium is negligible (so-called instantaneous recycling). At least for the supernova type II explosions of short-lived massive stars, this is a good approximation.

The yield p_i is defined as the mass ratio for an element i that is produced in a new generation of stars divided by the mass that remains locked up in objects such as white dwarfs or neutron stars. $10^{-1} - 10^{-2}$ are typical values for p_i which is assumed to be constant over the many generations of stars. Furthermore, Z_i is defined as the total mass of an element i

$$Z_i = X_i \cdot g \quad (5.14)$$

The change in Z_i , δZ_i when forming a new generation of stars is – due to instantaneous recycling approximation – given by

$$\delta Z_i = p_i \delta s - X_i \delta s \quad (5.15)$$

where δs is the mass locked up in the stellar remnants. This equation accounts for a positive contribution due to processed material re-injected into the interstellar medium and a negative contribution from the locked matter.

The abundance change of X_i is then

$$\delta X_i = \delta \left(\frac{Z_i}{g} \right) = \frac{\delta Z_i}{g} - \frac{Z_i}{g^2} \delta g = \frac{1}{g} (\delta Z_i - X_i \delta g) \quad (5.16)$$

Combining this with Eqn. 5.15 and the condition for a closed system,

$$\delta s = -\delta g \quad (5.17)$$

we find

$$\delta X_i = \frac{1}{g} (p_i \delta s - X_i \delta s - X_i \delta g) = -p_i \frac{\delta g}{g}. \quad (5.18)$$

Integration assuming a constant p_i yields

$$X_i(t) - X_i(0) = p_i \cdot \ln \left(\frac{g(0)}{g(t)} \right) \quad (5.19)$$

This leads already to an interesting consequence. As $g(0)$ is the total mass M in the Simple model, one can see that the mass fraction X_i of an element i is increasing with decreasing interstellar gas. This result is expected as the massive stars formed out of the interstellar medium eventually return some enriched matter into the medium while some fraction of the gas mass stays locked up into low-mass objects leading all in all to a decrease of gas. In detail, the yields will highly depend on stellar chemical evolution (as well as on the SFR and AMR).

So far, the discussion was restricted to whole systems where the quantities mentioned here are interpreted as mean quantities over the whole system. For inhomogeneous systems (such as most galaxies where abundance gradients have been observed), the system can be divided into small volume elements with the equations applied to these individually. In that case, one must also describe or make assumptions to mixing processes. Closed box models are in use as well as dynamical models allowing for mass exchange between the different regions.

The Simple model provides a good basic understanding is already capable of – qualitatively – explaining basic aspects observed such as abundance patterns. However, for a good quantitative description, some assumptions of the Simple model must be dropped. In the following, several predictions made by these models are presented and a way to pin down the a priori unknown SFR and AMR of a system from observations is discussed.

5.3 Examples for Model Predictions and Observational Constraints

5.3.1 Determination of Star Formation Rates and Age–metallicity relations (in the SMC)

A powerful way to determine the star formation rate and the age–metallicity relation for a system (over the history of this system) is to observe a *colour magnitude diagram* (CMD), similar to the Hertzsprung-Russell diagram as described in Sect. 2.1.2 but e.g. plotting V versus $V - I$ (see Fig. 5.2).

The main idea then is to model the observed distribution of (many!) stars in the CMD based on a set of elementary stellar populations calculated for various ages t and metallicities Z . Many linear combinations of such populations each of them forming a synthetic CMD are then compared to the observation. The parameters – meaning the time-dependent SFRs and AMRs – of the best fitting combined synthetic population should then represent the real star formation history of the system.

For example, from the CMD in Fig. 5.2 it is already clear that there must have been subsequent phases of star formation due to presence of both evolved red giants and more massive young stars on the main sequence.

Harris & Zaritsky (2004) find a quite pronounced epoch of star formation during the earliest phases more than 8.4 Gyr ago followed by a more quiescent epoch and then more or less continuous star formation from 3 Gyr ago to the present. Figure 5.4 indicates that the SMC metallicity remained quite low up to ~ 3 Gyr ago followed by a steady enrichment to the present-day value of about 1/5 solar.

In similar studies, Chiosi & Vallenari (2007) find a low rate of star formation until 6 Gyr ago and after that two main periods of pronounced star formation around 3–6 Gyr and around 0.3–0.4 Gyr ago. Noël et al. (2009) find two main phases of star formation throughout the SMC at ~ 10 Gyr and ~ 5 Gyr ago as well as young star formation in eastern and most central fields.

5.3.2 Element Ratios in Various Environments

Relative abundances of the elements may be different depending on the environment. Therefore, abundance patterns other than the solar one (e.g. Grevesse & Sauval 1998) may arise. For example, elements primarily produced in supernovae type II explosions of massive stars are supposed to be distributed relatively early into the interstellar medium due to the fast evolution of these stars. The ratio of such an element with respect to elements which are produced more slowly is thus expected to vary with the age of a system.

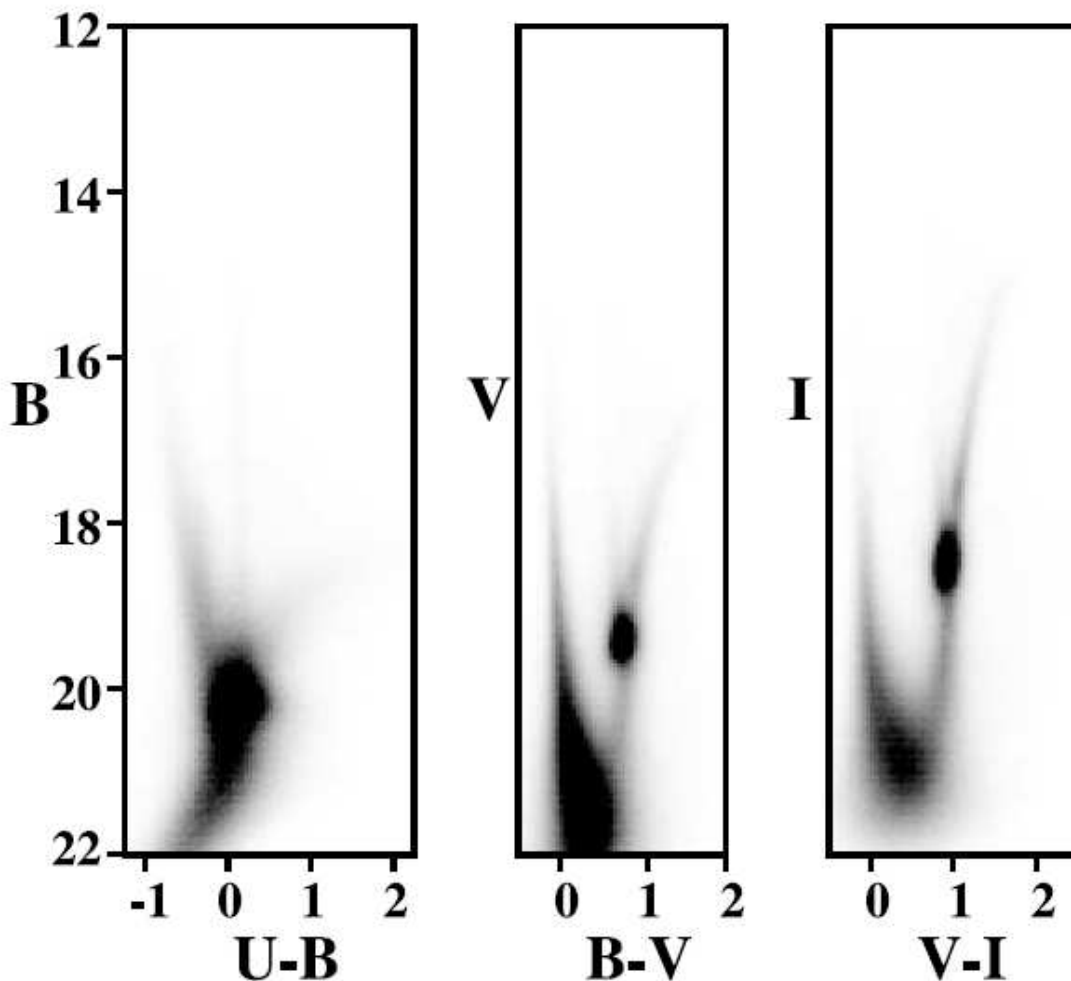


Figure 5.2: Example for colour–magnitude diagrams (CMD) from photometry of ~ 6 million stars in the Small Magellanic cloud (from Harris & Zaritsky 2004). The red giants (“clump”, RGB) can be better distinguished at visual and infrared wavelengths (V and I).

For example, Fig. 5.5 (left) shows the S/O ratios with respect to oxygen abundance for various Galactic and extragalactic H II regions. The results are consistent with yield ratios which are constant (and solar) with respect to changing O abundance and thus also with respect to the age of the system. This indicates that the formation of oxygen and sulfur is connected. In contrast, Fig. 5.5 (right) implies that the C/O ratio varies with metallicity which is likely due to strong mass-loss from high- and intermediate-mass stars.

The abundances of all (/most) metals increase with the age of a system through more and more generations of stars which eject their nuclear processed material enriched with metals into the galaxy. Thus, many elements are suitable in order to serve as a “clock” for measuring the age of the system. However, also due to the good observability of iron (lines), iron is mostly used to parameterise the age of a system or of parts of that system.

Figure 5.3: Star formation rate as a function of time as deduced from fitting combinations of CMDs of synthetic populations for various times and metallicities to the observation in Fig. 5.2 (from Harris & Zaritsky 2004). The figure shows two time intervals for better presentation. The time axis runs from small to large ages of the system where an age zero corresponds to stars currently forming.

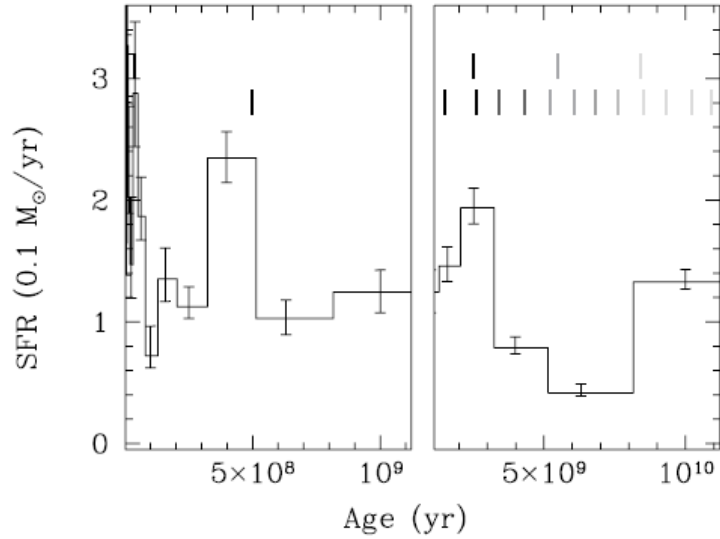
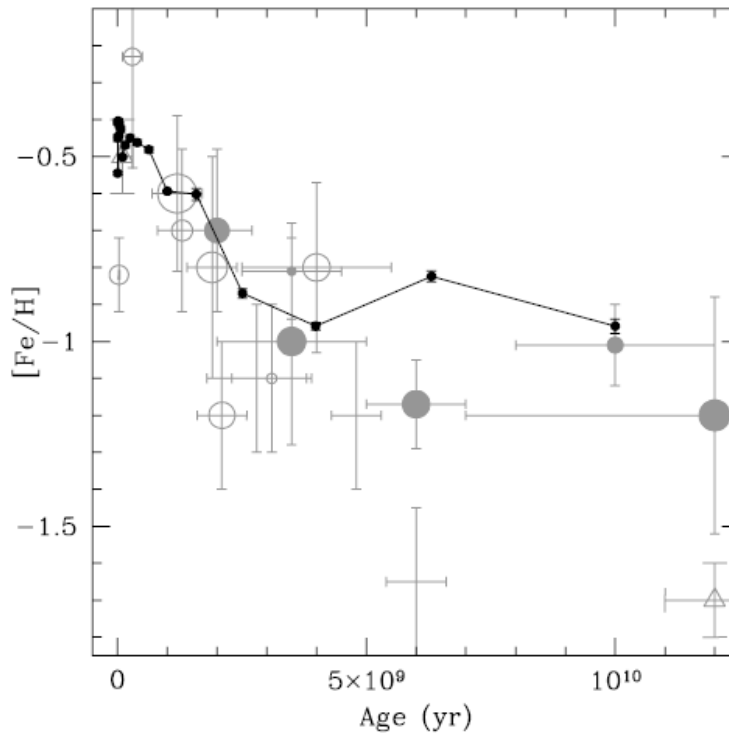


Figure 5.4: Age–metallicity relation as a function of time as deduced from fitting combinations of CMDs of synthetic populations for various times and metallicities to the observation in Fig. 5.2 (from Harris & Zaritsky 2004). The derived AMR is shown by the small points connected straight lines. Overplotted are observational results from star clusters and other objects, see Harris & Zaritsky (2004) for a detailed discussion.



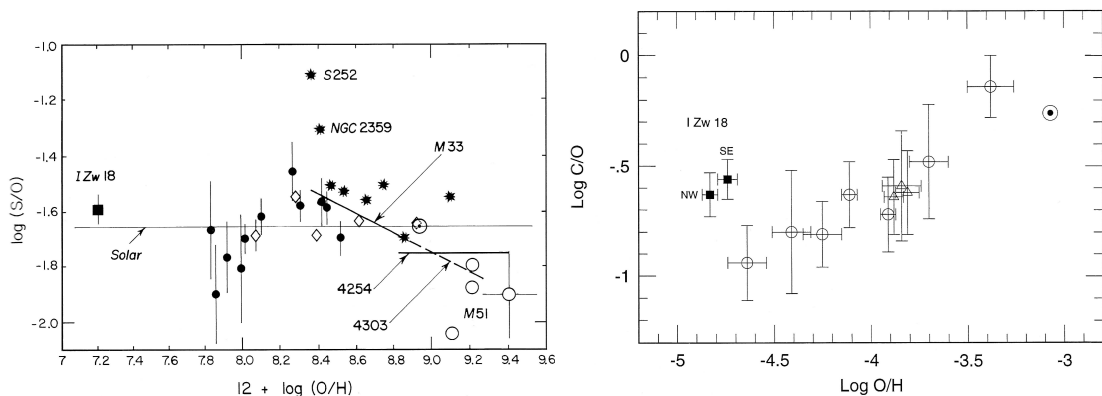


Figure 5.5: *Left*: S/O ratio vs O/H in Galactic and extragalactic H II regions (from Pagel 1997, see Pagel 1992). *Right*: C/O ratio vs O/H in Galactic and extragalactic H II regions (from Pagel 1997, see Garnett et al. 1995).

Figure 5.6 shows such a plot of abundances from multiple elements (oxygen and α -elements) with respect to the iron abundance which is then interpreted as a kind of time axis (with model fits, from Pagel 1995). The results imply that for a young system or for parts of the system which formed early (low $[\text{Fe}/\text{H}]$ values) the elemental abundance is quite constant. From $[\text{Fe}/\text{H}] \gtrsim -1$ on, the abundances (from observations and from the models) relative to iron start to decrease – rather factitious in the fit due to the relatively simple models. This behaviour is explained by the significant iron contribution from SNIa which appear relatively late in the history of the system (at high $[\text{Fe}/\text{H}]$) due to an delay by the evolution time of their progenitor stars.

In principle, the shape of the theoretical curves of $[\text{X}/\text{Fe}]$ vs $[\text{Fe}/\text{H}]$ as in Fig. 5.6 may give some good indications on the star formation history of the system as illustrated in Fig. 5.7. Suppose the star formation happened relatively fast compared to the solar neighbourhood (denoted S.N. in the figure) as it may be the case in the central bulge of the Milky Way this means that there is a lot of contribution of metal enrichment from the massive stars before the low-mass stars may inject the quite strongly iron-enriched material in SNIa explosions. Therefore, the $[\text{Fe}/\text{O}]$ stays high even at high $[\text{Fe}/\text{H}]$. In contrast, if star formation happens on much longer timescales or if the star formation is concentrated in bursts giving the low-mass stars more time to evolve and contribute to the metal (iron) content, the $[\text{X}/\text{Fe}]$ is decreased earlier. This may apply to the Magellanic Clouds as indicated.

However, the abundances derived from observations are usually not precise enough in order to constrain the SFH. Moreover, the shape of such curves may also be influenced by matter ejected from the system in galactic winds or inflow from outside the system. For the Magellanic Clouds, stripping of material through the tidal interaction with each other and with the Milky Way may lead to such effects.

5.3.3 Abundance Gradients

Equation 5.19 from the Simple model predicts another interesting feature when it is applied locally to various divisions of a system/galaxy into small volume elements.

Figure 5.6: Fits of element-to-iron ratios in the Milky Way from Pagel (1995). The observational points come from various sources as indicated therein. The metal-weak objects (with small $[\text{Fe}/\text{H}]$ values) are mostly located in the Galactic thick disc.

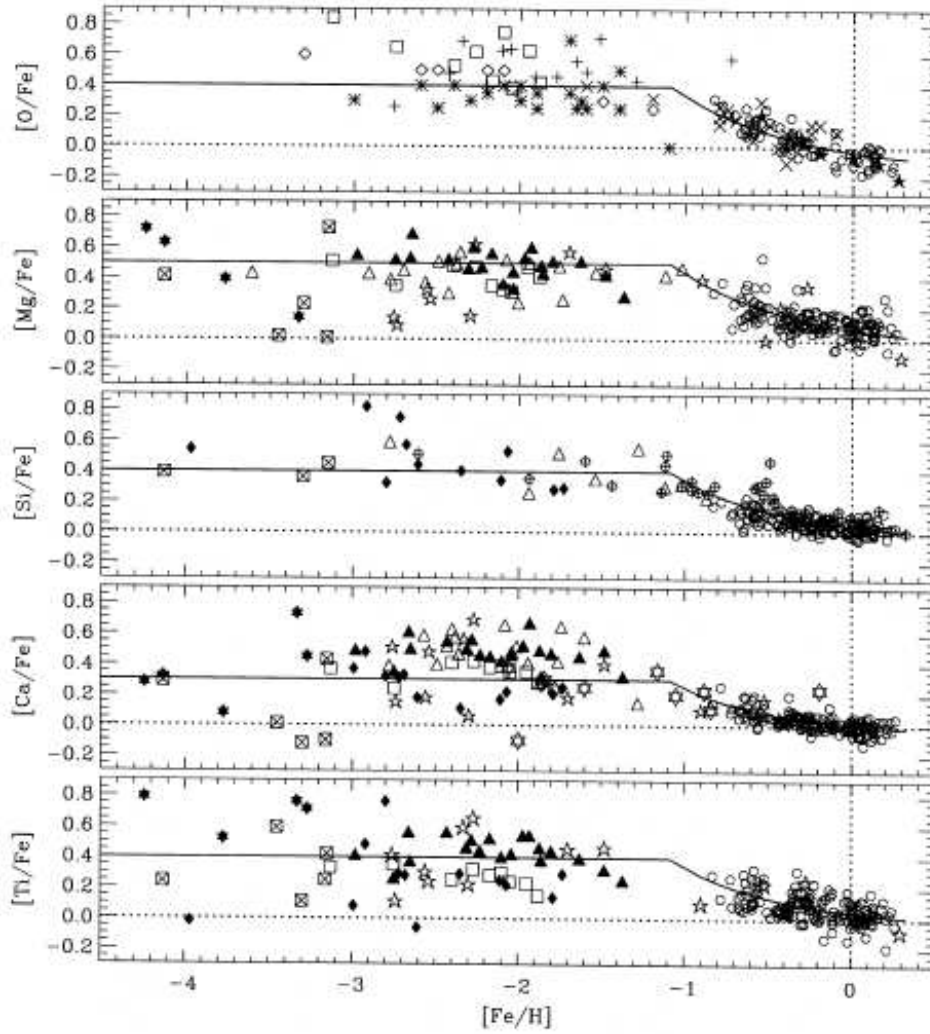
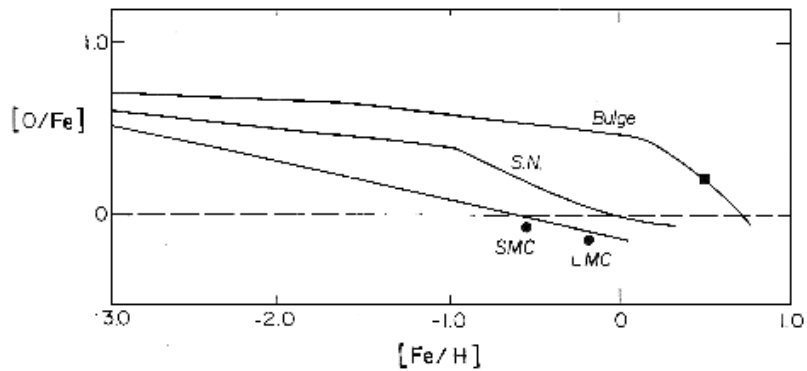


Figure 5.7: Predicted $[\text{O}/\text{Fe}]$ vs $[\text{Fe}/\text{H}]$ relations in different environments (from Pagel 1997, see Matteucci 1991). The horizontal line stands for solar $[\text{O}/\text{Fe}]$.



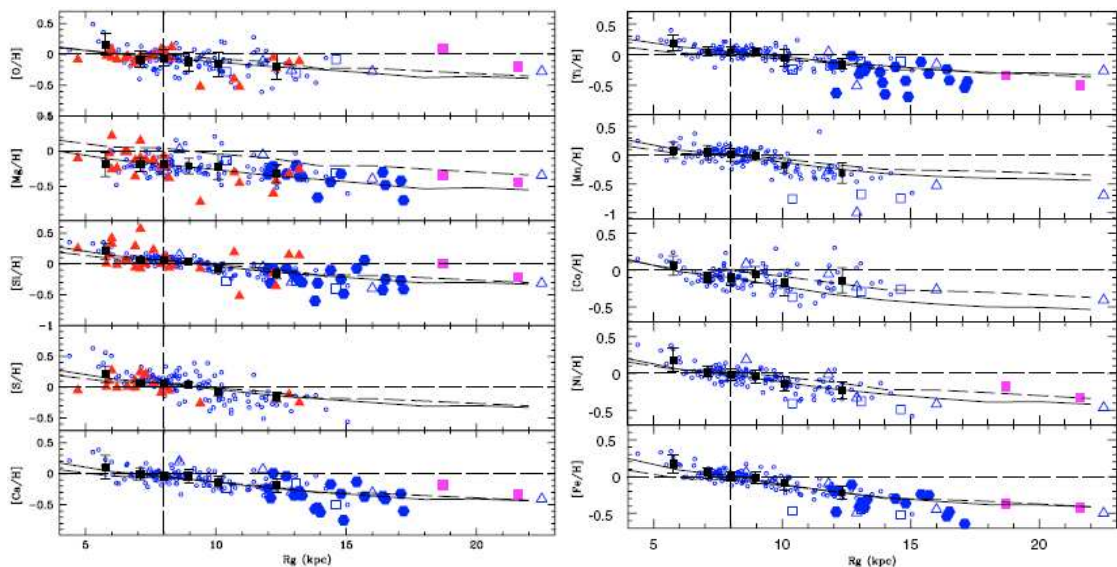


Figure 5.8: Galactic abundance gradients for O, Mg, Si, S, Ca, Ti, Mn, Co, Ni, and Fe (from Cescutti et al. 2007). The lines show predictions from their Milky Way evolution models while the points represent observations compiled from a large number of objects from various sources (including Cepheids, OB stars, red giants, and open clusters; see Cescutti et al. 2007 and references therein for further information).

For higher (local) gas masses $g(0)$ and thus densities one expects a higher star formation rate consuming the gas faster (smaller $g(t)$) and thus a higher yield of metal abundances through fusion processes in stars. Therefore, when applied to galaxies, this means that in the denser parts of a galaxy which lie usually closer to the center the metal abundance should also be higher resulting in *abundance gradients*. Such a behaviour of decreasing metal abundances with increasing distance from the galactic center is observed in many galaxies – mainly in (the discs) of spiral galaxies as our own Milky Way.

A nice comparison of galactic evolution theory with a large number of observations for the Milky Way was made by Cescutti et al. (2007) as shown in Fig. 5.8. They derive gradients of ~ 0.05 dex/kpc quite consistently for all elements (ranges from 4 to 14 kpc considered). However, there is still discussion in the literature on the strengths of these gradients and a possible dependence on the considered species and on time.

Theories describing these abundance patterns and the overall structure of the Milky Way (consisting of a central bulge, a spherical halo, as well as of a thin and a thick disc) usually have to include several aspects such as inflow from outside the Galaxy as well as the assimilation of dwarf galaxies by the Milky Way in order to explain the observations. However, new models by Schönrich & Binney (2008) agree with the observations without large contributions from these effects. They suggest instead that radial mixing plays an important role in galactochemical evolution through “blurring” (radial migration) and “churning” (place change without moving to eccentric orbits).

6 Observational Data

This section gives an overview of the characteristics of the targets studied in the present work and the parameters of the corresponding observations made in order to obtain the high-quality spectra. These form the basis for the detailed quantitative spectral analysis (Sect. 7). The second part of the current section will summarise the steps necessary in order to convert the raw data into a form suitable for analyses (the so-called data reduction).

6.1 Overview of the Sample

Thirty-eight supergiants of spectral types B and A (BA supergiants) could be investigated in this analysis. The sample stars were mainly selected based on the SMC star catalogue of Azzopardi & Vigneanu (1982). The targets were selected from those objects which were assigned spectral types of B5 to A5 and a luminosity class of I. Furthermore, only stars with apparent visual magnitudes V brighter than 13.0 were considered as the planned investigations required high-quality data which again demand enough flux from each object.

The observational data for the quantitative analysis are high-resolution spectra from the Fiber-fed Extended Range Optical Spectrograph (FEROS, Kaufer 1999) with a resolving power of $R = \lambda/\Delta\lambda \sim 48\,000$ allowing for precise investigations of spectral line profiles. Moreover, the spectra cover a wavelength range of $\sim 3500 - 9200 \text{ \AA}$ which makes it possible to study a large number of spectral lines of many (ionic) species.

Fifteen targets were observed in 1999 when FEROS was attached to the 1.52m-telescope and 23 in 2006 at the 2.2m-telescope, both in La Silla. The acquisition of the 1999 data was planned and carried out by N. Przybilla. In order to do the quantitative analysis at the intended accuracy, a signal-to-noise ratio (S/N) of ~ 100 throughout most of the spectral range is necessary and thus exposure times of $\gtrsim 1 \text{ h}$. The fainter targets were thus observed with longer exposure times. For the fainter targets observed in 2006, this required multiple observations as each observation was limited by ESO to $\leq 1 \text{ h}$. Stars observed in 1999 could be handled in one run as the one hour limit did not apply then and as these stars are generally brighter than the ones observed in 2006.

The location of the targets in the plane of the sky within the SMC is illustrated by Figs. 6.1 and 6.2. Where available, star designations as given by Azzopardi & Vigneanu (1982) are employed.

Figure 6.1 nicely shows the relative positions of the targets within the SMC by comparing the plotted coordinates (lower part) with a photograph (upper part) of an almost identical sector in the sky. Three targets (SK194, SK196, and SK202) are too far eastward (left, at higher right ascension α) for the displayed range.

Figure 6.2 presents *all* the targets, and this time in a more space-saving manner. The four objects further in the SMC wing are shown in an inset into the plot of the main SMC region. From now on, Fig. 6.2 will be the standard frame for plotting the sample stars with respect to their position in the sky.

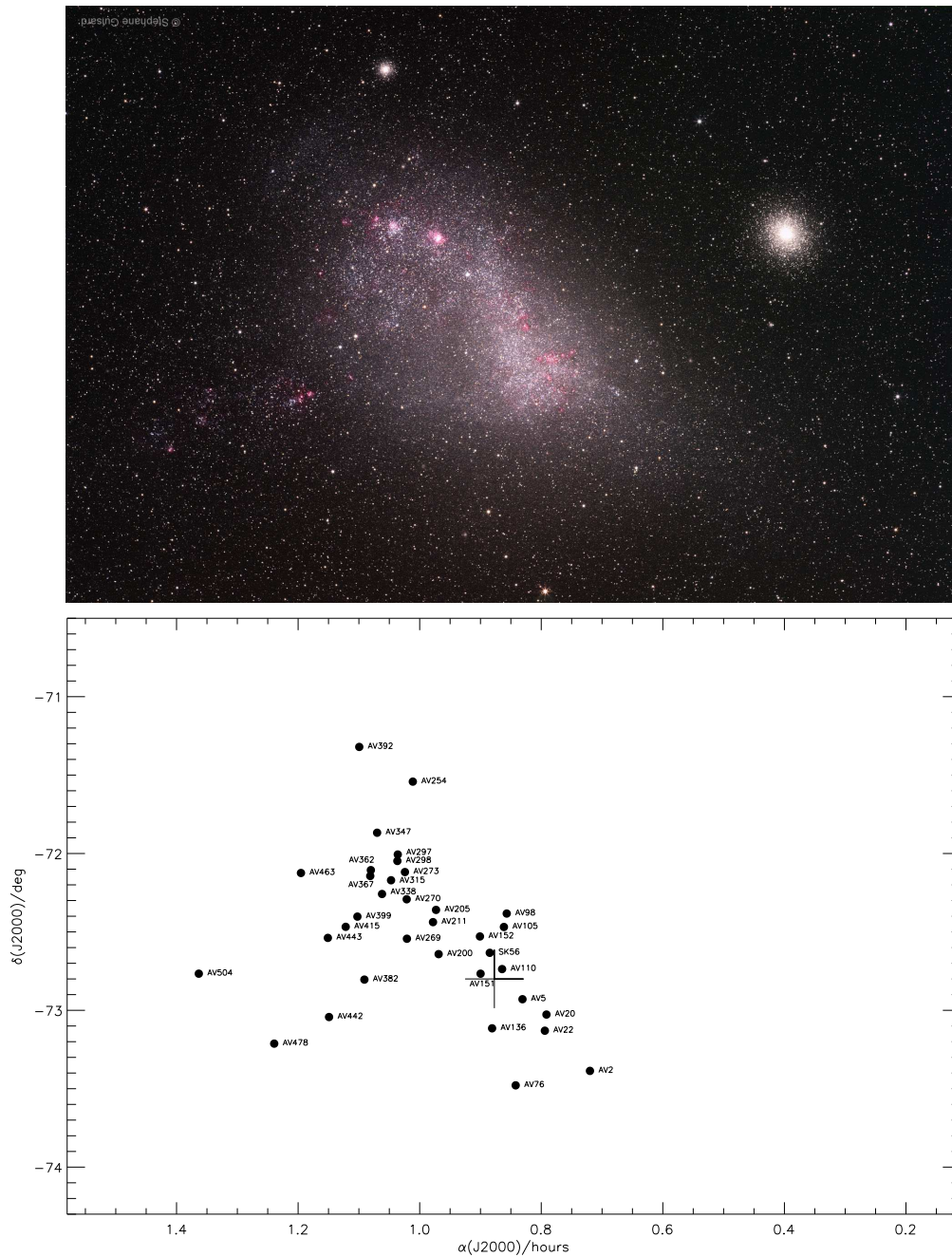


Figure 6.1: *Upper panel*: Photograph of the Small Magellanic Cloud by Stéphane Guisard (as taken from “<http://apod.nasa.gov/apod/ap071001.html>”), rotated by 180° . The so-called SMC wing extends (up) left towards the direction of the LMC. The bright spherical objects up and right are NGC 362 and NGC 104 (= 47 Tuc) respectively – two globular clusters still lying in our own Galaxy in front of the SMC. *Lower panel*: Location of (most) stars of our sample according to their J2000 coordinates. The range was chosen so that it coincides best with the photograph, however, there is a slight warp between the figures due to $\delta \neq 0$. Four stars lying further in the SMC wing (larger α) are missing in this frame. The cross denotes the center of the SMC as inferred from the Simbad database at CDS.

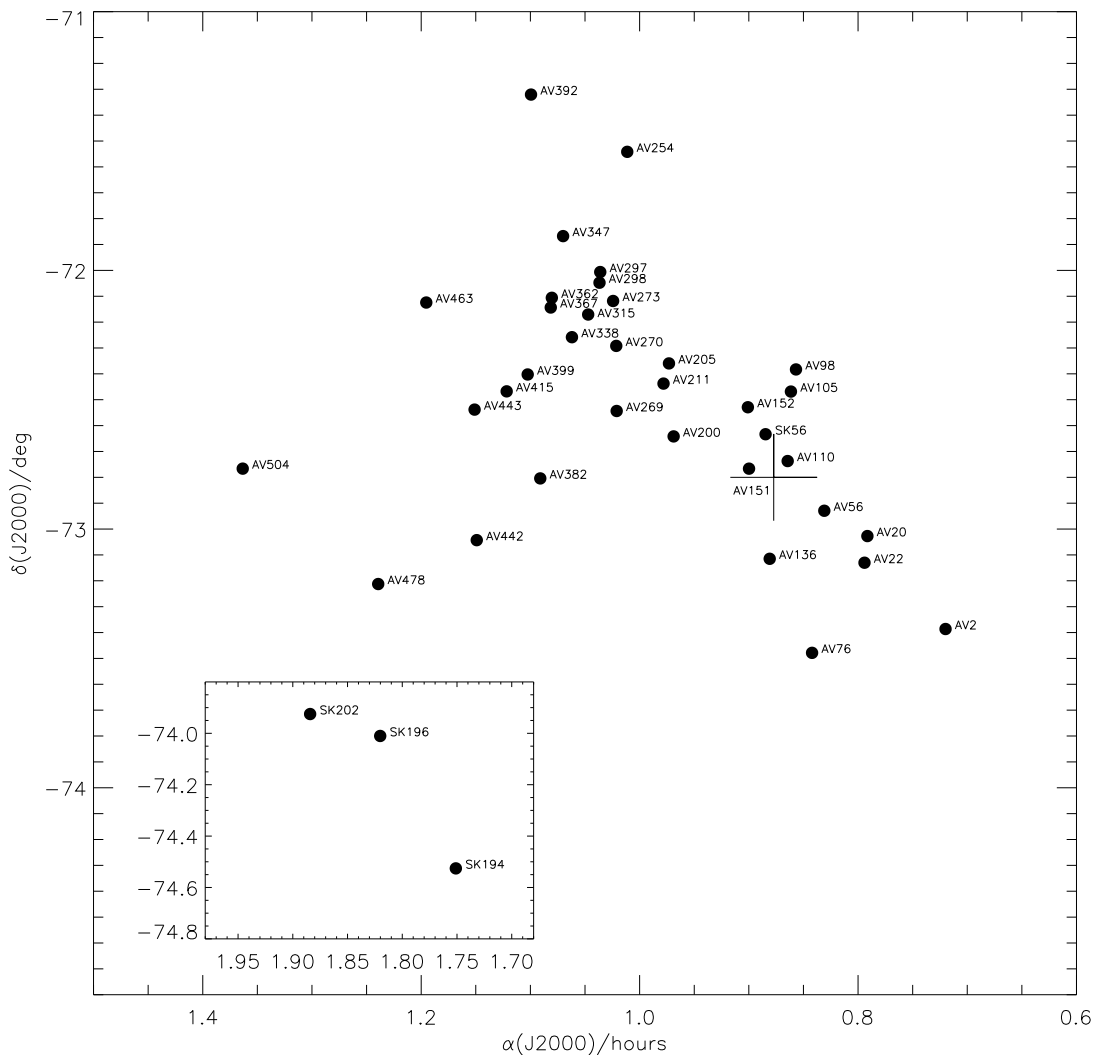


Figure 6.2: Similar to Fig. 6.1, lower panel. The coordinate ranges were modified and an additional sub-frame shows the three supergiants omitted in Fig. 6.1. This will be the standard coordinate frame when further stellar quantities are plotted with respect to the location of the stars in the SMC.

Table 6.1 summarises basic characteristics of the sample stars such as spectral type as well as observed magnitudes and colours. Moreover, it gives a detailed overview of the underlying observational material of each target such as the date of the observation, the respective exposure time (Exp. T.), the S/N, and the radial velocity v_{rad} (see also Sect. 6.2). If more than one observation with FEROS was required in order to meet the desired S/N (in the 2006 data), multiple entries in the date, exposure time, and S/N column are given. In this case, the S/N ratio refers to the spectrum of the individual observation. At the end of the data reduction of the single spectra they can be combined to one final spectrum with thus increased S/N.

Table 6.1: Observational summary of the sample stars. Coordinates are adopted from the Simbad database at CDS. The sources for photometry and spectral classification are given: (1) Massey (2002), (2) Ardeberg & Maurice (1977), (3) Ardeberg (1980), (4) Udalski et al. (1998), (5) Lee et al. (2005), (6) Azzopardi et al. (1975), (7) Azzopardi (1981), (8) Sanduleak (1968), (9) Humphreys (1983). Most of the photometry sources employ photoelectric measurements. Only (1) and (4) use CCD photometry. Explanation of notes: PI = pressure inversion in the final model (see Sect. 7.1), LBV = star is a known luminous blue variable.

Object	α (J2000)	δ (J2000)	Sp.T. (Src.)	V Δ	$B - V$ Δ	# obs.	Date(s) (dd.mm.jjjj)	Exp. T. (s)	S/N	v_{rad} km s^{-1}	Phot. Src.	Note
AV2	00:43:11.6347	-73:23:10.814	B6Iae (2)	11.99 ± 0.01	0.04 ± 0.00	2	08.09.2006 08.09.2006	2350 2350	66 66	99	(2)	
AV20	00:47:29.21	-73:01:37.4	B8Ia (7)	12.12 ± 0.01	0.29 ± 0.01	2	08.09.2006 08.09.2006	2350 2350	63 48	163	(3)	
AV22	00:47:38.75	-73:07:48.4	B2Ia (7)	12.225 ± 0.025	-0.015 ± 0.039	2	09.09.2006 09.09.2006	2550 2550	69 64	140	(4)	
AV56	00:49:51.27	-72:55:45.2	B2Ia (2)	11.15 ± 0.01	0.00 ± 0.00	1	20.11.1999	3400	105	140	(2)	
AV76	00:50:31.5815	-73:28:42.583	A0Ia (2)	11.19 ± 0.01	0.10 ± 0.00	1	17.11.1999	4000	86	170	(2)	
AV98	00:51:24.5977	-72:22:58.592	B9Ia (2)	11.45 ± 0.01	0.06 ± 0.00	1	09.09.2006	3180	90	163	(2)	
AV105	00:51:41.24	-72:28:06.7	A0Iab (7)	12.22 ± 0.01	0.04 ± 0.01	2	10.09.2006 10.09.2006	2650 2650	70 71	159	(3)	
AV110	00:51:51.986	-72:44:13.57	A0Ia (7)	12.08 ± 0.01	0.07 ± 0.01	3	01.10.2006 22.09.2006 01.10.2006	2400 2400 2400	60 52 60	152	(3)	
AV136	00:52:51.2374	-73:06:53.632	A0Ia (2)	10.97 ± 0.01	0.13 ± 0.00	1	16.11.1999	2800	106	146	(2)	
SK56	00:53:04.8879	-72:38:00.150	B8.5Ia (2)	10.87 ± 0.01	0.04 ± 0.01	1	20.11.1999	2700	86	148	(2)	

Table 6.1: Observational summary of the sample stars (*continued*).

Object	α (J2000)	δ (J2000)	Sp.T. (Src.)	V Δ	$B - V$ Δ	# obs.	Date(s) (dd.mm.jjjj)	Exp. T. (s)	S/N	v_{rad} km s^{-1}	Phot. Src.	Note
AV151	00:53:59.38	-72:45:59.5	B5Ia (7)	12.26 ± 0.01	-0.02 ± 0.01	2	01.10.2006 01.10.2006	2650 2650	54 63	117	(1)	
AV152	00:54:03.21	-72:31:44.7	A3Iab (2)	11.86 ± 0.01	0.17 ± 0.01	2	24.09.2006 24.09.2006	2110 2110	92 86	140	(2)	PI
AV200	00:58:07.90	-72:38:30.5	OB (8)	12.17 ± 0.01	0.07 ± 0.01	2	01.10.2006 01.10.2006	2300 2300	47 51	177	(2)	
AV205	00:58:23.26	-72:21:34.9	A2Ia (7)	12.32 ± 0.01	0.12 ± 0.01	2	02.10.2006 02.10.2006	2650 2650	59 67	169	(1)	
AV211	00:58:41.2226	-72:26:15.548	A0Ia (2)	11.52 ± 0.01	0.10 ± 0.00	1	18.11.1999	5000	99	174	(2)	
AV254	01:00:40.756	-71:32:30.28	A3Ia (2)	11.62 ± 0.01	0.14 ± 0.00	4	10.09.2006 10.09.2006 10.09.2006 10.09.2006	2100 2100 2100 2100	37 75 77 88	174	(2)	PI
AV269	01:01:15.65	-72:32:36.9	A1Ia (2)	11.41 ± 0.01	0.13 ± 0.00	1	19.11.2006	4500	90	153	(2)	PI
AV270	01:01:17.0034	-72:17:31.135	A0Ia (2)	11.42 ± 0.01	0.03 ± 0.01	1	17.11.1999	4800	87	117	(2)	
AV273	01:01:27.43	-72:07:06.1	A1Ib (7)	12.16 ± 0.01	0.07 ± 0.01	2	03.10.2006 03.10.2006	2550 2550	71 87	118	(2)	
AV297	01:02:09.80	-72:00:23.3	B7Ia (7)	12.10 ± 0.00	-0.03 ± 0.00	2	11.09.2006 11.09.2006	2550 2550	58 69	169	(1)	
AV298	01:02:12.23	-72:02:51.7	A0Iab (7)	12.47 ± 0.01	0.03 ± 0.01	4	13.09.2006 05.10.2006 13.09.2006 05.10.2006	3050 3050 3050 3050	41 49 30 51	156	(1)	

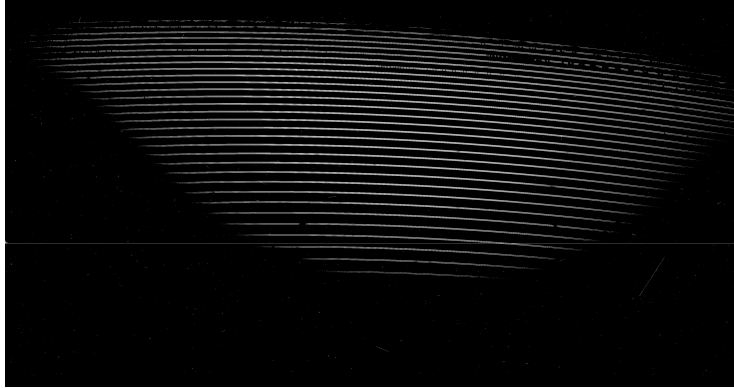
Table 6.1: Observational summary of the sample stars (*continued*).

Object	α (J2000)	δ (J2000)	Sp.T. (Src.)	V Δ	$B - V$ Δ	# obs.	Date(s) (dd.mm.jjjj)	Exp. T. (s)	S/N	v_{rad} km s^{-1}	Phot. Src.	Note
AV315	01:02:49.6050	-72:10:14.443	B9Ia (2)	10.90 ± 0.01	0.06 ± 0.00	1	17.11.1999	3000	68	151	(2)	
AV338	01:03:43.05	-72:15:29.9	A0Iab (2)	12.54 ± 0.00	0.03 ± 0.00	2	05.10.2006 05.10.2006	3050 3050	49 48	159	(1)	
AV347	01:04:12.2636	-71:52:03.279	A0Ia (7)	12.13 ± 0.01	0.00 ± 0.01	2	05.10.2006 05.10.2006	2500 2500	68 57	149	(2)	
AV362	01:04:49.351	-72:06:21.79	B3Ia (2)	11.36 ± 0.01	-0.02 ± 0.00	1	20.11.1999	4900	112	198	(2)	
AV367	01:04:52.908	-72:08:36.71	B7Ia (2)	11.22 ± 0.01	0.07 ± 0.01	1	16.11.1999	3800	100	192	(2)	
AV382	01:05:27.4813	-72:48:15.007	B8Ia (2)	11.41 ± 0.01	0.06 ± 0.01	1	18.11.1999	4600	84	156	(2)	
AV392	01:05:57.941	-71:19:13.62	A3Ib (7)	12.57 ± 0.01	0.03 ± 0.01	3	11.09.2006 11.09.2006 11.09.2006	3050 3050 3050	56 51 60	184	(6)	
AV399	01:06:08.96	-72:24:08.9	B7Ib (7)	12.33 ± 0.01	0.01 ± 0.01	2	05.10.2006 05.10.2006	2850 2850	55 52	141	(1)	
AV415	01:07:18.2179	-72:28:03.658	B9Iae (2)	10.52 ± 0.00	0.10 ± 0.00	1	18.11.1999	2000	97	171	(2)	LBV PI
AV442	01:08:56.854	-73:02:34.25	A3Ia (2)	11.35 ± 0.01	0.13 ± 0.01	1	19.11.1999	4200	77	191	(2)	PI
AV443	01:09:03.9511	-72:32:17.649	B3Ia (2)	10.97 ± 0.01	-0.06 ± 0.00	1	20.11.1999	3200	87	247	(2)	

Table 6.1: Observational summary of the sample stars (*continued*).

Object	α (J2000)	δ (J2000)	Sp.T. (Src.)	V Δ	$B - V$ Δ	# obs.	Date(s) (dd.mm.jjjj)	Exp. T. (s)	S/N	v_{rad} km s^{-1}	Phot. Src.	Note
AV463	01:11:43.20	-72:07:27.6	A2Ib	12.10	0.09	4	13.09.2006	2600	38	164	(1)	
				± 0.00	± 0.00		05.10.2006	2600	56			
							13.09.2006	2600	25			
							05.10.2006	2600	47			
AV478	01:14:21.6445	-73:12:44.805	A0Ia (2)	11.54	0.10	1	16.11.1999	5000	91	175	(2)	PI
				± 0.01	± 0.01							
AV504	01:21:48.2352	-72:45:59.034	B9Ia (2)	11.91	-0.03	2	09.09.2006	2100	77	145	(2)	
				± 0.01	± 0.01		09.09.2006	2100	86			
SK194	01:45:03.828	-74:31:32.49	B9Ia (2)	11.74	0.02	1	01.09.2006	3195	81	172	(2)	
				± 0.01	± 0.01							
SK196	01:49:12.573	-74:00:37.060	B8Ia (2)	12.04	-0.02	3	12.09.2006	2400	58	178	(2)	
				± 0.01	± 0.01		11.09.2006	2400	52			
							12.09.2006	2400	69			
SK202	01:53:03	-73:55.5	B5I (9)	12.32	-0.09	5	02.10.2006	2750	56	163	(2)	
				± 0.01	± 0.01		10.10.2006	2750	45			
							12.09.2006	2750	55			
							02.10.2006	2750	60			
							10.10.2006	2750	39			

Figure 6.3: Example of a raw spectrum from the FEROS spectrograph as employed in this study. The (slightly curved) horizontal diffraction orders are clearly visible. Darker regions within these orders indicate spectral lines. Bright spots all over the CCD (mostly) correspond to impacts of cosmic rays.



6.2 Data Reduction

The stellar spectrum directly obtained from the instrument, the so-called raw data, needs to be further processed before a quantitative analysis. The exact steps of this *data reduction* vary from instrument to instrument. This section shall give an overview of the typical steps applied in the reduction of an Echelle spectrum as provided by the FEROS spectrograph.

Classical spectrographs separate the wavelengths in one dimension. Therefore, the covered wavelength range or the resolution of the spectrum are strongly limited by the size of the CCD chip which finally detects the light. Moreover, the full area of the CCD chip is used rather inefficiently. An Echelle spectrograph provides an improvement in these respects. Its grating produces a highly dispersed spectrum in high and overlapping diffraction orders. Each order contains a small part of the whole spectrum (e.g. some 180 \AA at a total coverage from ~ 3500 to 9200 \AA in the case of FEROS). The overlapping diffraction orders are separated by an additional dispersion element perpendicular to the distribution of the first grating. In this way, a “two-dimensional” spectrum is produced.

Figure 6.3 shows an example of such a 2-D FEROS spectrum. The bright (and slightly curved) lines are the various diffraction orders placed in this way by the second dispersion element. Several darker spots in these orders indicate spectral lines. Due to the construction of the instrument the intensity varies between different orders and also within one order.

With this quite complex setup, Echelle spectrographs are able to offer both high-resolution and large wavelength coverage while efficiently using the CCD area and thus the limited observation time. The high resolution and large wavelength coverage are a prerequisite for comprehensive and precise quantitative analyses of e.g. chemical abundances in stars. However, Echelle spectrographs usually imply a more complex data reduction than simple longslit spectrographs. The individual steps are briefly discussed in the following.

- *Bias*. Converting the generated charges in the CCD to an electronic signal introduces systematic effects caused by the detector electronics. In order to remove this bias signal, a zero-seconds-exposure is read out from the chip and subtracted from the observation.

- *Dark current.* Thermal excitation creates charges in the CCD which are then of course not the result of an illumination of star light. This effect may be accounted for with images without light exposure. The dark current can also be reduced by cooling the detector which is done in the case of FEROS (to about -110°C). Moreover, in case of relatively bright targets such as the SMC supergiants of the present work, the dark current is negligible. Therefore, dark exposures are not produced for FEROS every day if not explicitly demanded. Comparing reduced spectra with and without dark correction revealed indeed no measurable difference for a selection of stars. Thus, dark current was neglected in the data reduction.
- *Flat field.* Each CCD pixel is supposed to show a (slightly) different quantum efficiency and thus a different sensitivity. Illuminating the detector with a uniform source with a continuous spectrum (such as a halogen lamp) – so-called flat field exposures – may account for that. Moreover, flat field exposures can be used to determine the location of the various diffraction orders on the CCD and to correct for the Blaze function – an intensity distribution caused by the spectrograph. Flat field exposures can be made by illuminating the dome or with an internal lamp producing a continuous spectral energy distribution. Flat fields employed in this work all come from an internal lamp.
- *Order detection and extraction.* So-called guess files which are indicating the location of the 39 diffraction orders on the CCD chip are provided for FEROS by ESO. The flux within these defined ranges is then summed up perpendicular to the direction of an order and converted to a one-dimensional spectrum. During this process, it is possible to correct for cosmics, bright spots (very few pixels wide) on the image due to the impact of cosmic rays. Moreover, the pixels between the orders can be used to subtract background contributions.
- *Wavelength calibration.* The raw observation provides only information over the intensity with respect to pixel position. In order to assign the wavelength information to the position on the CCD, a spectrum of a special lamp with well-defined spectral lines is used (in case of FEROS lamps with Th, Ar, and Ne).
- *Merging.* The 39 one-dimensional parts of the spectrum (from the 39 diffraction orders) are combined to one single spectrum covering the whole wavelength range. Most orders partly overlap, only at longer wavelengths there are wavelength ranges not covered at ~ 8530 and at $\sim 8860 \text{ \AA}$.
- *Normalisation.* Comparing absolute fluxes is difficult for Echelle spectrographs due to loss of intensity at the slit (where light enters a spectrograph) and its rather complex setup. Thus, only the relative fluxes shall be of interest in the present work and the observed spectral continuum (the spectral ranges without absorption lines) is also normalised to one. This was done by manually fitting low-order polynomials (step by step) to ranges of about 150 \AA in the reduced (as described so far) and merged spectrum.

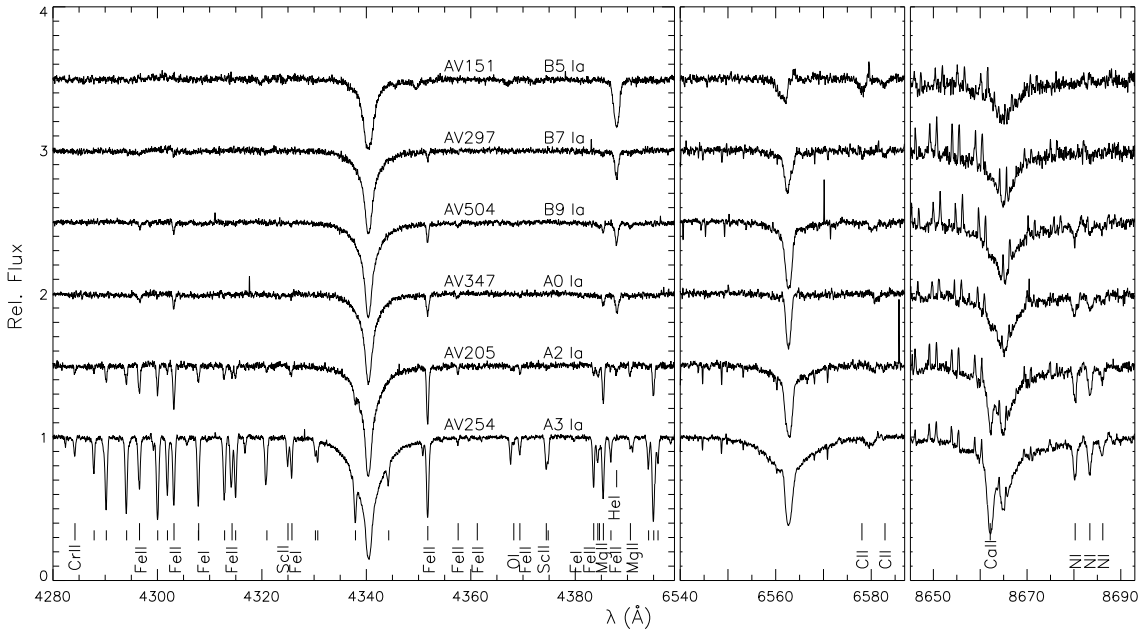


Figure 6.4: Examples for reduced (including normalisation) spectra for stars with different spectral types. No variations with the luminosity class are plotted as most stars are of the same luminosity class Ia or Iab. Vertical lines along the bottom mark spectral lines visible (depending on the spectral type). Short lines denote Ti II lines. One can nicely see how hydrogen and most metal lines are getting weaker towards higher temperatures or earlier spectral types while the strength of the helium line(s) increases. The spectra are vertically shifted by 0.5 relative to each other.

- *Averaging.* In case multiple spectra were obtained from the same object an averaging to one spectrum was performed. The individual (normalised) spectra were weighted with their squared S/N implying a higher contribution of the “better” spectrum. This step leads to a higher S/N of the combined spectrum. The S/N was calculated as the 1σ scatter of the normalised observed continuum around the mean value ($=1$) in a wavelength range devoid of spectral lines, typically $\sim 4725 - 4730 \text{ \AA}$.
- *Radial velocity correction.* The observed spectrum is generally shifted in wavelength due to the radial velocity of the star (Doppler effect). A cross correlation of the observation with a synthetic spectrum calculated at rest wavelengths is used to correct for this. The Balmer lines of hydrogen in the BA supergiants of this work should be avoided for this comparison as they are very likely influenced by the stellar wind, producing asymmetric line profiles unreliable for this purpose.

The data reduction was performed with the FEROS environment within the MIDAS package. This pipeline is provided by ESO and allows almost automatic cosmetics correction, subtraction of bias current, flatfielding, wavelength calibration with

barycentric correction and merging of the Echelle orders. After that, the spectra were manually normalised, averaged, and corrected for the radial velocity. In addition, the final observed spectrum could be averaged over three wavelength points as the resolution of the CCD detector was better than the spectral resolution provided by the dispersive elements. This improves the S/N further.

Examples for the thus obtained observed spectra are shown in Fig. 6.4. Several spectra of SMC BA supergiants are plotted for stars with various spectral types.

7 Quantitative Spectral Analysis

Basic atmospheric parameters such as effective temperature T_{eff} , surface gravity $\log g$, microturbulent velocity ξ , helium abundance $n(\text{He})$ ($= N_{\text{He}}/(N_{\text{H}} + N_{\text{He}})$) as well as projected rotational velocity $v \sin i$, macroturbulent velocity ζ , and stellar abundances are derived by comparing observed and synthetic spectra. This section introduces the method for calculating the synthetic spectra (the basic assumptions are discussed in Sect 4) as well as the spectral analysis strategy with which parameters are derived from observed spectra.

7.1 Model Atmospheres and Synthetic Spectra Using a Hybrid non-LTE Approach

As explained at the end of Sect. 4.3, deviations from the LTE approach have to be accounted for in order to reduce systematic errors. However, the temperature-pressure stratification is often only little affected by deviations from LTE. This allows to use a so-called hybrid non-LTE approach, as illustrated in detail by Przybilla et al. (2006).

In this approach, it is assumed that the atmospheric structure is well described in LTE and only the line formation as well as the radiative transfer need special non-LTE treatment. This has been shown to be a good approximation for BA supergiants and keeps the computational effort at a modest level.

Figure 7.1 provides an overview (of the non-LTE part) of the procedure to compute a synthetic spectrum. The first step in this approach is to calculate the atmospheric structure, a so-called model atmosphere, in LTE. This is done with the ATLAS9 routine developed by Kurucz (1993), in the version of M. Lemke as obtained from the CCP7 library (<http://ccp7.dur.ac.uk/>). Further modifications (Przybilla et al. 2001b) allowed to overcome model convergence problems close to the Eddington limit, which turns out to be crucial in the case of the supergiants.

The ATLAS9 input consists of the atmospheric parameters effective temperature T_{eff} , surface gravity $\log g$, microturbulent velocity ξ , helium abundance $n(\text{He})$, and the overall metallicity $[M/H]$. Moreover, ATLAS9 needs so-called opacity distribution functions (ODFs). ODFs include tabulated opacities. They are an efficient method in order to account for the *line-blanketing* in a stellar atmosphere: the restriction of the photon flux due to absorption lines leads to a steeper temperature gradient with backwarming and surface cooling. Furthermore, the strong absorption of photons in the UV range due to strong spectral lines leads to a re-distribution of photons towards higher wavelengths affecting the overall spectral energy distribution. The ODFs employed in this work by Kurucz (1992) were calculated and tabulated for various metallicities and microturbulences. Higher metallicities imply an enhanced contribution of the numerous metal lines to the opacity. Higher microturbulence also strengthens the line blanketing effect because the spectral features become stronger. Of course, the ODF should be consistent with the final abundances and microturbulences derived for the stellar atmosphere.

The LTE model atmosphere computed with ATLAS9 provides then the distributions of e.g. temperature and pressure with depth. In order to keep the hybrid non-LTE approach justified, the model atmosphere must be calculated down to depth

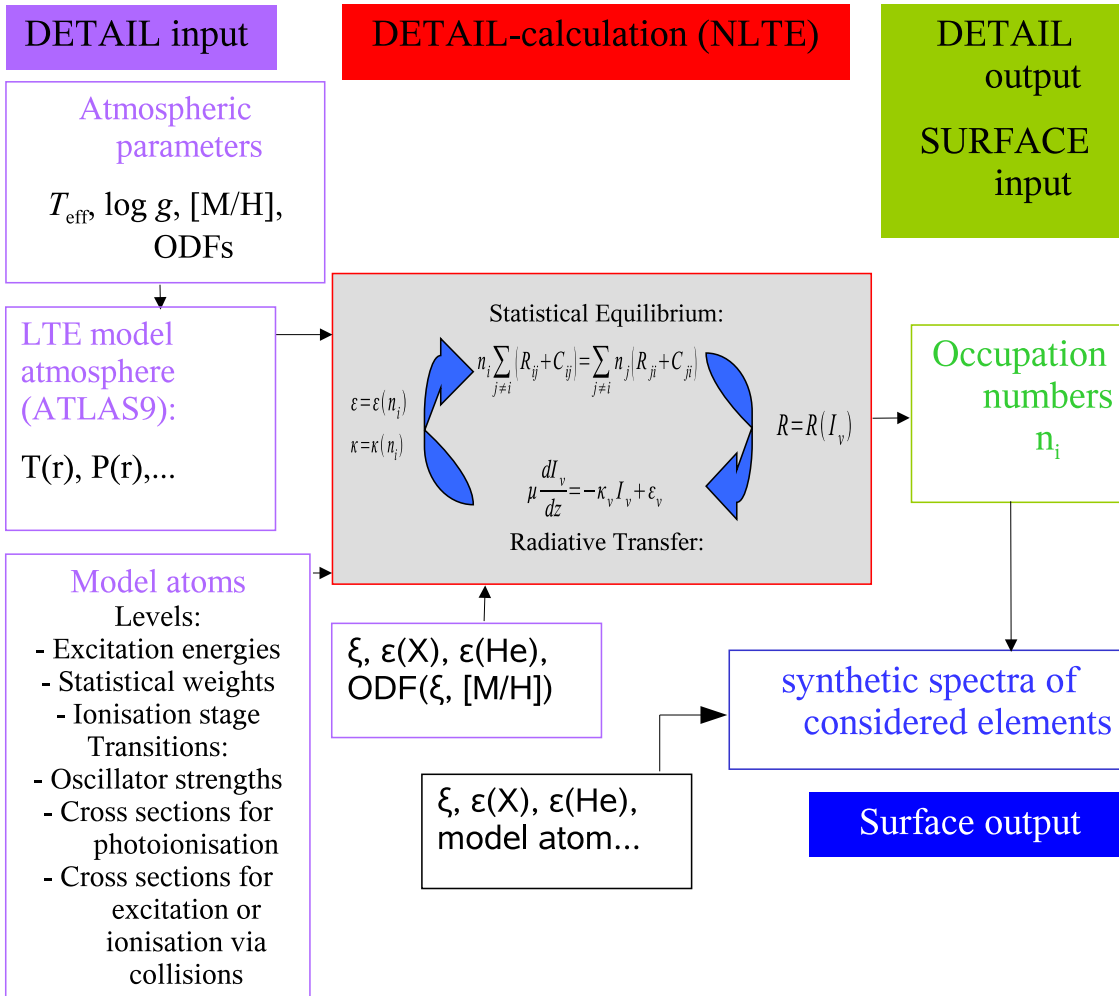


Figure 7.1: Illustration of the non-LTE calculations with DETAIL and SURFACE.

points deep enough so that the radiation field is well described in LTE. Here, the model atmospheres extend to a value of τ_{ROSS} (Rosseland optical depth) of ~ 180 , which is sufficient.

Another crucial input for the non-LTE calculations are various sets of atomic data. This includes information on excitation energies and statistical weights for all relevant ionisation stages as well as oscillator strengths and cross sections for ionisation and excitation by photons and collisions. Although vast amounts of atomic data are required for the non-LTE modelling, one might expect that all necessary information is available because atomic physics is a mature field of research and well understood. However, this is not the case and more difficulties arise as the atomic data must be tested by comparison with observations and transformed into so-called model atoms which can be read by the codes. Constructing such a model atom – even for a small number of ionisation stages and for a limited parameter range – can easily require the work of a whole Ph.D. thesis. Fortunately, such well tested model atoms are

Table 7.1: Non-LTE model atoms.

Ion	Source
H	Przybilla & Butler (2004)
He I	Przybilla (2005)
C I/II	Przybilla et al. (2001b), Nieva & Przybilla (2006, 2008)
N I/II	Przybilla & Butler (2001)
O I/II	Przybilla et al. (2000) combined with Becker & Butler (1988), the latter with updated atomic data
Mg I/II	Przybilla et al. (2001a)
S II/III	Vrancken et al. (1996), with updated atomic data
Ti II	Becker (1998)
Fe II	Becker (1998)

available for this work (see Table 7.1). Of course, the information on ionisation states and transitions implemented in these model atoms defines the lines which can be investigated from the theoretical point of view.

Model atmosphere and model atoms are then the input for computing the non-LTE occupation numbers of the various atomic levels. This is done by simultaneously solving the equations for statistical equilibrium and radiative transfer (Eqs. 4.13 and 4.24) as depicted in the central box of Fig. 7.1. The equation of statistical equilibrium must be solved for the occupation numbers n_i . However, the coefficients R_{ij} depend on the radiative processes in the stellar atmosphere and thus on the specific intensity I_ν . This in turn is obtained from the radiative transfer equation with coefficients κ_ν and ϵ_ν which describe the absorption and emission characteristics of the atmospheric material. These are again a function of the occupation numbers providing only a formal solution in the first place.

The problem needs to be solved with several iterations. The program used in this work, DETAIL (Giddings 1981; Butler & Giddings 1985; recently updated by K. Butler), makes use of an *accelerated/approximate lambda iterations* (ALI) approach in order to solve the statistical equilibrium and the radiative transfer. For that, the intensity $I_{\mu\nu}$ results from the source function $S_{\mu\nu}$ through the *lambda operator*:

$$I_{\mu\nu} = \Lambda_{\mu\nu}[S_{\mu\nu}] \quad (7.1)$$

where μ indicates the direction of radiation and ν the frequency. The problem with the classical lambda iteration is the slow convergence of the calculations. The idea behind the *accelerated* lambda iterations is then to split the lambda operator as

$$I^n = \Lambda^* S^n + (\Lambda - \Lambda^*) S^{n-1} = \Lambda^* S^n + \Delta I^{n-1} \quad (7.2)$$

where n indicates the n -th iteration step and Λ^* is the *approximate* lambda operator (indices for direction and frequency were omitted). This way, the intensity is expressed in terms of the source function S^n (which needs to be determined) and the known ΔI^n from the previous iteration. Convergency is then obviously achieved when $S^n = S^{n-1}$. Good choices for Λ^* are diagonal forms decoupling the depth de-

pendence or tridiagonal from taking into account only nearest neighbour interactions. See Rybicki & Hummer (1991) for details.

In addition to model atmospheres and model atoms, DETAIL also needs elemental abundances, microturbulences, and ODFs as input. The reason for this is that DETAIL occupation numbers are usually calculated for each atomic species separately in order to speed up the computations. This is a reasonable assumption as coupling between lines of different atomic species is very small in the stars investigated. Nevertheless, the effect of the omitted species on the opacity and thus on the source function needs to be accounted for which is done by employing the same pre-tabulated ODFs as used in the LTE ATLAS9 calculations.

Hydrogen and helium are – by far – the most abundant elements in the atmospheres of the stars in this work and, therefore, need to be always accounted for as background opacity in parallel with the particular element under investigation.

Finally, the occupation numbers computed with DETAIL are the basis for the last step, the line formation calculations with SURFACE (Giddings 1981; Butler & Giddings 1985; recently updated by K. Butler). SURFACE uses a much more sophisticated line formation (i.e. broadening) treatment as implemented in DETAIL. SURFACE also requires microturbulence, abundances, the model atmosphere, as well as various atomic quantities as input parameters describing mechanisms of line broadening.

After taking into account the effects of radial velocity, projected rotational velocity, and macroturbulence (Sect. 4.7) the synthetic spectra may be directly compared to the observation. Note that the spectrograph causes an additional broadening of the observed lines which is accounted for as *instrumental profile*. It leads to an additional Gaussian broadening contribution with width

$$\sigma(\lambda) = \Delta\lambda \cdot \frac{1}{2\sqrt{\ln 2}} \quad (7.3)$$

where $\Delta\lambda$ is the resolution of the spectrograph. With

$$v = \frac{\sigma(\lambda)}{\lambda} \cdot c \quad (7.4)$$

the instrumental profile can be described in velocity space via the Doppler formula. In the case of FEROS, a value of 3.75 km s^{-1} is obtained.

First of all, Fig. 7.2 summarises the basic idea for deriving stellar parameters. Synthetic spectra are calculated for an adopted set of parameters and compared to the observation. In order to improve the agreement between theory and observations, the parameters are altered until satisfying agreement is established. This can happen either by (automatically) fitting *a lot* of synthetic spectra to the observation searching for the best χ^2 or by calculating a few spectra based on educated guesses on how a synthetic spectrum will react to parameter variations. Both approaches based on two sets of hybrid non-LTE models were used in this work to some extent.

An extensive grid of synthetic spectra (as described in Kudritzki et al. 2008) covering effective temperatures from 8300 to 15 000 K and surface gravities from 0.75 to 2.70 dex gave a good starting point for the parameter determination. Although the

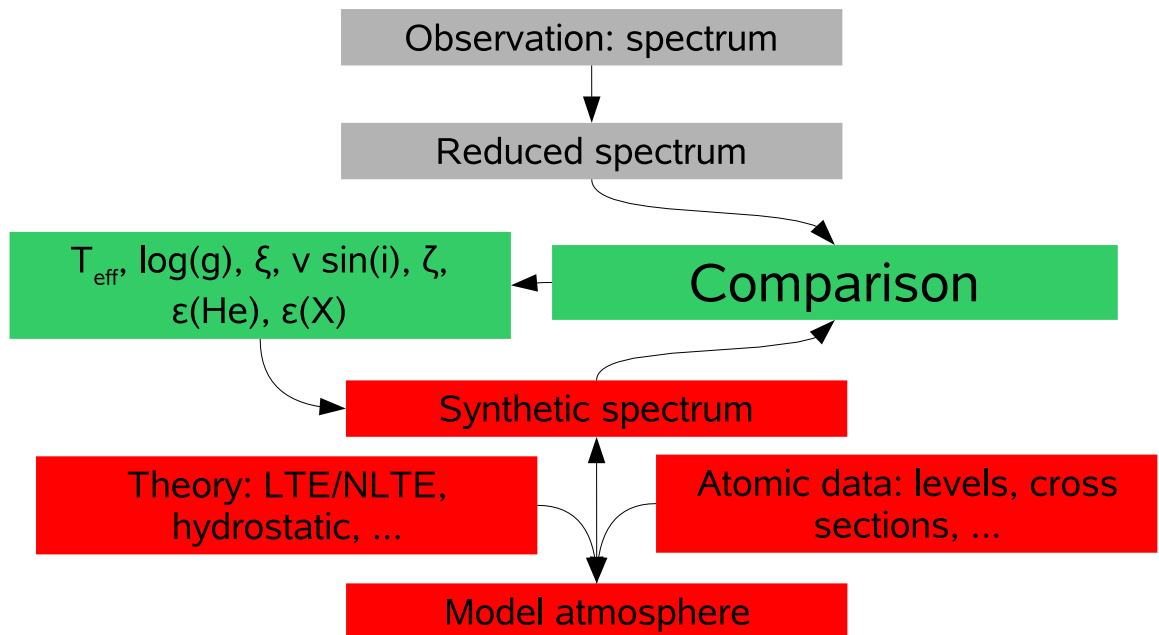


Figure 7.2: A basic scheme for quantitative spectral analyses. The central point is the comparison of the observations with synthetic spectra calculated based on several assumptions for a specific set of parameters. The model parameters are altered until a satisfying agreement is achieved.

grid was also calculated for SMC metallicity, it is limited to a fixed helium number fraction (0.09 at SMC metallicity) and fixed microturbulence (depending on T_{eff} and $\log g$, mostly 8 km s^{-1} for the present sample).

Changing the helium abundance has similar effects on the models as changing the surface gravity through its impact on the mean molecular weight (Kudritzki 1973). Similarly, the microturbulence affects the absorption of radiation in the stellar plasma and is thus also influencing the line strengths. Fortunately, the high quality of the observational material in this study allowed to determine these parameters independently. In order to reduce systematic errors in the present analysis, it was therefore decided to perform several more iteration steps using new models specifically adjusted for each star, thus fixing all parameters consistently. This represents the second “set” of synthetic spectra.

Supergiant model atmospheres cooler than $T_{\text{eff}} \sim 8300 \text{ K}$ may be subject to pressure inversion and thus density inversion depending mostly on the model surface gravity. Inversion is a problem for the parameter determination as it leads e.g. to a huge sensitivity of the Balmer lines which is mostly an artefact of the models. Moreover, the inversion happens usually at $\tau_{\text{ROSS}} \sim 1$ in the models which means that the formation of many lines will be systematically affected. Stars subject to pressure inversion (indicated in Table 6.1) are therefore omitted from the further analysis. For a detailed discussion on this matter, see Przybilla et al. (2006). As a guide, the ATLAS9 atmospheres did not show pressure inversion at $T_{\text{eff}} = 8300 \text{ K}$,

$\log g = 1.00$ dex or at $T_{\text{eff}} = 8000$ K, $\log g = 1.40$ dex (calculated for 1/5 solar metallicity, $n(\text{He})=0.09$, $\xi = 4 \text{ km s}^{-1}$). At lower temperatures or lower surface gravities, pressure inversion is then likely to occur.

7.2 Spectroscopic Indicators for Various Atmospheric Parameters

Several spectroscopic features used to constrain the atmospheric parameters are discussed in the following. Note that although the quantities and their related indicators are discussed separately all quantities were derived in an iterative process forcing simultaneous agreement between theory and observation for all indicators at the end. All derived parameters are summarised in Table 8.1.

7.2.1 Effective Temperature and Surface Gravity

These most important atmospheric parameters were derived by fitting the *Balmer line series* as well as various *ionisation equilibria*. Based on the available model atoms, ionisation equilibria for Mg I/II, N I/II, O I/II, and S II/III are examined. Figure 7.3 shows the basic strategy for determining T_{eff} and $\log g$. At fixed ξ , $n(\text{He})$, and $[M/H]$, one searches at various temperature values for the $\log g$ value with the best agreement to observation. Generally, ionisation equilibria are extremely sensitive to temperature changes whereas the Balmer lines are mainly sensitive to changes in $\log g$. Due to these different sensitivities, it is possible to find a unique best solution in the intersection of the two trends.

If possible, ionisation equilibria from multiple elements were used. However, due to the generally low metallicity in the SMC and thus weak metal lines, only one ionisation equilibrium could be investigated in most cases. For the sample SMC supergiants Mg I/II works in a temperature range from ~ 8000 to $10\,000$ K, N I/II from $\sim 10\,000$ to $14\,000$ K, O I/II above $\sim 14\,000$ K and S II/III at above $\sim 16\,000$ K in general. At $T_{\text{eff}} \gtrsim 10,000$ K, Mg I becomes too weak due to ionisation. Similarly, N I is too strongly ionised at $T_{\text{eff}} \gtrsim 14,000$ K while N II lines need at least $\sim 10\,000$ K for the respective levels to be excited. Similar arguments apply for O I/II and S II/III at higher temperatures.

Table 8.1 gives all derived atmospheric parameters as well as abundance information concerning the element(s) of the ionisation equilibria examined. Figure 7.4 shows example fits of Balmer lines and an ionisation equilibrium for a hot (AV443 at $T_{\text{eff}} = 16\,250$ K) and a cool (AV273 at $T_{\text{eff}} = 8200$ K) object. Both objects show emission contributions even in the higher Balmer lines. The figure also includes model spectra for parameters modified according to the uncertainties. These were always adopted based on the strength, quality, and number of suitable lines in a spectrum and the intensity of their responses to parameter variations. Generally, the cool objects have smaller uncertainties because the Mg I/II equilibrium is extremely sensitive to temperature changes and also quite sensitive to changes in $\log g$.

Many objects show emission in the Balmer lines due to a stellar wind making it necessary to concentrate on the higher Balmer lines which are less affected as well as to focus on the blue wings in case even the higher Balmer lines show wind-affected profiles.

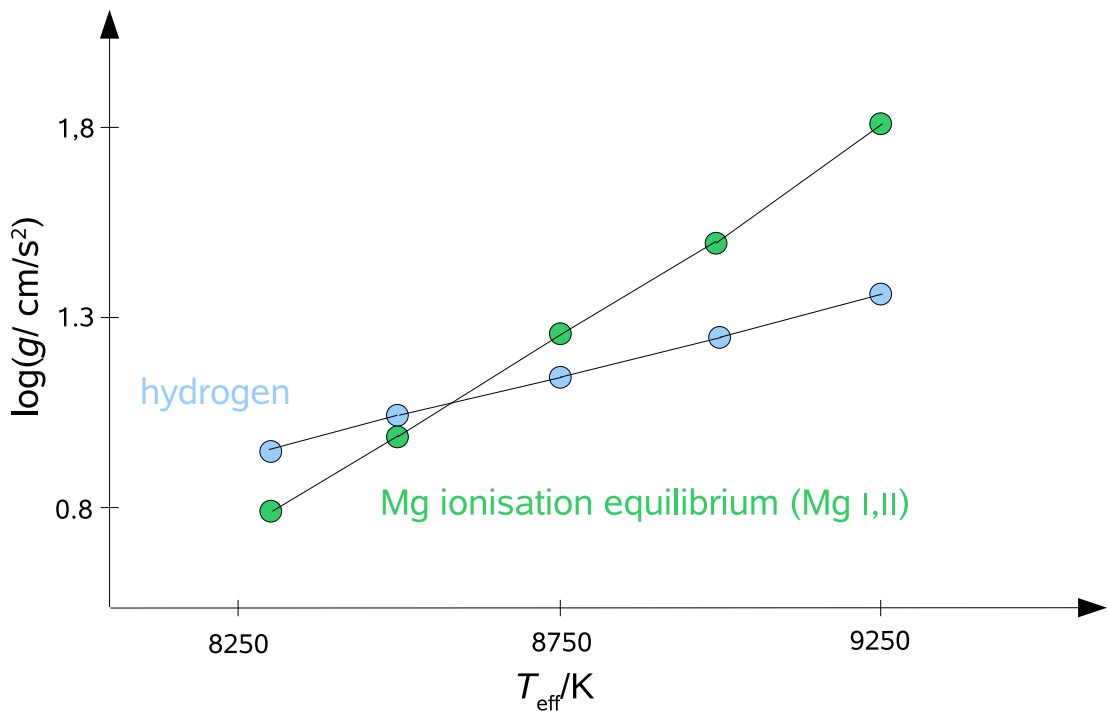


Figure 7.3: Example for the determination of $\log g$ and T_{eff} employing Balmer lines of hydrogen and an ionisation equilibrium (i.e. lines of multiple ionisation stages of one element fitting simultaneously at the same abundance) while keeping the microturbulence, metallicity, and helium abundance fixed. Each indicator alone cannot independently determine $\log g$ and T_{eff} . The degeneracy can only be solved by considering two independent indicators which are sensitive to changes in $\log g$ and T_{eff} by different degrees. In general, the ionisation equilibria are more sensitive to temperature changes than the Balmer lines. For Mg I/II, raising the temperature and thus the ionisation of Mg I makes the Mg I lines too weak with respect to the Mg II lines. This is accounted for by a higher surface gravity implying a higher density in the stellar atmosphere compensating the ionising effects of the high temperature. This can be understood as an interplay of excitation and ionisation (see Sect. 4.2).

At parameter ranges where the Mg I lines are weak ($W_{\lambda} \lesssim 30 \text{ m}\text{\AA}$), one faces some difficulties with them. According to several analyses (N. Przybilla and M. Farnstein, priv. comm.), the ionisation of Mg as implemented in the employed model atom is very likely too large, producing too weak Mg I lines. Determining effective temperatures from establishing the Mg I/II equilibrium would thus underestimate T_{eff} . This discrepancy is a problem at effective temperatures around 9500 K and is getting larger with lower gravities (where the Mg I lines are getting weaker). The solution of N. Przybilla and M. Farnstein in a study of galactic supergiants was to use the – presumably more reliable – N I/II equilibrium instead. However, this is not an option in the metal-poor environment of the SMC as the N II lines are not strong enough to be investigated at these relatively low temperatures.

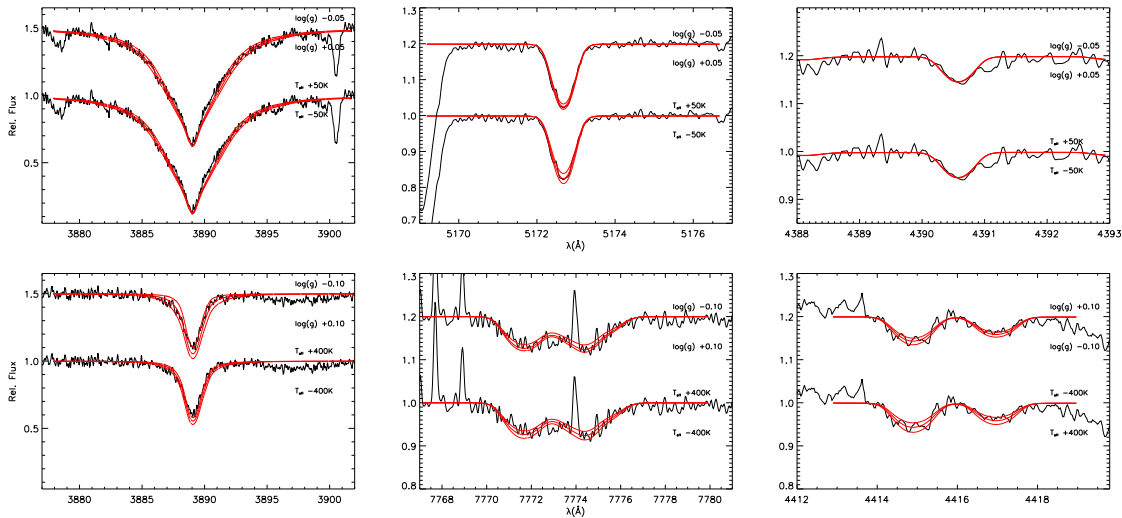


Figure 7.4: Examples for spectral line fits. *Top* row (left to right): H8, Mg I, and Mg II for AV273 at $T_{\text{eff}} = 8200 \text{ K}$; *Bottom* row (left to right): H8, O I, and O II for AV443 at $T_{\text{eff}} = 16250 \text{ K}$. Besides the models for the final parameters (*central red* line) model spectra for parameter changes of the order of the adopted uncertainties are also plotted. The upper spectra in each frame are shifted by $+0.5$ for the Balmer lines or $+0.2$ for the metal lines.

In order to avoid systematic errors on the basic atmospheric parameters which would also lead to significant errors in the derived abundances it was decided to perform fits of the overall *spectral energy distribution* (SED) in addition to the Balmer lines to fix T_{eff} and $\log g$. Fitting SEDs can not provide as accurate parameters as ionisation equilibria and requires an assumption on the extinction which is rather difficult to constrain. However, this was accepted for the relevant objects in order to avoid the much larger errors which could be made by relying on the Mg I lines. Objects for which the SED was used instead of the Mg I/II equilibrium are marked in Table 8.1 with “y” in the SED column.

To reliably constrain the basic atmospheric parameters T_{eff} and $\log g$ this way, a good coverage of the flux distribution from the ultraviolet to the infrared is needed. The Echelle spectra from the FEROS spectrograph – the main data for the quantitative spectral analysis – are not suitable for examining the SED. Although Echelle spectrographs offer both excellent resolution and wavelength coverage making them powerful instruments to study the *relative* flux in a stellar spectrum their complex setup including multiple diffraction elements makes it practically impossible to reconstruct any *absolute* flux information. Another reason for this in the case of FEROS is the usage of fiber optics and a circular entry for the light (instead of a slit). Due to atmospheric diffraction, different colours may then be partly shifted outward of this entry.

UV information for several of the relevant targets can be obtained from the database of UV spectra taken by the IUE satellite (as extracted from the INES archive at <http://sdc.laeff.inta.es/cgi-ines/IUEdbsMY>). Flux-calibrated, low-dispersion spectra with large aperture from 1150 to 1980 Å and from 1850 to 3290 Å are used. In

Table 7.2: Underlying data for fits of the spectral energy distribution. UV spectra are from the IUE satellite (<http://sdc.laeff.inta.es/cgi-ines/IUEdbsMY>); IR photometry for the JHK bands comes from the online catalogue of the 2MASS project (Cutri et al. 2003); R photometry was also obtained from this catalogue.

Object	UV spectra from IUE		R mag	J mag	H mag	K mag
	far UV	near UV				
AV98	SWP44955LL	LWP23322LL	11.38	11.272	11.241	11.228
AV110	...	LWP21936LL	12.19	11.754	11.710	11.716
AV315	SWP18054LL	LWR14206LL	10.82	10.665	10.592	10.555
AV338	SWP46131LL	LWP24262LL	12.50	12.474	12.459	12.432
AV382	SWP44930LL	LWP23307LL	11.19	11.235	11.181	11.183

addition, magnitudes in the infrared (J, H, K) could be obtained from the Two Micron All Sky Survey survey (2MASS, Cutri et al. 2003). Table 7.2 summarises information (in addition to the UB V magnitudes from the sources in Table 6.1) of targets for which SED fits were performed.

Figure 7.5 shows an example for a fit of such a SED and the responses to temperature changes. The synthetic fluxes are obtained from ATLAS9. The various magnitudes are transformed into fluxes by adopting zero points according to Heber et al. (2002, their Table 3). The observed fluxes were dereddened (corrected for extinction) using a reddening law as described by Cardelli et al. (1989), assuming a ratio of extinction to colour excess $A_V/E(B - V) = 3.1$. In general, this ratio depends on the composition of the interstellar medium. For the SMC, slightly lower values down to 2.7 are proposed. For the analysis, 3.1 is adopted which is also justified since the main contribution to extinction comes from the Milky Way foreground for most objects.

Five objects with possibly unreliable Mg I lines in theory (AV98, AV110, AV315, AV338, and AV382) could be investigated with SED fits based on the available UV and IR data and are found to have significantly higher temperatures indicated by the SEDs than by the Mg ionisation equilibrium. In the – rather extreme – cases of AV98 or AV315 which have both a very low surface gravity the discrepancy is of the order of 800K. For the other objects at higher surface gravities it is only few hundred K. Uncertainties in T_{eff} are adopted based on the sensitivity of the synthetic flux to temperature changes as well as the quality of the observational material.

Another object (AV270) could not be examined with respect to their SEDs because the UV flux is likely contaminated with the flux from a hot companion not visible in the examined FEROS spectrum. A companion based on the radial velocity variation was first proposed by Thackeray (1978). Based on the experience from the SED fits an empirical temperature correction with respect to the results of the Mg I/II ionisation equilibrium was applied in this case.

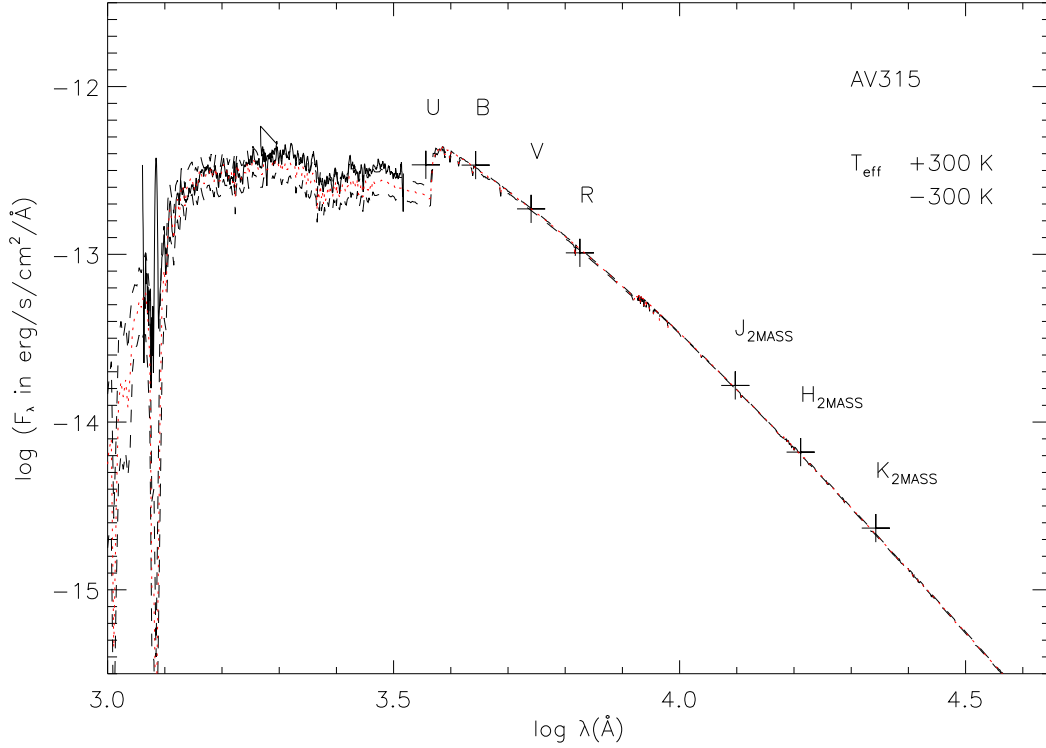


Figure 7.5: Fit of the spectral energy distribution (SED) of AV315 combining the photometric information as listed in Table 6.1 as well as UV flux from the IUE satellite (*solid black* curves) and infrared photometry from the 2MASS project (see Table 7.2). The SED is primarily sensitive to the effective temperature and, to a much lesser extent, to the surface gravity. In addition to the best fit (*dotted, red* curve), additional synthetic (*dashed, black* curves) fluxes with T_{eff} changed by the amount of the adopted uncertainties are overplotted (extinction is left constant). The synthetic fluxes are obtained from the ATLAS9 routine and normalised to the V magnitude. In the UV, more weight is given to the far UV part, as the optical UV part lies close to the Balmer jump (near the U magnitude) which is hard to reproduce with ATLAS9 (N. Przybilla, priv. comm.). Moreover, there are also problems as the extinction in this range does not correlate well with the typical reddening law.

7.2.2 Helium Abundance

Usually, one starts from the a helium abundance of 0.09 which is about the solar value since the generally lower initial helium abundance of the SMC stars is expected to be already increased due to rotationally induced mixing. It was often necessary to change the helium abundance in order to bring Balmer lines, ionisation equilibrium, *and* helium lines into agreement with theory simultaneously. This is not only a matter of just matching the helium lines since the helium abundance also affects the ionisation equilibria and the Balmer line widths. To give a rough idea about the effects, changing the helium abundance from 0.09 to 0.13 (at $T_{\text{eff}} = 12000\text{K}$ and $\log g = 1.70$) has the same effect as raising $\log g$ by ~ 0.05 dex when fitting the

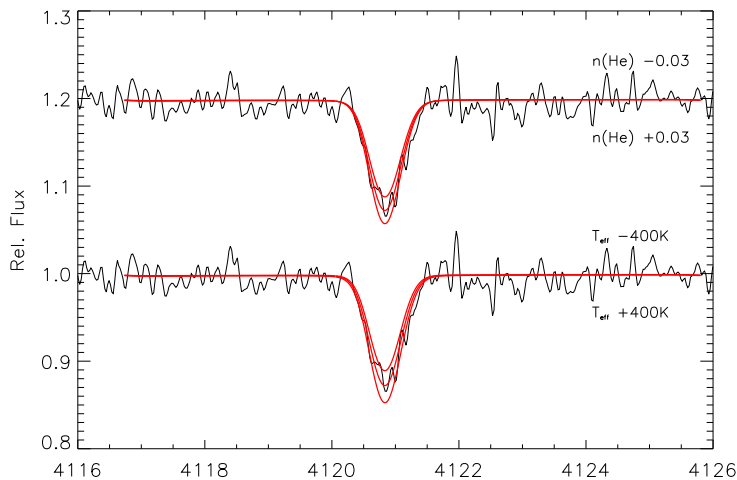


Figure 7.6: Example for a helium line fit for AV297. Besides the models for the final parameters (*central red line*, see Table 8.1) variations in helium abundance (± 0.03) and in T_{eff} (± 400 K) are also plotted. The upper set of spectra is shifted by $+0.2$.

Balmer lines. Fig. 7.6 shows a fit of a helium line for AV297 as well as its response to parameter changes. Note that while the temperature changes correspond to the adopted uncertainties, the changes indicated for the helium abundance do not. The profiles for the various helium abundances are just meant to illustrate the response of the model spectrum to abundance changes. Uncertainties in $n(\text{He})$ are always derived from the scatter of line-to-line abundances given by multiple helium lines.

7.2.3 Metallicity and Microturbulence

Both metallicity and microturbulence affect the line strengths and consequently the magnitude of the line-blanketing. Thus, they should be treated as free parameters making further iterations necessary. A detailed discussion on this subject is given in Przybilla et al. (2006).

Based on the specific abundances obtained from fitting ionisation equilibria as well as from the subsequent abundance analysis one can obtain a good estimate of the overall metallicity of a supergiant. As a result, the models for each star were calculated for one fifth (or -0.7 dex) solar metallicity in the respective opacity distribution functions (ODFs).

The microturbulence leads to a non-linear behaviour of the Doppler widths as a function of the thermal velocity, (see Eqn. 4.33). It has a larger effect for lines which are formed in regions with lower temperature. Stronger spectral lines are due a larger opacity at the corresponding colour which implies that these photons escape from the star in regions lying more outward. More outward usually also means cooler and thus a reduced photon flux (Stefan-Boltzmann law). All in all, it follows that strong lines – which originate from cooler regions – are more affected by effects of the microturbulence. The microturbulence is therefore determined on the condition that there is no dependence of the abundance on the equivalent width for a particular ionic species. According to the effective temperature in the atmosphere, different elemental species can/have to be used. In case of the metal-poor supergiants in this work Ti II is suitable for this task for $T_{\text{eff}} \lesssim 9000$ K and Fe II for $T_{\text{eff}} \lesssim 12000$ K

because these elements provide a sufficient number of lines of various strengths. At higher temperatures a newly constructed model atom (N. Przybilla, priv. comm.) for Si II/III was used.

7.2.4 Projected Rotational Velocity and Macroturbulence

Finally, comparisons between observed and theoretical line profiles allowed to derive the projected rotational velocity $v \sin i$ and the (radial-tangential) macroturbulent velocity ζ . Two approaches were combined for this task.

Firstly, automatic χ^2 fits of convolved synthetic profiles to metal lines (mostly Fe II and Ti II) carefully selected in terms of strength and symmetry (to exclude line blends) were performed. Only obviously unblended lines with equivalent widths between $\sim 20 - 130 \text{ m}\text{\AA}$ were considered. Besides a fixed Gaussian instrumental profile the synthetic profiles were convolved with multiple values for $v \sin i$ and ζ from between 0 to $\sim 50 \text{ km s}^{-1}$ in steps of 1 km s^{-1} for both parameters.

Secondly, synthetic and observed line profiles were also compared by eye. This is always a good idea in order to make sure that an automatic procedure is not misled by tiny blends, artifacts, and other spectral features not accounted for in an automatic fit. Moreover, when it comes to the hotter stars in the present sample ($T_{\text{eff}} \gtrsim 13\,000 \text{ K}$), the number of suitable lines for the described automatic procedure is swiftly decreasing making it necessary to also consider *the proper parts* of blended or slightly disturbed lines.

Uncertainties in $v \sin i$ and ζ are estimated based on several points. One major aspect is the standard deviation of the distribution from the automatic best fits to a selection of lines. However, this requires a certain number of lines to be significant which is especially an issue in the hotter stars of the sample. Therefore, it was also accounted for the line strength in the spectrum, its S/N ratio, as well as the sensitivity of the lines to changes in $v \sin i$ and ζ . For example, if either rotation or macroturbulence is dominating, the other one will usually have a larger uncertainty since the dominant one has a greater impact on the line profile. This is illustrated by Fig. 7.7.

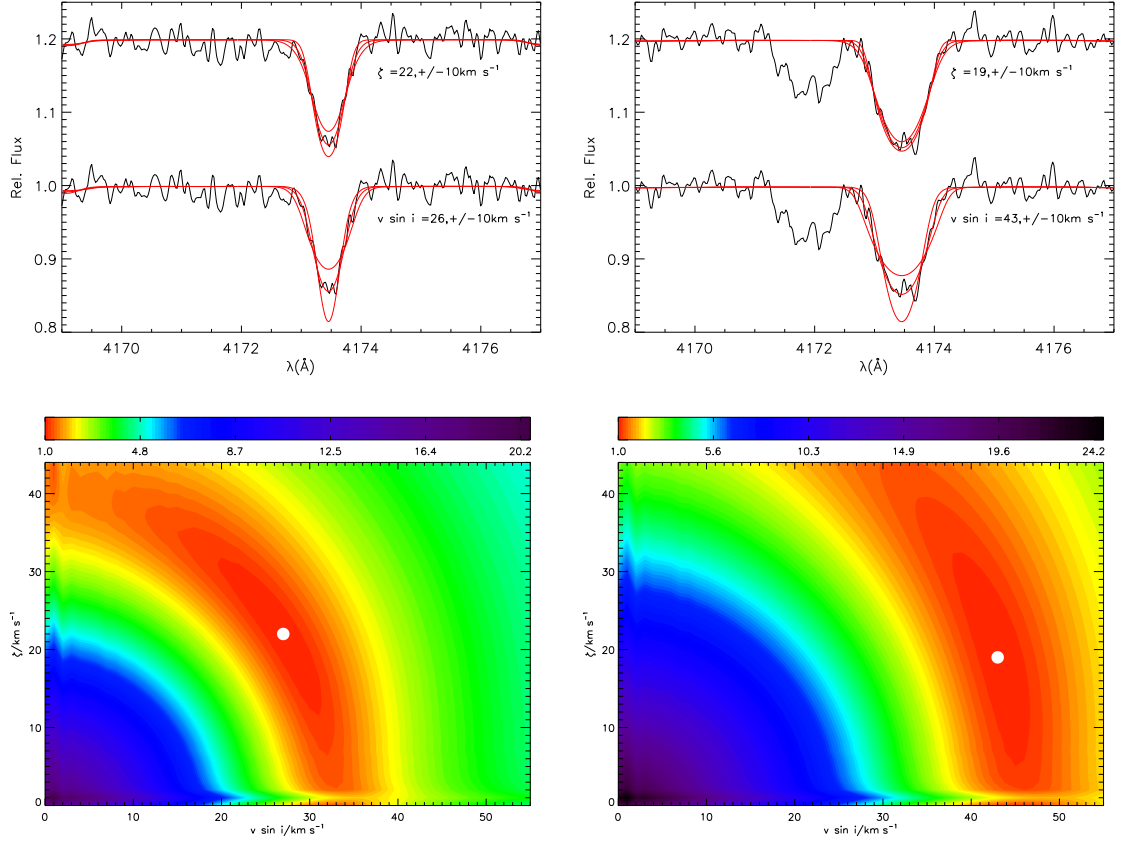


Figure 7.7: *Upper panels:* Comparison of the observation (*black line*) with theoretical spectra convolved with various values for the projected rotational velocity $v \sin i$ and the macroturbulence (*red lines*). Shown are fits of the Fe II line at 4173.45 Å for AV110 (*left*) and AV392 (*right*). The central red lines show the theoretical profiles convolved with values of $v \sin i$ and ζ corresponding to the best fits to this line as indicated. The other red lines show the responses of the synthetic profiles to variations of 10 km s^{-1} in both parameters. The high value of $v \sin i$ for AV392 (right frame) of 43 km s^{-1} implies that the line profile is dominated by $v \sin i$ and the line is less sensitive to variations in ζ for AV392 than for AV110 in the left frame. This means the uncertainties of the component which is not dominating are in general relatively larger.

Lower panels: Contour plots of $\sqrt{\chi^2}$ values for combinations of $v \sin i$ and ζ for the lines and stars above. *Left:* AV110, *right:* AV392. The goodness of the agreement between the observation and a theoretical spectrum convolved with the respective values (in steps of 1 km s^{-1}) is presented via the colour as indicated by the legend above each plot. The white dot marks the best fitting parameters (as denoted also in the upper panels). The slope of the lines of constant χ^2 is a measure of the relative sensitivity of a line to variations of $v \sin i$ and ζ . Nearly horizontal slopes mean that the line profile is not very sensitive to changes in $v \sin i$ whereas nearly vertical slopes mean that the profile is rather insensitive to changes in ζ . This is the case in the right hand frame describing the line profile for AV392. The best fit for this iron line is at $v \sin i = 43$ and $\zeta = 19 \text{ km s}^{-1}$. Around that point at high $v \sin i$, the steep slope indicates that ζ has a much smaller effect on the line profile leading to larger uncertainties – as discussed for the upper panels.

8 Basic Atmospheric Parameters

8.1 Results for the Sample Stars

Basic atmospheric parameters such as T_{eff} , $\log g$, $n(\text{He})$, ξ , $v \sin i$, and ζ could be reliably determined for 31 of the 38 SMC supergiants as shown in Table 8.1. Six objects (AV269, AV415, AV442, AV478, AV152, and AV254) show pressure inversion in their model atmospheres for the final parameters (see. Sect. 7.1) rendering these parameters unreliable. Moreover no ionisation equilibrium was available for AV2. Although the parameters could in principle be *estimated* by *assuming* a helium abundance or by fitting the spectral energy distribution (SED), there are no lines suitable for a determination of the microturbulence and many lines, including all available Balmer lines, helium lines and even metal lines are noticeably affected by emission in the stellar wind. In order to avoid the corresponding large (systematic) uncertainties it was decided to neglect this problematic object to guarantee a consistent analysis for all stars of the sample.

Therefore, the mentioned objects were omitted in the further analysis and are not listed in the table. Table 8.1 also presents the abundances of those chemical elements for which ionisation equilibria could be used and indicates whether a fit of the SED was favoured over the Mg I/II equilibrium (see Sect. 7.2). For AV270, this was not possible due to the UV flux contribution from a companion star. Instead of fitting the SED, an empirical temperature correction with respect to the temperature indicated by the Mg I/II equilibrium was applied leading to an intentional discrepancy. If the Mg I abundance is flagged by a colon in Table 8.1, it is regarded as uncertain.

Table 8.1: Overview of basic atmospheric parameters and ionisation equilibria. Uncertainties of the quantities are given in every second line (see Sect. 7.2 for a discussion).

Object	T_{eff} K	$\log g$ dex	$n(\text{He})$	ξ	$v \sin i$ km s^{-1}	ζ	V	$E(B$ $-V)$	$\epsilon(X) = \log(x/H) + 12$								SED (y)
									Mg I	Mg II	N I	N II	O I	O II	S II	S III	
AV20	8700	1.10	0.13	6	29	20	12.12	0.25	6.83	6.83	
±	50	0.05	0.01	1	2	3	0.01	0.01	0.01	0.00	
AV22	14600	1.90	0.13	5	32	23	12.225	0.10	7.92	7.94	
±	500	0.10	0.01	2	5	8	0.025	0.04	0.01	0.01	
AV56	16150	2.00	0.11	7	42	19	11.15	0.13	8.04	8.04	6.34	6.31	
±	250	0.10	0.02	1	5	8	0.01	0.01	0.01	0.04			
AV76	10250	1.30	0.12	6	39	25	11.19	0.10	8.20	8.18	
±	500	0.10	0.01	2	5	8	0.01	0.02	0.04		
AV98	9650	1.35	0.13	6	27	20	11.45	0.06	y
±	300	0.05	0.01	1	2	3	0.01	0.01	
AV105	9350	1.60	0.10	5	27	20	12.22	0.06	6.92	6.82	
±	75	0.05	0.02	1	2	3	0.01	0.01	0.05	0.01	
AV110	9500	1.40	0.17	5	23	21	12.08	0.08	y
±	400	0.05	0.01	1	3	2	0.01	0.01	
AV136	8250	0.95	0.13	6	28	21	10.97	0.07	6.89	6.92	
±	50	0.05	0.01	1	2	4	0.01	0.01	0.03	0.05	
SK56	12500	1.70	0.11	6	41	21	10.87	0.11	8.11	8.09	
±	500	0.10	0.01	1	4	10	0.01	0.02		0.05	
AV151	16750	2.25	0.13	8	48	24	12.26	0.14	8.23	8.22	6.46	6.47	
±	250	0.10	0.01	2	5	10	0.01	0.01	0.04	0.03			
AV200	12000	1.70	0.12	6	33	23	12.17	0.14	8.07	8.08	
±	500	0.10	0.01	1	6	10	0.01	0.02	
AV205	8850	1.35	0.09	4	18	10	12.32	0.11	6.90	6.90	
±	75	0.05	0.01	1	2	6	0.01	0.01	0.04	0.01	

Table 8.1: Overview of basic atmospheric parameters and ionisation equilibria (*continued*).

Object	T_{eff} K	$\log g$ dex	$n(\text{He})$	ξ	$v \sin i$ km s^{-1}	ζ	V	$E(B$ $-V)$	$\epsilon(X) = \log(x/H) + 12$								SED (y)
									Mg I	Mg II	N I	N II	O I	O II	S II	S III	
AV211	10 250	1.45	0.09	7	30	17	11.52	0.11	7.92	7.94	
±	400	0.10	0.01	1	4	5	0.01	0.02	0.07		
AV270	9500	1.40	0.09	6	32	21	11.42	0.03	7.03:	6.79	
±	500	0.05	0.01	1	3	5	0.01	0.02		0.04	
AV273	8200	1.35	0.09	4	25	17	12.16	0.06	6.79	6.78	
±	50	0.05	0.00	1	3	7	0.01	0.01	0.04	0.03	
AV297	11 750	1.80	0.10	5	20	19	12.10	0.04	7.98	7.98	
±	400	0.10	0.01	2	4	6	0.00	0.01	
AV298	8850	1.50	0.09	3	4	7	12.47	0.03	6.63	6.62	
±	50	0.05	0.01	1	3	3	0.01	0.01	0.02	0.09	
AV315	9700	1.35	0.11	6	29	17	10.90	0.06	y
±	300	0.05	0.02	1	3	4	0.01	0.01	
AV338	9750	1.80	0.08	4	40	21	12.54	0.07	y
±	300	0.05	0.02	1	4	7	0.01	0.01	
AV347	10 500	1.60	0.09	7	24	22	12.13	0.03	8.11	8.15	
±	400	0.10	0.01	1	3	3	0.00	0.01	0.04		
AV362	14 000	1.95	0.15	8	40	24	11.36	0.09	8.12	8.12	7.92	7.92	
±	125	0.10	0.01	2	4	7	0.01	0.01	0.06	0.02	0.03		
AV367	10 500	1.30	0.09	7	33	26	11.22	0.07	7.95	7.97	
±	400	0.10	0.01	2	3	6	0.01	0.02	0.02		
AV382	9900	1.45	0.10	5	27	23	11.41	0.07	y
±	300	0.05	0.02	1	2	3	0.01	0.01	
AV392	8550	1.70	0.09	3	41	21	12.57	0.04	6.93	6.93	
±	75	0.05	0.01	1	3	5	0.01	0.01	0.04	0.01	

Table 8.1: Overview of basic atmospheric parameters and ionisation equilibria (*continued*).

Object	T_{eff} K	$\log g$ dex	$n(\text{He})$	ξ	$v \sin i$ km s^{-1}	ζ	V	$E(B$ $-V)$	$\epsilon(X) = \log(x/H) + 12$						SED (y)		
									Mg I	Mg II	N I	N II	O I	O II		S II	S III
AV399	9650	1.75	0.09	2	5	7	12.33	0.04	6.80	6.71
±	150	0.05	0.01	1	3	4	0.01	0.01	0.02	0.02
AV443	16 250	1.95	0.12	8	47	23	10.97	0.06	8.19	8.19
±	400	0.10	0.01	2	5	10	0.01	0.01	0.04	0.03
AV463	8000	1.40	0.09	4	26	14	12.10	0.07	6.75	6.76
±	50	0.05	0.00	1	2	3	0.01	0.01	0.04	0.06
AV504	11000	1.80	0.10	6	19	20	11.91	0.03	7.93	7.91
±	500	0.10	0.01	1	4	6	0.01	0.02	0.05
SK194	11 500	1.65	0.10	6	42	25	11.74	0.07	8.09	8.09
±	500	0.10	0.01	1	6	10	0.01	0.02
SK196	12600	1.75	0.10	7	28	28	12.04	0.06	8.01	7.99
±	400	0.10	0.01	2	5	7	0.01	0.02	0.08
SK202	15 400	2.25	0.09	6	28	19	12.32	0.05	8.00	8.01
±	400	0.10	0.01	2	4	8	0.01	0.01	0.04	0.04

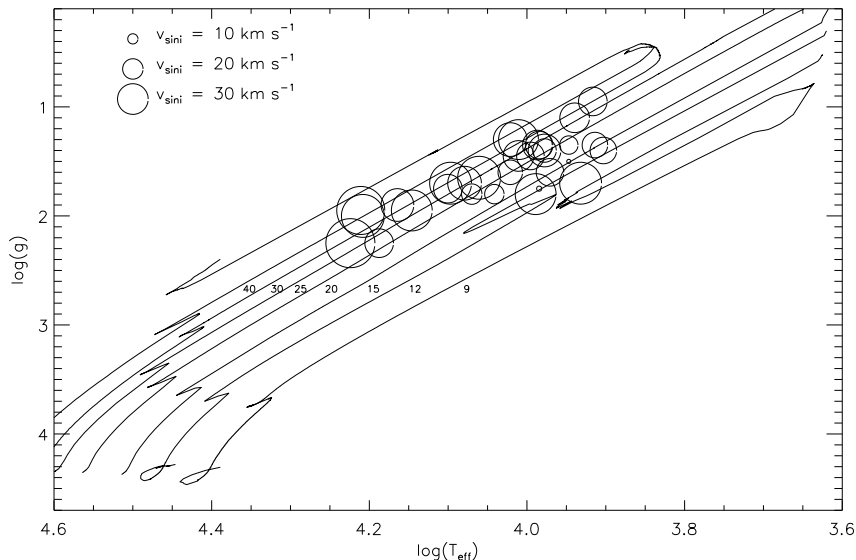


Figure 8.1: Overview of projected rotational velocities for the sample stars coded via the symbol size as indicated in the legend. Stellar evolution tracks at SMC metallicity from Maeder & Meynet (2001) for 9 to 25 M_{\odot} (ZAMS mass) and Meynet & Maeder (2005) for 30 and 40 M_{\odot} are overplotted as denoted. Note the tiny points at $T_{\text{eff}} \sim 3.95$ and $\log g \sim 1.6$ marking the exceptional stars AV298 and AV399.

8.2 Projected Rotational Velocity and Macroturbulence

Figures 8.1 and 8.2 summarise the results for the projected rotational velocity $v \sin i$ and the macroturbulence ζ respectively. No trends for ζ with T_{eff} or $\log g$ can be recognised. Throughout the parameter range of the sample macroturbulent velocities close to $\sim 20 \text{ km s}^{-1}$ are found.

Exceptions worth mentioning are AV298 and AV399. These objects do not only show very small values in ζ but also for ξ as well as for $v \sin i$.

Fig. 8.1 indicates a trend in rotational velocities with respect to the atmospheric parameters. For smaller $\log g$ the mean $v \sin i$ is smaller by trend and there are no relatively large ($v \sin i \gtrsim 40 \text{ km s}^{-1}$) rotational velocities for $\log g \lesssim 1.5$ dex. This is in agreement with the idea of angular momentum conservation when a star is expanding while evolving towards the red (super)giant phase.

8.3 Comparison with Previous Analyses

The atmospheric parameters derived here are compared with several objects from other works in Table 8.2. Venn (1999) provided an investigation in LTE with additional non-LTE corrections while Lee et al. (2005) performed a study using model atmospheres in full non-LTE. Moreover, Trundle et al. (2004) as well as Trundle & Lennon (2005) employ full non-LTE (hydrodynamic) model atmospheres.

We have eight stars in common with the study of Venn (1999). We omitted three (AV254, AV442, and AV478) of them because of the pressure inversion problem

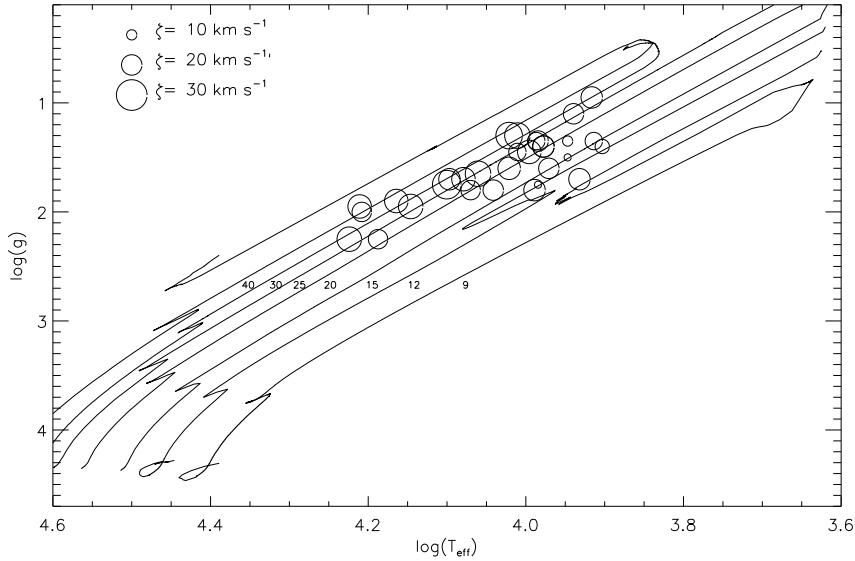


Figure 8.2: Same as Fig. 8.1 but for macroturbulent velocities coded via the symbol size. Similar to the $v \sin i$ plot in Fig. 8.1, AV298 and AV399 at $T_{\text{eff}} \sim 3.95$ and $\log g \sim 1.6$ show remarkably small values for ζ

(see Sect. 7.2.1). For the remaining five stars, effective temperatures and surface gravities are well within the given uncertainties for most stars the only exception being AV298 which is remarkable with respect to very low values for ξ , $v \sin i$, and ζ . $v \sin i$ is difficult to compare as Venn (1999) did not investigate the macroturbulence. However, $v \sin i$ values seem generally in good agreement except for AV392 with a higher velocity derived in the present analysis. Excellent agreement is achieved in terms of the microturbulence.

The study of Lee et al. (2005) has three stars in common with the present sample with T_{eff} and $\log g$ agreeing (fairly) well for all of them. A comparison for the microturbulence is not possible as they only present their results for two *assumed* values of ξ .

AV20 and AV362 have also been analysed by Trundle et al. (2004). T_{eff} is in excellent agreement for both stars while $\log g$ differs for AV362. This star shows (strong) emission contributions in all Balmer lines in the spectrum even in the cores and the red wings of the highest Balmer within the spectral range of FEROS. This might lead to an underestimation of $\log g$. The microturbulence for AV22 is significantly smaller in the present analysis. For AV362 Trundle et al. (2004) were not able to derive the microturbulent velocity but simply adopted $\xi = 10 \text{ km s}^{-1}$. Macroturbulence was not derived independently but is a contribution to their $v \sin i$'s which would well combine the broadening affects of our two contributions from $v \sin i$ and ζ .

In a similar study, Trundle & Lennon (2005) have examined three stars from the present sample. Again, there is good agreement in T_{eff} for all stars. Very good agreement is also found in $\log g$ for two stars (AV56 and AV443) while modest agreement is found for AV151 with the values still lying within the combined uncertainties. The

Table 8.2: Comparison of atmospheric parameters for literature sources – ordered by source and growing right ascension. Sources: *t.w.* (this work), (1) Venn (1999), (2) Lee et al. (2005), (3) Trundle et al. (2004), (4) Trundle & Lennon (2005).

Object	T_{eff} K	$\log g$ dex	ξ	$v \sin i$ km s^{-1}	ζ	Src.
AV110	9500±300	1.40±0.05	5±1	23±3	21±2	<i>t.w.</i>
	9500±200	1.4±0.1	4±1	25±5		(1)
AV136	8250±50	0.95±0.05	6±1	28±2	21±4	<i>t.w.</i>
	8200±100	1.0±0.1	6±1	20±5		(1)
AV298	8850±50	1.50±0.05	3±1	4±3	7±3	<i>t.w.</i>
	9400±200	1.7±0.1	3±1	15±5		(1)
AV392	8550±50	1.70±0.05	3±1	41±3	21±5	<i>t.w.</i>
	8500±200	1.7±0.1	3±1	25±5		(1)
AV463	8000±50	1.40±0.05	4±1	26±2	14±3	<i>t.w.</i>
	8000±100	1.3±0.1	4±1	25±5		(1)
SK194	11 500±500	1.65±0.10	6±1	42±6	25±10	<i>t.w.</i>
	11 700/ 11 500	1.7	10/ 20			(2)
SK202	15 400±400	2.25±0.10	6±2	28±4	19±8	<i>t.w.</i>
	14 750	2.2	10/20			(2)
AV22	14 600±500	1.90±0.10	5±2	32±5	23±8	<i>t.w.</i>
	14 500±1500	1.90±0.15	10	46		(3)
AV362	14 000±125	1.95±0.10	8±2	40±4	24±7	<i>t.w.</i>
	14 000±1500	1.70±0.15	10	51		(3)
AV56	16 150±250	2.00±0.10	7±1	42±5	19±8	<i>t.w.</i>
	16 500±2000	2.05±0.20	10	80		(4)
AV151	16 750±250	2.25±0.10	8±2	48±5	24±10	<i>t.w.</i>
	16 000±1500	2.10±0.15	15	62		(4)
AV443	16 250±400	1.95±0.10	8±2	47±4	23±7	<i>t.w.</i>
	16 500±2000	1.95±0.20	11	73		(4)

projected rotational velocities are significantly higher in their study for most cases even if the values of the present work for $v \sin i$ and ζ are combined. As in Trundle et al. (2004), the microturbulence is systematically lower in the current analysis.

Although some of these studies use codes accounting for *full* non-LTE or even hydrodynamic effects, the present hydrostatic, hybrid non-LTE approach is much more sophisticated with respect to the implemented atomic data and the treatment of ionisation via photons or collisions. This point is crucial and generally more important as shown e.g. by Przybilla et al. (2006) or by Nieva (2007) for OB stars. Another improvement in the present work is the individual treatment of rotation and macro-

turbulence. The results clearly indicate that contributions from macroturbulence are required in order to reproduce the line profiles satisfactorily. Together with the high quality of the observational material, these are the reasons for the small uncertainties of the derived parameters.

9 Chemical Abundance Analysis

9.1 Results for the Sample Stars

Elemental abundances for various elements and ionic species were derived through fits of synthetic line profiles to the observation. The results from the analysis of the 31 supergiants in the sample are summarised in Table 9.1 combining all ionic species for an element. Abundances labeled with a colon in the table should be treated with caution as there may be some problems in the respective model atoms (C II at high temperatures, see Sect. 9.2.1 for a discussion). Such abundances are omitted when examining e.g. N/C ratios or abundance gradients in the next sections. For AV270, the Mg I abundance is not reliable (see Sect. 7.2.1 and Sect. 8.1) and thus ignored in the following. However, the Mg II abundance can be regarded reliable.

Good consistency could be achieved throughout the sample. The line-to-line scatter for He, C, N, O, as well as Mg is very small (≤ 0.05 dex) in almost all objects. The scatter for S, Ti, Fe is slightly larger adding up to typically $\lesssim 0.10$ dex with almost all uncertainties being less than < 0.15 dex.

For the further discussion of chemical mixing in massive stars (see Sect. 9.4, N/C ...), Table 9.1 also includes the combined abundances of C, N, and O (denoted as ΣCNO , where the abundances are added on the linear scale) as well as N/C and N/O ratios if respective lines could be examined in a star. The latter two are given as *mass* ratios. Corresponding uncertainties are derived from the line-to-line scatter for each element with Gaussian error propagation. Thus, they are only given if more than one line could be investigated for either element.

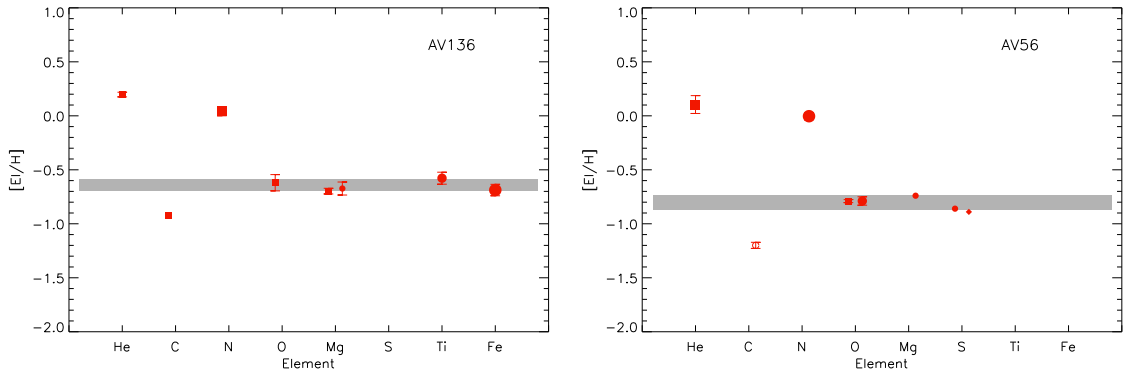


Figure 9.1: Examples for abundances (relative to the solar composition of Grevesse & Sauval 1998) determined from a cool (*left*) and a hot (*right*) object. The symbol size indicates the number of spectral lines analysed – small: 1 to 5, medium: 6 to 10, large: more than 10. Boxes: neutral, circles: single-ionised, diamonds: double-ionised species. The error bars represent 1σ -uncertainties from the line-to-line scatter. The grey shaded area marks the metallicity of the objects with 1σ -errors (see text) as deduced from the average of O, Mg, S, Ti, and Fe abundances if available. Abundance patterns for the rest of the sample can be found in Fig. 9.2.

Table 9.1: Overview of basic atmospheric parameters and elemental abundances. 1σ -uncertainties from the line-to-line scatter are given in every second line. Note that the N/C and N/O ratios are given as *mass* fractions.

Object	T_{eff}	$\log g$	ξ	n	$\epsilon(X) = \log(x/H) + 12$								$m(X)/m(Y)$		
	K	dex	km s^{-1}	He	C	N	O	Mg	S	Ti	Fe	ΣCNO	N/O	N/C	[M/H]
AV20	8700	1.10	6	0.13	...	7.87	8.11	6.83	6.62	4.36	6.75	...	0.50	...	-0.68
±				0.01	...	0.03	0.01	0.01		0.12	0.12		0.04	...	0.09
AV22	14 600	1.90	5	0.13	6.85:	7.93	7.93	6.97	6.39	0.87	...	-0.77
±				0.01	0.02:	0.04	0.02		0.03		0.09	...	0.15
AV56	16 150	2.00	7	0.11	7.32:	7.92	8.04	6.84	6.32	0.66	...	-0.80
±				0.02	0.03:	0.03	0.04		0.02		0.07	...	0.07
AV76	10 250	1.30	6	0.12	7.62	8.19	8.23	6.92	6.52	...	6.83	8.57	0.80	4.36	-0.65
±				0.01		0.03			0.03	...	0.09				0.04
AV98	9650	1.35	6	0.13	7.19	8.17	8.13	6.77	6.55	4.61	6.88	8.47	0.97	11.14	-0.62
±				0.01		0.05	0.02	0.01	0.07	0.10	0.14		0.11		0.18
AV105	9350	1.60	5	0.10	...	7.80	8.18	6.87	...	4.38	6.74	...	0.36	...	-0.67
±				0.02	...	0.03	0.02	0.06	...	0.10	0.12		0.03	...	0.09
AV110	9500	1.40	5	0.17	7.82	7.97	8.16	6.76	6.63	4.45	6.79	8.48	0.55	1.64	-0.65
±				0.01		0.06	0.02			0.09	0.15		0.08		0.13
AV136	8250	0.95	6	0.13	7.60	7.96	8.21	6.89	...	4.36	6.81	8.47	0.49	2.68	-0.64
±				0.01		0.04	0.08	0.04	...	0.06	0.05		0.10		0.05
SK56	12 500	1.70	6	0.11	7.29	8.09	6.37	...	6.96	7.48	-0.68
±				0.01	0.05	0.04	0.04	1.11	0.20
AV151	16 750	2.25	8	0.13	7.02:	7.83	8.22	6.96	6.47	0.35	...	-0.66
±				0.01	0.04:	0.03	0.03		0.01		0.04	...	0.07
AV200	12 000	1.70	6	0.12	7.41	8.07	8.17	6.79	6.41	...	7.10	8.47	0.70	5.46	-0.66
±				0.01	0.05	0.01			0.07	...	0.05			0.63	0.18

Table 9.1: Overview of basic atmospheric parameters and elemental abundances (*continued*).

Object	T_{eff} K	$\log g$ dex	ξ km s^{-1}	n He	$\epsilon(X) = \log(x/H) + 12$								$m(X)/m(Y)$		
					C	N	O	Mg	S	Ti	Fe	ΣCNO	N/O	N/C	[M/H]
AV205	8850	1.35	4	0.09	7.78	7.77	8.27	6.90	6.66	4.42	6.88	8.49	0.27	1.13	-0.58
±				0.01		0.06	0.03	0.03	0.01	0.11	0.09		0.04		0.07
AV211	10 250	1.45	7	0.09	7.57	7.92	8.24	6.78	6.37	...	6.85	8.46	0.42	2.64	-0.72
±				0.01	0.02	0.06	0.02		0.04	...	0.07		0.07	0.41	0.11
AV270	9500	1.40	6	0.09	...	8.00	8.14	6.79	6.57	4.68	6.76	...	0.64	...	-0.62
±				0.01	...	0.03	0.06	0.04		0.05	0.15		0.10	...	0.21
AV273	8200	1.35	4	0.09	7.41	7.76	8.15	6.79	...	4.11	6.81	8.35	0.36	2.63	-0.75
±				0.00	0.01	0.03	0.01	0.04	...	0.13	0.11		0.03	0.21	0.07
AV297	11 750	1.80	5	0.10	7.52	7.98	8.19	6.63	6.47	...	6.93	8.45	0.54	3.40	-0.72
±				0.01	0.04	0.00	0.03		0.09	...	0.11		0.04	0.28	0.17
AV298	8850	1.50	3	0.09	7.20	7.72	8.11	6.63	6.49	4.09	6.64	8.30	0.35	3.86	-0.82
±				0.01		0.05	0.02	0.06		0.13	0.14		0.05		0.10
AV315	9700	1.35	6	0.11	...	8.09	8.31	6.83	6.45	4.70	6.89	...	0.53	...	-0.57
±				0.02	...	0.03			0.08	0.16	0.14			...	0.21
AV338	9750	1.80	4	0.08	...	7.90	8.16	6.93	...	4.55	6.91	...	0.48	...	-0.57
±				0.02	...	0.04		0.03	...	0.06	0.18			...	0.13
AV347	10 500	1.60	7	0.09	...	8.11	8.21	6.89	6.54	...	6.92	...	0.71	...	-0.64
±				0.01	...	0.04	0.08	0.06	0.05	...	0.11		0.14	...	0.05
AV362	14 000	1.95	8	0.15	7.21	8.12	7.92	6.64	6.14	8.36	1.37	9.40	-0.97
±				0.01	0.06	0.03	0.02		0.02		0.11	1.37	0.08
AV367	10 500	1.30	7	0.09	7.44	7.95	8.25	...	6.56	...	6.83	8.47	0.45	3.85	-0.63
±				0.01	0.06	0.02	0.02	...	0.09	...	0.14		0.03	0.59	0.04
AV382	9900	1.45	5	0.10	7.44	7.89	8.31	6.89	6.44	4.70	6.97	8.49	0.34	3.31	-0.55
±				0.02		0.03	0.05		0.04	0.14	0.12		0.05		0.20

Table 9.1: Overview of basic atmospheric parameters and elemental abundances (*continued*).

Object	T_{eff} K	$\log g$ dex	ξ km s^{-1}	n He	$\epsilon(X) = \log(x/H) + 12$								$m(X)/m(Y)$		
					C	N	O	Mg	S	Ti	Fe	ΣCNO	N/O	N/C	$[M/H]$
AV392	8550	1.70	3	0.09	7.57	7.35	8.16	6.93	...	4.57	6.92	8.31	0.14	0.71	-0.57
±				0.01		0.04	0.01	0.03	...	0.14	0.14		0.01		0.14
AV399	9650	1.75	2	0.09	7.76	7.83	8.13	6.75	6.49	4.27	6.86	8.41	0.43	1.37	-0.71
±				0.01	0.01	0.01	0.02	0.05	0.03	0.16	0.09		0.02	0.04	0.07
AV443	16 250	1.95	8	0.12	6.94:	7.94	8.19	6.89	6.46	0.49	...	-0.69
±				0.01	0.04:	0.05	0.03				0.06	...	0.05
AV463	8000	1.40	4	0.09	7.53	7.26	8.18	6.75	...	4.35	6.78	8.31	0.11	0.63	-0.70
±				0.00		0.03	0.05	0.04	...	0.13	0.13		0.01		0.10
AV504	11 000	1.80	6	0.10	7.41	7.92	8.20	6.86	6.53	...	6.96	8.42	0.47	3.80	-0.64
±				0.01		0.04	0.02		0.13	...	0.11		0.05		0.08
SK194	11 500	1.65	6	0.10	7.63	8.09	8.19	6.88	6.47	...	7.23	8.51	0.70	3.36	-0.59
±				0.01		0.00			0.05	...	0.07				0.21
SK196	12 600	1.75	7	0.10	7.12	8.00	8.15	...	6.32	...	7.20	8.40	0.62	8.80	-0.62
±				0.01	0.04	0.06		...	0.14	...	0.12			1.53	0.29
SK202	15 400	2.25	6	0.09	6.78:	7.57	8.01	6.78	6.30	0.32	...	-0.84
±				0.01	0.07:	0.04	0.04	0.01	0.08		0.04	...	0.05

An overview of all accessible elemental abundances for an example of a hot and a cool object are shown in Fig. 9.1 with respect to the solar values of Grevesse & Sauval (1998). Similar plots for the other objects of the sample are summarised in Fig. 9.2. Significant nitrogen enrichment and carbon depletion was found for all our objects given that nitrogen or carbon lines could be analysed in the respective spectrum. Strong variations in the C and N abundance are found from star to star, however, the *sum* of C, N, and O abundances (ΣCNO in Table 9.1) are very similar for all objects. These abundance patterns are signs of conversions between C, N, and O within the CNO cycle and of pronounced mixing of the atmosphere with processed matter from the stellar core. See Sect. 9.4 for a more extensive discussion of this subject.

Figure 9.1 also indicates the metallicity of an object with the grey-shaded area (see also Table 9.1). Mean and scatter of the metallicity are always based on the abundances for O, Mg, S, Ti, and Fe if available with all elements weighted equally. Abundance patterns are in very good agreement with the solar pattern for the vast majority of the objects with the 1σ -scatter of the metallicity being $\lesssim 0.1$ dex. Larger scatter can (almost) always be seen as the result of either Fe or Ti abundances being off the overall metallicity indicated by O, Mg, and S. This might indicate problems in the respective model atoms. This issue is far beyond the scope of the present project but should be kept on the agenda for further improvements.

9 CHEMICAL ABUNDANCE ANALYSIS

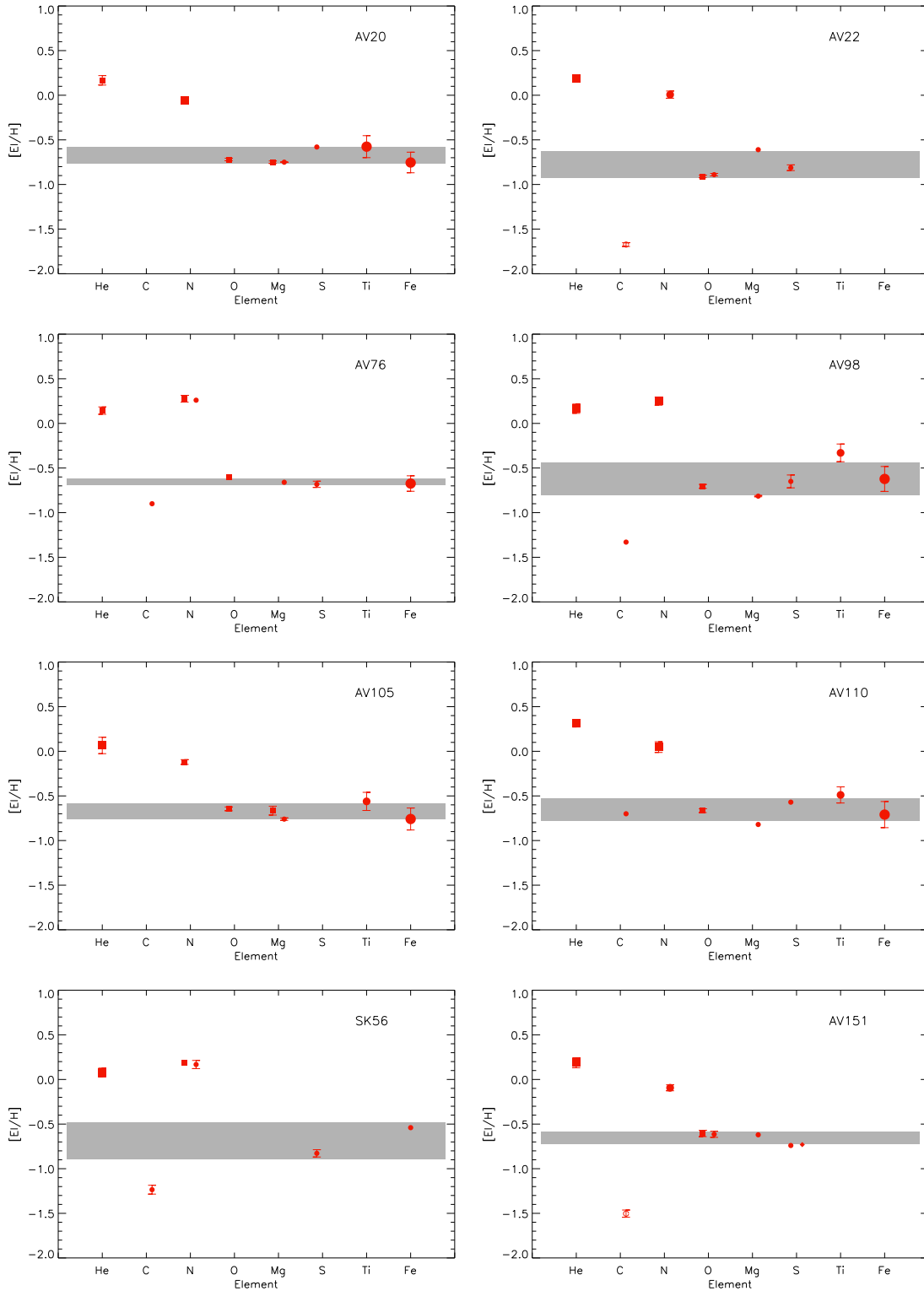


Figure 9.2: Similar to the plots of Fig. 9.1. The abundance patterns for all other stars (if applicable) are shown. Possibly unreliable abundances (indicated with a colon in Table 9.1) are shown as open symbols.

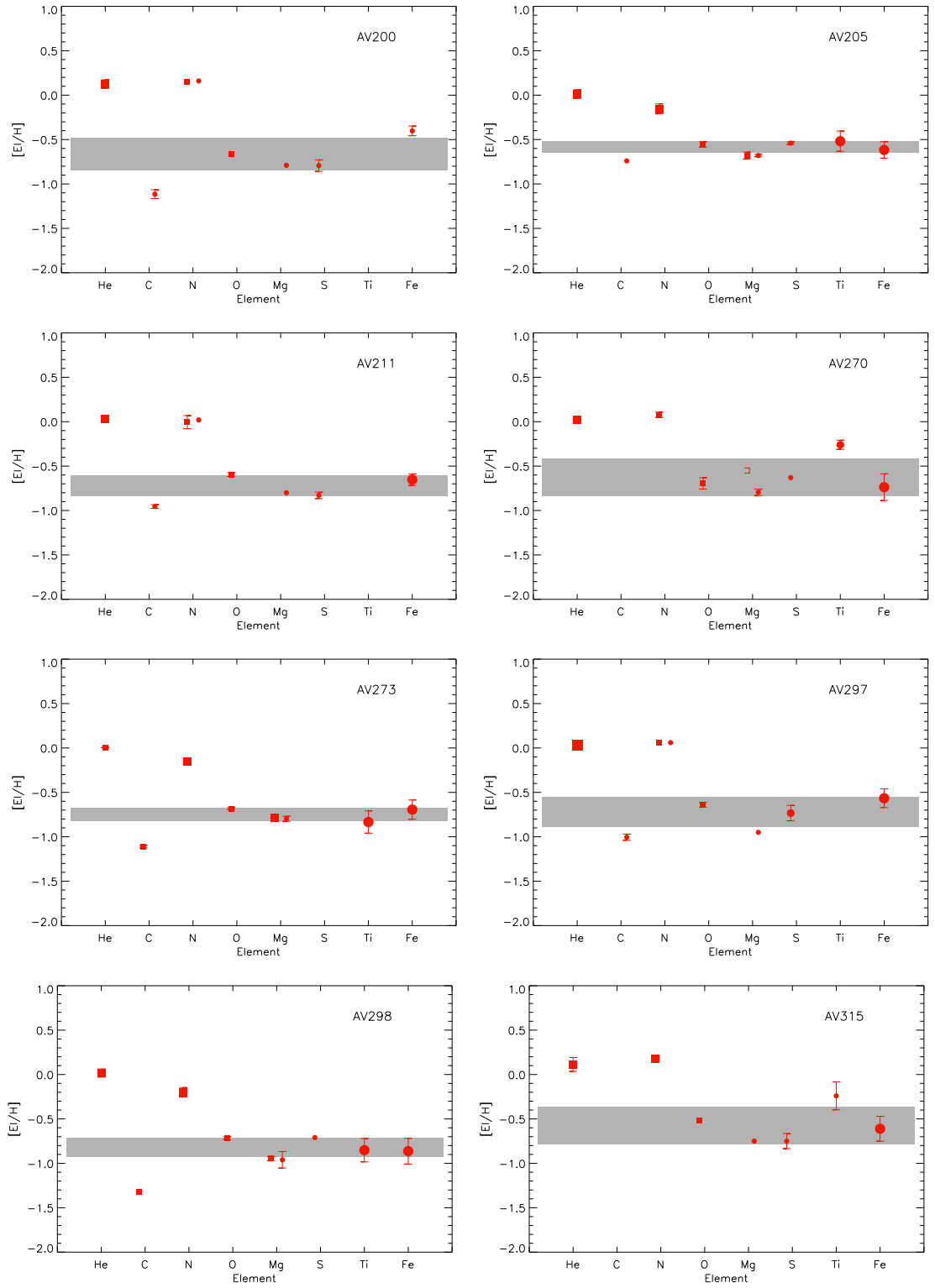


Figure 9.2: *continued*

9 CHEMICAL ABUNDANCE ANALYSIS

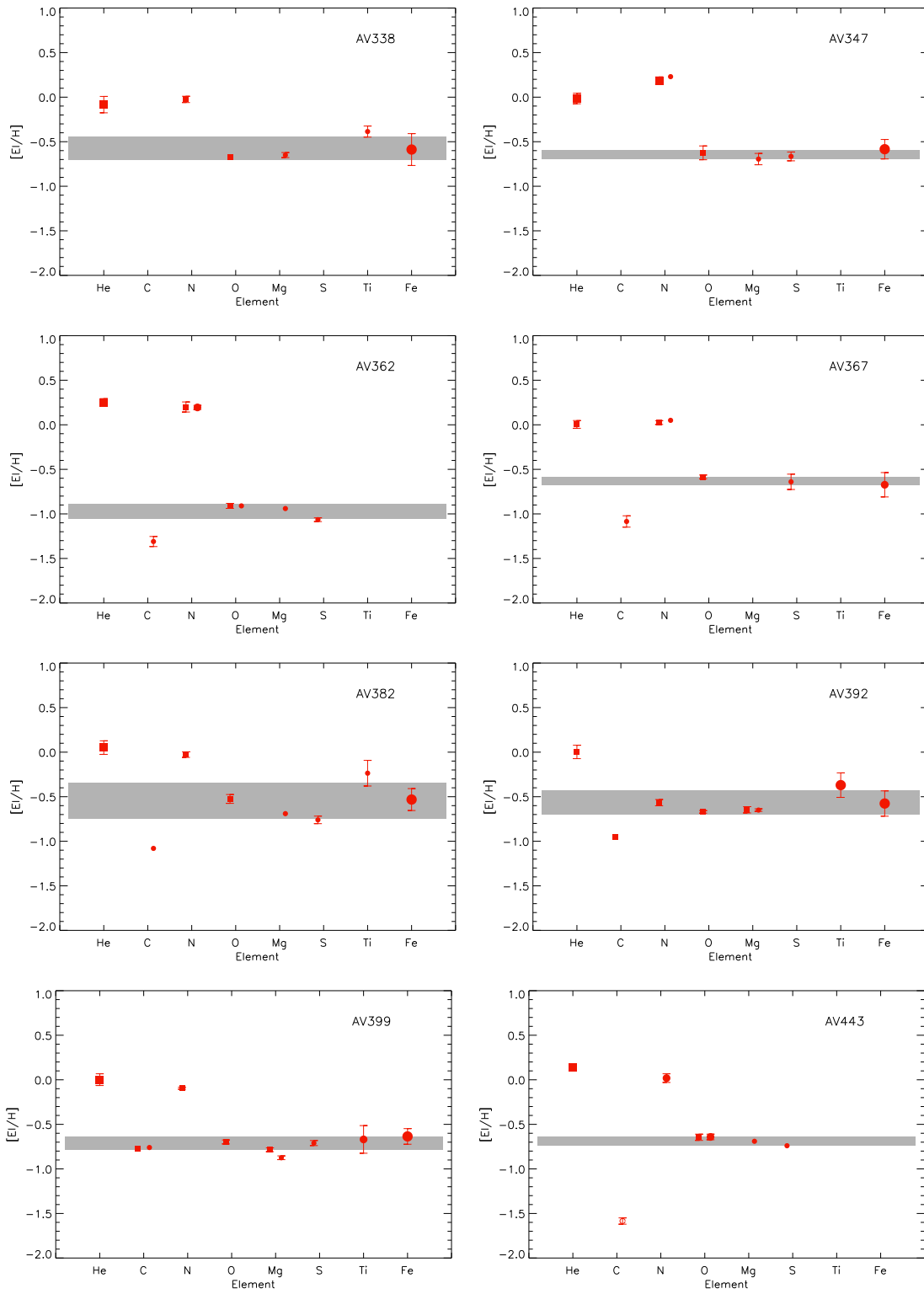
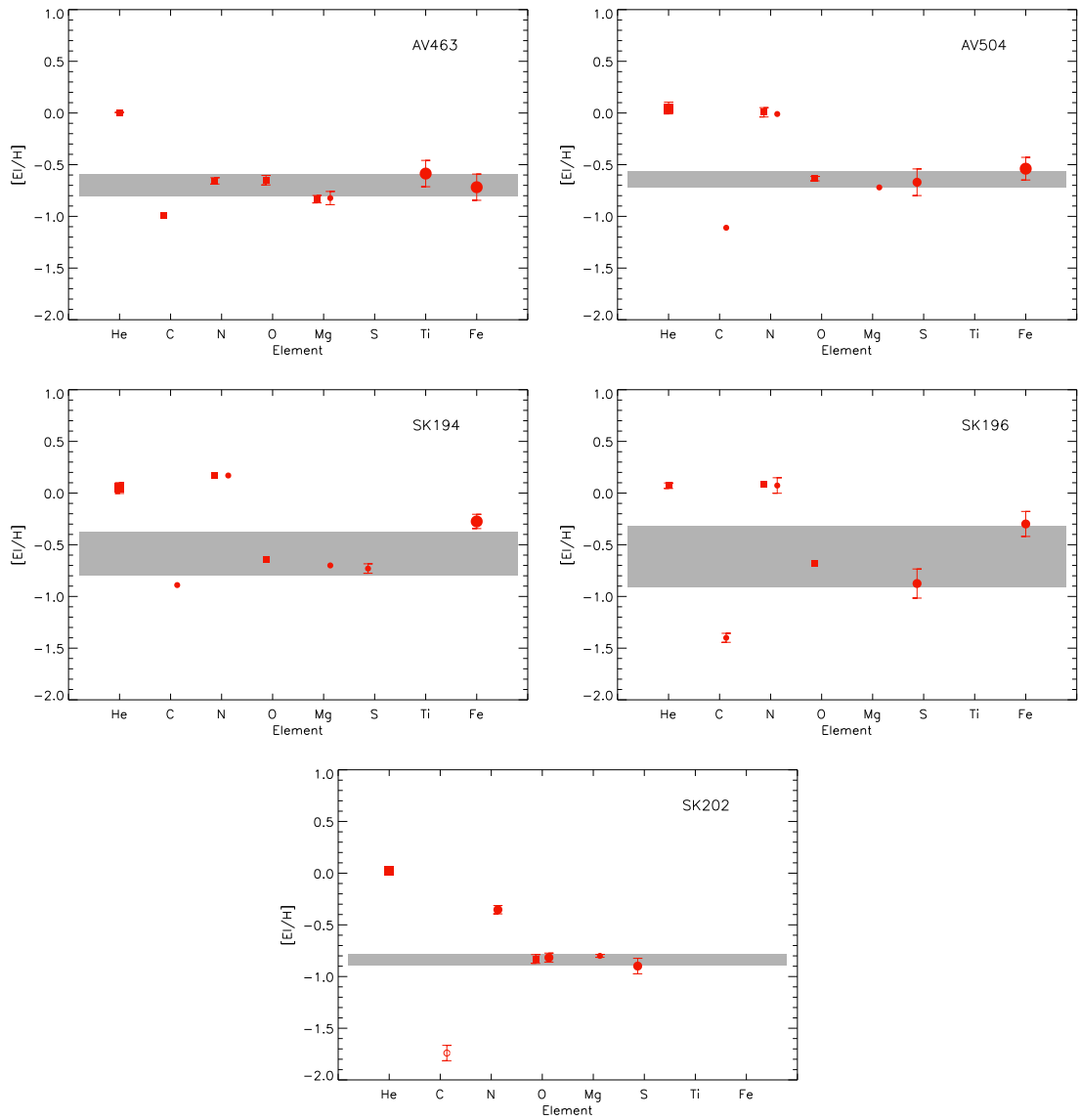


Figure 9.2: *continued*

Figure 9.2: *continued*

9.2 Systematics in Abundances

9.2.1 Trends with the Temperature

As a consistency check, it is reasonable to look for any systematic trend of the derived abundances with respect to the atmospheric parameters of the respective star. The most important atmospheric parameter influencing the strength of a metal line – apart from the abundance itself – is the effective temperature. Therefore, Fig. 9.3 is presenting the derived abundances as a function of the effective temperature of the respective star.

In general, the good news is that the ionisation equilibria N, O, Mg, and S show no (significant) trends with the effective temperature – an argument for the reliability of the derived atmospheric parameters. Only the O and S abundances at high temperatures seem systematically lower. However, the point in the O and the S plot at 14 000 K – corresponding to AV362 – is supported by *two* ionisation equilibria (N I/II and O I/II). This makes the temperature and abundances for this object quite secure so that the low abundances for this star are very likely real. Moreover, it strengthens the trust in temperatures (and thus abundances) derived with the O I/II equilibrium for objects at $T_{\text{eff}} \gtrsim 14\,000$ K. However, it should be noted that O I/II strongly relies for O I on the lines at 7770 Å which are usually difficult to model as they are quite sensitive to changes in the microturbulence and because of their – in general – large equivalent width (in the low-metallicity environment of SMC, this problem is less important).

The temperature basis in the case of Ti is too small for any significant trend to be found. For Fe, however, there seems to be a rather clear effect where quite large abundance are found for $T_{\text{eff}} \geq 11\,000$ K. In combination with the rather large 1σ scatters found for the iron abundances in most stars (see Table 9.1) or the deviation of the Fe abundance from the “usual” pattern in some objects (Fig. 9.2), this might indicate some inconsistencies in the underlying atomic data as implemented in the used model atom. A detailed investigation of the model atom is far beyond the scope of the present work but should be performed in the future. Of course, the high Fe abundances in the stars could also be real. Despite this apparent systematic trend, which is rather small compared to uncertainties given by some other studies on supergiants, these abundances are still suitable for further discussions (e.g. on galactic gradients) within some restrictions.

A special note is also indicated for carbon. Almost all abundances are derived from C II while C I could only be studied for the coolest stars around 8000 K. These C II lines are mostly the lines at 4267 Å as well as around 6580 Å. These lines can be quite a challenge to model (in non-LTE) which is described in detail by Nieva & Przybilla (2006, 2008). They constructed a new model atom based on up-to-date atomic data and careful investigation of observed stellar spectra and were thus able to solve this problem. The model atoms was calibrated with early-type main-sequence star in the Milky Way. The low metallicity and low density of the (atmospheres of) SMC supergiants might enhance the problem in this respect as we find the C abundances to be lower at high temperatures.

In principle, one could also think of a selection effect to explain these low abun-

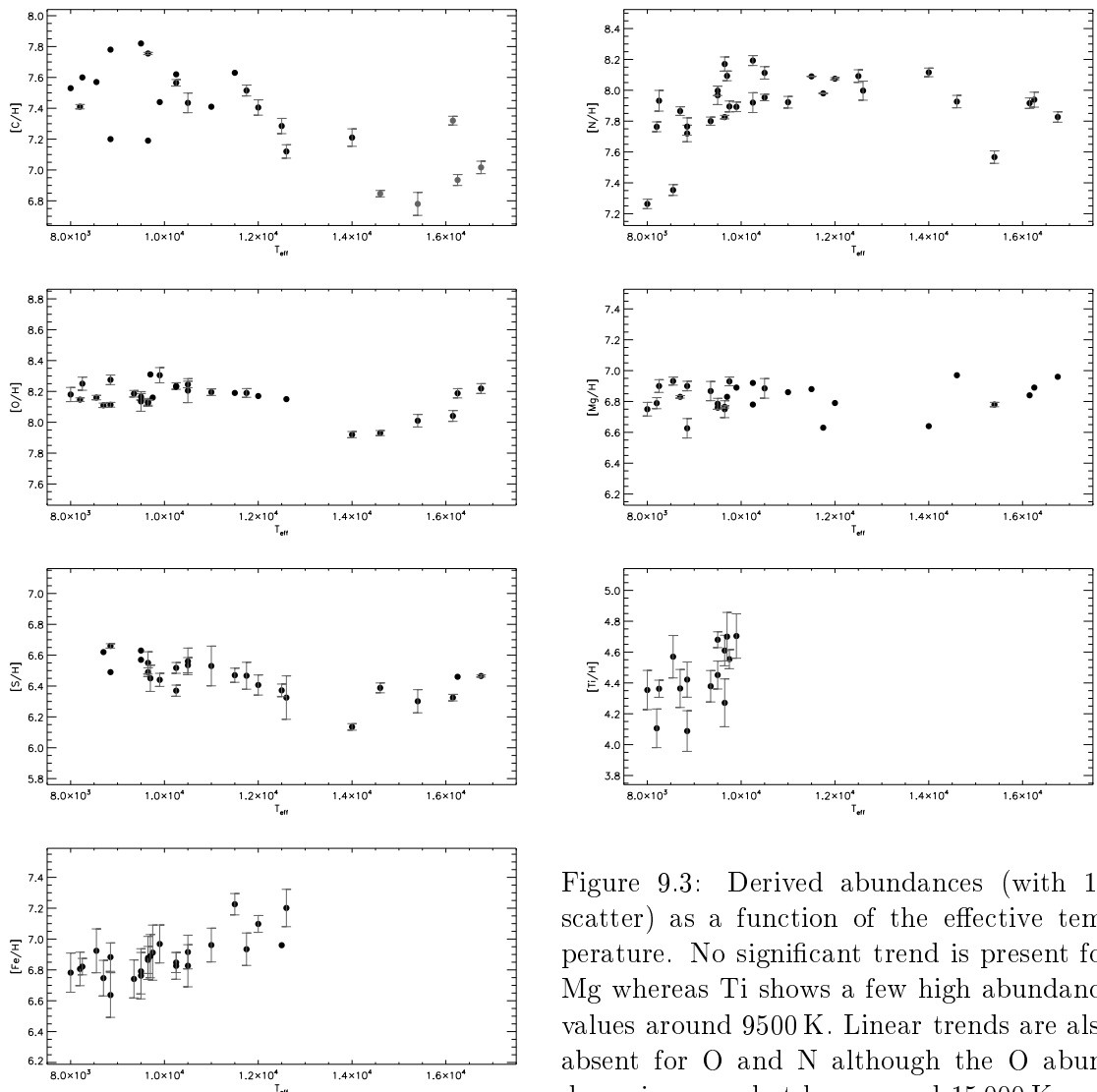


Figure 9.3: Derived abundances (with 1σ scatter) as a function of the effective temperature. No significant trend is present for Mg whereas Ti shows a few high abundance values around 9500 K. Linear trends are also absent for O and N although the O abundance is somewhat low around 15 000 K.

However, the statistics at these temperatures is not good enough to suggest a systematic effect. There may be a slight trend for S indicating smaller abundances at higher temperatures. Rather clear systematic effects are found for C and Fe meaning systematically smaller/larger abundances at 15 000 K or 12 000 K respectively. The corresponding carbon abundances for C at stars with high effective temperatures (AV22, AV151, AV443, SK196, and SK202, indicated by grey circles) may be the result of problems in the model atom (see discussion in the text). They are thus probably not reliable and will be omitted in the further discussion of e.g. N/C ratios.

dances. At high temperatures, the sample consists only of rather massive stars (see e.g. Fig. 8.1) which are supposed to experience stronger enrichment of the atmosphere with nuclear processed matter from the core. The low C abundance would then be created by effects of the CNO cycle. However, this would imply a simultaneous pronounced enhancement of the nitrogen abundance. As this can not be seen, the low C

abundances (from the singly ionised stage) for higher temperatures are more likely a problem of the modelling. Therefore, these abundances (marked with grey symbols in Fig. 9.3 and with a colon in Table 9.1) are excluded in the following when carbon abundances are compared (e.g. also in the discussion of the N/C ratios in Sect. 9.4).

9.2.2 Systematic Uncertainties from Parameter Variations

In order to better estimate the systematic uncertainties of the derived atmospheric abundances, the change in these abundances when modifying the basic atmospheric parameters is examined. Table 9.2 compares the final abundances with ones corresponding to parameter changes for a “cool” (AV136), a “warm” (AV297), and a “hot” (SK202) object. These changes are not the parameter uncertainties as adopted for those objects, but shall represent uncertainties (a bit higher than) typically found in the respective parameter ranges. E.g., the Mg I/II equilibrium shows smaller uncertainties than the 200 K difference investigated for AV136 as it shall also give an idea for objects with parameter determinations based on SEDs (with uncertainties of about 300 K).

Examining Table 9.2, one finds that the effective temperature uncertainties have the largest impact on the determined abundances. This is especially the case for the ionisation equilibria (Mg I/II, N I/II, and O I/II) whose abundances react – except for Mg – in opposite ways allowing small error bars for T_{eff} to be adopted. Note that although Mg I and Mg II lines react in the same ways to parameter changes, this is more than compensated by the extreme sensitivity of the Mg I lines.

The changes of the ionic abundances when modifying the stellar parameters as indicated amount to typically ≤ 0.1 dex. Exceptions are only the reactions of Fe II and Ti II lines to temperature variations and some ions employed for ionisation equilibria. However, in the latter case, the *elemental* abundances averaged over the ionisation states will be less affected and thus more stable.

Thus, the systematic uncertainties of the elemental abundances due to uncertainties in the atmospheric parameters are comparable to the statistical uncertainties inferred from the line-to-line scatter (see e.g. Table 9.1).

9.3 Comparison with Abundance Results for the Sample Stars in the Literature

The stars of our sample which have been analysed in previous studies (see also Sect. 8.3) can also be compared to the results of the present work with respect to the derived abundances. An overview of mean abundances and uncertainties is given in Table 9.3 for various literature sources: *t.w.* (this work), (1) Venn (1999), (2) Lee et al. (2005), (3) Trundle et al. (2004), (4) Trundle & Lennon (2005). Only elements treated in the present study are listed. Note that the uncertainties from (3) and (4) are not derived from the line-to-line scatter as done in this work but include their pronounced systematic uncertainties (e.g. from simply adopting a microturbulence in 3). In particular, these two studies could only investigate one Mg II line (at 4481Å the same as in this work) at the high temperatures.

Table 9.2: Estimate of systematic abundance uncertainties from abundances based on modified atmospheric parameters for three selected objects. The abundances presented in the first line for each star are the ones derived for the final atmospheric parameters as indicated next to the designation of each star. The following lines give the abundances which may be derived when one atmospheric parameter is modified as indicated.

	$\epsilon(X) = \log(x/H) + 12$										
	C I	C II	N I	N II	O I	O II	Mg I	Mg II	S II	Ti II	Fe II
AV136: $T_{\text{eff}} = 8250 \text{ K}$, $\log g = 0.95 \text{ dex}$, $\xi = 6 \text{ km s}^{-1}$											
	7.60	...	7.93	...	8.25	...	6.89	6.92	...	4.36	6.82
$T_{\text{eff}} + 200 \text{ K}$:	7.83	...	8.03	...	8.32	...	7.26	6.95	...	4.73	6.97
$\log g + 0.05$:	7.54	...	7.93	...	8.24	...	6.79	6.91	...	4.31	6.81
$\xi + 1$:	7.58	...	7.91	...	8.25	...	6.85	6.90	...	4.30	6.78
AV297: $T_{\text{eff}} = 11750 \text{ K}$, $\log g = 1.80 \text{ dex}$, $\xi = 5 \text{ km s}^{-1}$											
	...	7.52	7.98	7.98	8.19	6.63	6.47	...	6.93
$T_{\text{eff}} + 350 \text{ K}$:	...	7.38	8.04	7.88	8.26	6.71	6.39	...	7.10
$\log g + 0.10$:	...	7.54	7.95	8.05	8.18	6.55	6.50	...	6.88
$\xi + 2$:	...	7.45	7.89	7.91	8.19	6.57	6.41	...	6.91
SK202: $T_{\text{eff}} = 15400 \text{ K}$, $\log g = 2.25 \text{ dex}$, $\xi = 6 \text{ km s}^{-1}$											
	...	6.78	...	7.57	8.00	8.01	...	6.78	6.30
$T_{\text{eff}} + 500 \text{ K}$:	...	6.71	...	7.41	8.08	7.86	...	6.89	6.38
$\log g + 0.10$:	...	6.80	...	7.62	7.99	8.10	...	6.74	6.30
$\xi + 2$:	...	6.71	...	7.48	7.99	7.96	...	6.74	6.27

We have derived abundances for five objects from Venn (1999) who determined the abundances based on LTE (ATLAS9) calculations with additional non-LTE corrections. The present study deals with the more sophisticated approach of full non-LTE population number computations. Good to excellent agreement is obtained for Fe and Ti abundance for all stars (except Ti for AV110). Good agreement is found for Mg for three stars (AV110, AV136, and AV392) while there are significant differences for AV298 and AV463. For AV298, this is – among other reasons – a consequence of the different atmospheric parameters (mainly T_{eff}). Very good agreement is found for all oxygen abundances and for the upper limits of her carbon abundances with respect to the carbon abundances derived in the present work. The nitrogen abundances (except for AV392) were taken from an update in Venn & Przybilla (2003). The updated values are higher than the original ones from Venn (1999) by typically 0.2–0.3 dex and lie thus much closer to the results of the present work. Nevertheless, their updated N abundances still lie about 0.1–0.2 dex lower in most cases.

Good agreement with the three objects in common with the non-LTE study of Lee et al. (2005) is found for almost all elements (C, N, O, and Mg) where abundances are given for two assumptions (10 and 20 km s^{-1} , left and right abundance

values respectively) on the microturbulence. The lower microturbulence generally means higher abundances which fit better to the abundances derived in the present work. The only exception are their nitrogen abundances which are larger for larger microturbulence. A very large discrepancy of the order of 1 dex is found for iron. Due to the similarity of the basic atmospheric parameters, this must be an issue of the underlying modelling codes and/or model atoms.

The study of Trundle et al. (2004) reveals for the two stars AV22 and AV362 fair (within ~ 0.2 dex) agreement in magnesium and in carbon – including the uncertainties which are quite large for carbon – and very good agreement for nitrogen (≤ 0.1 dex). The similar analysis of Trundle & Lennon (2005) also shows fair agreement in carbon for AV56 and AV443 while the carbon abundance for AV151 in the present study seem significantly higher. The nitrogen abundance for AV443 is well consistent with the present value while significantly higher or lower nitrogen abundances are found for AV151 and AV56 respectively. Although both studies account for non-LTE effects and even employ hydrodynamic model codes (FASTWIND, Puls et al. 2005), these codes rely on model atoms which are less sophisticated than the ones used here which might explain some differences.

None of the quantitative analyses which have objects in common with the present sample derive the helium abundance independently but *assume* the standard solar helium abundance of 0.09. Moreover, Lee et al. (2005) as well as Trundle et al. (2004) do not derive the microturbulence but only give abundances for assumptions on it. However, these parameters may have significant influence on the atmospheric parameters and also directly on the other stellar abundances (see Sect. 7.2). The present study accounts for non-standard helium abundance and microturbulence and can thus provide a consistent picture.

Taking these effects into account leads – in combination with the excellent atomic data implemented in the codes and model atoms – to a high degree of consistency. This is reflected – among other things – in the small statistical uncertainties of derived abundances where multiple lines indicate very similar values. This is a major improvement with respect to earlier studies. Prominent examples are the uncertainties in C and N of Trundle et al. (2004) and Trundle & Lennon (2005) compared to those from the present work. Such large uncertainties make it hard to discuss stellar evolution in terms of evolution of the N/C ratio as in Sect. 9.4.

Table 9.3: Comparisons with abundances from previous analyses (see Sect. 8.3 for sources).

Object	T_{eff} K	$\log g$ dex	$n(\text{He})$	$\epsilon(X) = \log(x/H) + 12$							Src.
				C	N	O	Mg	S	Ti	Fe	
AV110	9500	1.40	0.17±0.01	7.82	7.97±0.06	8.16±0.02	6.76	6.63	4.45±0.09	6.79±0.15	<i>t.w.</i>
	9500	1.40	...	<8.7	7.84±0.06	8.1	6.82±0.04	...	4.04±0.04	6.68±0.21	(1)
AV136	8250	0.95	0.13±0.01	7.60	7.96±0.04	8.21±0.08	6.89±0.04	...	4.36±0.06	6.81±0.05	<i>t.w.</i>
	8200	1.0	...	<8.2	7.73±0.05	8.1	6.79±0.13	...	4.26±0.12	6.82±0.21	(1)
AV298	8850	1.50	0.09±0.01	7.20	7.72±0.05	8.11±0.02	6.63±0.06	6.49	4.09±0.13	6.64±0.14	<i>t.w.</i>
	9400	1.7	...	<8.4	7.72±0.07	8.1	7.01±0.08	...	4.12±0.10	6.70±0.15	(1)
AV392	8550	1.70	0.09±0.01	7.57	7.35±0.04	8.16±0.01	6.93±0.03	...	4.57±0.14	6.92±0.14	<i>t.w.</i>
	8500	1.7	...	<8.1	< 7.2	8.2	6.83±0.08	...	4.48±0.16	6.76±0.17	(1)
AV463	8000	1.40	0.09±0.00	7.53	7.26±0.03	8.18±0.05	6.75±0.04	...	4.35±0.13	6.78±0.13	<i>t.w.</i>
	8000	1.3	...	<7.8	7.07	8.2	7.01±0.06	...	4.48±0.17	6.82±0.21	(1)
SK194	11 500	1.65	0.10±0.01	7.63	8.09±0.00	8.19	6.88	6.47±0.05	...	7.23±0.07	<i>t.w.</i>
	~11 700	1.7	7.9/8.0	...	6.8/6.6	6.2/6.1	(2)
SK202	15 400	2.25	0.09±0.01	6.78±0.07	7.57±0.04	8.01±0.04	6.78±0.01	6.30±0.08	<i>t.w.</i>
	14 750	2.1	...	6.8/6.8	7.6/7.4	...	6.7/6.6	(2)
AV22	14 600	1.90	0.13±0.01	6.85±0.02	7.93±0.04	7.93±0.02	6.97	6.39±0.03	<i>t.w.</i>
	14 500	1.90	...	7.07±0.27	7.92±0.16	...	6.83±0.09	(3)
AV362	14 000	1.95	0.15±0.01	7.21±0.06	8.12±0.03	7.92±0.02	6.64	6.14±0.02	<i>t.w.</i>
	14 000	1.70	...	7.12±0.48	8.22±0.25	...	6.72±0.06	(3)
AV56	16 150	2.00	0.11±0.02	7.32±0.03	7.92±0.03	8.04±0.04	6.84	6.32±0.02	<i>t.w.</i>
	16 500	2.05	...	7.19±0.53	8.27±0.32	...	6.68±0.09	(4)
AV151	16 750	2.25	0.13±0.01	7.02±0.04	7.83±0.03	8.22±0.03	6.96	6.47±0.01	<i>t.w.</i>
	16 000	2.10	...	6.85±0.12	7.55±0.19	...	6.70±0.08	(4)
AV443	16 250	1.95	0.12±0.01	6.94±0.04	7.94±0.05	8.19±0.03	6.89	6.46	<i>t.w.</i>
	16 500	1.95	...	6.99±0.36	7.96±0.22	...	6.72±0.08	(4)

9.4 Constraints on Chemical Mixing in Massive Stars

As illustrated in Sect. 3.4, it should be possible to detect the products of CN-processed matter in the atmosphere of a massive star through mixing of the atmosphere with matter from the stellar core. The degree of the nitrogen enrichment and carbon depletion depends on the efficiency of the mixing process. It was already mentioned in this section (see e.g. Figs. 9.1 and 9.2) that – if corresponding lines could be analysed – there are clear signs of pronounced N enrichment and C depletion (with respect to the deduced metallicity) for all of the sample stars. This is accompanied by slight helium enrichment. Typically, the N enrichment and C depletion (compared to $[M/H]$) are of the order of 0.6 and 0.4 dex respectively.

For a more detailed discussion of this matter and a comparison to the predictions of stellar evolution theory, Fig. 9.4 presents the N/C *mass* ratios for all objects with respect to their N/O *mass* ratio. For explicit numbers, see Table 9.1. Of course, only objects where abundances of all three elements could be derived based on the available spectral lines are included. Moreover, typical error bars for a few objects based on the line-to-line scatter from lines of each elemental species are provided. For the rest of the objects, the error bars are omitted for clarity and since in some cases only one line could be investigated for C, N, or O.

There is a rather tight trend between the N/C and N/O ratios when considering the statistical uncertainties from the line-to-line scatters. If one accounts in addition for possible systematic effects, the relation becomes even more convincing.

The theoretical predictions in Fig. 9.4 indicates that the shape and slope of the N/C vs. N/O curves is almost constant with respect to mass (and depends more on the physics of the models). However, higher masses imply higher values of N/C and N/O at which the lines end indicating more efficient mixing for higher masses in the evolution phases covered (until the end of central helium burning).

The different significantly different slopes in Fig. 9.4 of the two models – “classical” star and Wolf-Rayet star models – is mainly caused by the adopted initial chemical composition of stars in the SMC. The Wolf-Rayet models are calculated with a scaled solar mixture of CNO elements whereas an α -enhanced composition was adopted for the classical models. The latter implies also higher O abundances, and thus smaller N/O ratios and a steeper slope. These different initial chemical patterns in the models also explain why the models do not start at the same point in the lower left corner.

The comparison of the observational trend with the predictions for the evolution of the N/C vs. N/O ratio in stars at SMC metallicity in Fig. 9.4 reveals two fundamental discrepancies.

- The “classical” models seem to typically overestimate the N/C ratios for given N/O ratios while the Wolf-Rayet star models underestimate the deduced relation. It is of major importance to note that this statement is only valid when theoretical abundances predicted for the *major part* of a stellar life up to the end of central helium burning in the red supergiant regime are considered.
- If only the abundance evolutions predicted for a stellar evolution from the main sequence to a lower temperature around 10 000 K (thick part of the lines in Fig.

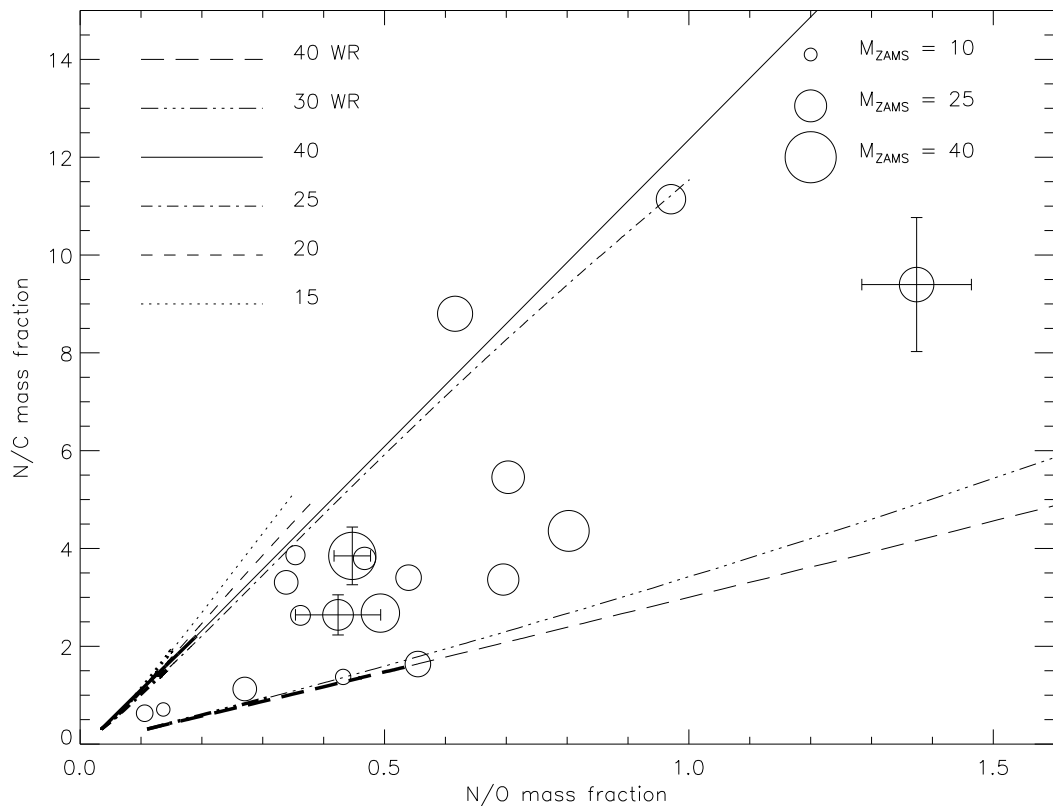


Figure 9.4: Mass fraction of N/C versus N/O for objects with determined abundances. The symbol size codes the ZAMS mass as inferred from the evolutionary tracks in Fig. 9.5. Theoretical predictions for the evolution of these ratios in 15, 20, 25, and 40 M_{\odot} stars from Maeder & Meynet (2001) and for 30 and 40 M_{\odot} Wolf-Rayet stars from Meynet & Maeder (2005, “30/40 WR”) as indicated. The thick part of each curve corresponds to the evolutionary phase from the main sequence towards the red supergiant stage until $T_{\text{eff}} = 10\,000$ K is reached (see e.g. Fig. 9.5). Representative uncertainties for a few objects are indicated.

9.4) are considered, one faces the severe problem that the theoretical N/C and N/O ratios do *not* grow high enough in time to match the observed ones.

The conclusion from the first discrepancy for the stellar evolution is thus that physics and parameters corresponding to the “golden mean” would best fit the measured trend. This would demand tailored calculations for the special SMC abundance pattern of CNO elements (see also Sect. 9.6).

The second discrepancy is somewhat more complicated. One explanation could be that the vast majority of the objects must have already undergone the first dredge-up in the red supergiant stage where pronounced mixing takes places. Most of the sample stars would have to be on the way back to the blue or be caught in a blue loop even at these high masses. This is hard to explain with the current stellar evolution models.

Another possibility to explain the second discrepancy is that mixing in massive

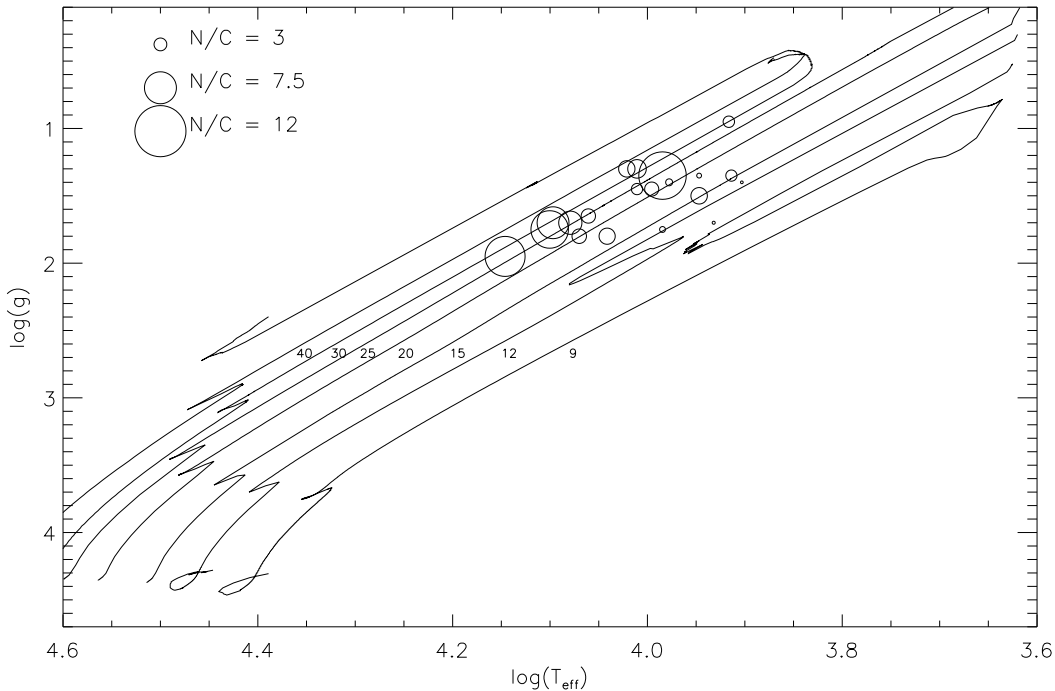


Figure 9.5: Location of our sample stars in the $T_{\text{eff}}\text{-log } g$ -plane. Only stars where nitrogen and carbon abundances could be derived are shown with the symbol size coding the N/C mass fraction. Evolutionary tracks from Maeder & Meynet (2001) for 9 to 25 M_{\odot} (ZAMS mass) and Meynet & Maeder (2005) for 30 and 40 M_{\odot} (Wolf-Rayet star models) are overplotted as denoted. The beginnings of the track in the lower left part of the figure corresponds to the main sequence in a HRD.

stars prior to the red supergiant stage is much more efficient than assumed up to now. (This would happen mainly on the main sequence due to the relatively fast evolution towards the red after leaving the main sequence.) The models at SMC metallicity already account for rotationally induced mixing of the atmosphere with processed matter from the stellar core – an important step to adequately describe a star. Still, this seems to be not enough considering the results of the present work. Rotation is either more efficient than implemented in the models so far or an additional mechanism enhances the mixing. One possibility in this respect is the interplay of rotation with magnetic fields (Maeder & Meynet 2005) which was shown to strongly enhance the mixing efficiency.

Another interesting point which may be inferred from Fig 9.4 (and Fig. 9.5) is the dependency of the ratio on the (initial) mass of a star. Although the largest masses (symbol size in Fig 9.4, location in Fig. 9.5) are not found at the highest N/C or N/O ratios, stars with high N/C or high N/O ratio show by trend a relatively high mass. This supports the established idea of more pronounced mixing at higher masses (see also Sect. 3.4).

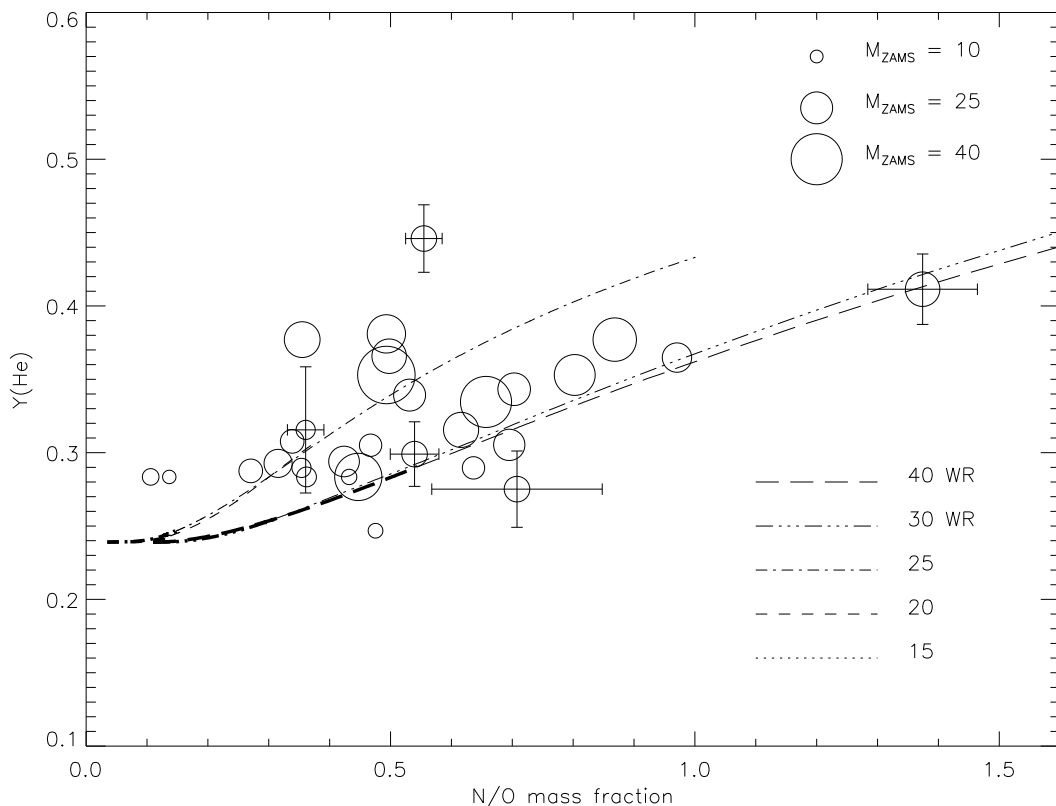


Figure 9.6: Similar to Fig. 9.4, but for the mass fraction of helium versus the N/O mass fraction for objects with determined abundances. The symbol size codes the ZAMS mass as inferred from the evolutionary tracks in Fig. 9.5.

Helium abundances offer a further opportunity to compare results from the present work with predictions from stellar evolution theory as done in Fig. 9.6. Similar to Fig 9.4, only a few representative error bars are implemented for reasons of clearness and as some uncertainties for N/O mass ratios are not derived because of a limited number of spectral lines.

Very similar notes and conclusions as made investigating the N/C vs. N/O plot can be given here. There is a clear and rather tight (including statistical uncertainties and possible systematic ones) trend indicating higher helium abundance with higher N/O ratio. It means that helium – the net result of hydrogen burning – is mixed into the atmosphere as well as the other signatures of hydrogen burning in the CNO cycle (N up, C down). Thus, it is not surprising that this is in agreement with stellar evolution theory – although the observed slope seems a bit shallower.

However, there are still some issues for debates left. The points are the same as in the discussion of N/C vs. N/O. Again, it seems that the “golden mean” between classical and Wolf-Rayet star models would best describe the findings. And again, the mixing of the material within the time it takes the star to leave the main sequence and cool down to $\sim 10\,000$ K (corresponding to the thick part of the curves in Fig 9.4)

seems to be too inefficient. And finally, stars with high N/O and especially high He abundance also possess very likely a high mass implying stronger mixing for more massive stars. The discussion is thus fully analogue to the one before.

9.5 Chemical Homogeneity of the Small Magellanic Cloud

The chemical elements not affected by the fusion and mixing processes which have taken place so far in a star allow a discussion of the distribution of elements in the SMC. Here, the individual objects serve as probes of the metal content of the SMC at various points. The relative young ages of the sample stars ensure that this content is practically the same as that of the surrounding medium. Moreover, the targets in this work cover well the SMC as visible in the field-of-view (see Figs. 6.1 and 6.2) thus allowing to search for abundance patterns throughout this galaxy.

The distribution of the stellar atmospheric abundances (except C and N which are affected by nuclear processes in the sample stars) is shown in Figs. 9.7 and 9.8 with a two-dimensional presentation over the field-of-view of the SMC and as a function of the two-dimensional distance of the objects (right frames). Linear regression values inferred from the latter are also listed in Table 9.4 together with mean abundances and 1σ scatter derived from the various values of individual stars.

These linear regressions (fitted with all stars weighted equally) reveal no significant abundance gradient based on the two-dimensional position of the targets in the SMC. Regarding the relatively small abundance ranges as well as the statistical (line-to-line scatter) and possible systematic (e.g. effects of atmospheric parameters, Sect. 9.2) uncertainties, the derived abundances indicate a quite homogeneous (present-day) composition of the SMC. This can also be seen with the 1σ scatters of the abundances *over all stars* (Table 9.4) which may be explained with the (statistical and systematic) uncertainties *in a single star*. Only for the small uncertainties found for O, and Mg (and S to some extent), one *could* think of a small real variation of the abundance. In Sect. 10.5, this discussion is continued in three dimensions.

At this point, even with the high accuracy and consistency achieved in the present work pinning down atmospheric abundances to 10–20 %, no clear chemical inhomogeneity is observed.

Table 9.4: Possible gradients and average abundances in the SMC. Given are the gradients as derived from distribution of stars in the two-dimensional field of view, see also Figs. 9.7 and 9.8. Additionally, the simple average of abundances from all stars (ignoring their location) as well as the 1σ scatter are presented.

Element	linear trend		average abundances/dex		\varnothing relative to solar/dex
	central/dex	slope/dex/kpc	\varnothing	1σ scatter	
O	8.16 ± 0.04	0.010 ± 0.029	8.16	0.09	-0.67
Mg	6.84 ± 0.04	-0.018 ± 0.031	6.83	0.09	-0.75
S	6.47 ± 0.05	0.001 ± 0.043	6.46	0.12	-0.74
Ti	4.44 ± 0.11	0.005 ± 0.093	4.44	0.20	-0.50
Fe	6.84 ± 0.04	0.021 ± 0.033	6.89	0.14	-0.61
Overall SMC metallicity:					-0.65

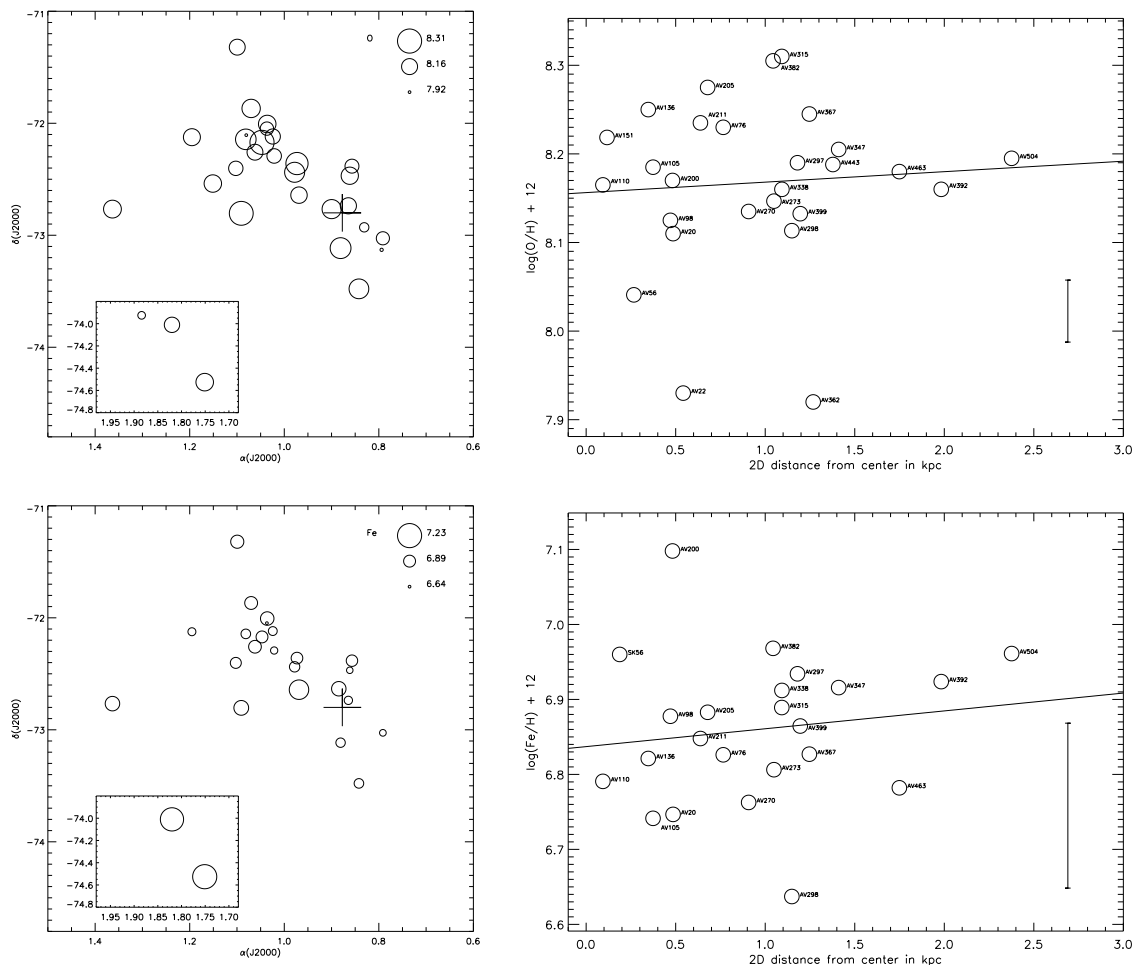


Figure 9.7: Mean abundances of the sample stars and their respective position in the SMC. *Left panels:* stellar abundances for oxygen and iron in the SMC field of view. Star designations were omitted for reasons of clarity. Fast identifications are nevertheless possible using Fig. 6.2 which shows the same field of view. Abundances are indicated via the symbol size. The cross denotes again the center of the SMC. *Right panels:* Stellar abundances for oxygen and iron as a function of the (two-dimensional) distance of a star from the SMC center. The error bars indicate typical uncertainties from the line-to-line scatter of the employed spectral lines. The distance in kpc was calculated based on the coordinates and an adopted distance modulus of 19.0 mag. Overplotted for each element is a simple regression line fitted to the data points with each star weighted equally and an error bar representing the average abundance uncertainty for a single object. Only stars within the main frames of the left frames are considered here, the stars of the inset (further away in the wing) are ignored in this case.

geneity or pattern (in two dimensions) among the young supergiants – and thus in the present-day composition – of the SMC can be found. Nevertheless, the present results well constrain the present-day chemical composition of the SMC to -0.65 dex or one fifth with respect to the solar values of Grevesse & Sauval (1998).

9 CHEMICAL ABUNDANCE ANALYSIS

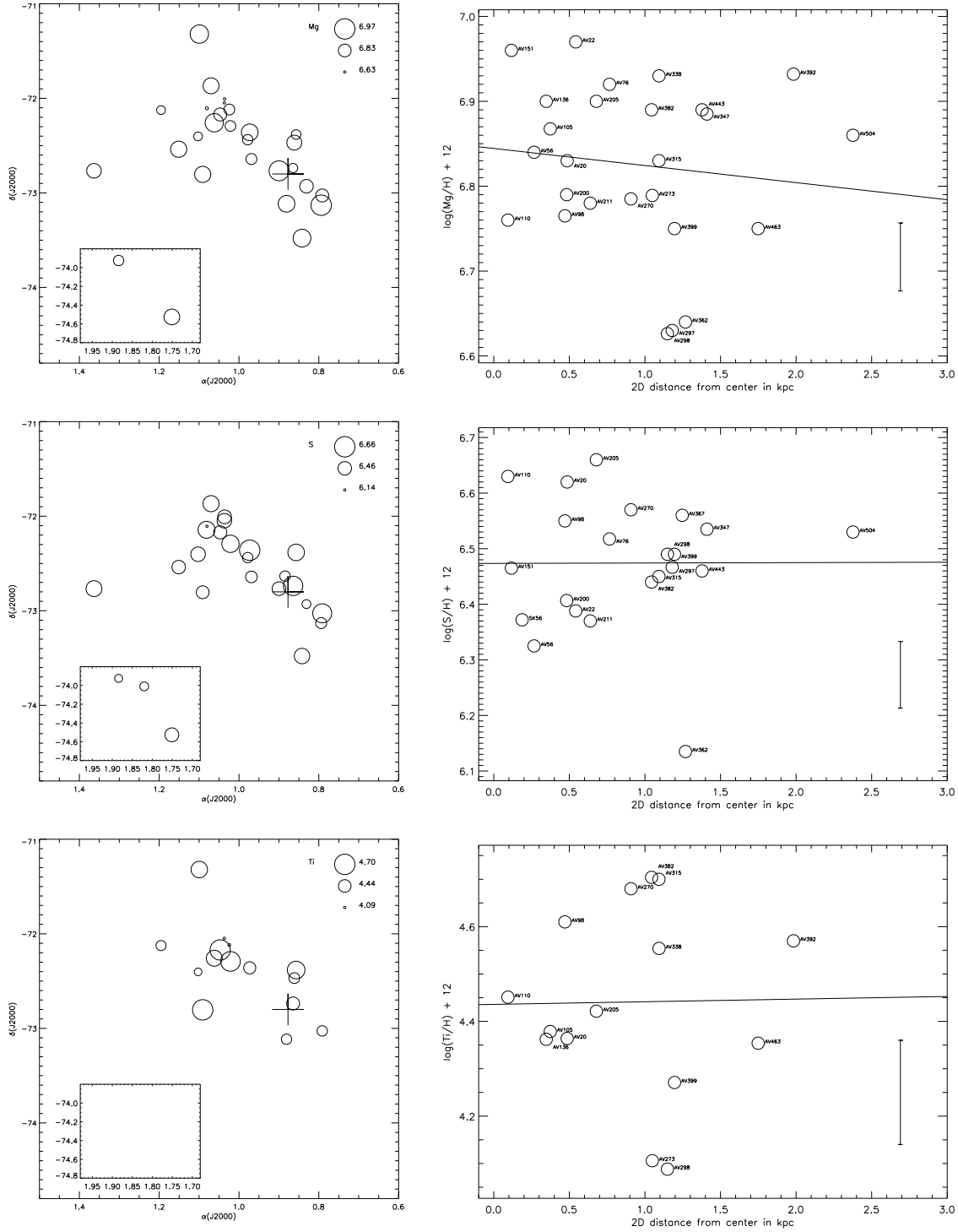


Figure 9.8: Similar to Fig. 9.7, but for Mg, S, and Ti.

9.6 Previous Abundance Studies in the SMC

The abundance findings for the BA supergiants derived in this work are compared to the results of a large number of studies treating various kinds of objects. A summary is given by Table 9.5.

9.6.1 Young Stellar Populations

Young stellar populations such as OB stars or supergiants are thought to well represent the present-day chemical composition of their surrounding except for nuclear processed material mixed into their atmospheres (such as CN-cycled matter) through mixing during and before the dredge-ups in the red supergiant regime. Results from other analyses should therefore be directly comparable to the findings in this work within these restrictions.

Cepheids as pulsating stars of several solar masses and ages of ~ 100 Myr should also reflect the (almost) present-day composition of the medium they were born in. However, abundance studies of Cepheids mainly rely on the estimation of overall blanketing effects from photometry introducing large uncertainties e.g. through extinction. Only mean metallicities such as $[\text{Fe}/\text{H}]$ are determined in most cases. Numerous early studies with very similar results exist. The works of Harris (1983) from a study of 45 Cepheids and of Luck & Lambert (1992) of seven Cepheids/supergiants are mentioned here exemplarily. Good agreement is found with the overall metallicity of Harris (1983). The Mg, S, Ti, and Fe values are higher in Luck & Lambert (1992) than in the present work while good agreement is found for O. The α elements of the Cepheids are found to be overabundant with respect to supergiants. Carbon and nitrogen show a large scatter due to different mixing with CN-processed matter (as in the present work). The lower C and higher N abundance of the present work may indicate more efficient mixing than was present in the – not as massive – Cepheids on the mean. A later study of Luck et al. (1998) finds similar results as Luck & Lambert (1992).

More recent studies such as of Keller & Wood (2006) or Mottini et al. (2006) indicate overall metallicities in good agreement with the “typical” SMC metallicity which was also confirmed in the present study.

F supergiants Abundances of other supergiants of various spectral types can be compared with the present work. First, a comparison is made with supergiants of spectral type F which lie closer to the red supergiant region and the dredge-up(s) occurring there. An investigation of several elements for three supergiants was conducted by Spite et al. (1989a), (1989b), and Spite & Spite (1990). There is quite good agreement between these studies and the present work for O and Mg. For the heavier elements such as S, Ti, and Fe they tend to systematically overestimate the abundances. A similar study for eight F supergiants based on photometry and spectroscopy was presented by Russell & Bessell (1989) and indicated slightly higher abundances for Mg with respect to the current work. The iron abundance fits remarkably well.

A and B supergiants The work of Venn (1999) was already mentioned before as abundances for five of her stars were also determined in this work. Very good agreement was found except for N and C for a few stars. Very good to excellent agreement is also found for the elements which are unaffected by CN-processed material up to now: O, Mg, S, Ti, as well as Fe. Like in the present work, a relative abundance pattern very similar to the solar one (Grevesse & Sauval 1998) is found by Venn (1999) for these elements.

The studies of Trundle et al. (2004), Dufton et al. (2005), Trundle & Lennon (2005) as well as of Lee et al. (2005) reveal comparable abundances to the present work for O and Mg whereas Fe is much less abundant according to Lee et al. (2005). Moreover, they also show a considerable scatter in the C and N abundances which is an indication for variously efficient mixing with CN-processed matter from the stellar core (the carbon abundance is systematically and significantly smaller).

B stars Recent work on large samples of B stars (supergiants and less luminous stars) is provided by Hunter et al. (2007, 2009) and Trundle et al. (2007). Fair agreement with respect to the present work is found for the heavier metals O, Mg, and Fe as well as for C. In fact, their C abundance is even lower than found for the more evolved supergiants of the present work, which are supposed to show the stronger depletion due to more effective mixing. This would be very surprising but might come from the *estimated corrections* they applied to their C abundances.

9.6.2 Old Stellar Populations (Red Giants)

When comparing the abundance pattern of old stars to ours, one has to keep in mind that it provides information on the metal enrichment history during the time between the formation of those objects and of the young supergiants. Nevertheless, they can also be used to discuss the chemical homogeneity of the SMC. Some recent investigations of larger samples are presented for this purpose in the following.

Carrera et al. (2008) derive metallicities $[M/H]$ from Ca II triplet spectroscopy in red giant branch stars employing a – rather simple – formula relating the metallicity to the sum of the three equivalent widths and the magnitude of the star. Abundances of the 350 stars of various ages (up to ~ 10 Gyr) indicate for the first – and only – time a metallicity gradient. The average metallicity was ~ -1 in the central region decreasing to about -1.6 towards the outer regions (more than 4° away from the center). However, Carrera et al. (2008) conclude that this gradient can be explained as an age gradient.

A similar analysis of the Ca II triplet from red giant branch stars by Parisi et al. (2010), however, finds no gradient at all but consistently $[Fe/H] \sim -1$. There is only an indication for the field stars to be slightly more metal-poor than the cluster stars. Similar results are found by Cioni (2009) from an analysis of the ratio of AGB star types.

Although these results are not directly comparable to the young objects (and are subject to substantial systematic uncertainties), they provide at least the indication that the SMC has a homogeneous composition at populations of various ages.

Table 9.5: Overview of mean abundances from other studies treating various kinds of objects. Direct comparisons are made for elements which are also investigated in the present study. Abundances are given in the usual logarithmic notation $\log x/H + 12$ (except for helium), negative values indicate differences to the solar composition (Grevesse & Sauval 1998).

Source	Method	El.(s)	mean value	1σ -scatter	remarks
<i>This work</i>	BA supergiants, spectroscopy, non-LTE	He	0.11	0.02	
		C	7.47/−1.05	0.20	
		N	7.90/−0.02	0.21	
		O	8.16/−0.67	0.09	
		Mg	6.83/−0.75	0.09	
		S	6.46/−0.74	0.12	
		Ti	4.44/−0.50	0.20	
	Fe	6.89/−0.61	0.14		
Harris (1983)	Cepheids, photometry	[M/H]	−0.65	(~ 0.3)	
Keller & Wood (2006)	Cepheids, light curves	[M/H]	−0.64	0.04	
Mottini et al. (2006)	Cepheids, spectral anal- ysis	[M/H]	−0.75	0.08	
Luck & Lam- bert (1992)	Cepheids/ Supergiants, spectral analysis	C	7.65	0.32	α elements in Cepheids overabundant with respect to supergiants
		N	7.71	0.35	
		O	8.26	0.20	
		Mg	−0.45	0.12	
		S	−0.41	0.15	
		Ti	−0.55	0.17	
Spite et al. (1989a, 1989b), Spite & Spite (1990)	F supergiants, spectral analysis, LTE	Fe	−0.53	0.12	
		C	7.77	0.08	
		O	8.1	0.08	
		Mg	6.89	0.05	
		S	6.70	0.12	
		Ti	4.39	0.26	
Russell & Bessell (1989)	F supergiants, photometry/ spectroscopy, LTE	Fe	7.02	0.10	
		C	7.56	0.06	
		Mg	7.00	0.12	
		Ti	4.51	0.11	
Venn (1999), N updates by Venn & Przy- billa (2003)	A supergiants, spectral analysis, non-LTE	Fe	6.78	0.18	
		N	7.52	0.38	
		O	8.14	0.10	
		Mg	6.83	0.11	
		Ti	4.29	0.15	
	Fe	6.71	0.14		

Table 9.5: Overview of mean abundances from other studies (*continued*).

Source	Method	El.(s)	mean value	1 σ -scatter	remarks
Trundle et al. (2004), Trundle et al. (2005)	B supergiants, spectroscopy, non-LTE	C	6.93	0.15	
		N	7.72	0.33	
		O	8.13	0.14	
Lee et al. (2005)	B supergiants, spectroscopy, non-LTE	Mg	6.83	0.11	
		C	6.9	0.3	
		N	7.7/7.6	0.2/0.3	targets in SMC wing
		O	8.3/8.0		
Dufton et al. (2005)	B supergiants, spectroscopy, non-LTE	Mg	6.7/6.6	0.1/0.1	
		Fe	6.2		
		C	7.06	0.12	
		N	7.42	0.15	
Hunter et al. (2007, 2009), Trundle et al. (2007)	B stars, FLAMES survey, spectroscopy, non-LTE	O	8.09	0.12	
		Mg	6.70	0.10	
		C	7.30	0.28	Fe in LTE, estimated corrections for C, supergiants excluded for N
		N	7.28	0.31	
O	7.99	0.21			
Mg	6.72	0.18			
Carrera et al. (2008)	red giants, Ca II triplet	Fe	6.92	0.15	
		[M/H]	-1 to -1.6		first detection of gradient, due to age
Parisi et al. (2010)	red giants, Ca II triplet	[M/H]	~ -1	~ 0.2	no gradient even for different ages
		[M/H]	~ -1.25	~ 0.3	no gradient
Cioni (2009)	AGB stars, ratio of C and M types	[M/H]	~ -1.25	~ 0.3	no gradient
Dufour (1984)	H II regions, spectroscopy	He	0.08	0.003	
		C	7.16	0.04	relatively strong depletion of C and N
		N	6.46	0.12	
		O	8.02	0.08	
		S	6.49	0.14	
Garnett (1999)	H II regions, spectroscopy	C	7.4		relatively strong depletion of C and N, new HST observations
		N	6.5		
		O	8.0		
		S	6.3		
Vermeij & van der Hulst (2002)	H II regions, spectroscopy	He	0.085	0.004	
		N	6.45	0.09	
		O	7.96	0.06	
		S	6.18	0.12	

9.6.3 Interstellar Medium: H II Regions

Abundances from the interstellar medium are mainly based on emission-line spectroscopy of H II regions. Early studies of the 1970s and 1980s (Aller et al. 1974, Dufour 1975, Lequeux et al. 1979, Dufour & Harlow 1977, Pagel et al. 1978, Aller et al. 1975, and Dufour et al. 1982) are summarised by Dufour (1984). No trend of abundances with respect to position is detected and all studies indicate quite consistent abundances. Therefore, only the review abundances are listed in Table 9.5. A more recent review is given by Garnett (1999) including also studies of Dennefeld & Stasińska (1983), Heydari-Malayeri et al. (1988), and Russell & Dopita (1990). Abundances based on updated atomic data are proposed by Kurt & Dufour (1998) implying slight changes of $\lesssim 0.1$ dex. Little has changed since then. Another study worth mentioning here comes from Vermeij & van der Hulst (2002) who investigated several elements in three SMC H II regions. Their mean and 1σ -scatter of these three objects is also given in Table 9.5.

Generally, abundances for O, Ne, S, Ar, Si, Cl, and Ar consistently show lower abundances by ~ 0.7 – 0.8 dex with respect to the standard solar abundances of Grevesse & Sauval (1998). However, carbon and especially nitrogen indicate still much lower relative abundances of the order of -1.1 to -1.5 . (The underabundance with respect to values derived for the local interstellar medium is slightly smaller.)

It should be noted that studies of the emission lines of H II regions are still subject to considerable systematic uncertainties. Several calibrations relating measured fluxes to abundances are in use and yield values differing by up to an order of magnitude. A crucial point is also the determination of the temperature of the electron gas. A nice discussion and an example on how different calibrations lead to different abundances is given by Kudritzki (2010).

Nevertheless, good agreement in general is found between the abundances from H II regions (Table 9.5) and the mean abundances from the present study (Table 9.4). Oxygen abundances fit very well while sulfur abundances still agree well with better agreement for earlier abundances. Abundances for carbon and nitrogen are hard to compare due to the CN-processed matter in the stellar atmosphere of massive stars but seem extraordinarily small in the H II regions. The helium abundances of the H II regions are a good lower limit for the ones found in the present work. The C abundances derived from H II regions are even lower than in most studies of Cepheids, supergiants, or B stars where the C abundance is expected to be already smaller than in their surroundings due to nuclear processes. This can be explained by the efficient depletion of C from the gas phase into a condensed dust phase, which is a known phenomenon in the interstellar medium. The N abundance in the H II regions shows the greatest discrepancies between stars and gas (by about 1.5 orders of magnitude). In contrast to C, N is not readily bound into dust grains. The low N abundance in H II regions thus seems to be real implying a low pristine abundance. As most of the N is likely produced in AGB stars via neutron capture of C cores, the low abundance of this seed core would result in a smaller N abundance. In the supergiants, N can then be strongly enriched by the CNO process and mixing.

9.6.4 Summary and Connection to the Present Supergiant Sample

In summary, it can be noted that there is fair agreement between the abundances derived from the B and A supergiants in the present work and other studies from the literature dealing with objects of similarly young age.

Overall metallicities from Cepheids fit well to the ones from the present work. However, in this work, it was possible to give much more detailed abundance information comprising several elemental species.

Studies about F supergiants in non-LTE provide rather good agreement for most elements but also show systematical offsets e.g. for S or Mg – possibly due to a modelling only in LTE which may be violated to some degree in the low-density atmospheres of these stars. Good to excellent agreement with the non-LTE study of A supergiants by Venn (1999) (with updates for N by Venn & Przybilla 2003) is found. Moreover, the spread in abundances from star to star is comparably low.

Abundances from B supergiants and B stars in the literature are generally in fair agreement with the present work for O, Mg, and partly Fe. For the B stars, the FLAMES surveys find lower abundances for O and Mg. C and N abundances are systematically lower than in the present work. These systematics may be due to less sophisticated atomic data, to neglecting non-LTE effects (e.g. for Fe), and to estimated abundance corrections (e.g. for C). For the elements which are still unaffected by stellar evolution (O, Mg, and Fe) and which were also studied in the present work, smaller 1σ -scatters of the abundances from star to star are found here.

It was already noted that C and N abundances in H II regions are very small compared to the supergiants (depletion into dust for C). Remarkably, the metals unaffected by CN-processed material, O and S, are in fair agreement with the present results if all uncertainties (relatively large systematics for H II regions) are taken into account. Interestingly, the earlier the abundances were derived, the better the agreement with the the BA supergiants of this work.

All in all, the present study finds relatively good agreement for most elements (excluding C and N) with previous abundance studies, however at significantly reduced statistical and systematic uncertainties. The thorough determination of stellar parameters and the use of up-to-date atomic data for non-LTE modelling are key ingredients for the accuracy and reliability achieved. The present work may be regarded as the most consistent evaluation of chemical abundances in the SMC so far and the most comprehensive in terms of the supergiant population of the SMC. With that, the highest degree of chemical homogeneity in the SMC up to now was determined.

10 Distance and Depth Extension of the SMC – the Flux-weighted Gravity–Luminosity Relationship (FGLR)

Deriving distances is one of the key problems in astronomy. In principle, distances can be inferred from

$$f_\nu = F_\nu \frac{R^2}{d^2} \quad (10.1)$$

or

$$m - M = -2.5 \log \left(\frac{l}{L} \right) = 5 \cdot \log d - 5 + A_V. \quad (10.2)$$

with f_ν and F_ν being the flux densities at the stellar surface (radius R) and for an observer at distance d , L and l the corresponding luminosities, A_V the interstellar extinction, and m/M the apparent/absolute magnitude. However, neither F nor absolute magnitudes (M) can usually be derived directly.

The only direct distance estimate is based on the *parallax*, a slightly different position of an object in the sky due to the movement of the earth around the Sun. The angular difference π (measured at time intervals of six months) is related to the distance d via the simple relation

$$d = \frac{1}{\pi} \quad (10.3)$$

where π is given in mas (milli arc seconds) and d in kpc (kilo parsec). This simplicity is due to the definition of a parsec as the distance from which the diameter of earth's orbit around the Sun is seen under an angle of 1 arc second. The limiting factor for this kind of distance estimate is the accuracy with which parallaxes can be measured, which is $\gtrsim 1$ mas at best for bright targets. Reliable distance estimates based on the current technical equipment (such as the Hipparcos satellite) are thus confined to objects well within distances of 1 kpc. Future missions such as the GAIA satellite are expected to significantly reduce the uncertainties but will still be limited to distances around 100kpc.

The second possibility for distance estimates relies on *variable stars* such as *Cepheids* (named after δ Cephei). Cepheids are pulsating stars which periodically change their luminosity in parallel to their radius and their atmospheric mean density. It was first found by Leavitt in 1912 from Cepheids in the Small Magellanic Cloud that these variables obey a period–luminosity relationship of the form

$$M \approx -2.88 \log P - 1.24. \quad (10.4)$$

The constant offset was not yet known to Leavitt. It has to be determined independently – ideally from parallaxes of Cepheids. This could be achieved only for a few Milky Way objects (combined with light echoes), so that one also relies e.g. on main-sequence fitting of CMDs of clusters. Effects which may influence this relationship are dimming by interstellar matter or metallicity dependence. However, investigations to constrain these effects usually are or must be omitted, introducing significant

uncertainties to distances derived this way. Despite the mentioned problems variable stars such as Cepheids are the standard objects for deriving extragalactic distances. Several other ways to estimate distance such as RR Lyrae stars or red clump stars are in use but are subject to similar uncertainties.

For much larger distances one relies on supernovae of type Ia which are thought of as standard candles. However, this is still a matter of debate and requires a careful calibration e.g. with the help of Cepheids.

Therefore, another possibility to derive distances is well appreciated. Such a possibility is given by the *flux-weighted gravity–luminosity relationship* (FGLR, Kudritzki et al. 2003) for blue supergiants evolving towards the red supergiant stage.

10.1 Theoretical and Observational Motivation

The FGLR relies on two basic assumptions. First, massive stars from $\approx 12 M_{\odot}$ to $\approx 40 M_{\odot}$ evolve through the BA-type supergiant stage at almost constant luminosity L (see Fig. 3.7). Furthermore, the evolution through that regime happens on relatively short timescales (of the order of 20 000 years for a $20 M_{\odot}$ star) implying that mass-loss may well be neglected and thus that the mass is constant. This has interesting consequences for the relationship of gravity and effective temperature:

$$M \propto gR^2 \propto L \cdot \frac{g}{T_{\text{eff}}^4} = Lg_{\text{F}} = \text{const.} \quad (10.5)$$

indicating a constant flux-weighted gravity

$$g_{\text{F}} = \frac{g}{T_{\text{eff}}^4} \quad (10.6)$$

for the evolution at constant luminosity through the BA-type supergiant domain. This means also that during this whole evolutionary phase, the luminosity of a star is fully determined by its effective temperature and the surface gravity – two basic parameters of stellar atmospheres which can be determined through spectral analyses. It is only in the last decade(s) that quantitative analyses have become reliable and accurate enough to allow for a trustworthy calibration and application of the FGLR.

Employing the mass–luminosity relation (Eqn. 3.2) one finds

$$L^{1-\alpha} \propto \left(\frac{g}{T_{\text{eff}}^4} \right)^{\alpha}. \quad (10.7)$$

Expressed in absolute bolometric magnitudes $M_{\text{bol}} \propto -2.5 \log L$, the *flux-weighted gravity–luminosity relationship* for blue supergiants adopts the following form

$$-M_{\text{bol}} = a_{\text{FGLR}}(\log g_{\text{F}} - 1.5) + b_{\text{FGLR}} \quad (\text{FGLR}) \quad (10.8)$$

where the constants depend on the exponent of the mass–luminosity relation, i.e.

$$a_{\text{FGLR}} = 2.5 \cdot \frac{\alpha}{1 - \alpha}. \quad (10.9)$$

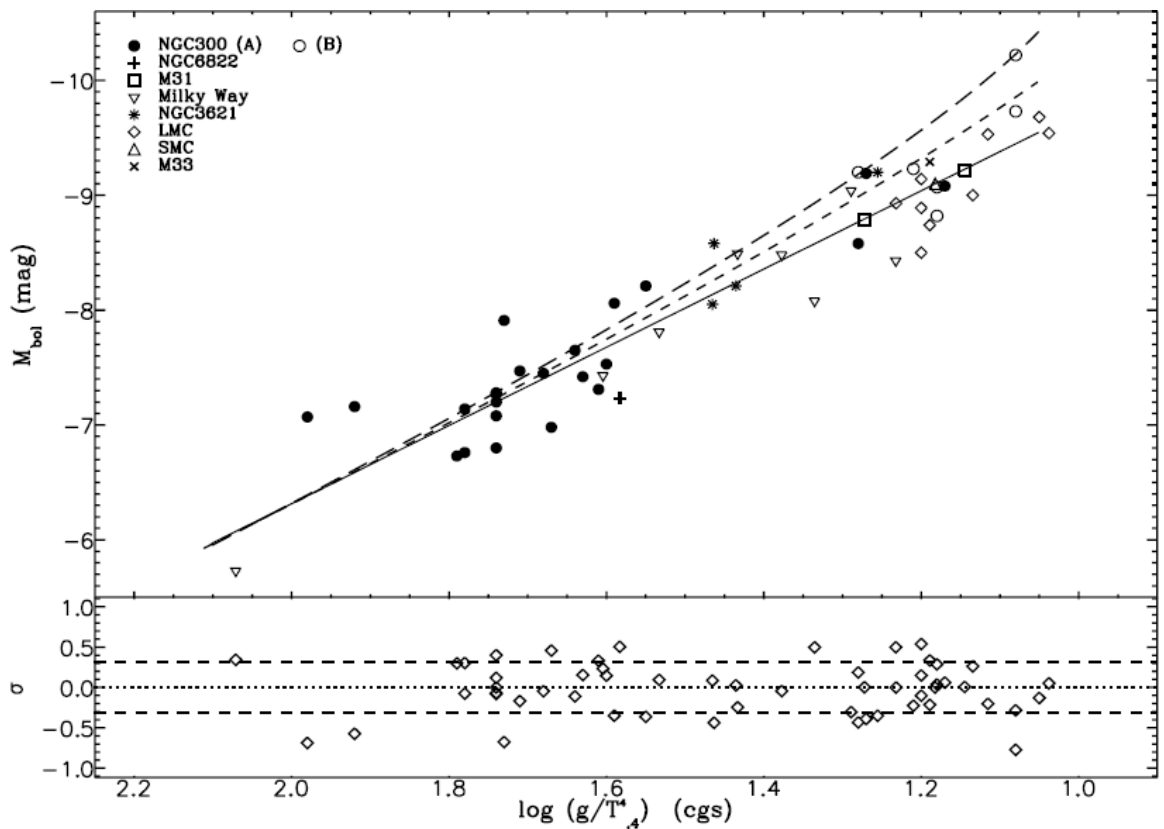


Figure 10.1: Flux-weighted gravities (the temperature T_4 is given in units of 10 000 K) and absolute bolometric magnitudes from Kudritzki et al. (2008) for their sample of stars in various galaxies. A linear fit (*solid line*) reveals a slope of the FGLR of -3.41 . The stellar evolution FGLRs (Meynet & Maeder 2005, Maeder & Meynet 2001) for models with rotation are superimposed (*dashed*: Milky Way metallicity, *long-dashed*: SMC metallicity).

Once the slope a and the offset b are calibrated with observations, it is thus possible to derive distances to individual stars as well as galaxies (from a sample of supergiants). Of course, before applying the FGLR as distance indicator, an observational calibration is mandatory.

The state-of-the-art calibration for the FGLR was provided by Kudritzki et al. (2008, in the following abbreviated as Kud08) in a study of 24 supergiants of spectral type B and A from NGC 300 together with other supergiants from seven other galaxies. The combined results are shown in Fig. 10.1 and indicate

$$\begin{aligned} a_{\text{FGLR,Kud08}} &= -3.41 \pm 0.16 \\ b_{\text{FGLR,Kud08}} &= 8.02 \pm 0.04. \end{aligned} \quad (10.10)$$

Note that in the figure as well as from now on, $\log g_F$ is *not* simply the logarithm of g_F but defined as

$$\log g_F = \log g/T_{,4}^4 = \log g - 4 \cdot \log \left(\frac{T_{\text{eff}}}{10\,000\text{ K}} \right) \quad (10.11)$$

Good agreement between the observations and theory (dashed lines in the figure) was found. Significant deviations occurred only at the lowest g_F values or the highest luminosities or absolute bolometric magnitudes where the theoretical FGLRs tend to bend upward.

According to the discussion in Maeder (2009), their Sect. 24.3, 25.2 and Fig. 25.6, the exponent of the mass–luminosity relation α varies with the mass of a star and its evolutionary phase. This is due to changes in nuclear reaction rates, radiation pressure, and opacities. α is maximal on the main sequence of solar metallicity around solar-mass stars ($\alpha \sim 4.5$) and slowly decreasing towards higher masses (~ 2 at $100 M_\odot$). Although these values are derived for main sequence stars, the principles behind them may also be applied to more evolved stars. With that, higher masses imply smaller α and with Eqn. 10.9 also higher absolute values of a_{FGLR} (as long as $\alpha > 1$, which is the case for reasonable assumptions on the stellar parameters). Higher masses in turn can be expected at higher luminosities and thus lower $\log g_F$ values. As a result, the slope of the theoretical FGLR relations is steeper meaning higher absolute values of a_{FGLR} at low $\log g_F$ as it is the case in Fig. 10.1.

Mass-loss during the stellar life is less pronounced at lower metallicity in a stellar atmosphere (e.g. Kudritzki & Puls 2000). Thus, supergiants in the SMC will have lost less mass during their previous evolution compared to stars at \sim solar metallicity. Looking at two stars – one metal-poor and one metal-rich – of the same effective temperature and luminosity, the metal-poor one will still possess more of its original mass and thus a higher $\log g$. As mass-loss rates are generally higher at higher masses, this will have a larger effect in ranges with high luminosities. This is a second contribution to the bend in the theoretical FGLR at high luminosities and causes the deviation between the theoretical curves in Fig. 10.1 at SMC and solar metallicity.

10.2 An Attempt to Calibrate the FGLR in the low-Metallicity Environment of the SMC

The coefficients a and b of the FGLR depend on the exact form of the mass–luminosity relation and may thus vary in different environments such as the low-metallicity environment of the SMC compared to the Milky Way or other galaxies. The first approach was therefore to *calibrate* the FGLR by *deriving the constants a and b* . This can be done when distances and thus absolute bolometric magnitudes are known for each object.

The distance of each object was adopted to be equal to the mean distance of the SMC which is a good solution *in case* the depth extension in the line of sight is small compared to the distance of about 60 kpc. The distance of the SMC has been a matter of debate through many decades now (see Sect. 10.4). It was decided to work with the canonical distance modulus of 19.0 (corresponds to ~ 63 kpc) as distances for the SMC and all of the targets.

For a calibration of the FGLR, the flux-weighted gravity g_F and the absolute bolometric magnitude M_{bol} then had to be determined for each object. g_F is directly derived from the atmospheric parameters T_{eff} and $\log g$ derived in Sect. 8 via Eqn. 10.11.

To determine the absolute bolometric magnitude, several contributions must be taken into account. Combining Eqs. 2.12 and 2.14 one finds

$$M_{\text{bol}} = m_V - (m_V - M_V)_0 + B.C. - A_V \quad (10.12)$$

The apparent visual magnitudes have been measured in photometric observations (photoelectric measurements for most stars and CCD photometry for a few objects). Values from multiple sources were employed (see Table 6.1). $(m_V - M_V)_0$ is the distance modulus for each object and was set to 19.0 as described above. The bolometric correction can be inferred either from an analysis of the energy distribution of the model atmosphere or from an analytical fit formula (as discussed in Kud08, their formula 6):

$$\begin{aligned} B.C.(T_{\text{eff}}, \log g, [Z]) = & f_{\text{max}} \left[1 - a \exp \left(-\frac{\log g_F - x_{\text{min}}}{h} \right) \right] \\ & - 4.3 \log \frac{T_{\text{eff}}}{10\,000\text{ K}} \cdot \left(1 + \log \frac{T_{\text{eff}}}{10\,000\text{ K}} \right) \\ & + 0.09[Z] \cdot (1 + 0.26[Z]) \end{aligned} \quad (10.13)$$

with $a = 1 - f_{\text{min}}/f_{\text{max}}$, $f_{\text{min}} = -0.39$, $f_{\text{max}} = -0.265$, $x_{\text{min}} = 1.075$, and $h = 0.17$. This formula was employed for all bolometric corrections.

Finally, the extinction A_V can be derived with Eqn. 2.13. Extinction towards the SMC is dominated by the Milky Way foreground for most objects (based on the equivalent widths of the SMC and MW components of the interstellar Na D lines). Thus, working with a typical R_V of 3.1 for the Milky as well as with a Galactic reddening law is justified.

The colour excess $E(B - V)$ (Eqn. 2.11) in turn is determined from a comparison of observed $-(B - V)$ and synthetic $-(B - V)_0$ colours based on the model atmosphere for the final parameters of each object.

The resulting flux-weighted gravities and bolometric magnitudes are plotted in Fig. 10.2 as filled symbols for a reduced sample. This excludes targets for which atmospheric parameters could not be reliably determined. A simple linear regression to the SMC BA-type supergiants would reveal the following calibration:

$$\begin{aligned} a_{\text{FGLR,SMC}} &= -3.37 \pm 0.35 \\ b_{\text{FGLR,SMC}} &= 7.86 \pm 0.07. \end{aligned} \quad (10.14)$$

Comparing these results with the calibration from Kud08 reveals excellent agreement in terms of the slope of the FGLR in the SMC and in the average over eight galaxies and modest agreement in terms of the vertical offset. Note that the uncertainty in b is *not* the scatter of deviations from the linear regression but the

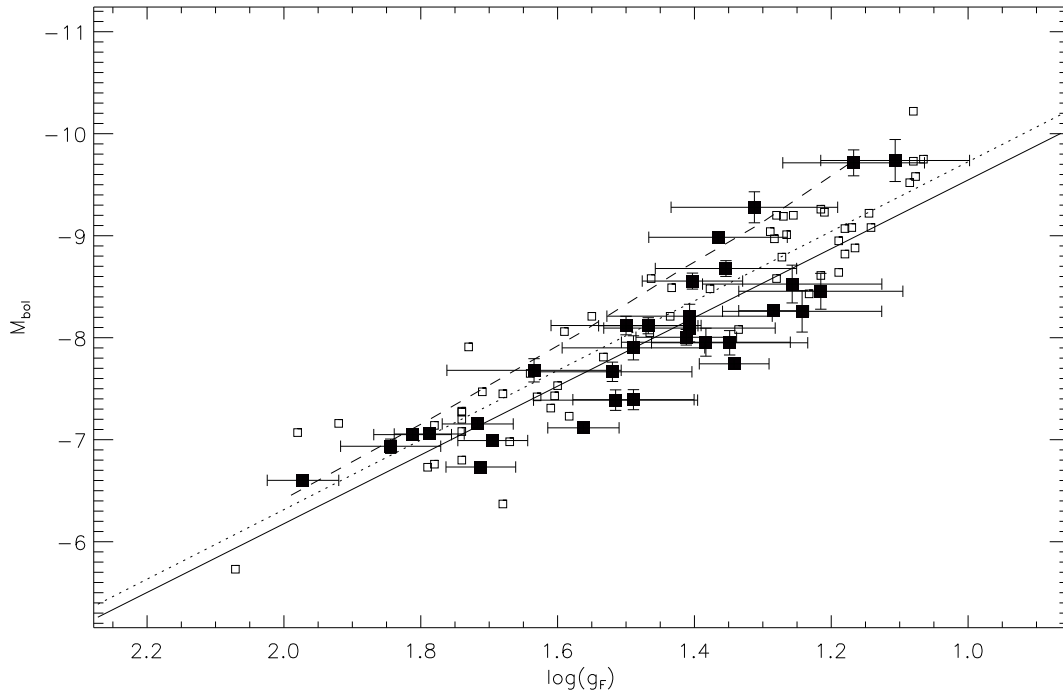


Figure 10.2: Flux-weighted gravities g_F and absolute bolometric magnitudes M_{bol} for the BA supergiant sample of this work (31 stars with reliable atmospheric parameters) as filled squares. The solid line is the simple linear regression fitted to these targets with each object weighted equally. See text for a discussion of the error bars. Open squares denote the targets from the state-of-the-art calibration of the FGLR from Kud08 from the average over eight galaxies. The dotted line marks the linear regression to their objects. There is excellent agreement in terms of the slope of the two relations. The dashed curve is the theoretical FGLR as inferred from stellar evolution models for 12, 15, 20, and 25 M_{\odot} from Maeder & Meynet (2001) and for 30 and 40 M_{\odot} from Meynet & Maeder (2005). Their models are calculated for an initial rotational velocity of 300 km s^{-1} and for SMC metallicity (one fifth solar).

uncertainty in the offset parameter of the fitted line (with $\log g_F = 1.5$ as the zero point).

It is now appropriate to discuss the individual uncertainties of g_F and M_{bol} of the program stars and the overall scatter around the FGLR fit. At first, the scatter of the BA-type supergiants of the present study in Fig. 10.2 around the linear fit would seem reasonable as it is of a similar order of magnitude as the scatter of the Kud08 objects. *However*, the scatter of the SMC sample treated in the present work is expected to be significantly smaller than the Kud08 sample for two basic reasons.

- Firstly, stellar parameters in the present work could be determined more accurately and consistently. Although both analyses made use of the same model codes, there are some differences in the analysis strategy and the quality of

Table 10.1: Flux-weighted gravities $\log g_F$ from the parameter determination and absolute bolometric magnitudes M_{bol} inferred under the assumption of the same distance modulus of 19.0 for the program stars in Fig. 10.2. These values were derived to *calibrate* the FGLR for the SMC. The last column contains the theoretical distance moduli (tDM) which can be derived when *adopting* the (fixed) FGLR calibration from Kud08 (see below for a discussion of the uncertainties). The objects are ordered by growing right ascension (as in Table 6.1).

Object	$\log g_F$ dex	M_{bol} mag	tDM mag
AV20	1.34±0.05	-7.74±0.05	19.82±0.18
AV22	1.24±0.12	-8.26±0.20	19.64±0.45
AV56	1.17±0.10	-9.71±0.13	18.44±0.38
AV76	1.26±0.13	-8.53±0.19	19.32±0.48
AV98	1.41±0.07	-8.00±0.08	19.32±0.26
AV105	1.72±0.05	-7.15±0.04	19.13±0.18
AV110	1.49±0.09	-7.39±0.10	19.66±0.32
AV136	1.28±0.05	-8.26±0.04	19.49±0.18
SK56	1.31±0.12	-9.28±0.15	18.38±0.44
AV151	1.35±0.10	-8.68±0.08	18.84±0.36
AV200	1.38±0.12	-7.96±0.14	19.46±0.44
AV205	1.56±0.05	-7.12±0.04	19.69±0.18
AV211	1.41±0.12	-8.21±0.12	19.13±0.43
AV270	1.49±0.10	-7.90±0.12	19.16±0.37
AV273	1.69±0.05	-6.99±0.04	19.36±0.18
AV297	1.52±0.12	-7.67±0.10	19.29±0.41
AV298	1.71±0.05	-6.73±0.04	19.56±0.18
AV315	1.40±0.07	-8.56±0.08	18.80±0.26
AV338	1.84±0.07	-6.94±0.07	18.91±0.26
AV347	1.52±0.12	-7.39±0.10	19.58±0.42
AV362	1.37±0.10	-8.98±0.05	18.49±0.35
AV367	1.22±0.12	-8.46±0.18	19.54±0.45
AV382	1.47±0.07	-8.12±0.08	19.01±0.26
AV392	1.97±0.05	-6.60±0.04	18.81±0.18
AV399	1.81±0.06	-7.05±0.05	18.91±0.20
AV443	1.11±0.11	-9.74±0.21	18.62±0.42
AV463	1.79±0.05	-7.06±0.04	18.98±0.18
AV504	1.63±0.13	-7.68±0.11	18.88±0.45
SK194	1.41±0.13	-8.09±0.14	19.24±0.45
SK196	1.35±0.11	-7.95±0.12	19.59±0.41
SK202	1.50±0.11	-8.12±0.09	18.90±0.38

the observational material. The present work was based on line profile fits to various Balmer lines and (multiple) ionisation equilibria being more sensitive to temperature changes than the size of the Balmer jump employed in Kud08 (together with Balmer lines). This was possible because of a higher quality of the observational material. The present work could investigate high-resolution

($R = 48\,000$), high S/N spectra (~ 100) whereas the majority of targets in Kud08 was observed at medium resolution ($R = 1\,000$) and lower S/N (~ 40). The lower quality of the data (the objects are much fainter and thus harder to observe) made it necessary to use less sensitive spectral features and leads to larger uncertainties for each object.

Another important point with respect to the atmospheric parameters is the consistency of an analysis in terms of an independent determination of other atmospheric parameters. To be precise, the model grids employed by Kud08 did account for various effective temperatures, surface gravities, and metallicities, however, *assumed* fixed values for the helium abundance and the microturbulence. These model grids were also the starting point for the parameter determination of this work, however, additional refinements due to individually adapted helium abundances and microturbulences with additional calculations were possible because of the high quality of the observational material. A helium abundance and microturbulence different than the expected value would also demand a modification on the other parameters T_{eff} and $\log g$. If this is the case, ignoring these effects will lead to additional systematic errors.

- Secondly, besides the issue of parameter accuracies, one can also expect the inhomogeneity of the Kud08 sample to enlarge the scatter around the FGLR linear fit. As can be seen e.g. in the theoretical curves of Fig. 10.1, different environments such as different metallicities *may* imply (slightly) different calibrations. As the calibration employed from Kud08 includes stars from eight galaxies comprising environments of various metallicities (mostly objects around 1/2 solar metallicity), an effect on the scatter around the linear fit cannot be fully ignored. In the present study, all targets are located in the same environment, were observed with the same instrument, and analysed with the same methods.

Therefore, one would expect a significantly smaller scatter for the present SMC study than for the Kud08 analysis. However, the 1σ -scatter of deviations from the linear fit in the present study (0.40 mag) is even larger than in Kud08 (0.32 mag). Thus, there could be an effect unaccounted for so far.

Before a deeper discussion on this matter, let us first discuss the order of magnitude of the uncertainties in M_{bol} in the present study. Uncertainties may originate from several sources (see the individual terms in Eqn. 10.12):

- *Photometry.* Uncertainties from photometric observations may represent a non-negligible contribution. Observed magnitudes such as m_V and $(B - V)$ necessary for deriving M_{bol} often had to be taken from rather early studies in the 1970's and 1980's (see Table 6.1 for an overview on photometry sources). Later studies often excluded the very objects analysed in this work due to a possible saturation of these bright targets in the observation. This is one of the rare occasions where the high luminosity of BA supergiants – a major advantage making extragalactic stellar spectroscopy possible – is actually a disadvantage. All photometric investigations for the program stars assume uncertainties in

the apparent magnitudes of few hundredths of magnitudes (Table 6.1). A more conservative estimate based on the scatter of magnitude values for the same stars from different studies would be $\lesssim 0.1$ mag. In this regard, it should also be noted that supergiants may be subject to intrinsic variability (pulsations). Bresolin et al. (2004) found them to be of the order of 0.1 mag and to have no significant effect on the calibration of the FGLR.

- *Extinction.* The extinction A_V depends on observed photometry as well as on spectroscopically derived atmospheric parameters (through a change of synthetic colours from the model atmosphere). The uncertainty contribution from the derived atmospheric parameters are chosen based on the reaction of the $(B-V)_0$ colour when changing T_{eff} and $\log g$ according to their uncertainties so that the effects add up. This is a conservative estimate and leads to uncertainties in A_V (combined with the observational uncertainties) of the order of $\lesssim 0.05$ to $\lesssim 0.1$ mag for the cool and hot objects of the current sample respectively. Cooler objects have smaller uncertainties due to the high precision for T_{eff} derived from the extremely sensitive Mg I/II ionisation equilibrium (if applicable).
- *Bolometric correction.* Similar to the extinction, the uncertainty in the bolometric correction is also a function of the uncertainties in the atmospheric parameters. Again, the uncertainty in $B.C.$ was – conservatively – derived from the change according to Eqn. 10.13 when T_{eff} and $\log g$ are altered according to their uncertainties so that the effects add up. $\lesssim 0.05$ to $\lesssim 0.15$ mag for the cool and hot objects of the sample are the result.

Combining these effects by simple Gaussian error propagation leads to quite conservative uncertainties for M_{bol} of typically $\sim 0.05 - 0.15$ (see Table 10.1).

When discussing the (vertical) distances of the stars in Fig. 10.2, one must also account for another uncertainty contribution:

- *Stellar parameters.* The stellar parameters may also directly influence the distance of a star from the linear FGLR fit through a horizontal shift. Uncertainties in $\log g_{\text{F}}$ of ~ 0.05 to < 0.10 dex for cool and hotter objects respectively translate to uncertainties in M_{bol} of ~ 0.1 to 0.2 mag. Note that the combined uncertainty of T_{eff} and $\log g$ to $\log g_{\text{F}}$ is actually smaller than the individual ones due to a higher sensitivity of the spectral indicators to changes in $\log g_{\text{F}}$ (see Kud08, their Sect. 6.1 for a detailed discussion). Here, a very *conservative* estimate based on Gaussian error propagation of T_{eff} and $\log g$ to $\log g_{\text{F}}$ is adopted.

In order to estimate the overall uncertainty of the distance (in mag) of an object to the derived FGLR line (which may be written as $M_{\text{bol}} - M_{\text{bol},\text{FGLR}}(\log g_{\text{F}})$), one must take into account that the uncertainty contributions are *correlated*. For example, if the effective temperature was underestimated, the object would move to higher temperatures and thus to lower $\log g_{\text{F}}$ values. In a plot such as in Figs. 10.1 or 10.2 the star would move to the right. However, raising the effective temperature also affects the theoretical colours as the flux in the blue band will grow faster than in the visual band. Thus, the B magnitude will *decrease* faster than V implying a smaller

colour $(B - V)_0$. With Eqn. 2.11, this means that the colour excess will increase and that one must correct for a larger extinction A_V . Finally, one arrives at smaller M_{bol} 's (see Eqn. 10.12) or (intrinsically) brighter targets. The star moves upward in Figs. 10.1 or 10.2.

To summarise this consideration, changing the atmospheric parameters T_{eff} and $\log g$ cannot directly (i.e. horizontally in the FGLR plots) bring the star closer to the linear fit of the FGLR, there will always be a motion more parallel to the linear regression – in other words a kind of evasion manoeuvre. Evasions also happen as reactions to $\log g$ changes, although with reduced responses. Therefore, uncertainties in $M_{\text{bol}} - M_{\text{bol,FGLR}}(\log g_{\text{F}})$ are even smaller than for M_{bol} alone.

Thus, the uncertainty estimates made for the sample stars are conservative in two respects. First, concerning the estimate of the uncertainty in $\log g_{\text{F}}$ from simple error propagation and second, in terms of the contributions to the uncertainty in the theoretical distance moduli by ignoring correlation effects. This provides additional security meaning that conclusions based on these uncertainties can be expected to be quite significant.

With these uncertainties in mind, one comes to the conclusion that the scatter of the distance of the program stars to the linear FGLR (Fig. 10.2) is too large to be explained solely by the uncertainties discussed. Most stars do *not* lie within the (conservative) error bars on the linear fit in contrast to Fig. 10.1. Therefore, the assumption of equal distances for all objects cannot be fully sustained. The SMC is likely to have a significant extension in the line of sight.

In that case, the SMC would not be suitable to calibrate the FGLR as different individual distance moduli would have to be applied in order to obtain a proper estimate of b_{FGLR} . Nevertheless, the *slope* of the relation should be hardly affected if the number of objects is large enough. With that, one could at least say, that no significant deviation (at the accuracy which can be achieved at present) of the slope is found between about solar and one fifth solar metallicity.

10.3 Probing the Depth Extension of the Small Magellanic Cloud

In order to further discuss such an extension in the line of sight, Fig. 10.3 shows a histogram of distance moduli for the program stars in Fig. 10.2. The distance moduli are now *derived* based on the FGLR as *already calibrated* by Kud08 from the average over eight galaxies. (Although they may be systematic effects for the FGLR due to the different environment in the SMC, the relative distances should be hardly affected.) For that, the *apparent* bolometric magnitude m_{bol} is first determined similarly as M_{bol} in Eqn. 10.12 but without the distance modulus $(m_V - M_V)_0$. The theoretical distance moduli are then derived as

$$tDM = m_{\text{bol}} - M_{\text{bol,FGLR}}(\log g_{\text{F}}) \quad (10.15)$$

where $M_{\text{bol,FGLR}}(\log g_{\text{F}})$ is the absolute bolometric magnitude indicated by the given FGLR due to the value of $\log g_{\text{F}}$ from the atmospheric parameters.

As mentioned before, even when accounting for the uncertainties as discussed in the last section, the spread among the sample is too large to be compatible with *one*

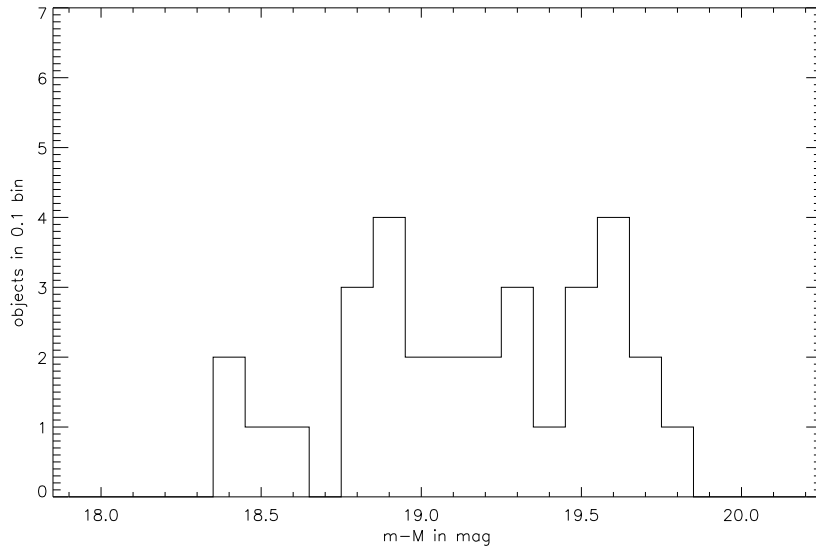


Figure 10.3: Histogram of distance moduli (binned to 0.1 mag) for single stars derived from the difference of the apparent bolometric magnitude and the absolute bolometric magnitude indicated by a given FGLR as calibrated by Kud08: Eqn. 10.10 or the *dotted* line in Fig. 10.2). Stars located above this dotted FGLR thus produce a distance modulus smaller than the 19.0 adopted for plotting Fig. 10.2 and would lie closer to us. Stars below this FGLR produce a distance modulus larger than 19.0 and would be further away.

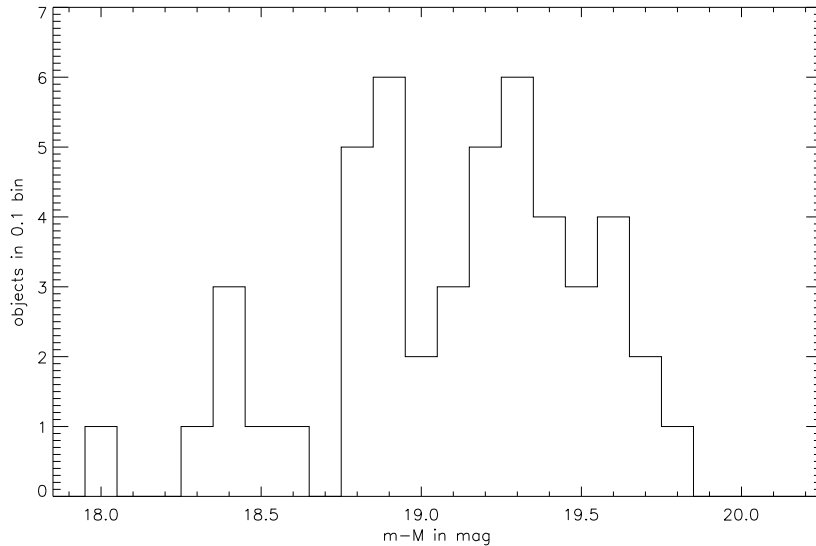


Figure 10.4: Same as Fig. 10.3 but with additional early B supergiants in the SMC from studies of Trundle et al. (2004) and Trundle & Lennon (2005) as re-investigated by M. Urbaneja (priv. comm.).

10 DISTANCE AND DEPTH EXTENSION OF THE SMC – THE FLUX-WEIGHTED GRAVITY–LUMINOSITY RELATIONSHIP (FGLR)

Table 10.2: Parameters of the early B supergiants from M. Urbaneja (priv. comm.). Theoretical distance moduli (tDM) are derived in the same way as for the BA supergiants with the FGLR of Kud08.

Object	T_{eff} K	$\log g$ dex	m_V	$(B-V)$	$E(B-V)$	$B.C.$	tDM	RA (J2000)	DE (J2000)
AV10	17000	2.20	12.58	-0.02	0.12	-1.56	19.43	00:45:46.97	-73:39:54.7
AV18	19000	2.30	12.46	0.03	0.18	-1.81	19.19	00:47:12.21	-73:06:33.1
AV78	21500	2.40	11.05	-0.03	0.13	-2.17	17.96	00:50:38.39	-73:28:18.2
AV96	22000	2.55	12.59	-0.10	0.08	-2.17	19.28	00:51:23.13	-72:07:20.6
AV104	27500	3.10	13.17	-0.16	0.06	-2.71	18.83	00:51:38.49	-72:48:05.7
AV210	20500	2.40	12.60	-0.02	0.14	-2.00	19.37	00:58:35.79	-72:16:25.0
AV215	27000	2.90	12.69	-0.09	0.12	-2.67	18.78	00:58:55.64	-72:32:08.0
AV264	22500	2.55	12.36	-0.15	0.03	-2.22	19.29	01:01:07.76	-71:59:58.8
SK191	22500	2.55	11.86	-0.04	0.13	-2.33	18.37	01:01:57.22	-72:12:42.3
AV303	22500	2.75	12.78	-0.13	0.06	-2.23	18.92	01:02:21.45	-72:00:17.6
AV373	19000	2.30	12.17	-0.09	0.06	-1.81	19.27	01:04:58.06	-72:39:59.5
AV374	20000	2.65	13.04	-0.13	0.04	-1.93	19.19	01:05:01.75	-72:26:53.6
AV420	27000	3.05	13.09	-0.17	0.05	-2.66	18.89	01:07:32.52	-72:17:38.7
AV462	21000	2.50	12.54	-0.13	0.04	-2.05	19.37	01:11:25.92	-72:31:20.9
AV472	20000	2.50	12.62	-0.11	0.06	-1.93	19.23	01:13:01.91	-72:45:48.6
AV487	26000	2.80	12.58	-0.15	0.05	-2.55	19.12	01:15:53.36	-73:19:08.5

distance modulus or a negligible extension in the line of sight. In order to further improve the statistics of the distribution of distance moduli, Fig. 10.4 includes early B supergiants from studies of Trundle et al. (2004) and Trundle & Lennon (2005) as re-investigated by M. Urbaneja (priv. comm., parameters are given in Table 10.2). Note that these objects were observed with different instruments and analysed with different codes and techniques than employed in the present study. This might lead to systematical effects between the two samples. Moreover, the hotter and brighter early B supergiants populate a region where theory predicts a significant curvature of the FGLR and a deviation from a linear relation (see e.g. the dashed curves in Fig. 10.1).

Nevertheless, there are no obvious signs for clear systematical effects between the BA-type supergiant sample in Fig. 10.3 and the combination of the two samples in Fig. 10.4. Only the few objects in the early B supergiant sample producing very small distance moduli (such as AV78) probably do so because their large brightness could make it necessary to account for a curved FGLR (in this luminosity regime) as predicted by theory. Nevertheless, it was decided to concentrate on the empirical linear calibration by Kud08.

Even when this is taken into account, Fig. 10.3 and especially Fig. 10.4 clearly indicate a significant extension of the SMC in the line of sight. A conservative estimate – based on the two maxima around 18.9 and 19.3 – is a typical width of the distribution and a depth extension of 0.4 mag which translates to an extension of $10^{0.4/5} = 20\%$ with respect to the distance of the SMC. Adopting a distance of

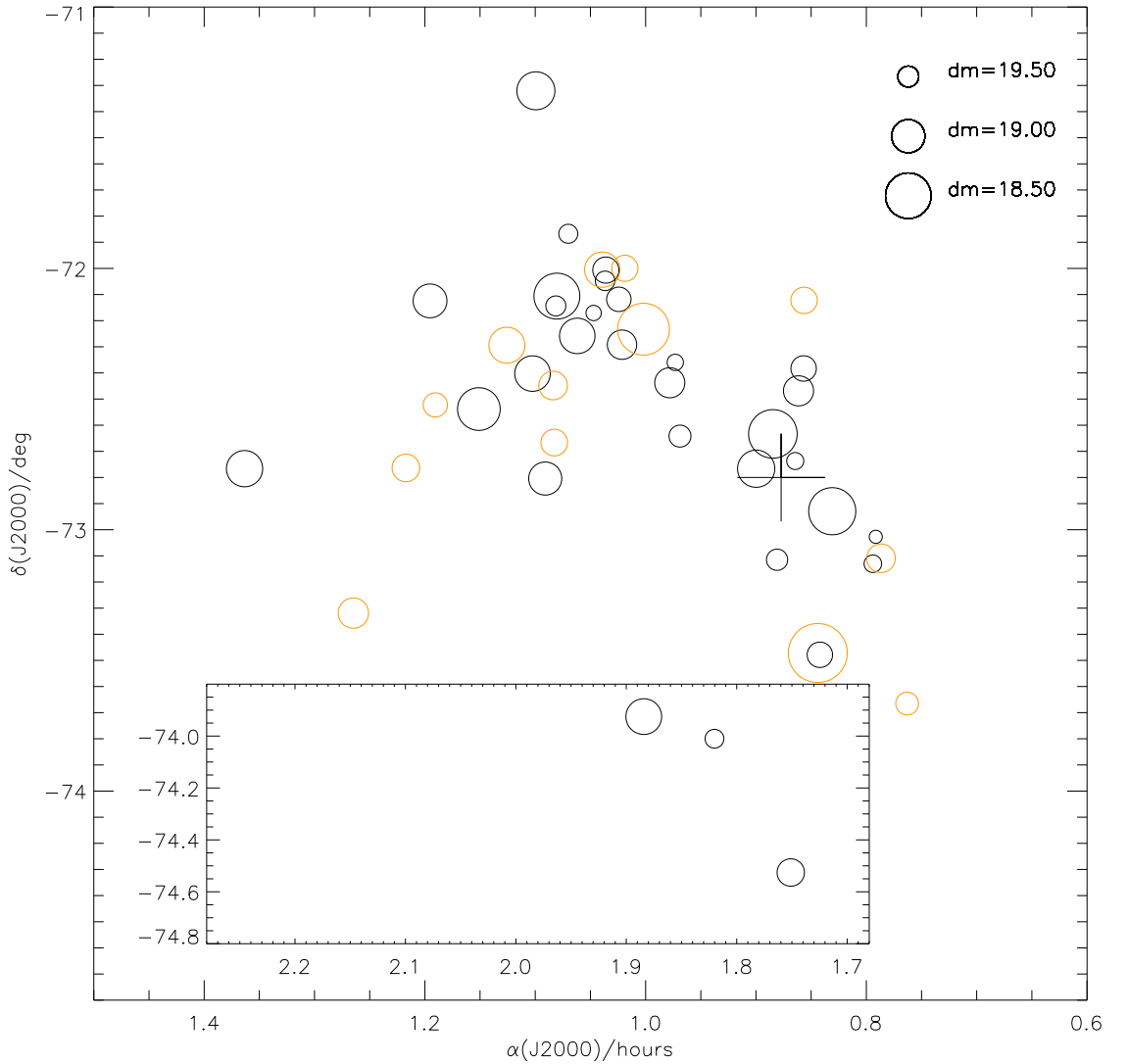


Figure 10.5: The distance moduli derived with the Kud08 FGLR for our BA supergiants sample as black circles. The size of the circles denotes the derived distance as indicated by the legend. Small symbols indicate large distances and large symbol stars which lie closer to us. Star designations were omitted for clarity, however, quick identification for the objects of the present work is possible with Fig. 6.2. The supergiants from the early B objects from M. Urbaneja are overplotted as red circles.

~ 63 kpc (distance modulus of 19.0) this implies an extension of enormous ~ 13 kpc. This means that the SMC extends beyond its tidal radius of ~ 4 kpc and is in the process of irreversible disintegration due to gravitational forces of the near-by LMC and the Milky Way.

As a comparison, the width of the SMC from the distribution of stars in the plane of the sky is only ~ 4000 pc. The SMC would thus be 4 times as long as it is

apparently wide and resemble a cigar viewed from the front or the end. Moreover, the figures may indicate a bimodal depth distribution of stars in the SMC. Fig. 10.5 shows the sample of the BA supergiants together with the early B supergiants on the plane of the sky with the symbol size coding the correspondent distance moduli. No significant correlation of small or large distances with the position (or the radial velocity) can be found.

10.4 Distance and Depth Extension of the Small Magellanic Cloud in the Literature

After several decades of intense discussion on the matter of the proper distance to *both* Clouds and of a possible significant extension in the line of sight of the SMC, one must still admit that these issues are not sufficiently well constrained. A (necessarily limited) overview of the discussion in the literature is therefore recommended and will be compared to the findings of this work.

The distances to the Clouds and the Small Magellanic Cloud in particular have been derived with the aid of several object classes or techniques. An important method is the distance determination using the period–luminosity (PL) or period–luminosity–colour (PLC) relations for Cepheids such as in Eqn. 10.4 as derived by Madore & Freedman (1991) for the LMC. Here, one already faces the first difficulties as several calibrations of the PL (or the PLC) are proposed in literature (for the SMC). Moreover, both relations are sensitive to metallicity or reddening. These effects sometimes can not be or are not taken into account when calibrating or using the relations. Nevertheless, Cepheids are *the* standard candles for extragalactic distances.

RR Lyrae stars are also pulsating variables with relatively small brightness variations (usually less than a magnitude) and small periods (less than a day). RR Lyrae stars are all of similar age and mass. The absolute magnitudes of the RR Lyrae stars are all about $M_V = 0.6 \pm 0.3$ although a metallicity correction may be necessary as proposed e.g. by Feast (1988)

$$M_V(RR) = 0.92 + 0.2 \cdot [Fe/H]. \quad (10.16)$$

Several other distance determinations techniques such as main sequence fitting or eclipsing binaries have been used in the literature. A proper discussion of these goes beyond the scope of the present project.

Table 10.3 summarises distances, line-of-sight depths, and structure models as discussed in this section. The main focus will be on analyses investigating or discussing a possible depth extension. The SMC was long thought to possess a considerable extent in depth e.g. by Johnson (1961) or Hindman (1964, 1967) who proposed three expanding gas shells based on studies of the H I distribution.

Two separate H I distributions were also seen in velocity-space by Mathewson & Ford (1984) proposing that the SMC was torn apart by its last close encounter with the LMC some 200–400 Myrs ago creating a slower fragment, the Small Magellanic Cloud Remnant (SMCR) in front of a faster fragment, the Mini-Magellanic Cloud. The two systems are found to be separated by about 6 kpc and 30 km s^{-1} .

Table 10.3: An overview of mean distance moduli $(m - M)_0$, depth extensions of the SMC ($\Delta(m - M)_0$) in the line of sight (los), and derived information on its structure if indicated in the respective paper. See text for further discussion.

Source	Method	$(m - M)_0$ (mag)	Δ_{los} (mag)	comments on the SMC structure
Caldwell & Coulson (1986)	Cepheids (PL, PLC), H I regions	18.97±0.07	0.10–0.13	near, fast arm NE and far, slow arm SW
Mathewson et al. (1986)	Cepheids (PL)		~1.2	two components with depth 6 kpc each
Laney & Stobie (1986)	Cepheids (PL, PLC)	19.05±0.05	0.56	wing up to 0.4 mag closer
Welch et al. (1987)	Cepheids (PL, PLC in JHK)	18.93±0.05	0.12	no extension behind the tidal radius
Stothers (1988)	Cepheids (PL, PLC, new [Z] calibration)	18.80±0.06		
Groenewegen (2000)	Cepheids (PL in <i>IJK_S</i>)	19.11±0.11 19.04±0.17	~0.5	SMC inclined with NE part closer
Reid & Strugnell (1986)	RR Lyrae (M_V = 0.75)	18.78±0.15		
Walker & Mack (1988)	RR Lyr. in NGC 121 ($M_V=0.60$) SMC field	18.86±0.07 19.2		
Szewczyk et al. (2009)	RR Lyrae	18.97±0.03		no significant depth
Garmany et al. (1987)	OB stars: Spec. Parallax and ZAMS fitting	19.1±0.1 18.9		
Arellano Ferro et al. (1991)	F supergiants: Spec. Parallax	19.33±0.31		
Massey et al. (1995)	OB stars: Spec. Parallax	19.1±0.3		
Mathewson & Ford (1984)	H I regions		~0.2	2 H I distributions separated by 6 kpc and 30-40 km s ⁻¹ , near+slow and far+fast

10 DISTANCE AND DEPTH EXTENSION OF THE SMC – THE FLUX-WEIGHTED GRAVITY–LUMINOSITY RELATIONSHIP (FGLR)

Table 10.3: Mean distance moduli and depth extensions from the literature. *continued*

Source	Method	$(m - M)_0$ (mag)	Δ_{los} (mag)	comments on the SMC structure
Mathewson & Ford (1984)	H I regions		~ 0.2	2 H I distributions separated by 6 kpc and $30\text{-}40 \text{ km s}^{-1}$, near+slow and far+fast
Mathewson & Ford (1988)	H I regions and Cepheids (PL)	18.8	~ 0.8	slow, NE arm 10 kpc closer than fast SW arm
Martin et al. (1989)	H I and H II regions, young stars		$\lesssim 0.4$	4 velocity components; slow components in front
Hatzidimitriou & Hawkins (1989)	Horizontal branch (HB)/clump		~ 0.7	deeper NE regions, two depth components for older population
Subramanian & Subramanian (2009)	red clump stars		0.34	maybe an SMC bulge
Harries et al. (2003) and Hilditch et al. (2005)	Eclipsing binaries	18.91 ± 0.03		
North et al. (2009)	Eclipsing binaries	19.05 ± 0.04	0.36	

Caldwell & Coulson (1986) derived a mean distance modulus of 18.97 ± 0.07 from an analysis of 63 Cepheids and H I velocities in the SMC. From the scatter of the distance modulus, they conclude that a planar model is barely adequate to describe the SMC and that the line-of-sight scatter after taking into account individual uncertainties must still be $0.10\text{--}0.13$ mag (based on a planar model for the SMC). The north east (NE) part of the SMC (larger values of declination and right ascension) seems to be closer than the south west (SW) part. Moreover, some material was apparently pulled out of the SMC center. The far arm in the SW was identified with a lower-velocity H I component and the near NE arm with a higher-velocity component

– contrary to Mathewson & Ford (1984).

In a later study by Mathewson et al. (1986) measuring distances to 161 Cepheids, a significant extension from 43 to 75 kpc, with a maximum concentration at 59 kpc was detected. A nearly complete sample for Cepheids with periods smaller than 10 days reveals two components with a depth of about 6 kpc each with the centres separated by 12 kpc. The results again agree with a near-collision with the LMC some 200–400 My ago.

Laney & Stobie (1986) come to similar conclusions and find that the SMC wing which lies towards the direction of the LMC also is closer to us and thus also closer to the LMC in the line of sight (0.27 mag or 8 kpc on average). Based on the scatter in the sample, they infer that the SMC is significantly elongated along the line of sight with a total depth of 18 kpc.

Welch et al. (1987) find from an analysis of 94 SMC Cepheids that only a very small extension of the SMC is necessary in order to explain their scatter around the PL relations. Accordingly, a dispersion of 0.12 mag or 3.3 kpc is enough indicating that the SMC does *not* extend beyond its tidal radius of ~ 4 kpc under reasonable assumptions of the galaxy masses ($< 10^{12} M_{\odot}$ for the Milky Way and $10^9 M_{\odot}$ for the SMC).

In a further development of their model Mathewson et al. (1988) investigated 61 Cepheids along the SMC bar with respect to radial velocities and distances and combined that with a high-resolution H I survey of this region. They find that the SMC has at least a depth of 20 kpc with derived distances ranging from 52 to 72 kpc. Moreover, the NE section of the SMC is found to be closer than the SW part by 10–15 kpc on average. There seems to be a relation between distance and radial velocity implying higher larger velocities for larger distances which is supported by the H I regions and by OB stars and F-M supergiants from other studies – in agreement with a collisional model for an encounter 250 Myrs ago.

An extensive study on the structure and motions of the SMC was provided by Martin et al. (1989) on the basis of the H I velocity distributions along 12 cuts parallel to a major axis (Caldwell & Coulson (1986) and Mathewson & Ford (1984) only investigated projections to the major axis) as well as of radial velocities of over 300 young stars and 35 H II regions. Four H I components, VH, H, L, and VL (for very high, high, low, and very low radial velocity) are distinguished where the L and the H component correspond reasonably well to the SMCR and MMC as introduced by Mathewson & Ford (1984). The L components extend further to the SW and are thought to lie in front of the the H components. In the south(-west) part of the SMC, the depth is relatively high with most of the young stars still being within a depth of < 10 kpc – smaller than derived by Mathewson et al. (1986, 1988) or Caldwell & Coulson (1986).

Again a larger extent in depth of the SMC was found by Hatzidimitriou & Hawkins (1989) from horizontal branch (HB)/clump stars with 17 kpc on average and up to 23 kpc in a NE region. The deeper NE regions are explained with the tidal deformation due to the last encounter with the LMC. A two-component structure as suggested from previous study for the young stellar population is also proposed for the older population of their sample.

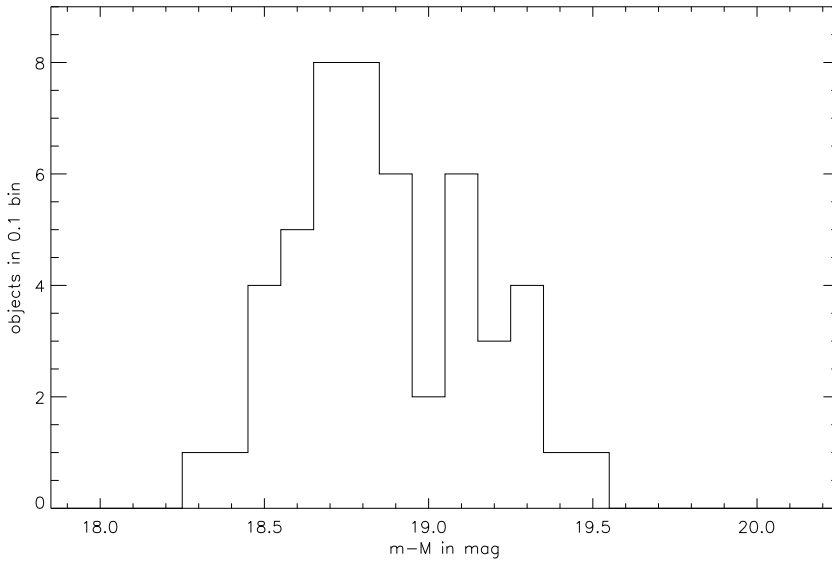


Figure 10.6: The distance moduli (binned to 0.1 mag) of the 50 eclipsing binaries from Harries et al. (2003) and Hilditch et al. (2005). The distribution of distance moduli from the binaries is very similar to the distribution derived in this work with the help of the FGLR. Both patterns conform to a bimodal distribution with a minimum at the same position (19.0) and a depth extension of ~ 0.4 dex or $\sim 10\text{--}15$ kpc. Differences such as relatively more objects at smaller distances may be due to different a distribution of sample stars (the binaries concentrate in the SW part around $\alpha = 0.85$ and $\delta = -73$ whereas most of the targets of this work lie in the NE part) or due to brightness selection effects removing fainter (hence more distant) binaries from the sample.

Based on combined data from the OGLE, DENIS, and 2MASS survey, for over 5000 Cepheids in total Groenewegen (2000) found a significant intrinsic depth of about 14 kpc. This impressively good statistics also indicates an inclined SMC with the NE part being closer to us.

Two studies of eclipsing binaries by Harries et al. (2003) and Hilditch et al. (2005) for 50 binaries in total suggest a mean distance modulus for the SMC of 18.91 with 1σ width of 0.28. Although they do not explicitly comment on the distribution of the distance moduli of the individual stars, a histogram of these is quite enlightening (see Fig. 10.6). It shows a very similar overall behaviour as the current study (Fig. 10.3) with a bi-modal structure with a minimum the same distance. Their histogram shows a larger bump at shorter distances which may be explained by a selection effect in their sample removing fainter (hence more distant) binaries. Another explanation would lie in the distribution of targets throughout the SMC field-of-view as their targets concentrate in the SW part whereas the stars in the present work lie mostly in the NE. This would indicate that stars in the SW are closer to us.

A recent investigation by North et al. (2009) of 33 eclipsing binaries determines a distance of 19.05 ± 0.04 and significant depth of 0.36 mag or 10.6 kpc. Finally, a

study by Subramanian & Subramanian (2009) estimate the SMC depth based on photometry of red clump stars (OGLEII, MCPS) a depth of 0.34 mag or 9.53 kpc.

To conclude, there is still no final agreement in literature in terms of the mean distance of the SMC – e.g. whether the short (~ 18.8) or long ($\sim 19.0/19.1$) distance scale is the best – or in terms of a depth extension (negligible depth extension up to ~ 30 kpc). The various analyses include different kinds of objects, cover different parts of the SMC, or are subject to different systematic effects. This might explain several discrepancies between the presented studies.

Nevertheless, the results from the literature imply that the SMC possesses very likely a rather complicated depth structure (in addition to the irregular shape in the field-of-view). In agreement to the results in this work, several studies find a significant extension in the line of sight. The FGLR results on the depth extension are quite consistent with Laney & Stobie (1986), Groenewegen (2000), Mathewson & Ford (1988), Martin et al. (1989), Hatzidimitriou & Hawkins (1989), Subramanian & Subramanian (2009), Harries et al. (2003) and Hilditch et al. (2005), and North et al. (2009). Our independent estimate of the spatial extent of the SMC in the line of sight adds an important contribution to the growing evidence that the radial extension of the SMC is $\sim 10\text{--}15$ kpc. Our results also support the idea that the SMC possesses a bimodal depth structure (Mathewson et al. 1986, Martin et al. 1989, Hatzidimitriou & Hawkins 1989, Harries et al. 2003 and Hilditch et al. 2005).

10.5 Searching for Abundance Patterns in Three Dimensions

The information on the distances of individual stars provided by the FGLR will now be employed to extend the discussion about possible abundance patterns or gradients from Sect. 9.5 from two to three dimensions. For that, Fig. 10.7 presents the mean abundances of the sample stars with respect to their position along the line-of-sight for metals supposed to be unaffected by stellar evolution processes.

The distance of the SMC center, i.e. the zero point of the x axis, was shifted by 8 kpc corresponding to a distance modulus of 19.2. This is *not* to be understood as a new determination of the mean distance of the SMC. Currently, there is a lot of debate going on about systematic effects on the calibration of the FGLR – mainly in the offset b_{FGLR} . This could be a reason why the average distance of the sample stars in this work is 19.2 instead of the canonical ~ 19.0 from the literature. In view of this, the adopted 19.2 should be rather seen as an empirical correction in order to obtain a symmetric distribution of stars along this adopted center (as it is now the case in Fig. 10.7).

With that, it is now possible to search for gradients of abundances with respect to the three dimensional distance of the SMC center in Fig. 10.8. As noted in Sect. 9.5, there is a high degree of chemical homogeneity among the young supergiants of the present work. And even including the distance information for each star it is hard to find any significant abundance gradient. Table 10.4 summarises information on the gradients derived.

For Ti, the number of stars is very small. Together with relatively high statistical uncertainties, no gradient can be claimed. The case for Fe is similar although more objects with derived iron abundances are available.

10 DISTANCE AND DEPTH EXTENSION OF THE SMC – THE FLUX-WEIGHTED GRAVITY–LUMINOSITY RELATIONSHIP (FGLR)

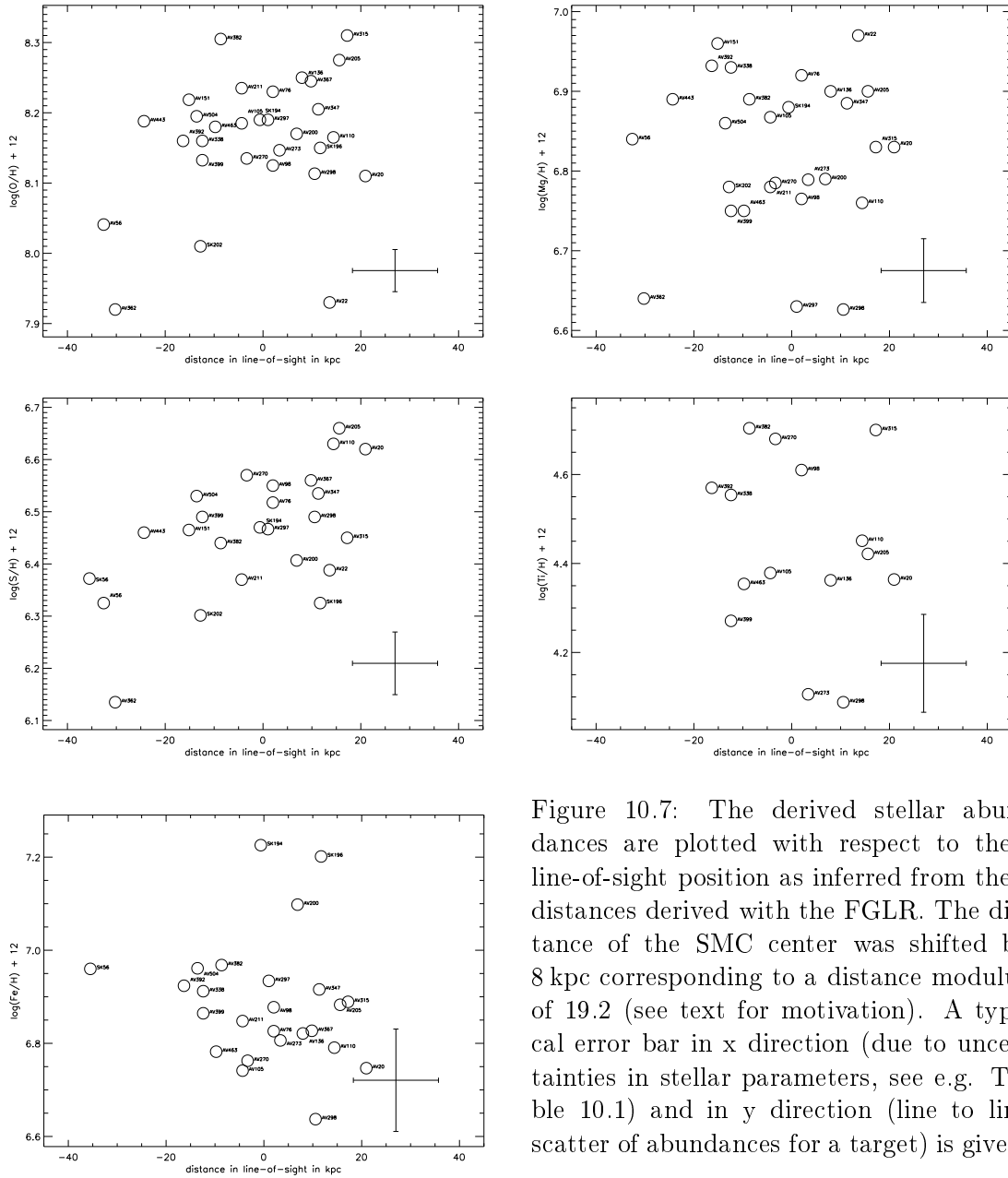


Figure 10.7: The derived stellar abundances are plotted with respect to their line-of-sight position as inferred from their distances derived with the FGLR. The distance of the SMC center was shifted by 8 kpc corresponding to a distance modulus of 19.2 (see text for motivation). A typical error bar in x direction (due to uncertainties in stellar parameters, see e.g. Table 10.1) and in y direction (line to line scatter of abundances for a target) is given.

The only elements where there may be an indication of an abundance gradient with respect to the three-dimensional distance to the SMC center are O and S. This formulation is kept very cautiously as claiming a gradient of few thousandth dex per kpc when there are statistical and systematic uncertainties of the order of one tenth dex is rather bold. Moreover, this depends mostly on very few objects.

Thus, there may be subtle indications for a reduced metallicity of stars far from the SMC center (mostly a line-of-sight effect). However, as this is extremely uncertain, it is concluded that the present-day chemical compositions of the SMC is highly homogeneous and that no definitely reliable gradients can be found – even with the

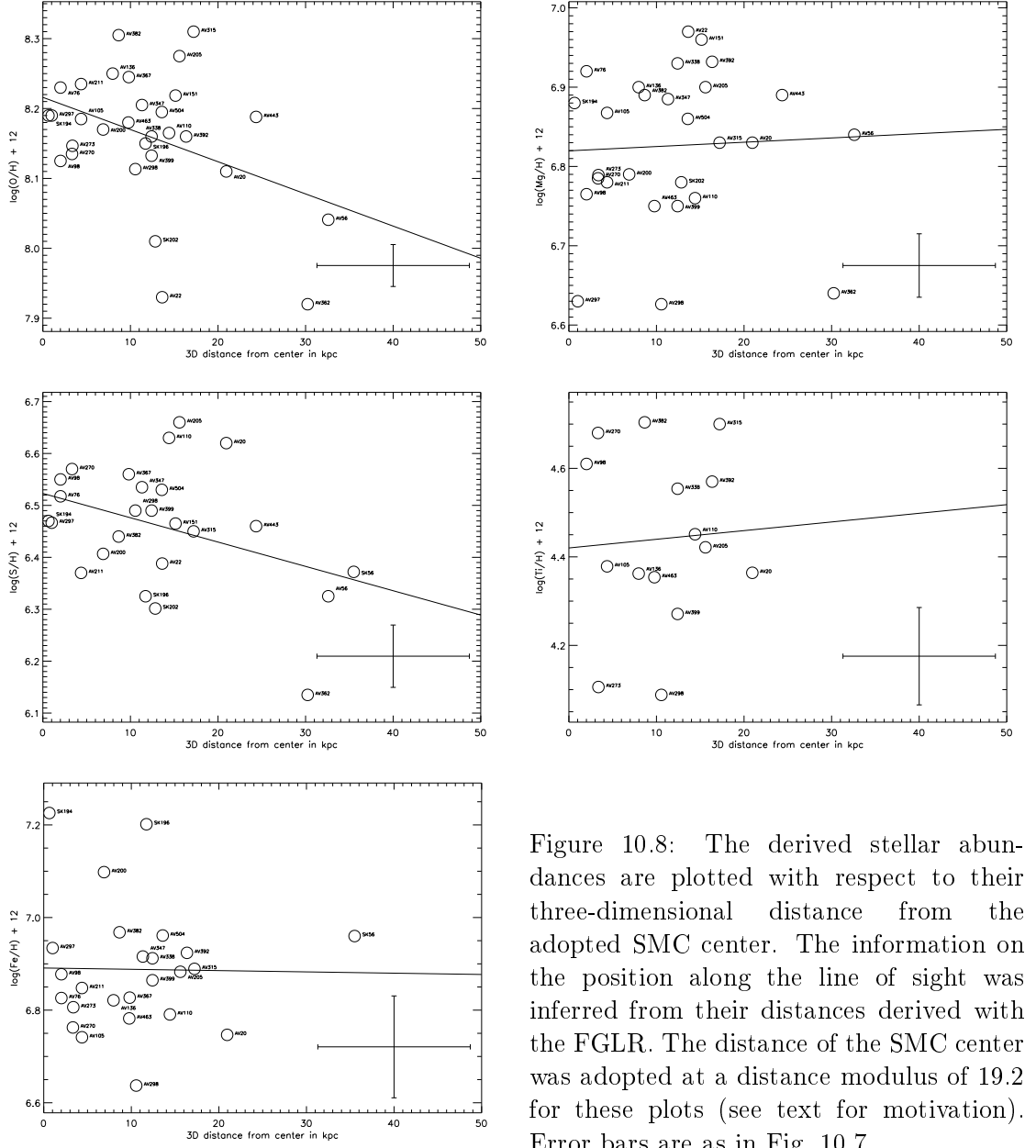


Figure 10.8: The derived stellar abundances are plotted with respect to their three-dimensional distance from the adopted SMC center. The information on the position along the line of sight was inferred from their distances derived with the FGLR. The distance of the SMC center was adopted at a distance modulus of 19.2 for these plots (see text for motivation). Error bars are as in Fig. 10.7.

high degree of consistency and accuracy achieved in the present study.

10.6 Microturbulence and Luminosity

Employing the information on the absolute bolometric magnitude from the FGLR, we compare the derived microturbulences of a star with this magnitude in Fig. 10.9. There is a clear trend of smaller microturbulent velocities for intrinsically fainter stars. This is in agreement with recent theoretical results by Cantiello et al. (2009) who argue on the basis of a proposed convection zone (associated with iron ionisation) below the stellar atmosphere. They also find a metallicity dependence of

10 DISTANCE AND DEPTH EXTENSION OF THE SMC – THE FLUX-WEIGHTED GRAVITY–LUMINOSITY RELATIONSHIP (FGLR)

Table 10.4: Abundance gradients inferred from the three-dimensional distance of an object to the SMC center.

Element	gradient (dex/kpc)	zero-point (dex)
O	-0.0046 ± 0.0020	8.22 ± 0.03
Mg	0.0005 ± 0.0022	6.82 ± 0.03
S	-0.0047 ± 0.0024	6.52 ± 0.04
Ti	0.0020 ± 0.0095	4.42 ± 0.11
Fe	-0.0003 ± 0.0037	6.89 ± 0.05

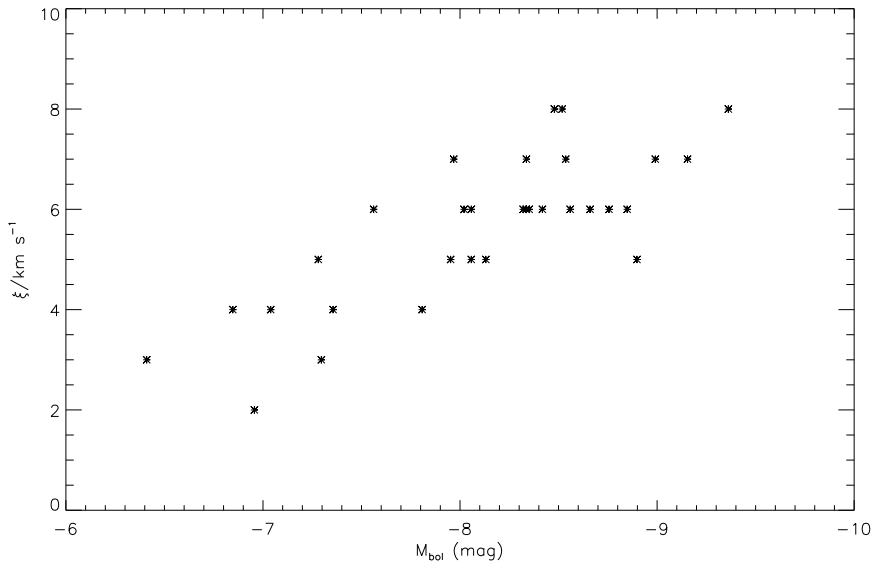


Figure 10.9: Derived microturbulent velocities as a function of the absolute bolometric magnitude for the sample stars. There is a clear trend of higher ξ at smaller M_{bol} , i.e. intrinsically brighter stars. Uncertainties in ξ are $1\text{--}2 \text{ km s}^{-1}$.

the microturbulence suggesting larger microturbulence at higher metallicities. This effect is also observationally supported when the present sample of low-metallicity supergiants is compared to a sample of similar stars in the Galaxy at roughly solar metallicity. In the ranges of overlapping absolute magnitudes, the more metal-rich Galactic supergiants show systematically higher microturbulences, by $\sim 2 \text{ km s}^{-1}$ (M. Firnstein, priv. comm.).

11 Conclusions

The major synopsis of this work is that BA supergiants are extremely powerful tools for extragalactic stellar astrophysics – *if* they are carefully analysed with the proper tools. As evolved massive stars they allow predictions of stellar evolution theories to be tested for galactic environments different than those found in the Milky Way. Moreover, as they can be observed in locations tracing the whole extent of galaxies, abundance gradients and patterns can be studied which allows the galactochemical evolution of these systems to be constrained.

High quality spectra of 38 BA supergiants in the Small Magellanic Cloud (SMC) with good signal-to-noise ratio (~ 100) were investigated in this work, constituting the largest sample of this kind of star that has been analysed beyond the Milky Way at high spectral resolution ($R \sim 48\,000$) to date. The analysis was based on synthetic spectra which account for departures from the classical assumption of local thermodynamic equilibrium (LTE). Non-LTE effects were shown to have a significant impact on a variety of spectral lines in BA supergiants (as well as in other stars) by several studies (e.g. Przybilla et al. 2006). Accounting for non-LTE effects is therefore a major step for determining reliable atmospheric parameters as well as stellar abundances from a fit of synthetic line profiles to observation. An aspect which must not be underestimated in this respect is the use of state-of-the-art atomic data for the analysis, available in form of well-tested model atoms.

Besides high-quality observations and realistic models a third ingredient was required to obtain highly consistent results: careful application of a comprehensive analysis methodology. This means that – if feasible – all important parameters characterising a stellar atmosphere have been determined consistently in a thorough way. This was achieved in an iterative process in which all relevant parameters were re-adjusted until a self-consistent solution was obtained. Systematic uncertainties in the atmospheric parameters and (directly as well as indirectly) in the stellar abundances were considerably reduced by this procedure.

With this strategy, it was possible to determine basic atmospheric parameters (such as effective temperatures T_{eff} , surface gravities $\log g$, microturbulence ξ , helium abundance $n(\text{He})$, and metallicity $[M/H]$) as well as atmospheric abundances in a very consistent way for 31 stars (modelling problems arose for seven stars) with unprecedented precision. T_{eff} could be constrained to few per cent, $\log g$ to 0.05–0.10 dex, and ξ to 1–2 km s⁻¹. Helium and metal abundances for individual stars show very low statistical uncertainties (based on the line-to-line scatter) of typically 10% for most species and $\sim 30\%$ for Ti and Fe. Typical uncertainties in the literature for T_{eff} and $\log g$ amount to $\lesssim 10\%$ and 0.15–0.20 dex, respectively. In particular, the typical abundance uncertainties of a factor of ~ 2 make it hard to draw any thorough conclusions concerning the evolution of massive stars or abundance patterns/gradients in a galaxy.

The abundances derived in this work on the other hand place tight observational constraints to stellar evolution theory in terms of chemical signatures in the atmosphere caused by mixing with CN(O)-processed matter from the stellar core (C de-

pletion and N enrichment there). Important quantities in this respect are thus the observed abundances of He, C, N, and O in the atmosphere. Helium tends to be slightly enriched to 0.11 in number fraction (mean over all stars), while significant enrichment/depletion by $\sim 0.6/0.4$ dex for N or C respectively (with respect to the mean metallicity relative to the solar pattern) is found. Rather tight trends of increasing helium abundance and N/C mass fraction with higher N/O mass fraction are found. The slope of the N/C vs. N/O relation is inconsistent with the initial relative compositions of the CNO elements in the evolution models and calls for a refinement of the models in this respect. More importantly, it was found that the mixing from the stellar core to the atmosphere as implemented so far in stellar evolution models is not efficient enough to create the high N/C and N/O ratios and the high helium abundances if the stars come directly from the main sequence. To solve this discrepancy, two solutions are imaginable. Either most of the stars are far more evolved and have already experienced convective mixing in the red supergiant stage or the mixing in the earlier phases of stellar evolution is much more pronounced than previously thought. This higher mixing efficiency could be achieved by the interplay of rotation and magnetic fields as found by Maeder & Meynet (2005) for models at solar metallicity. It is important to note that high N/C and N/O ratios as well as high helium abundances are predominantly found in stars with larger masses. This is consistent with recent stellar evolution theory which predicts stronger mixing with increasing stellar mass.

The accurate atmospheric abundances in individual stars are also reflected in the good agreement of abundances of one element throughout all stars. It could be shown that the SMC is chemically homogeneous to a very high level with a typical scatter for most elements of 0.1 dex or 25%. Larger scatter is found for Ti (0.20 dex) and to a lesser degree for Fe (good 0.14 dex) which is more likely an issue of remaining systematics because of an incompleteness of the model atoms than a real pattern. It is not surprising that – considering this observed high degree of homogeneity – no clear abundance pattern or gradient is found in two dimension throughout the field-of-view. The relatively short basis of few kpc in the field-of-view makes the detection of gradients even more difficult.

The flux-weighted gravity–luminosity relationship (FGLR) for B and A supergiants provides a completely independent distance estimate based on the two fundamental atmospheric parameters (T_{eff} and $\log g$). It can be used to determine distances to individual stars and consequently to galaxies (from a sample of supergiants) up to a few Mpc with an accuracy comparable to the classic distance indicators (Kudritzki et al. 2008, Urbaneja et al. 2008), the Cepheids. A sufficient accuracy (statistical as well as systematic effects) in the atmospheric parameters (few hundred K for T_{eff} and $\lesssim 0.1$ – 0.15 dex in $\log g$) is needed in order to obtain significant results with this method. This requires spectra of an adequate quality as well as detailed theoretical tools. It has only been in the last decade(s) that the modelling tools match these requirements by including non-LTE effects and detailed atomic data. Now, one must also actually use these tools which require some more effort (compared to other objects) but are vital in order to achieve the feasible consistency.

An extensive use of the FGLR as distance determination technique requires a certain effort on its calibration. An important step in this respect is the work of Kudritzki et al. (2008). In the present study, we tried to extend this work to a metal-poor environment such as the SMC. However, as it turned out, the results indicate a significant intrinsic depth of the SMC along the line-of-sight rendering the assumption of the same distance of all stars unjustified and thus the calibration infeasible. Instead, we employed the given FGLR as calibrated by Kudritzki et al. (2008) to determine the distances to our sample stars, thus probing the depth extension of the SMC.

Accounting for the uncertainties of the individual stars, their distance distribution still suggests a significant extent in the line-of-sight of the SMC of the order of 10–15 kpc – a remarkable number given its mean distance of about 63 kpc and its extension in the field-of-view of only 4 kpc. The literature provides extensive investigations and debates concerning the spatial extension of the SMC. Suggestions for the line-of-sight extensions range from zero to enormous 30 kpc. Our estimate of 10–15 kpc is fully independent from the other studies (different objects as well as a different method) and consistent with the mean of the published values. Our results may also suggest a bimodal distribution of stars in the radial direction.

The distance to individual stars found with the help of the FGLR allowed us to search for a gradient with respect to the three-dimensional distance of a star from the SMC center. The conclusion is that the present-day composition of the SMC as reflected in the abundances of O, Mg, S, Ti, and Fe can be (again, as in two-dimensional field-of-view) regarded as very homogeneous where the small scatter in abundances from star to star may be fully explained with statistical and systematic uncertainties.

A List of Investigated Spectral Lines

In this section, detailed information on the investigated spectral lines (helium and metals) are presented. The first part summarises all spectral lines in a table which were examined in at least one object. The columns give the designation of the ionic species, transition wavelength λ (in Å), excitation energy of the lower level χ (in eV), adopted oscillator strength $\log gf$, and an accuracy indicator. The sources for the gf values as well as for the Stark broadening parameters are given after the line list. Lines where the wavelength information is put in italics are always (for every object) contributions to the transition above which is not in italics. Due to broadening mechanisms, they are not separated in the spectrum.

The second part lists the lines analysed for specific stars as well as the abundances (in the usual notation $X = \log x/H + 12$, except for He) derived from the respective lines. If more than one transition of the same species contribute to the same spectral feature, only one transition (the one with the shortest wavelength and the one not put in italics in the first table) is indicated in the second part. Usually, the transitions at 6155.96 Å and 6156.74 Å also strongly overlap for most objects except for a few objects with small $v \sin i$. If 6156.74 is not explicitly mentioned in the second part, it means thus that it was analysed together with the 6155.96 transitions and counted as one line.

A.1 Overview About all Employed Spectral Lines with Atomic Information

Table A.1:

Ion	$\lambda/\text{Å}$	χ/eV	$\log gf$	Acc.	Src.	He I	$\lambda/\text{Å}$	χ/eV	$\log gf$	Acc.	Src.
						He I	<i>4120.99</i>	20.96	-2.44	B	WSG
						He I	4143.76	21.22	-1.20	B	WSG
He I	3819.60	20.96	-0.97	B	WSG	He I	4168.97	21.22	-2.34	A	WSG
He I	<i>3819.61</i>	20.96	-1.19	B	WSG	He I	4387.93	21.22	-0.88	A	WSG
He I	<i>3819.76</i>	20.96	-1.67	B	WSG	He I	4437.55	21.22	-2.03	B	WSG
He I	3867.47	20.96	-2.06	B	WSG	He I	4471.47	20.96	-0.20	A	WSG
He I	<i>3867.48</i>	20.96	-2.28	B	WSG	He I	<i>4471.49</i>	20.96	-0.42	A	WSG
He I	<i>3867.63</i>	20.96	-2.75	B	WSG	He I	<i>4471.68</i>	20.96	-0.90	A	WSG
He I	3926.54	21.22	-1.65	A	WSG	He I	4713.14	20.96	-1.23	B	WSG
He I	3964.73	20.62	-1.30	A	WSG	He I	<i>4713.16</i>	20.96	-1.45	B	WSG
He I	4009.26	21.22	-1.47	C	WSG	He I	<i>4713.38</i>	20.96	-1.93	B	WSG
He I	4026.18	20.96	-2.63	A	WSG	He I	4921.93	21.22	-0.44	A	WSG
He I	<i>4026.19</i>	20.96	-0.63	A	WSG	He I	5875.60	20.96	-1.52	A	WSG
He I	<i>4026.20</i>	20.96	-0.85	A	WSG	He I	<i>5875.61</i>	20.96	+0.48	A	WSG
He I	<i>4026.36</i>	20.96	-1.32	A	WSG	He I	<i>5875.63</i>	20.96	-0.34	A	WSG
He I	4120.81	20.96	-1.74	B	WSG	He I	<i>5875.64</i>	20.96	+0.14	A	WSG
He I	<i>4120.82</i>	20.96	-1.96	B	WSG	He I	<i>5875.97</i>	20.96	-0.22	A	WSG

A LIST OF INVESTIGATED SPECTRAL LINES

C I	9078.29	7.48	-0.58	B	WFD	O I	6158.19	10.74	-0.41	B+	WFD
C I	9088.51	7.48	-0.43	B	WFD	O I	7001.90	10.99	-1.49	B	WFD
C II	3920.69	16.33	-0.23	B	WFD	O I	7001.92	10.99	-1.01	B	WFD
C II	4267.00	18.05	+0.56	C+	WFD	O I	7002.17	10.99	-2.66	B	WFD
C II	4267.26	18.05	+0.74	C+	WFD	O I	7002.20	10.99	-1.49	B	WFD
C II	6578.05	14.45	-0.03	B	WFD	O I	7002.23	10.99	-0.74	B	WFD
C II	6582.88	14.45	-0.33	B	WFD	O I	7002.25	10.99	-1.36	B	WFD
N I	7423.64	10.33	-0.71	B+	WFD	O I	7771.94	9.15	+0.37	A	WFD
N I	7442.30	10.33	-0.38	B+	WFD	O I	7774.17	9.15	+0.22	A	WFD
N I	7468.31	10.34	-0.19	B+	WFD	O I	7775.39	9.15	+0.00	A	WFD
N I	8567.74	10.68	-0.66	B	WFD	O II	4069.62	25.63	+0.15	B+	WFD
N I	8594.00	10.68	-0.33	B	WFD	O II	4069.88	25.64	+0.34	B+	WFD
N I	8680.28	10.34	+0.35	B+	WFD	O II	4072.16	25.65	+0.55	B+	WFD
N I	8683.40	10.33	+0.09	B+	WFD	O II	4075.86	25.67	+0.69	B+	WFD
N I	8686.15	10.33	-0.31	B+	WFD	O II	4351.26	25.66	+0.23	B+	WFD
N I	8703.25	10.33	-0.32	B+	WFD	O II	4351.46	25.66	-1.00	B	WFD
N I	8711.70	10.33	-0.23	B+	WFD	O II	4349.43	23.00	+0.06	B	WFD
N I	8718.84	10.34	-0.34	B+	WFD	O II	4366.89	23.00	-0.35	B	WFD
N I	8728.90	10.33	-1.07	B+	WFD	O II	4414.91	23.44	+0.17	B	WFD
N II	3955.85	18.47	-0.81	B	WFD	O II	4416.97	23.42	-0.08	B	WFD
N II	3995.00	18.50	+0.21	B	WFD	O II	4590.97	25.66	+0.35	B+	WFD
N II	4447.03	20.41	+0.23	B	WFD	O II	4641.81	22.98	+0.05	B	WFD
N II	4601.48	18.46	-0.43	B+	WFD	O II	4649.13	23.00	+0.31	B	WFD
N II	4607.15	18.46	-0.51	B+	WFD	O II	4661.63	22.98	-0.28	B	WFD
N II	4630.54	18.48	+0.09	B+	WFD	O II	4676.24	23.00	-0.39	B	WFD
N II	4643.09	18.48	-0.36	B+	WFD	Mg I	3829.36	2.71	-0.21	B	WSM
N II	5005.15	20.67	+0.59	B	WFD	Mg I	3832.30	2.71	+0.27	B	WSM
N II	5045.10	18.46	-0.41	B+	WFD	Mg I	3838.29	2.72	+0.49	B	WSM
N II	5666.63	18.47	-0.05	A	WFD	Mg I	4702.99	4.35	-0.42	C+	BMZ
N II	5676.02	18.46	-0.37	A	WFD	Mg I	5172.68	2.71	-0.38	B	WSM
N II	5679.56	18.48	+0.25	A	WFD	Mg I	5183.60	2.72	-0.16	B	WSM
N II	5686.21	18.47	-0.55	A	WFD	Mg I	5528.41	4.35	-0.40	C+	BMZ
N II	5710.77	18.48	-0.52	A	WFD	Mg II	4384.64	10.00	-0.79	C+	WSM
O I	5329.10	10.74	-1.24	C+	WFD	Mg II	4390.51	10.00	-1.71	D	WSM
O I	5329.68	10.74	-1.02	C+	WFD	Mg II	4390.57	10.00	-0.53	D	WSM
O I	5330.73	10.74	-0.87	C+	WFD	Mg II	4433.99	10.00	-0.90	C+	WSM
O I	6155.96	10.74	-1.36	B+	WFD	Mg II	4481.13	8.86	+0.73	B+	FW
O I	6155.97	10.74	-1.01	B+	WFD	Mg II	4481.15	8.86	-0.57	B+	FW
O I	6155.99	10.74	-1.12	B+	WFD	Mg II	4481.33	8.86	+0.58	B+	FW
O I	6156.74	10.74	-1.49	B+	WFD	Mg II	5401.54	11.63	-0.08	C	CA
O I	6156.76	10.74	-0.90	B+	WFD	Mg II	6545.97	11.63	+0.41	C	CA
O I	6156.78	10.74	-0.69	B+	WFD	Mg II	7877.05	10.00	+0.39	C+	WSM
O I	6158.15	10.74	-1.84	B+	WFD	Mg II	7896.04	10.00	-0.30	C+	WSM
O I	6158.17	10.74	-1.00	B+	WFD	Mg II	7896.37	10.00	+0.65	C+	WSM

A.1 Overview About all Employed Spectral Lines with Atomic Information

S II	4153.07	15.90	+0.62	D-	WSM	Ti II	4805.09	2.06	-1.10	D-	MFW
S II	4162.67	15.94	+0.78	D-	WSM	Ti II	4911.18	3.12	-0.34	D	MFW
S II	4294.40	16.13	+0.58	D-	WSM	Ti II	5188.68	1.58	-1.21	D-	MFW
S II	4815.55	13.67	+0.09	D	WSM	Ti II	5336.78	1.58	-1.70	D-	MFW
S II	5009.57	13.62	-0.28	D	WSM	Fe II	3938.29	1.67	-3.89	D	MFW
S II	5014.04	14.07	+0.10	D	WSM	Fe II	3945.21	3.89	-2.72	X	KB
S II	5032.43	13.67	+0.27	D	WSM	Fe II	4122.64	2.58	-3.38	D	FMW
S II	5320.72	15.07	+0.50	D	WSM	Fe II	4124.79	2.54	-4.20	D	FMW
S II	5345.71	15.07	+0.36	D	WSM	Fe II	4173.46	2.58	-2.18	C	FMW
S II	5428.66	13.58	-0.13	D	WSM	Fe II	4178.86	2.58	-2.47	C	FMW
S II	5432.80	13.62	+0.26	D	WSM	Fe II	4233.17	2.58	-2.00	C	FMW
S II	5453.86	13.67	+0.48	D	WSM	Fe II	4273.32	2.70	-3.34	D	FMW
S II	5473.61	13.58	-0.18	D	WSM	Fe II	4296.57	2.70	-3.01	D	FMW
S II	5509.71	13.62	-0.14	D	WSM	Fe II	4303.17	2.70	-2.49	C	FMW
S II	5606.15	13.73	+0.31	D	WSM	Fe II	4385.39	2.77	-2.57	D	FMW
S II	5660.00	13.68	-0.05	D	WSM	Fe II	4416.83	2.78	-2.61	D	FMW
S III	4253.50	18.24	+0.36	D	WSM	Fe II	4489.19	2.83	-2.97	D	FMW
Ti II	3900.56	1.13	-0.45	D	MFW	Fe II	4491.40	2.86	-2.70	C	FMW
Ti II	3913.48	1.12	-0.53	D	MFW	Fe II	4508.28	2.86	-2.31	D	KB
Ti II	4028.36	1.89	-1.00	D	MFW	Fe II	4515.34	2.84	-2.48	D	FMW
Ti II	4163.63	2.59	-0.40	D	MFW	Fe II	4520.23	2.81	-2.60	D	FMW
Ti II	4171.92	2.60	-0.56	D	MFW	Fe II	4522.63	2.84	-2.11	C	KB
Ti II	4287.88	1.08	-2.02	D-	MFW	Fe II	4541.52	2.86	-3.05	D	FMW
Ti II	4290.22	1.16	-1.12	D-	MFW	Fe II	4549.47	2.83	-1.75	C	FMW
Ti II	<i>4290.34</i>	2.06	-1.53	X	KB	Fe II	4555.89	2.83	-2.32	D	KB
Ti II	4294.09	1.08	-1.11	D-	MFW	Fe II	4576.33	2.84	-3.04	D	FMW
Ti II	4300.06	1.18	-0.77	D-	MFW	Fe II	4580.06	2.58	-3.73	X	KB
Ti II	4301.92	1.16	-1.16	D-	MFW	Fe II	4582.84	2.84	-3.10	C	FMW
Ti II	4312.87	1.18	-1.16	D-	MFW	Fe II	4620.51	2.83	-3.28	D	FMW
Ti II	4314.97	1.16	-1.13	D-	MFW	Fe II	4629.34	2.81	-2.37	D	FMW
Ti II	4330.24	2.04	-1.51	D	MFW	Fe II	4635.33	5.96	-1.65	D-	FMW
Ti II	<i>4330.72</i>	1.18	-2.04	D-	MFW	Fe II	4666.75	2.83	-3.33	D	FMW
Ti II	4394.02	1.22	-1.59	D-	MFW	Fe II	4731.44	2.89	-3.36	D	FMW
Ti II	4395.00	1.08	-0.66	D-	MFW	Fe II	4993.35	2.81	-3.65	E	FMW
Ti II	4399.79	1.24	-1.27	D-	MFW	Fe II	5276.00	3.20	-1.94	C	FMW
Ti II	4417.72	1.16	-1.43	D-	MFW	Fe II	5316.62	3.15	-1.85	C	FMW
Ti II	4443.78	1.08	-0.70	D-	MFW	Fe II	5325.56	3.22	-3.22	X	KB
Ti II	4450.50	1.08	-1.45	D-	MFW	Fe II	5362.87	3.20	-2.74	X	KB
Ti II	4468.52	1.13	-0.60	D-	MFW	Fe II	5425.25	3.20	-3.36	D	FMW
Ti II	4501.27	1.12	-0.75	D-	MFW	Fe II	5534.83	3.24	-2.93	D	FMW
Ti II	4563.77	1.22	-0.96	D-	MFW	Fe II	6147.74	3.89	-2.72	X	KB
Ti II	4571.96	1.57	-0.53	D-	MFW	Fe II	6149.26	3.89	-2.72	X	KB
Ti II	4779.98	2.05	-1.37	D-	MFW						

A LIST OF INVESTIGATED SPECTRAL LINES

accuracy indicators – uncertainties within: AA: 1%; A: 3%; B: 10%; C: 25%; D: 50%; E: larger than 50%; X: unknown

sources of gf -values – BMZ: Butler et al. (1993); CA: Coulomb approximation (Bates & Damgaard (1994); FMW: Fuhr et al. (1988); KB: Kurucz & Bell (1995); MFW: Martin et al. (1988); WFD: Wiese et al. (1996); WSG: Wiese et al. (1966)*; WSM: Wiese et al. (1969)*; when available^(*), improved gf -values from Fuhr & Wiese (1998, FW) are favoured.

sources for Stark broadening parameters – H I: Stehlé & Hutcheon (1999), Vidal et al. (1973); He I: Barnard et al. (1969), Dimitrijević & Sahal-Bréchet (1990); C I: Griem (1974), Cowley (1971); C II: Griem (1964, 1974), Cowley (1971); N I/II: Griem (1964, 1974), Cowley (1971); O I/II: Cowley (1971); Mg I: Dimitrijević & Sahal-Bréchet (1996), Cowley (1971); Mg II: Griem (1964, 1974), Cowley (1971); S II/III: Cowley (1971);

A.2 Lines Employed in Specific Stars with Abundance Information

Table A.2:

Ion	$\lambda/\text{\AA}$	X						
			Ti II	4805.09	4.52	He I	4713.14	0.12
			Ti II	4911.18	4.22	C II	4267.00	6.84
			Ti II	5188.68	4.41	C II	6578.05	6.87
AV20			Fe II	4122.64	6.77	C II	6582.88	6.83
			Fe II	4173.46	6.46	N II	3995.00	7.85
He I	4026.18	0.12	Fe II	4178.86	6.83	N II	4447.03	7.93
He I	4387.93	0.14	Fe II	4273.32	6.73	N II	4601.48	7.95
He I	4471.47	0.11	Fe II	4296.57	6.80	N II	4607.15	7.94
He I	4713.14	0.12	Fe II	4303.17	6.68	N II	4630.54	7.96
He I	4921.93	0.14	Fe II	4385.39	6.60	N II	4643.09	7.91
N I	7423.64	7.88	Fe II	4416.83	6.58	N II	5005.15	7.99
N I	7442.30	7.83	Fe II	4491.40	6.65	N II	5045.10	7.90
N I	7468.31	7.83	Fe II	4508.28	6.77	N II	5666.63	7.91
N I	8680.28	7.90	Fe II	4515.34	6.69	O I	7771.94	7.91
N I	8683.40	7.87	Fe II	4522.63	6.94	O I	7774.17	7.93
N I	8686.15	7.89	Fe II	4541.52	6.79	O II	4416.97	7.95
N I	8711.70	7.88	Fe II	4549.47	6.90	O II	4641.81	7.93
N I	8718.84	7.84	Fe II	4555.89	6.78	Mg II	4481.33	6.97
O I	6155.96	8.12	Fe II	4576.33	6.74	S II	4815.55	6.43
O I	6158.15	8.10	Fe II	4620.51	6.72	S II	5345.71	6.37
Mg I	5172.68	6.82	Fe II	4629.34	6.68	S II	5428.66	6.41
Mg I	5183.60	6.84	Fe II	4666.75	6.76	S II	5432.80	6.35
Mg II	4390.51	6.83	Fe II	4993.35	6.72	S II	5453.86	6.38
Mg II	4433.99	6.83	Fe II	5276.00	6.52			
S II	5032.43	6.62	Fe II	5316.62	6.78			
			Fe II	5325.56	6.81			
			Fe II	5362.87	6.88	AV56		
Ti II	3913.48	4.46	Fe II	5534.83	6.84			
Ti II	4163.63	4.50	Fe II	6147.74	6.83	He I	3926.54	0.11
Ti II	4171.92	4.45	Fe II	6149.26	6.91	He I	4009.26	0.13
Ti II	4290.22	4.41				He I	4120.81	0.13
Ti II	4314.97	4.38	AV22			He I	4168.97	0.09
Ti II	4395.00	4.36				He I	4437.55	0.12
Ti II	4443.78	4.21	He I	3867.47	0.14	He I	4713.14	0.09
Ti II	4450.50	4.24	He I	3964.73	0.15	C II	6578.05	7.30
Ti II	4468.52	4.14	He I	4009.26	0.13	C II	6582.88	7.34
Ti II	4501.27	4.23	He I	4120.81	0.13	N II	3955.85	7.94
Ti II	4563.77	4.47	He I	4168.97	0.13	N II	3995.00	7.89
Ti II	4571.96	4.46	He I	4437.55	0.12			

A LIST OF INVESTIGATED SPECTRAL LINES

N II	4601.48	7.86	S II	5432.80	6.50	S II	5453.86	6.47
N II	4607.15	7.92	S II	5453.86	6.56	Ti II	3913.48	4.67
N II	4630.54	7.95	Fe II	4173.46	6.63	Ti II	4290.22	4.68
N II	4643.09	7.90	Fe II	4178.86	6.84	Ti II	4294.09	4.70
N II	5005.15	7.93	Fe II	4233.17	6.89	Ti II	4395.00	4.62
N II	5045.10	7.94	Fe II	4303.17	6.87	Ti II	4443.78	4.55
N II	5676.02	7.95	Fe II	4385.39	6.89	Ti II	4501.27	4.44
N II	5686.21	7.86	Fe II	4416.83	6.85	Fe II	4122.64	6.89
N II	5710.77	7.94	Fe II	4491.40	6.86	Fe II	4173.46	6.35
O I	7771.94	8.03	Fe II	4515.34	6.95	Fe II	4178.86	6.94
O I	7774.17	8.05	Fe II	4520.23	6.86	Fe II	4233.17	7.11
O II	4069.62	8.01	Fe II	4522.63	6.86	Fe II	4273.32	6.81
O II	4072.16	8.05	Fe II	4549.47	6.79	Fe II	4296.57	6.92
O II	4075.86	8.09	Fe II	5276.00	6.71	Fe II	4303.17	6.80
O II	4366.89	8.02	Fe II	5316.62	6.74	Fe II	4385.39	6.84
O II	4590.97	8.00				Fe II	4416.83	6.75
O II	4641.81	8.06	AV98			Fe II	4489.19	6.84
O II	4649.13	8.10				Fe II	4491.40	6.79
O II	4661.63	8.05	He I	3819.60	0.12	Fe II	4508.28	6.87
O II	4676.24	7.99	He I	3867.47	0.15	Fe II	4515.34	6.87
Mg II	4481.33	6.84	He I	3964.73	0.14	Fe II	4520.23	6.89
S II	5453.86	6.34	He I	4026.18	0.12	Fe II	4522.63	6.99
S III	4253.50	6.31	He I	4120.81	0.11	Fe II	4541.52	6.89
			He I	4143.76	0.13	Fe II	4549.47	6.93
			He I	4471.47	0.12	Fe II	4555.89	6.89
			He I	4713.14	0.11	Fe II	4576.33	6.92
AV76			He I	4921.93	0.13	Fe II	4620.51	6.92
			C II	4267.00	7.19	Fe II	4629.34	6.79
He I	3964.73	0.13	N I	7423.64	8.15	Fe II	4666.75	6.79
He I	4026.18	0.11	N I	7442.30	8.13	Fe II	5276.00	6.69
He I	4120.81	0.11	N I	7468.31	8.12	Fe II	5316.62	6.88
He I	4471.47	0.13	N I	8680.28	8.15	Fe II	5325.56	6.99
He I	4713.14	0.12	N I	8683.40	8.22	Fe II	5362.87	7.04
C II	4267.00	7.62	N I	8686.15	8.21	Fe II	5534.83	7.02
N I	7468.31	8.18	N I	8703.25	8.24	Fe II	6147.74	7.01
N I	8680.28	8.17	N I	8711.70	8.14	Fe II	6149.26	7.03
N I	8683.40	8.24	O I	6155.96	8.14			
N II	3995.00	8.18	O I	6158.15	8.11	AV105		
O I	6158.15	8.23	Mg II	4390.51	6.77	He I	4026.18	0.08
Mg II	4390.51	6.92	Mg II	6545.97	6.76	He I	4387.93	0.12
S II	4815.55	6.48	S II	4815.55	6.57	He I	4471.47	0.08
S II	5032.43	6.53	S II	5032.43	6.61	He I	4713.14	0.11
						He I	4921.93	0.11

A.2 Lines Employed in Specific Stars with Abundance Information

He I	5875.60	0.12	Fe II	5362.87	6.92	Fe II	4416.83	6.66
N I	7468.31	7.81	Fe II	5534.83	6.87	Fe II	4489.19	6.78
N I	8680.28	7.76	Fe II	6147.74	6.91	Fe II	4491.40	6.64
N I	8686.15	7.83	Fe II	6149.26	6.93	Fe II	4508.28	6.73
N I	8703.25	7.81				Fe II	4515.34	6.72
N I	8711.70	7.79	AV110			Fe II	4520.23	6.74
O I	6155.96	8.17				Fe II	4522.63	6.87
O I	6158.15	8.20	He I	3964.73	0.15	Fe II	4541.52	6.87
Mg I	3838.29	6.95	He I	4026.18	0.16	Fe II	4549.47	6.83
Mg I	5183.60	6.88	He I	4120.81	0.18	Fe II	4555.89	6.81
Mg II	4390.51	6.81	He I	4143.76	0.17	Fe II	4576.33	6.83
Mg II	4433.99	6.83	He I	4387.93	0.17	Fe II	4620.51	6.72
Ti II	3913.48	4.47	He I	4471.47	0.15	Fe II	4629.34	6.68
Ti II	4294.09	4.48	He I	4713.14	0.18	Fe II	4635.33	7.19
Ti II	4300.06	4.45	He I	4921.93	0.18	Fe II	4666.75	6.78
Ti II	4395.00	4.31	C II	4267.00	7.82	Fe II	4731.44	6.92
Ti II	4443.78	4.27	N I	7442.30	7.89	Fe II	5276.00	6.54
Ti II	4468.52	4.24	N I	7468.31	7.94	Fe II	5316.62	6.76
Ti II	4563.77	4.43	N I	8680.28	7.98	Fe II	5362.87	6.95
Fe II	4173.46	6.38	N I	8683.40	8.02	Fe II	6147.74	6.89
Fe II	4178.86	6.80	N I	8686.15	8.06	Fe II	6149.26	6.90
Fe II	4233.17	6.77	N I	8703.25	7.97	AV136		
Fe II	4273.32	6.79	N I	8711.70	7.91			
Fe II	4296.57	6.87	O I	6155.96	8.15	He I	4026.18	0.13
Fe II	4303.17	6.64	O I	6158.15	8.18	He I	4471.47	0.13
Fe II	4385.39	6.64	Mg II	4390.51	6.76	He I	5875.60	0.14
Fe II	4416.83	6.63	S II	5453.86	6.63	C I	9078.29	7.60
Fe II	4489.19	6.77	Ti II	3900.56	4.53	N I	7423.64	7.96
Fe II	4491.40	6.68	Ti II	4294.09	4.57	N I	7442.30	7.93
Fe II	4508.28	6.67	Ti II	4300.06	4.44	N I	7468.31	7.84
Fe II	4515.34	6.75	Ti II	4395.00	4.46	N I	8567.74	7.94
Fe II	4520.23	6.76	Ti II	4443.78	4.28	N I	8680.28	8.05
Fe II	4522.63	6.79	Ti II	4468.52	4.35	N I	8683.40	8.00
Fe II	4541.52	6.82	Ti II	4501.27	4.47	N I	8686.15	7.96
Fe II	4549.47	6.80	Ti II	4563.77	4.52	N I	8703.25	7.86
Fe II	4555.89	6.68	Ti II	4571.96	4.44	N I	8711.70	7.93
Fe II	4576.33	6.81	Fe II	4122.64	6.80	N I	8718.84	7.85
Fe II	4582.84	6.70	Fe II	4173.46	6.43	O I	6155.96	8.28
Fe II	4620.51	6.79	Fe II	4178.86	6.79	O I	6158.15	8.22
Fe II	4629.34	6.67	Fe II	4233.17	7.00	Mg I	3829.36	6.89
Fe II	4666.75	6.73	Fe II	4273.32	6.83	Mg I	3838.29	6.86
Fe II	5276.00	6.48	Fe II	4303.17	6.69	Mg I	5172.68	6.92
Fe II	5316.62	6.71				Mg I	5183.60	6.87

A LIST OF INVESTIGATED SPECTRAL LINES

Mg II	4433.99	6.85	N I	8680.28	8.11	S II	5453.86	6.46
Mg II	6545.97	6.97	N II	3995.00	8.08	S III	4253.50	6.47
Mg II	7877.05	6.90	N II	4447.03	8.14			
Mg II	7896.04	6.94	N II	4630.54	8.03			
Ti II	3900.56	4.40	N II	5679.56	8.10	AV200		
Ti II	4290.22	4.39	S II	5032.43	6.33	He I	3964.73	0.10
Ti II	4294.09	4.42	S II	5320.72	6.37	He I	4009.26	0.13
Ti II	4300.06	4.38	S II	5432.80	6.36	He I	4026.18	0.10
Ti II	4314.97	4.38	S II	5453.86	6.36	He I	4120.81	0.12
Ti II	4394.02	4.39	S II	5606.15	6.44	He I	4143.76	0.13
Ti II	4563.77	4.35				He I	4387.93	0.11
Ti II	4911.18	4.31	Fe II	4549.47	6.96	He I	4437.55	0.11
Ti II	5188.68	4.24				He I	4471.47	0.12
Fe II	4385.39	6.77	AV151			He I	4921.93	0.12
Fe II	4416.83	6.75				C II	4267.00	7.37
Fe II	4491.40	6.74	He I	3867.47	0.13	C II	6578.05	7.44
Fe II	4508.28	6.85	He I	3926.54	0.13			
Fe II	4520.23	6.94	He I	3964.73	0.15	N I	8680.28	8.07
Fe II	4522.63	6.86	He I	4009.26	0.13	N II	4630.54	8.08
Fe II	4555.89	6.80	He I	4168.97	0.12	O I	6155.96	8.17
Fe II	4580.06	6.74	He I	4437.55	0.11	Mg II	7896.04	6.79
Fe II	4620.51	6.81	He I	4713.14	0.15	S II	4815.55	6.41
Fe II	4993.35	6.84	C II	4267.00	6.98	S II	5032.43	6.34
Fe II	5325.56	6.82	C II	6578.05	7.06	S II	5453.86	6.47
Fe II	5362.87	6.84	C II	6582.88	7.01			
Fe II	5425.25	6.81	N II	3995.00	7.83	Fe II	4233.17	7.11
Fe II	5534.83	6.87	N II	4447.03	7.75	Fe II	4522.63	7.16
Fe II	6147.74	6.85	N II	4601.48	7.82	Fe II	4549.47	7.02
Fe II	6149.26	6.85	N II	4607.15	7.81	Fe II	5276.00	7.07
			N II	4630.54	7.84	Fe II	5316.62	7.13
SK56			N II	5005.15	7.87			
			N II	5045.10	7.85	AV205		
He I	3867.47	0.12	N II	5666.63	7.83			
He I	3926.54	0.10	N II	5676.02	7.84	He I	4026.18	0.09
He I	3964.73	0.10				He I	4120.81	0.09
He I	4009.26	0.09	O I	7771.94	8.25	He I	4143.76	0.08
He I	4026.18	0.09	O I	7774.17	8.20	He I	4471.47	0.09
He I	4120.81	0.11	O II	4069.62	8.17	He I	4713.14	0.09
He I	4143.76	0.12	O II	4075.86	8.25	He I	4921.93	0.11
He I	4387.93	0.10	O II	4349.43	8.25	C II	4267.00	7.78
He I	4437.55	0.11	O II	4414.91	8.21	N I	7468.31	7.74
He I	4471.47	0.11	O II	4590.97	8.20	N I	8680.28	7.73
C II	4267.00	7.25	Mg II	4481.33	6.96			
C II	6578.05	7.32						

A LIST OF INVESTIGATED SPECTRAL LINES

Fe II	4416.83	6.58	Mg II	4390.51	6.78	Fe II	4555.89	6.89
Fe II	4489.19	6.84	Mg II	4433.99	6.82	Fe II	4576.33	6.77
Fe II	4491.40	6.71	Mg II	7877.05	6.75	Fe II	4580.06	6.65
Fe II	4508.28	6.75	Mg II	7896.04	6.78	Fe II	4582.84	6.64
Fe II	4515.34	6.70	Ti II	4028.36	4.21	Fe II	4620.51	6.78
Fe II	4520.23	6.74	Ti II	4163.63	4.23	Fe II	4629.34	6.79
Fe II	4522.63	6.83	Ti II	4287.88	4.29	Fe II	4635.33	6.91
Fe II	4541.52	6.81	Ti II	4294.09	4.18	Fe II	4666.75	6.73
Fe II	4549.47	6.77	Ti II	4301.92	4.10	Fe II	4731.44	7.00
Fe II	4555.89	6.69	Ti II	4312.87	4.09	Fe II	4993.35	6.82
Fe II	4629.34	6.65	Ti II	4314.97	4.07	Fe II	5316.62	6.75
Fe II	4731.44	6.89	Ti II	4330.24	4.06	Fe II	5325.56	6.74
Fe II	5362.87	6.85	Ti II	4394.02	3.91	Fe II	5362.87	6.90
Fe II	5534.83	6.89	Ti II	4395.00	4.25	Fe II	5425.25	6.86
Fe II	6147.74	6.94	Ti II	4399.79	4.16	Fe II	5534.83	6.82
Fe II	6149.26	6.92	Ti II	4417.72	4.18	Fe II	6147.74	6.77
			Ti II	4450.50	3.93	Fe II	6149.26	6.82
AV273			Ti II	4468.52	3.94			
			Ti II	4501.27	3.90	AV297		
He I	4026.18	0.09	Ti II	4563.77	4.16	He I	3867.47	0.09
He I	4471.47	0.09	Ti II	4571.96	4.23	He I	3964.73	0.09
He I	5875.60	0.09	Ti II	4779.98	4.16	He I	4009.26	0.09
C I	9078.29	7.42	Ti II	4805.09	4.25	He I	4026.18	0.10
C I	9088.51	7.40	Ti II	4911.18	3.89	He I	4120.81	0.10
N I	7423.64	7.76	Ti II	5188.68	4.09	He I	4168.97	0.10
N I	7442.30	7.79	Ti II	5336.78	4.05	He I	4387.93	0.11
N I	7468.31	7.74	Fe II	3938.29	6.82	He I	4437.55	0.11
N I	8680.28	7.82	Fe II	3945.21	6.73	He I	4471.47	0.08
N I	8683.40	7.72	Fe II	4122.64	6.88	He I	4713.14	0.09
N I	8686.15	7.78	Fe II	4124.79	6.85	He I	4921.93	0.10
N I	8703.25	7.78	Fe II	4173.46	6.60	C II	3920.69	7.54
N I	8711.70	7.73	Fe II	4178.86	7.06	C II	4267.00	7.49
N I	8718.84	7.75	Fe II	4273.32	6.79	N I	8683.40	7.98
O I	5330.73	8.16	Fe II	4296.57	6.83	N II	3995.00	7.98
O I	6155.96	8.14	Fe II	4303.17	6.69	O I	6155.96	8.17
O I	6158.15	8.14	Fe II	4385.39	6.68	O I	6158.15	8.21
Mg I	3829.36	6.75	Fe II	4416.83	6.63	Mg II	7896.04	6.63
Mg I	3832.30	6.81	Fe II	4489.19	6.86	S II	4294.40	6.54
Mg I	3838.29	6.76	Fe II	4491.40	6.70	S II	4815.55	6.48
Mg I	4702.99	6.87	Fe II	4508.28	6.93	S II	5014.04	6.57
Mg I	5172.68	6.77	Fe II	4515.34	6.85	S II	5320.72	6.46
Mg I	5183.60	6.78	Fe II	4520.23	6.84	S II	5432.80	6.34
Mg I	5528.41	6.81	Fe II	4522.63	7.03			
			Fe II	4541.52	6.81			

A.2 Lines Employed in Specific Stars with Abundance Information

O I	7774.17	7.90	He I	4713.14	0.11	Fe II	6147.74	7.07
O II	4649.13	7.92	He I	4921.93	0.10	Fe II	6149.26	7.06
Mg II	4481.33	6.64	C II	4267.00	7.44	AV392		
S II	5432.80	6.12	N I	7442.30	7.91	-----		
S II	5453.86	6.15	N I	7468.31	7.92	He I	4026.18	0.08
AV367			N I	8680.28	7.89	He I	5875.60	0.10
-----			N I	8683.40	7.85	C I	9088.51	7.57
He I	4471.47	0.08	O I	6155.96	8.34	N I	7468.31	7.35
He I	4713.14	0.09	O I	6158.15	8.27	N I	8680.28	7.32
He I	4921.93	0.10	Mg II	4433.99	6.89	N I	8683.40	7.39
He I	5875.60	0.09	S II	4815.55	6.41	O I	6155.96	8.15
C II	4267.00	7.48	S II	5432.80	6.47	O I	6158.15	8.17
C II	6578.05	7.39	Ti II	4300.06	4.85	Mg I	3829.36	6.90
N I	8680.28	7.93	Ti II	4395.00	4.63	Mg I	5172.68	6.93
N I	8683.40	7.96	Ti II	4443.78	4.77	Mg I	5183.60	6.97
N II	3995.00	7.97	Ti II	4468.52	4.49	Mg II	4390.51	6.94
O I	6155.96	8.26	Ti II	4571.96	4.78	Mg II	7877.05	6.92
O I	6158.15	8.23	Fe II	4122.64	7.09	Ti II	3913.48	4.67
S II	5014.04	6.66	Fe II	4173.46	6.57	Ti II	4163.63	4.69
S II	5320.72	6.60	Fe II	4178.86	6.96	Ti II	4171.92	4.72
S II	5345.71	6.47	Fe II	4233.17	7.23	Ti II	4287.88	4.70
S II	5606.15	6.51	Fe II	4273.32	7.06	Ti II	4294.09	4.75
Fe II	4173.46	6.51	Fe II	4296.57	7.01	Ti II	4301.92	4.44
Fe II	4233.17	6.89	Fe II	4303.17	6.95	Ti II	4312.87	4.48
Fe II	4385.39	6.88	Fe II	4385.39	6.88	Ti II	4395.00	4.54
Fe II	4508.28	6.90	Fe II	4416.83	6.86	Ti II	4443.78	4.37
Fe II	4515.34	6.93	Fe II	4489.19	6.94	Ti II	4468.52	4.41
Fe II	4520.23	6.97	Fe II	4491.40	6.83	Ti II	4501.27	4.44
Fe II	4522.63	6.89	Fe II	4508.28	6.97	Ti II	5188.68	4.63
Fe II	4549.47	6.79	Fe II	4515.34	6.98	Fe II	3938.29	6.87
Fe II	4629.34	6.82	Fe II	4520.23	6.98	Fe II	4122.64	6.97
Fe II	5276.00	6.69	Fe II	4522.63	7.03	Fe II	4173.46	6.84
AV382			Fe II	4541.52	7.06	Fe II	4178.86	7.18
-----			Fe II	4549.47	7.04	Fe II	4233.17	7.17
He I	3964.73	0.10	Fe II	4555.89	6.94	Fe II	4296.57	7.03
He I	4026.18	0.08	Fe II	4576.33	6.97	Fe II	4303.17	6.80
He I	4120.81	0.11	Fe II	4629.34	6.88	Fe II	4385.39	6.82
He I	4143.76	0.12	Fe II	4731.44	7.07	Fe II	4491.40	6.95
He I	4471.47	0.08	Fe II	5276.00	6.77	Fe II	4508.28	6.78
			Fe II	5316.62	6.95	Fe II	4515.34	6.78
			Fe II	5362.87	7.05	Fe II	4520.23	6.84
			Fe II	5534.83	6.94			

A LIST OF INVESTIGATED SPECTRAL LINES

Fe II	4522.63	7.16	Ti II	4294.09	4.41	He I	3926.54	0.12
Fe II	4541.52	6.83	Ti II	4300.06	4.43	He I	4120.81	0.13
Fe II	4576.33	6.85	Ti II	4314.97	4.52	He I	4168.97	0.11
Fe II	4620.51	6.81	Ti II	4395.00	4.30	He I	4387.93	0.11
Fe II	4629.34	6.84	Ti II	4443.78	4.08	He I	4437.55	0.12
Fe II	4666.75	6.89	Ti II	4468.52	4.21	C II	4267.00	6.91
Fe II	4731.44	7.04	Ti II	4501.27	4.12	C II	6578.05	6.96
Fe II	5316.62	6.82	Ti II	4571.96	4.27	N II	3995.00	7.91
Fe II	5362.87	7.10	Fe II	3938.29	6.84	N II	4447.03	7.86
Fe II	5534.83	7.18	Fe II	4122.64	6.81	N II	4601.48	7.96
Fe II	6147.74	6.78	Fe II	4173.46	6.71	N II	4607.15	7.94
Fe II	6149.26	6.84	Fe II	4178.86	7.03	N II	4630.54	7.95
			Fe II	4233.17	7.05	N II	4643.09	7.88
AV399			Fe II	4273.32	6.90	N II	5005.15	7.99
			Fe II	4296.57	6.77	N II	5045.10	7.91
He I	3964.73	0.10	Fe II	4303.17	6.88	N II	5686.21	7.98
He I	4026.18	0.10	Fe II	4385.39	6.87	N II	5710.77	8.01
He I	4143.76	0.08	Fe II	4416.83	6.77	O I	7771.94	8.21
He I	4387.93	0.10	Fe II	4489.19	6.82	O I	7774.17	8.16
He I	4471.47	0.09	Fe II	4491.40	6.79	O II	4069.62	8.13
He I	4713.14	0.10	Fe II	4508.28	6.87	O II	4072.16	8.19
He I	4921.93	0.07	Fe II	4515.34	6.82	O II	4075.86	8.16
He I	5875.60	0.08	Fe II	4520.23	6.88	O II	4351.26	8.23
C I	9088.51	7.75	Fe II	4541.52	6.86	O II	4366.89	8.21
C II	4267.00	7.76	Fe II	4549.47	7.01	O II	4414.91	8.21
N I	7468.31	7.82	Fe II	4555.89	6.89	O II	4416.97	8.19
N I	8680.28	7.81	Fe II	4576.33	6.87	O II	4590.97	8.19
N I	8683.40	7.83	Fe II	4580.06	6.94	Mg II	4481.33	6.89
N I	8711.70	7.83	Fe II	4582.84	6.78	S II	5453.86	6.46
N I	8718.84	7.84	Fe II	4620.51	6.81			
O I	5330.73	8.14	Fe II	4629.34	6.75			
O I	6155.96	8.16	Fe II	4666.75	6.82			
O I	6156.74	8.11	Fe II	4731.44	6.93	AV463		
O I	6158.15	8.12	Fe II	5276.00	6.75			
Mg I	5172.68	6.78	Fe II	5316.62	6.91	He I	4471.47	0.09
Mg I	5183.60	6.81	Fe II	5325.56	6.88	He I	5875.60	0.09
Mg II	4390.51	6.69	Fe II	5362.87	7.02	C I	9078.29	7.53
Mg II	4433.99	6.72	Fe II	5425.25	6.91	N I	7468.31	7.23
S II	5032.43	6.47	Fe II	5534.83	7.00	N I	8680.28	7.29
S II	5453.86	6.51	Fe II	6147.74	6.81	N I	8686.15	7.27
Ti II	3900.56	4.31	Fe II	6149.26	6.78	O I	6155.96	8.13
Ti II	3913.48	4.06	AV443			O I	6158.15	8.22
						O I	7001.90	8.19
			He I	3867.47	0.13			

A LIST OF INVESTIGATED SPECTRAL LINES

Fe II	4385.39	7.22	S II	5432.80	6.17	N II	4447.03	7.56
Fe II	4508.28	7.26	S II	5453.86	6.22	N II	4607.15	7.57
Fe II	4515.34	7.31	S II	5473.61	6.53	N II	4630.54	7.49
Fe II	4520.23	7.30	S II	5606.15	6.37	N II	4643.09	7.53
Fe II	4522.63	7.21	Fe II	4233.17	7.25	N II	5005.15	7.61
Fe II	4549.47	7.18	Fe II	4508.28	7.33	N II	5045.10	7.59
Fe II	4555.89	7.20	Fe II	4515.34	7.36	N II	5666.63	7.55
Fe II	4629.34	7.24	Fe II	4549.47	7.06	N II	5679.56	7.58
Fe II	5276.00	7.13	Fe II	4629.34	7.18	O I	7771.94	8.03
Fe II	5316.62	7.24	Fe II	5276.00	7.05	O I	7774.17	7.97
			Fe II	5316.62	7.18	O II	4069.62	7.96
SK196						O II	4072.16	8.08
						O II	4075.86	8.02
			SK202			O II	4351.26	8.02
He I	3867.47	0.10				O II	4414.91	7.97
He I	4437.55	0.11	He I	3819.60	0.10	O II	4641.81	8.03
He I	4713.14	0.10	He I	3867.47	0.09	Mg II	4481.33	6.77
C II	4267.00	7.07	He I	3926.54	0.08	Mg II	7896.04	6.79
C II	6578.05	7.15	He I	3964.73	0.10	S II	4815.55	6.32
C II	6582.88	7.14	He I	4009.26	0.09	S II	5032.43	6.31
N I	8680.28	8.01	He I	4168.97	0.10	S II	5320.72	6.27
N II	3995.00	7.92	He I	4437.55	0.09	S II	5432.80	6.22
N II	4447.03	7.99	He I	4713.14	0.10	S II	5453.86	6.21
N II	5005.15	8.07	C II	3920.69	6.85	S II	5473.61	6.36
O I	6155.96	8.15	C II	4267.00	6.77	S II	5606.15	6.42
S II	4162.67	6.43	C II	6578.05	6.68			
S II	5320.72	6.23	C II	6582.88	6.82			
			N II	3995.00	7.62			

B Acknowledgements

I am deeply grateful to my whole family (especially parents, grandparents, my sister, uncles, aunts, ...) for their ongoing (more than financial) support throughout the years of my studies for the diploma and the Ph.D. phases. They have never had any doubt in what I was doing although they presumably did not always understand 100% of what the heck that actually was. Probably my fault...

I want to thank Uli Heber, my Ph.D. advisor and co-chief of the institute, for the opportunity to work on this interesting and extensive topic, for his permanently open door and open ears, for excellent guidance and pieces of advice, and – a point not to be underestimated – for maintaining one of the best working atmospheres at the observatory one can wish for.

Norbert Przybilla, the “co-supervisor” during the Ph.D. phase deserves many thanks for very similar reasons. As my roommate, he was likewise busy with discussing my work and providing advice. He can offer an amazing knowledge in a lot of astrophysical fields including atomic physics and the processes in stellar atmospheres. Despite his constantly high work load, this was never a problem. Furthermore, he provided the contact to Rolf-Peter Kudritzki at the Institute for Astronomy (IfA) in Hawai’i, which allowed for a stay abroad of six months.

This brings me to Rolf-Peter Kudritzki himself, director of the IfA, who gave me the opportunity to work at this center of astronomic research. The time there permitted to get to know several interesting people and fields in astronomy as well as to enjoy the overwhelmingly beautiful and awe-inspiring nature of Hawai’i. I had a great time there. Rolf-Peter Kudritzki also added the distance determination point to this thesis, had always an open door in Hawai’i, and showed strong interest and dedication to the work which was started in Hawai’i and continued in Bamberg. In addition, I want to thank him for helping several times on short notice (sorry) and for providing the second assessment of this thesis.

Concerning the work in Hawai’i, Miguel Urbaneja and Fabio Bresolin (both at the IfA) also deserve many thanks for support and interesting discussions.

I also appreciate the various pieces of advice from and the social activities with all the other people at the institute in Bamberg: the normal optical astronomers as well as the X-ray group. In particular, I would like to thank Ingo Kreykenbohm, Manfred Hanke, and Moritz Boeck for patient help with IDL, ISIS, and the institutes computer network, Markus Firnstein for a lot of fruitful discussions connecting his and my work (similar objects, different galaxies), Fernanda Nieva for a lot of advice as well as the contact to the MPA, and Andreas Irrgang for creating such a peaceful and harmonic atmosphere at the observatory (and of course for help in many work-related aspects). Together with Alfred, Mrs. Bues, Christian, Christoph, Cornelia, Felix, Fernanda, Fritz, Heiko, Horst, Ivica, Jörn, Johannes, Laura, Lew, Maria, Matthias Refiz, Sebastian, Stefan, Stephan, Thomas (x 2), Veronika, and Victoria there was an excellent atmosphere at the institute – and a considerable amount of birthday cakes. Special thanks go to my friends from university, especially Christian Schmitt (live long and prosper!), Volker Kuntermann, and Tilman Rügheimer.

Furthermore, I would like to acknowledge the financial support of the Bavarian

B ACKNOWLEDGEMENTS

Elite Program (Bayerische Eliteförderung) and the German National Academic Foundation (Studienstiftung des deutschen Volkes) throughout the Ph.D. phase as well as the non-financial support of the latter in the form of summer academies, personal tutorial groups, and other programs.

During my research, I have made extensive use of NASA's Astrophysics Data System Abstract Service, the various tools at CDS (Centre de Données astronomiques de Strasbourg), and the NIST atomic spectra database. This work is based on observations collected at the European Organisation for Astronomical Research in the Southern Hemisphere, Chile, with proposals 064.H-0106 and 078.D-0286(A).

References

- Aerts, C., Puls, J., Godart, M., & Dupret, M.-A. 2009, *A&A*, 508, 409
- Aller, L.H., Czyzak, S.J., Keyes, C.D., & Boeshaa, G. 1974, *PNAS*, 71, 4496
- Aller, L.H., Keyes, C.d., & Czyzyk, S.J. 1979, *PNAS*, 76, 1525
- Ardeberg, A., & Maurice, E. 1977, *A&AS*, 30, 261
- Ardeberg, A. 1980, *A&AS*, 42, 1
- Arellano Ferro, A., Mantegazza, L., & Antonello, E. 1991, *A&A*, 246, 341
- Azzopardi, M. 1981, Ph.D. Thesis, Paul Sabatier University of Toulouse, No. 979, Vol. 1
- Azzopardi, M, Vigneau, J. 1982, *A&AS*, 50, 291
- Azzopardi, M., Vigneau, J., Macquet, M. 1975, *A&AS*, 22, 285
- Barnard, A.J., Cooper, L., & Shamey, L.J. 1969, *A&A*, 1, 28
- Bates, D., & Damgaard, A. 1949, *Phil. Trans. R. Soc. London, Ser. A*, 242, 101
- Becker, S. R., & Butler, K. 1988, *A&A*, 201, 232
- Becker, S. R. 1998, in *Boulder-Munich II: Properties of Hot, Luminous Stars*, ed. I. D. Howarth (San Francisco: ASP), 137
- Bresolin, F., Kudritzki, R.-P., Mendez, R.H. & Przybilla, N. 2001, *ApJ*, 548, L159
- Bresolin, F., Gieren, W., Kudritzki, R. P., Pietrzyński, G., & Przybilla, N. 2002, *ApJ*, 567, 277
- Bresolin, F, Pietrzyński, G., Gieren, W., et al. 2004, *ApJ*, 600, 182
- Butler, K., & Giddings, J.R. 1985, in *Newsletter on Analysis of Astronomical Spectra*, No. 9 (London, Univ. London)
- Butler, K., Mendoza, C., & Zeippen, C.J. 1993, *J. Phys. B*, 26, 4409
- Caldwell, J.A.R., & Coulson, I.M. 1986, *MNRAS*, 218, 223
- Cantiello, M., Langer, N., Brott, I., et al. 2009, *A&A*, 499, 279
- Carrera, R., Gallart, C., Aparicio, A., et al. 2008, *AJ*, 136, 1039
- Cardelli, J.A., Clayton, G.C., & Mathis, J.S. 1989, *ApJ*, 345, 245
- Cescutti, G., Matteucci, F., François, P., & Chiappini, C. 2007, *A&A*, 462, 943
- Chiosi, E., & Vallenari, A. 2007, *A&A*, 466, 165

REFERENCES

- Cioni, M.-R.L. 2009, *A&A*, 506, 1137
- Cutri, R. M., et al. 2003, in NASA/IPAC Infrared Science Archive, The IRSA 2MASS All-Sky Catalog of Point Sources, <http://irsa.ipac.caltech.edu/applications/Gator>
- Cowley, C. 1971, *Observatory*, 91, 139
- Dennefeld, M., & Stasińska, G. 1983, *A&A*, 118, 234
- Dimitrijević, M.S., & Sahal-Bréchet, S. 1990, *A&AS*, 82, 519
- Dimitrijević, M.S., & Sahal-Bréchet, S. 1996, *A&AS*, 117, 127
- Dufour, R.J. 1975, *ApJ*, 195, 315
- Dufour, R.J. 1984, *IAUS* 108, 353
- Dufour, R.J., & Harlow, W.V. 1977, *ApJ*, 216, 706
- Dufour, R.J., Shields, G.A., & Talbot, R.J. 1982, *ApJ*, 252, 461
- Dufton, P.L., Ryans, R.S.I., Trundle, C., et al. 2005, *A&A*, 434, 1125
- Feast, M.W. 1988, *ASP Conf. Ser.*, 4, 9
- Fuhr, J.R., Martin, G.A., & Wiese, W.L. 1988, *J. Phys. & Chem. Ref. Data*, Vol. 17, Suppl. 4
- Fuhr, J.r., & Wiese, W.L., 1998, in *CRC Handbook of Chemistry and Physics*, 79th ed., eed. D.R. Lide (Boca Raton: CRC Press)
- Garmany, C.D., Conti, P.S., & Massey, Ph. 1987, *AJ*, 93, 1070
- Garnett, D.R., Skillman, E.D., Dufour, R.J., et al. 1995, *ApJ*, 443, 64
- Garnett, D.R. 1999, *IAUS* 190, 266
- Giddings, J.R., 1981, Ph.D. thesis, Univ. London
- Gray, D.F. 1976, *The observation and analysis of stellar photospheres*, New York - London - Sydney - Toronto, John Wiley & Sons
- Grebel, E.K., 1999, in: Whitelock P., Cannon R. (eds.), *The Stellar Content of Local Group Galaxies* (ASP, San Francisco), 17
- Grevesse N., & Sauval, A.J. 1998, *Space Sci. Rev.*, 85, 161
- Griem, H.R. 1964, *Plasma Spectroscopy* (New York: McGraw-Hill Book Company)
- Griem, H.R. 1974, *Spectral Line Broadening by Plasmas* (New York and London: Academic Press)
- Groenewegen, M.A.T. 2000, *A&A*, 363, 901

REFERENCES

- Hatzidimitriou, D. & Hawkins, M.R.S. 1989 MNRAS, 241, 667
- Harries, T. J., Hilditch, R. W., & Howarth, I. D. 2003, MNRAS, 339, 157
- Harris, H.C. 1983, AJ, 88, 507
- Harris, J., & Zaritsky, D. 2004, AJ, 127, 1531
- Heber, U., Moehler, S., Napiwotzki, R., Thejll, R., & Green, E.M. 2002, A&A, 383, 938
- Heger, A., & Langer, N. 2000, ApJ, 544, 1016
- Heger, A., Woosley, S. E., & Spruit, H. C. 2005, ApJ, 626, 350
- Heydari-Malayeri, M., Le Bertre, T., & Magain, P. 1988, A&A, 195, 230
- Hilditch, R. W., Howarth, I. D., Harries, T. J. 2005, MNRAS, 357, 304
- Hindman, J.V. 1964, IAU/URSI Symp. 20, 255
- Hindman, J.V. 1967, Aust. J. Phys. 20, 147
- Hirschi, R., Meynet, G., & Maeder, A. 2004, A&A, 425, 649
- Hubeny, I. 1997, in De Greve, J.P., Blomme, R., & Hensberge, H. (eds.), *Stellar Atmospheres: Theory and Observations*, Springer, Berlin, 1
- Humphreys, R.M. 1983, ApJ, 265, 176
- Hunter, I., Dufton, P.L., Smartt, S.J., et al. 2007, A&A, 466, 277
- Hunter, I., Brott, I., Langer, N., et al. 2009, A&A, 496, 841
- Husfeld, D., Butler, K., Heber, U., & Drilling, J. S. 1989, A&A, 222, 150
- Johnson, H.M. 1961, PASP 73, 20
- Karttunen, H., Kröger, P., Oja, H., Poutanen, M., & Donner, K., J. 1994, *Fundamental Astronomy*, Berlin Heidelberg New York, Springer-Verlag
- Kaufer, A., Stahl, O., Tubbesing, S. et al. 1999, The Messenger 95, 8
- Kaufer, A., Venn, K.A., Tolstoy, E., Pinte, C., Kudritzki, R.P. 2004, AJ, 127, 2723
- Keller, S.C., & Wood, P.R. 2006, ApJ, 642, 834
- Kippenhahn, R., & Weigert, A. 1990, *Stellar Structure and Evolution*, Berlin Heidelberg, Springer-Verlag
- Kroupa, P. 2001, MNRAS, 322, 231
- Kudritzki, R.P. 1973, A&A, 28, 103
- Kudritzki, R.P., & Puls, J. 2000, ARA&A, 38, 613

REFERENCES

- Kudritzki, R.P., Puls, J., Lennon, D.J., et al. 1999, A&A, 350, 970
- Kudritzki, R.-P., Bresolin, F., & Przybilla, N. 2003, ApJ, 582, L83
- Kudritzki, R.-P., Urbaneja, M.A., Bresolin, F., Przybilla, N., Gieren, W., & Pietrzyński, G. 2008, ApJ, 681, 269
- Kudritzki, R.-P. 2010, AN, 331, 459
- Kurt, C.M., & Dufour, R.J. 1998, Rev. Mex. Astron. Astrofis., 7, 202
- Kurucz, R. L. 1992, Rev. Mex. Astron. Astrofis., 23, 45
- Kurucz, R.L. 1993, Kurucz CD-ROM No. 13 (Cambridge, Mass.: Smithsonian Astrophysical Observatory)
- Kurucz, R.L., & Bell, B. 1995, Kurucz CD-ROM No. 23 (Cambridge, Mass.: Smithsonian Astrophysical Observatory)
- Laney, C.D., & Stobie, R.S. 1986, MNRAS, 222, 449
- Lee, J.-K., Rolleston, W. R. J., Dufton, P. L., & Ryans, R. S. I. 2005, A&A, 429, 1025
- Lequeux J., Peimbert, M., Rayo, J.F., Serrano, A., & Torres-Peimbert, S. 1979, A&A, 80, 155
- Luck, R.E., & Lambert, D.L. 1992, ApJS, 79, 303
- Luck, R.E. 1998, AJ, 115, 605
- Lucy, L.B. 1976, ApJ, 206, 499
- Madore, B.F., & Freedman, W.L. 1991, PASP, 103, 933
- Maeder, A. 2009, *Physics, Formation and Evolution of Rotating stars*, Berlin Heidelberg, Springer Verlag
- Maeder, A., & Meynet, G. 2001, A&A, 373, 555
- Maeder, A., & Meynet, G. 2005, A&A, 440, 1041
- Martin, G.A., Fuhr, J.R., & Wiese, W.L. 1988, J. Phys. & Chem. Ref. Data, Vol. 17, Suppl. 3
- Martin, N., Maurice, E., & Lequeux, J. 1989, A&A, 215, 219
- Massey, P. 2002, ApJS, 141, 81
- Massey, Ph., Lang, C.C., DeGioia-Eastwood, K., & Garmany, C.D. 1995, ApJ, 438, 188
- Mathewson, D.S., & Ford, V.L. 1984, IAUS 108, 225

REFERENCES

- Mathewson, D.S., Ford, V.L., & Visvanathan, N. 1986, ApJ, 301, 664
- Mathewson, D.S., Ford, V.L., & Visvanathan, N. 1988, ApJ, 333, 617
- Matteucci, F. 1991, in I.J. Danziger & K. Kj ar (eds.), ESO/EIPC Workshop: *SN 1978A and Other Supernovae*, ESO, Garching, 703
- Meynet, G., & Maeder, A. 2003, A&A, 404, 975
- Meynet, G., & Maeder, A. 2005, A&A, 429, 581
- Mihalas, D. 1970, *Stellar Atmospheres*, San Francisco, W. H. Freeman and Company
- Mottini, M., Romaniello, M., Primas, F., et al. 2006, Mem. S.A.It., 77, 156
- Nieva, M.F., & Przybilla, N. 2006, ApJ, 639, L39
- Nieva, M.F. 2007, Ph.D. thesis, University Erlangen-Nuremberg/Observatory Rio de Janeiro
- Nieva, M.F., & Przybilla, N. 2008, A&A, 481, 199
- No el, N. E. D., Aparicio, A., Gallart, C., et al. 2009, ApJ, 705, 1260
- North, P.L. Gauderon, R., & Royer, F. 2009, IAUS 256, 57
- Pagel, B.E.J. 1992, in D. Alloin & G. Stasinska (eds.), *The Feedback of Chemical Evolution on the Stellar Content of Galaxies*, Paris: Observatoire, 87
- Pagel, B.E.J., Edmunds, M.G., Fosbury, R.A.E., & Webster, B.L. 1978, MNRAS, 184, 569
- Pagel, B.E.J., & Tautvai ien , G. 1995, MNRAS, 276, 505
- Pagel, B.E.J. 1997, *Nucleosynthesis and Chemical Evolution of Galaxies*, Cambridge, Cambridge University Press
- Parisi, M.C., Geisler, D., Grocholski, A.J., Clari , J.J., & Sarajedini, A. 2010, AJ, 139, 1168
- Prialnik, D. 2010, *Theory of Stellar Structure and Evolution*, Cambridge, Cambridge University Press
- Przybilla, N. 2002, Ph.D. Thesis, Univ. Munich
- Przybilla, N. 2005, A&A, 443, 293
- Przybilla, N., Butler K., Becker S. R., Kudritzki, R. P., & Venn, K. A. 2000, A&A, 359, 1085
- Przybilla, N., & Butler, K. 2001, A&A, 379, 955
- Przybilla, N., Butler, K., Becker, S. R., & Kudritzki, R. P. 2001a, A&A, 369, 1009

REFERENCES

- Przybilla, N., Butler, K., & Kudritzki, R. P. 2001b, *A&A*, 379, 936
- Przybilla, N., & Butler, K. 2004, *ApJ*, 609, 1181
- Przybilla, N., Butler, K., Becker, S.R., & Kudritzki R.P. 2006, *A&A*, 445, 1099
- Puls, J., Urbaneja, M.A., Venero, R. et al. 2005, *A&A* 435, 669
- Reid, I.N., & Strugnell, P.R. 1986, *MNRAS*, 221, 887
- Russell, S.C., & Bessell, M.S. 1989, *ApJS*, 70, 865
- Russell, S.C., & Dopita, M.A. 1990, *ApJS*, 74 93
- Rybicki, G.B., & Hummer, D.G. 1991, *A&A*, 245, 171
- Salaris, M., & Cassisi, S. 2008, *Evolution of Stars and Stellar Populations*, Chichester, John Wiley & Sons
- Sanduleak, N. 1968, *AJ*, 73, 246
- Schoenrich, R., & Binney, J. 2009, *MNRAS*, 396, 203
- Spite, M., Barbuy, B., & Spite, F. 1989a, *A&A*, 222, 35
- Spite, F., Spite, M., & François, P. 1989b, *A&A*, 210, 25
- Spite, M., & Spite, F. 1990, *A&A*, 234, 67
- Stehlé, C., & Hutcheon, R. 1999, *A&AS*, 140, 93
- Stothers, R.B. 1988, *ApJ*, 329, 712
- Subramanian, S., & Subramaniam, A. 2009, *A&A*, 496, 399
- Szewczyk, O., Pietrzyński, G., Gieren, W. et al. 2009, *AJ*, 138, 1661
- Thackeray, A.D. 1978, *MNRAS*, 184, 699
- Trundle, C., Dufton, P.L., Hunter, I., et al. 2007, *A&A*, 471, 625
- Trundle, C., Lennon, D.J., Puls, J., & Dufton, P.L. 2004, *A&A*, 417, 217
- Trundle, C., & Lennon, D.J. 2005, *A&A*, 434, 677
- U, V., Urbaneja, M.A., Kudritzki, R.-P., et al. 2009, *ApJ*, 704, 1120
- Udalski, A., Szymanski, M., Kubiak, M., et al. 1998, *Acta Astron.*, 48, 147
- Unsöld, A., & Baschek, B. 1994, *Der neue Kosmos*, Berlin Heidelberg New York, Springer-Verlag
- Urbaneja, M. A., Herrero, A., Bresolin, F., et al. 2005, *ApJ*, 622, 862
- Urbaneja, M.A., Kudritzki, R.-P., Bresolin, F., & Przybilla, N. 2008, *ApJ*, 684, 118

REFERENCES

- Venn, K.A. 1999, ApJ, 518, 405
- Venn, K.A., Lennon, D.J., Kaufer, A., et al. 2001, ApJ, 547, 765
- Venn, K.A., McCarthy, J.K., Lennon, D. J., et al. 2000, ApJ, 541, 610
- Venn, K.A., & Przybilla, N. 2003, ASPC, 304, 20
- Venn, K.A., Tolstoy, E., Kaufer, A., et al. 2003, AJ, 126, 1326
- Vermeij, R., & van der Hulst, J.M. 2002, A&A, 391, 1081
- Vidal, C.R., Cooper, J., & Smith, E.W. 1973, ApJS, 25, 37
- Vrancken, M., Butler, K., & Becker, S. R. 1996, A&A, 311, 661
- Walker, A.R., & Mack, P. 1988, AJ96, 872
- Welch, D.L., McLaren, R.A., Madore,, B.F., & McAlary, Ch.W. 1987, ApJ, 321, 162
- Westerlund, B.E. 1997, *The Magellanic Clouds*, Cambridge, Cambridge University Press
- Wiese, W.L., Smith, M.W., & Glennon, B.M., 1966, Nat. Stand. Ref. Data Ser., Nat. Bur. Stand. (U.S.), NSRDS-NBS 4, Vol. I
- Wiese, W.L., Smith, M.W., & Miles, B.M., 1969, Nat. Stand. Ref. Data Ser., Nat. Bur. Stand. (U.S.), NSRDS-NBS 22, Vol. II
- Wiese, W.L., Fuhr, J.R., & Deters, T.M. 1996, J. Phys. & Chem. Ref. Data, Mon. 7
- Xu, H. Y., & Li, Y. 2004a, A&A, 418, 213
- Xu, H. Y., & Li, Y. 2004b, A&A, 418, 225

Lebenslauf

Name	Florian Schiller	
Geburtsdatum	31.03.1983	
Geburtsort	Sulzbach-Rosenberg	
Staatsangehörigkeit	deutsch	
Schulbildung	09/1989 – 07/1993	Grundschule: Jahnschule Sulzbach-Rosenberg
	09/1993 – 06/2002	Gymnasium: Herzog-Christian-August-Gymnasium Sulzbach-Rosenberg
Studium	10/2002 – 03/2006	Studium der Physik an der Friedrich-Alexander-Universität Erlangen-Nürnberg
	31.03.2006 seit 01.04.2006	Abschluss: Dipl.-Phys. Univ. Promotionsstudent an der Friedrich-Alexander-Universität Erlangen-Nürnberg, Sternwarte Bamberg; Betreuer: Prof. Dr. U. Heber
Berufliche Laufbahn	10/2005 – 03/2006	Studentische Hilfskraft an der Dr. Remeis-Sternwarte Bamberg
	04/2006 – 10/2007	Wissenschaftliche Hilfskraft an der Dr. Remeis-Sternwarte Bamberg
	11/2007 – 04/2008	Visiting research assistant am Institut für Astronomie in Honolulu
	05/2008 – 07/2010	Wissenschaftliche Hilfskraft an der Dr. Remeis-Sternwarte Bamberg
Stipendien	11/2006 – 02/2007	Promotionsstipendium der Bayerischen Eliteförderung
	03/2007 – 10/2007 & 05/2008 – 04/2010	Promotionsstipendium der Studienstiftung des deutschen Volkes

Curriculum Vitae

Name	Florian Schiller	
Date of Birth	March 31st 1983	
Place of Birth	Sulzbach-Rosenberg, Germany	
Citizenship	German	
Primary School	09/1989 – 07/1993	Jahnschule Sulzbach-Rosenberg
Secondary School	09/1993 – 06/2002	Herzog-Christian-August- Gymnasium Sulzbach-Rosenberg
University	10/2002 – 03/2006	Undergraduate studies of physics at the Friedrich-Alexander-University Erlangen-Nuremberg, Germany
	March 31st 2006 since April 1st 2006	Degree: Dipl.-Phys. Univ. Ph.D. student at the Friedrich- Alexander-University Erlangen- Nuremberg, Observatory Bamberg; Supervisor: Prof. Dr. U. Heber
Employment History	10/2005 – 03/2006	Student assistant at the Dr. Remeis Observatory Bamberg
	04/2006 – 10/2007	Scientific assistant at the Dr. Remeis Observatory Bamberg
	11/2007 – 04/2008	Visiting research assistant at the In- stitute for Astronomy in Honolulu
	05/2008 – 07/2010	Scientific assistant at the Dr. Remeis Observatory Bamberg
Scholarships	11/2006 – 02/2007	Ph.D. scholarship of the Bavar- ian Elite Program (Bayerische Elite- förderung)
	03/2007 – 10/2007 & 05/2008 – 04/2010	Ph.D. scholarship of the German Na- tional Academic Foundation (Stu- dienstiftung der deutschen Volkes)